The Fate and Mobility of Heavy Metals in East Anglian Salt Marsh Sediments

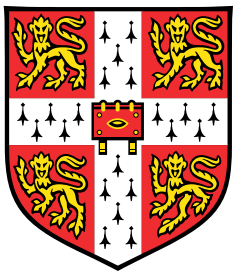

Alec Martin Hutchings

Department of Earth Sciences
University of Cambridge

This dissertation is submitted for the degree of
Doctor of Philosophy

Hughes Hall College

October 2020

Declaration

I hereby declare that except where specific reference is made to the work of others, the contents of this dissertation are original and have not been submitted in whole or in part for consideration for any other degree or qualification in this, or any other university. This dissertation is my own work and contains nothing which is the outcome of work done in collaboration with others, except as specified in the text and Acknowledgements. The total length does not exceed the 275 numbered page limit for the Degree Committee of Earth Sciences, including 225 pages of text, appendices, bibliography, footnotes, tables and equations.

Alec Martin Hutchings
October 2020

Abstract

The Fate and Mobility of Heavy Metals in East Anglian Salt Marsh Sediments

Alec Martin Hutchings

Measuring the evolution of redox conditions in Earth's atmosphere and oceans through time is a prominent challenge in Earth Sciences. Geochemical proxies in sedimentary rocks used to reconstruct past redox conditions—such as the speciation of iron mineralogy, δ^{98}Mo, and δ^{53}Cr—rely on the assumption that the geochemical signature acquired at the sediment surface is translated directly into the geologic record.

In this thesis, I have used East Anglian salt marsh anoxic pond sediments as a modern analogue to test the effect of diagenesis on these paleoredox proxies. This site is particularly applicable because of an intriguing geochemical dichotomy that exists; the anoxic sedimentary porewater beneath ponds either contains high concentrations of ferrous iron or aqueous sulfide, which are somewhat comparable to the ferruginous and euxinic ocean sediments of the mid-Proterozoic respectively.

I found that proximity of tidal creeks imparts a first order control on the spatial distribution of sulfide-rich and iron-rich pond sediments. Evidence is provided of a geochemical "switching" from iron-rich pond sediment chemistry to sulfide-rich pond chemistry which is hypothesised to be driven by an accumulation of organic carbon over time.

High resolution porewater and sedimentary δ^{98}Mo samples are used to infer the behaviour of Mo within these sediments. The speciation of iron mineralogy is the primary control on Mo distribution in iron-rich pond sediment. Two separate sulfide-rich pond sediments with similar sulfide concentrations have very different δ^{98}Mo profiles; it is hypothesised that these differences reflect the amount of time since that pond sediment was iron-rich. This suggests that sedimentary δ^{98}Mo can be altered during a diagenetic redox change.

A method to measure δ^{53}Cr using thermal ionisation mass spectrometry is developed and used to determine the Cr isotope composition of these pond sediments. The δ^{53}Cr in

iron-rich and sulfide-rich pond sediment occupies a narrow isotope range which is more similar to oxic marine settings than anoxic marine settings. This implies that the redox conditions of the water column, rather than the sediment porewater, dictates the δ^{53}Cr which is recorded.

The reaction of aqueous sulfide with iron minerals is a fundamental diagenetic reaction observed in these salt marsh pond sediments. I used a simple diagenetic model to illustrate how a significant proportion of mid-Proterozoic sedimentary rock samples classified as euxinic using conventional iron speciation classification could be explained by solely diagenetic conversion of iron mineralogy.

The work in this thesis addresses the hitherto underappreciated importance of early diagenetic reactions on paleoredox proxies. A better understanding of these reactions will help deconvolve what the actual paleoredox conditions were in the geological past.

Acknowledgements

There are so many people who have made the last three years a fantastic experience and deserve a thank you. I always had someone to turn to during this whole experience, and for that I am truly grateful.

I wish to first thank Sasha Turchyn. I felt very fortunate to have someone who could inspire me to continue when times were hard and who always provided positivity in any situation. Thank you for your support, your generosity and your kind-heartedness. I could not have asked for a better supervisor.

I also want to acknowledge my co-supervisor, Anirban Basu. I enjoyed our many coffees in the boilerhouse cafe and our in depth discussions about science. I always felt I gained a fresh perspective on a subject after meeting with you and your passion for science was an inspiration. I am sure you are glad to hear I will no longer be bringing worms into the lab.

I want to thank Alex Dickson for his molybdenum analysis method, for his vast geochemical knowledge and for teaching me to be a pedant in the lab. I also wish to thank my academic friends, Neil Davies and Ed Tipper, for making my academic progress meetings so relaxed and interesting. They both provided insights into my project I would never have thought of independently.

I thank Nick Tosca and Rachael James for making my viva a thoughtful, happy and memorable experience. Thank you for the positivity about my work.

I have to thank Mervyn Greaves for teaching me how to use the ICP-MS. I have to thank Sambuddha Misra for teaching me how to not break the ICP-MS.

I could dedicate a paragraph to each and every member of my lab group at Cambridge. Special thanks go to Gilad Antler, who I have to thank for teaching me to become a good field geochemist. I cannot thank him enough for taking me under his wing during my first year. I want to thank Harold Bradbury, for being a major source of support during my PhD and for countless hours talking through things. I also want to thank Katie Halloran, Emily Doyle, Chin Yik Lin, Jo Clegg, Caroline Daunt and Gabby Kleber for the help, conversations and laughs during my PhD.

I made a lot of good friends in the department who have always been there for a drink or a chat when I needed them. Thank you to Dan, Victoria, Mads, Katy and Will amongst many

others. I want to particularly thank Luke for countless afternoons and evenings of games, dinners and drinks.

Special mentions go to my friends from around the country who have had to deal with my absence at many points over the last three years. I thank you all for being patient and being there when I needed you.

I want to thank my family: my Mum, my Dad, Graham, Amanda, Steve, Marcus and Abbie. I could not have done this without your support. Thank you for providing somewhere where I could escape to when I needed it and always being a phone call away.

Finally, I want to thank Phoebe. There are not many people who would help me take sediment cores from Norfolk salt marshes in February (understandably). Thank you for being supportive beyond compare, for always being positive and for making me smile every single day of my PhD.

Table of contents

List of figures xv

List of tables xix

1 Introduction 1
- 1.1 Redox conditions through Earth history . . . 1
- 1.2 Paleoredox proxies and the role of diagenesis . . . 3
  - 1.2.1 Molybdenum and the δ^{98}Mo isotope system . . . 4
  - 1.2.2 Chromium and the δ^{53}Cr isotope system . . . 5
  - 1.2.3 Iron Speciation . . . 5
- 1.3 Early sedimentary diagenesis . . . 5
- 1.4 Salt marsh pond sediments as potential analogues . . . 6
- 1.5 East Anglian salt marsh pond sediments . . . 8
- 1.6 Thesis Roadmap . . . 9

2 Controls on the Spatial Distribution of Pond Sediment Geochemistry in East Anglian Salt Marshes 11
- 2.1 Introduction . . . 11
  - 2.1.1 Chapter outline . . . 11
  - 2.1.2 East Anglian salt marshes: a geochemical dichotomy in pond sediments 12
- 2.2 Methods . . . 13
  - 2.2.1 Field sites . . . 13
  - 2.2.2 Porewater collection . . . 15
  - 2.2.3 Analytical methods . . . 15
  - 2.2.4 Mapping of ponds . . . 16
  - 2.2.5 *In situ* sampling . . . 17
  - 2.2.6 Sediment core transect at Abbotts Hall Farm, Essex . . . 21
  - 2.2.7 Carbon content analysis . . . 21

2.3 Results . . . 22
2.3.1 Porewater geochemistry in sediment cores taken from 2013-2018 . 22
2.3.2 Mapping of pond distributions . . . 25
2.3.3 Pond characteristics and water depths . . . 29
2.3.4 *In situ* sampling from March 2017 – May 2018 . . . 29
2.4 Discussion . . . 31
2.4.1 Salt marsh pond sediment chemistry . . . 31
2.4.2 Iron-rich pond sediment chemistry . . . 32
2.4.3 Sulfide-rich pond sediment chemistry . . . 34
2.4.4 Intermediate pond sediment chemistry . . . 35
2.4.5 Spatial distribution of salt marsh pond sediment chemistry . . . 37
2.4.6 Potential switching of pond sediment geochemistry . . . 38
2.4.7 Potential hypotheses for controls on pond sediment chemistry . . . 39
2.4.8 Potential mechanism for pond sediment distribution . . . 45
2.5 Conclusion . . . 51
2.6 Implications for further chapters . . . 52

3 Method Development for Trace Element Analysis using ICP-MS and for Chromium Isotope Analysis on the Thermal Ionisation Mass spectrometer (TIMS) 53
3.1 Introduction . . . 53
3.1.1 Chapter outline . . . 53
3.2 Sample collection . . . 54
3.2.1 Sediment core collection . . . 54
3.2.2 Porewater extraction . . . 55
3.2.3 Sediment extraction . . . 56
3.3 Analysis of trace metals in saline porewaters and aqua regia leaches . . . 57
3.3.1 Trace metal determinations in porewaters . . . 58
3.3.2 Trace metal determination in aqua regia digests . . . 71
3.3.3 Section conclusions . . . 71
3.4 Development of method to measure δ^{53}Cr using TIMS . . . 72
3.4.1 Experimental methods . . . 72
3.4.2 Chromium purification procedure . . . 74
3.4.3 Preparation of samples for TIMS analysis . . . 81
3.4.4 Instrumental analysis of δ^{53}Cr . . . 84
3.4.5 Issues with method development . . . 86
3.4.6 Testing for potential interferences and background corrections . . . 90
3.4.7 Detection limit of Cr measurements on TIMS . . . 94

3.4.8 Complete methodology and long term reproducibility of SRM979 and NIST3112a standards . . . 94
3.4.9 Section conclusions . . . 94
3.5 Implications for further chapters . . . 96

4 The Geochemical Behaviour of Molybenum in Salt Marsh Pond Sediments 97
4.1 Introduction . . . 97
4.1.1 Chapter outline . . . 97
4.1.2 Molybdenum behaviour in aqueous environments . . . 98
4.1.3 The δ^{98}Mo isotope system . . . 98
4.1.4 Molybdenum and δ^{98}Mo behaviour in the absence of sulfide . . . 98
4.1.5 Molybdenum and δ^{98}Mo behaviour in the presence of sulfide . . . 99
4.1.6 Motivation for study . . . 100
4.2 Methods . . . 100
4.2.1 Field site and sample collection . . . 100
4.2.2 Porewater and sediment extraction . . . 102
4.2.3 Aqueous geochemical analyses . . . 102
4.2.4 Sedimentary analyses . . . 102
4.2.5 Mo isotope and concentration determination . . . 103
4.3 Results . . . 104
4.3.1 Redox chemistry . . . 104
4.3.2 Molybdenum concentration and isotopes . . . 105
4.4 Discussion . . . 111
4.4.1 Molybdenum behaviour in the iron-rich pond sediment . . . 111
4.4.2 Molybdenum behaviour in sulfide-rich pond sediment and intermediate pond sediment . . . 116
4.4.3 Bulk sediment Mo behaviour in pond sediments . . . 119
4.4.4 Early diagenetic overprinting of sediment δ^{98}Mo . . . 120
4.5 Conclusions . . . 121
4.6 Implications for further chapters . . . 123

5 The Behaviour of Chromium in Salt Marsh Pond Sediments 125
5.1 Introduction . . . 125
5.1.1 Chapter outline . . . 125
5.1.2 Chromium isotope system . . . 125
5.1.3 Chromium oxidation states in aqueous environments . . . 126
5.1.4 Cr isotope fractionation associated with redox and non-redox processes 126

5.1.5 Uses of the chromium isotope system . . . 129
5.1.6 Environmental cycling of chromium . . . 130
5.1.7 This study . . . 134
5.2 Methods . . . 135
5.2.1 Sediment and porewater extraction methods . . . 135
5.2.2 Cr isotope separation and analysis . . . 135
5.3 Results . . . 135
5.4 Discussion . . . 137
5.4.1 δ^{53}Cr in comparison to global oxic and anoxic sediments . . . 137
5.4.2 Differences between the fate of Cr in the iron-rich and sulfide-rich pond sediment . . . 143
5.4.3 Potential depth of pond geochemistry change . . . 146
5.4.4 Diagenetic alteration of δ^{53}Cr during iron reduction? . . . 147
5.4.5 The use of a coupled δ^{53}Cr and δ^{98}Mo system . . . 148
5.5 Conclusion . . . 148
5.6 Implications for further chapters . . . 150

6 Potential for Diagenesis in the Proterozoic Rock Record 151
6.1 Introduction . . . 151
6.1.1 Chapter outline . . . 151
6.1.2 Redox evolution of Earth's oceans . . . 153
6.1.3 The iron speciation paleoredox proxy . . . 153
6.1.4 Potential new model for euxinic conditions overprint ferruginous sediments . . . 155
6.2 Examination of the iron speciation proxy to diagenetic alteration . . . 156
6.2.1 Evidence of diagenesis from Fe_{HR}/Fe_T and Fe_{PY}/Fe_{HR} ratios . . . 156
6.2.2 Site specific models including a kinetic component . . . 159
6.2.3 Model results from the Bornholm Basin . . . 161
6.2.4 Re-evaluation of euxinic samples in the Sperling et al. (2015) dataset 163
6.2.5 Temporal variation in diagenetic overprinting . . . 163
6.3 Effect of diagenesis on trace metal enrichments and the δ^{98}Mo system . . . 167
6.3.1 Trace metal enrichments . . . 167
6.3.2 Sedimentary δ^{98}Mo . . . 167
6.3.3 Other potential geochemical proxies . . . 168
6.4 Paleoclimate implications . . . 168
6.5 Conclusion . . . 169

7 Conclusion **171**
7.1 Salt marsh geochemistry 171
7.2 Pond sediments as an analogue for Proterozoic ocean sediments 172
7.3 Early diagenetic processes on trace metal behaviour 173
7.4 The future of paleoredox proxies 174
7.5 Concluding remarks 175

References **177**

Appendix A Double Spike Calibration **195**

Appendix B Double Spike Inversion **199**

Appendix C Isotope Dilution Calculation **201**

Appendix D Sequential extractions of chromium from sediments **203**

Appendix E Data tables **205**
E.1 Data table index 205

List of figures

1.1 Evolution of atmospheric oxygen and oceanic conditions through Earth history. 2
1.2 Schematic of the conventional redox ladder. 7

2.1 Map showing locations of field sites used in this thesis 14
2.2 Photos showing spatial variation in surface sediment colour. 16
2.3 Photos showing the common characteristics used to define different pond sediments. 19
2.4 Flowchart showing the typical method of characterisation of pond sediments based on features visible and/or easily testable from the surface. 20
2.5 Comparative geochemical characteristics of iron-rich pond sediment and sulfide-rich pond sediment 23
2.6 Compilation of porewater Fe^{2+} concentrations and $\delta^{34}S_{SO_4}$ in sediment cores collected from various ponds by members of the Turchyn lab 24
2.7 Pond sediment classification in area 1 of the salt marsh in Blakeney. 26
2.8 Pond sediment classification in area 2 of the salt marsh in Blakeney. 27
2.9 Pond sediment classification of Abbotts Hall Farm salt marsh system 28
2.10 Characteristics and water depth of salt marsh ponds in Blakeney and Abbotts Hall 30
2.11 Porewater $\delta^{34}S_{SO_4}$ measured from a sulfide-rich pond and a suspected intermediate pond using *in situ* samplers 31
2.12 Evidence of bioturbation in an iron-rich pond sediment core at 4 cm and 12 cm depth 33
2.13 Dissolved iron and sulfide concentrations in pond sediment which contains transient sulfide production at the pond sediment surface 36
2.14 Dissolved iron and sulfide concentrations in a 61-cm deep sediment core extracted from a sulfide-rich pond in Warham. 39
2.15 Pictures from a remote timelapse study of a salt marsh pond in September 2019. Tidal heights over the duration of the timelapse are also shown. . . . 41

2.16 Distribution of organic carbon content (%) in the top 5 cm of pond sediment across Abbotts Hall Farm salt marsh 44
2.17 Porewater geochemistry of sediment cores taken across a core transect . . . 46
2.18 Porewater geochemistry of a sediment core extracted horizontally from a creek wall 46
2.19 Schematic of potential mechanisms driving pond chemistry heterogeneity over a salt marsh platform. 48
2.20 Photographic evidence of black iron-sulfide minerals staining the sediment away from the lining of burrows. 49
2.21 Photo showing the formation of a new pond at Abbotts Hall Farm salt marsh, Essex as a result of coring through the vegetated platform. 51

3.1 Porosity measurements made for (A) sulfide-rich pond sediments and (B) iron-rich pond sediments for a variety of cores used in this thesis. 56
3.2 Photo showing collection of sediment and porewater from a salt marsh sediment core 57
3.3 Effect of dilution on the measurements of Cr and U on ICP-MS. 61
3.4 A typical standard addition experiment used to calculate the concentration of an element in a unique matrix. 65
3.5 Relative variations in emission intensity for Cr, U, Mo, V and Co for (A) iron-rich porewater and (B) sulfide-rich porewater relative to IAPSO seawater standard 67
3.6 Porewater molybdenum concentrations determined by isotope dilution and by ICP-MS (Element). 70
3.7 Calibration of column 1 in chromium separation protocol 78
3.8 Calibration of column 2 in chromium separation protocol 79
3.9 The effect of poor resin packing on the separation of Cr in column 2. 79
3.10 Calibration of column 3 in chromium separation protocol 81
3.11 Measurements of a standard SRM979 which exhibited large degrees of mass independent fractionation as a result of poor double-spike and standard equilibration. 87
3.12 Effect of good and poor equilibration between double spike and standard mixture on the ionisation from Re filament. 89
3.13 δ^{53}Cr of standards (SRM979) passed through the entire column chemistry processed with and without a 1 M HCl precondition. 90
3.14 Results from an SRM979 measurement run using the final preparation method. 91

3.15 Intensity of the ^{52}Cr, ^{54}Cr and ^{56}Fe beam over the measurement run of ~50 ng of SRM979 (the lowest sample sized measured). 93
3.16 Schematic showing the full methodology for chromium isotope analysis of samples and standards using TIMS 95
3.17 Long term reproducibility of δ^{53}Cr for SRM979 and NIST3112a over the course of this project. 96

4.1 Locations of three sediment cores taken in ponds on the salt marsh platform at Abbotts Hall Farm, Essex. 101
4.2 Geochemical data for the iron-rich, sulfide-rich and intermediate cores . . . 106
4.3 Photos showing the visible redox zonation in the iron-rich and sulfide-rich pond sediment 107
4.4 Mineral abundances in iron-rich and sulfide-rich pond sediments determined by XRD 108
4.5 Composite plot of Mo concentration and isotope data for the iron-rich, sulfide-rich and intermediate pond sediments. 110
4.6 Cross-plot of dissolved porewater Mn concentration (ppm) against the δ^{98}Mo of the sediment (‰). 112
4.7 Schematic of processes affecting Mo behaviour in Zone II of the iron-rich pond sediment. 114
4.8 Model predictions of porewater Mo concentrations if controlled by an Fe-Mo-S mineral phase compared to actual porewater concentrations. 117
4.9 Composite sediment δ^{98}Mo data and accompanying schematic showing the effect of diagenetic overprinting on the sedimentary δ^{98}Mo signature 122

5.1 Eh/pH diagram showing aqueous Cr speciation over a range of oxidation and pH conditions. 127
5.2 Theory behind the use of Cr as a paleoredox proxy for atmospheric oxygen. 131
5.3 Relationship between Cr concentration and δ^{53}Cr in global oceans. Taken from Moos and Boyle (2019) 133
5.4 Porewater chemistry of the iron-rich and sulfide-rich pond sediment at Blakeney. 136
5.5 Authigenic δ^{53}Cr and authigenic Cr sediment concentrations in iron-rich and sulfide-rich pond sediment. 138
5.6 Sedimentary metal concentrations in sulfide-rich and iron-rich pond sediments. 141
5.7 Composite of δ^{53}Cr in global marine sediment samples compared to salt marsh pond sediments. 142

5.8 Schematic of the diagenetic processes which control the behaviour of Cr in the (a) sulfide-rich and (b) iron-rich pond sediment. 145
5.9 Hypothetical model of understanding the water and sediment conditions of an environment using coupled δ^{98}Mo and δ^{53}Cr signatures. 149

6.1 Estimates of dissolved iron, sulfate and oxygen in the oceans through Earth history and corresponding classification of the ocean redox conditions . . . 152
6.2 Iron speciation classification scheme from Poulton and Canfield (2011) . . 154
6.3 Model showing the potential effect of diagenetic sulfidisation on iron speciation classification. Data density plot of iron speciation dataset compiled by Sperling et al. (2015) 157
6.4 Sediment age plotted against (a) Fe_{PY}/Fe_{HR} and (b) Fe_{HR}/Fe_T ratios from sediment cores taken in the Bornholm Basin 158
6.5 Model estimate of the time taken for complete pyritisation of the highly reactive iron pool in sediment 160
6.6 Model estimates of the potential diagenetic effect on sediment samples from the Bornholm Basin (Liu et al., 2020) 162
6.7 Graphical representation of the selection criteria shown in model run 7 of Table 6.1 165
6.8 Proportion of age-binned iron speciation samples from Sperling et al. (2015) which could be explained by solely diagenetic effects 166

A.1 δ^{53}Cr produced from SRM979 with well calibrated values and poorly calibrated values of the double spike solution. 197

D.1 Sequential extraction of chromium from salt marsh iron-rich pond sediment using the BCR method. 204

List of tables

2.1 Typical characteristics associated with each type of pond classification. . . . 18
2.2 Ferrous iron concentrations in water from various creeks on Abbotts Hall salt marsh 47

3.1 Reported concentration ranges for trace elements of interest for this project. 59
3.2 Counts per second of various elements in porewater samples compared to acid blank and seawater values measured by ICP-MS 63
3.3 Concentrations measured by ICP-MS using the calibration standards compared to published values. 68
3.4 Isotopic composition of the single spike powders as reported by ISOFLEX. 73
3.5 Summary of published methods to separate Cr from matrix ions for isotopic analysis. 76
3.6 Relative selectivities of ions on to the AG1-X8 anion resin. 77
3.7 Summary of loading methods tested for analysis of δ^{53}Cr using TIMS from published methods. 83
3.8 Cup configuration for Cr isotope acquisition on TIMS. 85
3.9 δ^{53}Cr values of SRM979 standards spiked with varying amount of vanadium single element spikes. 92
3.10 Two repeats of SRM979 spiked with 100 ng of Fe with and without interference correction 92
3.11 δ^{53}Cr measurements of varying aliquots of SRM979. 93

4.1 Summary of identified minerals from XRD analysis. 109

5.1 Table of fractionation factors (ε) for common environmental minerals, organic acids, and environmentally common bacteria. 129
5.2 Sediment δ^{53}Cr and Cr concentrations in the sulfide-rich pond sediment from Blakeney. 139

5.3 Sediment δ^{53}Cr and Cr concentrations in the iron-rich pond sediment from Blakeney. . . . 140

6.1 Estimations of the proportion of samples originally identified as 'euxinic' in Sperling et al. (2015) which may be explained by diagenetic effects alone. . 164

A.1 The isotopic composition of the SRM979 standard and double spike solution. 196

E.1 Geochemical characteristics of porewater in the sulfide-rich pond sediment shown in Figure 2.5 . . . 206
E.2 Geochemical characteristics of porewater in the iron-rich pond sediment shown in Figure 2.5 . . . 207
E.3 Fe^{2+} concentrations and $\delta^{34}S_{SO_4}$ of porewater in multiple iron-rich pond sediment cores shown in Figure 2.6a/e (Table 1/2) . . . 208
E.4 Fe^{2+} concentrations and $\delta^{34}S_{SO_4}$ of porewater in multiple iron-rich pond sediment cores shown in Figure 2.6a/e (Table 2/2) . . . 209
E.5 Fe^{2+} concentrations and $\delta^{34}S_{SO_4}$ of porewater in multiple iron-rich pond sediment cores shown in Figure 2.6b/f (Table 1/2) . . . 210
E.6 Fe^{2+} concentrations of porewater in multiple iron-rich pond sediment cores shown in Figure 2.6b/f (Table 2/2) . . . 211
E.7 $\delta^{34}S_{SO_4}$ of porewater in multiple sulfide-rich pond sediment cores shown in Figure 2.6g (Table 1/2) . . . 212
E.8 Fe^{2+} concentrations and $\delta^{34}S_{SO_4}$ of porewater in multiple sulfide-rich pond sediment cores shown in Figure 2.6c/g (Table 2/2) . . . 213
E.9 Fe^{2+} concentrations and $\delta^{34}S_{SO_4}$ of porewater in multiple sulfide-rich pond sediment cores shown in Figure 2.6d/h . . . 214
E.10 $\delta^{34}S_{SO_4}$ of porewater over a 14-month period collected by *in situ* samplers in sulfide-rich pond sediment at Warham shown in Figure 2.11a . . . 215
E.11 $\delta^{34}S_{SO_4}$ of porewater over a 14-month period collected by *in situ* samplers in suspected intermediate pond sediment at Warham shown in Figure 2.11b 216
E.12 Geochemical data for V-Core 1 from the core transect at Abbotts Hall salt marsh (Figure 2.17) . . . 217
E.13 Geochemical data for V-Core 2 from the core transect at Abbotts Hall salt marsh (Figure 2.17) . . . 217
E.14 Geochemical data for V-Core 3 from the core transect at Abbotts Hall salt marsh (Figure 2.17) . . . 218
E.15 Geochemical data for I-Core from the core transect at Abbotts Hall salt marsh (Figure 2.17) . . . 218

E.16 Geochemical data for S-Core from the core transect at Abbotts Hall salt marsh (Figure 2.17) . . . 219
E.17 Geochemical data for Creek Core from the core transect at Abbotts Hall salt marsh (Figure 2.18) . . . 219
E.18 Organic carbon content (%) in the surface sediment in ponds as shown in Figure 2.16 . . . 220
E.19 Molybdenum isotope values and porewater chemistry in iron-rich pond sediments shown in Figure 4.2 and 4.5 . . . 221
E.20 Sedimentary Mo isotope composition and sedimentary concentrations of Mo, Mn, Fe and Al in iron-rich ponds shown in Figure 4.2 and 4.5 . . . 222
E.21 Molybdenum isotope values and porewater chemistry in sulfide-rich pond sediments shown in Figure 4.2 and 4.5 . . . 223
E.22 Major cation and pH measurements in sulfide-rich pond sediment porewater. These were the inputs for the model described in **Chapter 4** based on (Helz et al., 2011) . . . 224
E.23 Sedimentary Mo isotope composition and sedimentary concentrations of Mo, Mn, Fe and Ti in sulfide-rich ponds shown in Figure 4.2 and 4.5 . . . 225
E.24 Molybdenum isotope values and porewater chemistry in intermediate pond sediments shown in Figure 4.2 and 4.5 . . . 226
E.25 Major cation and pH measurements in intermediate pond sediment porewater. These were the inputs for the model described in **Chapter 4** based on (Helz et al., 2011) . . . 227
E.26 Sedimentary Mo isotope composition and sedimentary concentrations of Mo, Mn, Fe and Ti in intermediate ponds shown in Figure 4.2 and 4.5 . . . 228
E.27 Model inputs used for the model described by Helz et al. (2011) to predict Mo concentrations in sulfide-rich pond sediment porewaters . . . 229
E.28 Model inputs used for the model described by Helz et al. (2011) to predict Mo concentrations in intermediate pond sediment porewaters . . . 230
E.29 Porewater pH, ferrous iron concentrations and sulfide concentrations in the pond sediments collected for Cr isotope analysis. Data shown in Figure 5.4 231
E.30 Metal concentrations in sediments from the iron-rich pond sediment core for Cr isotope determination. Data shown in Figure 5.6 . . . 232
E.31 Metal concentrations in sediments from the sulfide-rich pond sediment core for Cr isotope determination. Data shown in Figure 5.6 . . . 233

Chapter 1

Introduction

1.1 Redox conditions through Earth history

One of the outstanding aims in the scientific community has been to constrain the evolution of Earth's atmospheric and oceanic redox state through history (Figure 1.1). The geological record is the key to reconstructing this redox evolution: the geochemical signals ultimately recorded in sedimentary rocks can potentially reveal the environmental conditions present at the time of deposition. Our current understanding of Earth's redox history is as follows: The atmosphere in the Archean Eon (4–2.5 Ga) contained negligible oxygen, instead consisting of some mixture of H_2O, CO_2, NH_3 and CH_4 which kept the Earth surface warm, despite the lower solar luminosity (Nisbet and Sleep, 2001; Sagan and Chyba, 1997). Early in the succeeding Proterozoic Eon (2.5–0.542 Ga), the disappearance of mass independent fractionation in sedimentary sulfide minerals suggests a large-scale global oxidation event occurred (Farquhar et al., 2000), possibly preceded by smaller whiffs of atmospheric oxygen (Anbar et al., 2007). This introduction of atmospheric oxygen, termed the Great Oxidation Event (2.4–2.1 Ga), is widely supported by a variety of geochemical and geological evidence such as the disappearance of detrital pyrite from river sediments, the appearance of red beds and a shift in δ^{53}Cr in banded iron formations (Frei et al., 2009; Holland, 2006; Konhauser et al., 2011).

The cause of this oxidation event is still unclear; the evolution of photosynthesis, a change in tectonic processes and internal feedbacks based on chemical cycles have all been posited (Alcott et al., 2019; Kump and Barley, 2007; Lenton et al., 2014). A tighter constraint on timing of the increase in oxygen would aid in establishing the causal mechanism, but there is disagreement among paleoredox proxies (Gumsley et al., 2017).

The ∼billion-year period that followed the GOE is known at the mid-Proterozoic or, more colloquially, the "boring billion". During this time, the atmosphere is hypothesised to

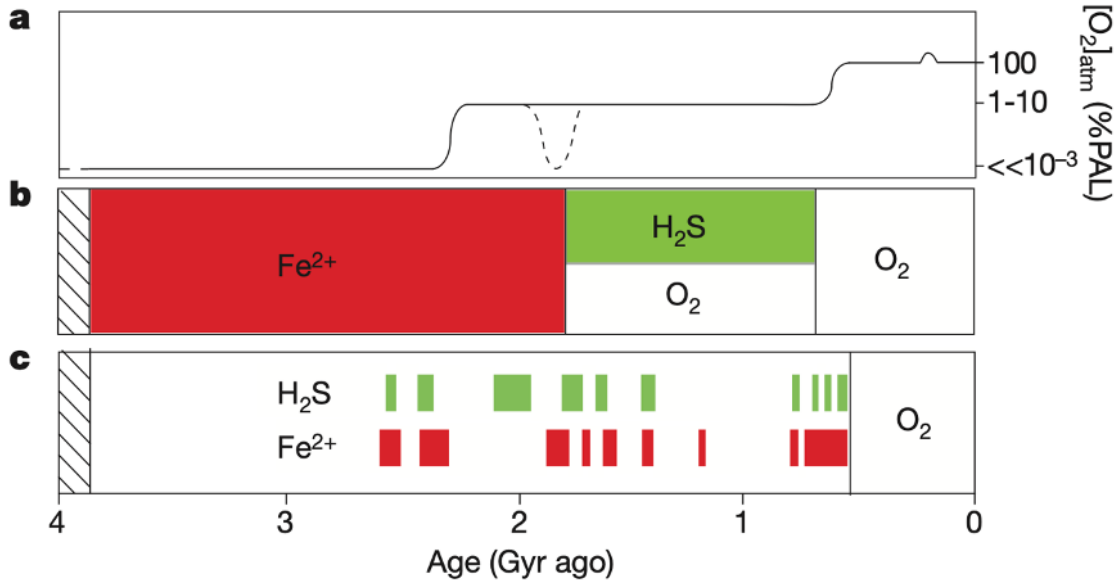

Fig. 1.1 - *Evolution of atmospheric oxygen and oceanic conditions through Earth history. (a) Oxygen concentrations of the atmosphere (for a more in depth representation of this plot, see (Lyons et al., 2014)). (b) Canonical view of the geochemistry of the deep ocean (Canfield, 1998; Holland, 1984; Rouxel et al., 2005) and, (c) revised view of deep ocean redox water conditions based on shale date from Planavsky et al. (2011). All of these reconstructions are based on paleoredox proxies. Figure from Planavsky et al. (2011)*

have contained between 0.1 and 10% of present atmospheric oxygen levels (PAL) (Laakso and Schrag, 2017; Planavsky et al., 2014). As a consequence, the surface ocean may have contained very small levels of oxygen, but the majority of the ocean would have remained anoxic. In the absence of oxygen, the oceans were initially proposed to contain widespread aqueous sulfide (Canfield, 1998), conditions which are similar to the modern Black Sea—or Euxine Sea according to the ancient Greeks—and thus are termed euxinic. More recent evidence has highlighted that ferruginous conditions—anoxic waters containing dissolved iron—were widespread in the deep oceans and that euxinic conditions were instead confined to shallow continental margins (Planavsky et al., 2011). The actual proportion of euxinic and ferruginous conditions at the time however, is not well constrained and there is disagreement among redox proxies (Gilleaudeau et al., 2019; Reinhard et al., 2013; Sperling et al., 2015). Understanding the extent, timing and geographical location of euxinia during this period is key; the early development and diversification of eukaryotes is hypothesised to have occurred during the mid-Proterozoic. Aqueous sulfide could have influenced the eukaryotic species that could have existed during this period (as sulfide is toxic to certain eukaryotes), although other factors, such as nutrient availability, may have also controlled eukaryotic evolution.

Following the "boring billion", a second oxidation event known as the Neoproterozoic Oxidation Event (NOE) (800–540 Ma) is thought to have occurred. It is in this period that atmospheric oxygen levels increased up to 50% of PAL and the first introduction of oxygen to the deep ocean has been hypothesised (Och and Shields-Zhou, 2012). The nature of this introduction of oxygen to the deep ocean is thought to have been stepwise until modern levels were reached (Fike et al., 2006; Sahoo et al., 2016).

1.2 Paleoredox proxies and the role of diagenesis

Constraining these redox conditions has required the incredible—yet unenviable—work of identifying, developing, and testing paleoredox proxies in the geological record to fingerprint both atmospheric oxygen and oceanic oxygen through Earth history. With almost every proxy, the basic premise is that a geochemical signature acquired at the sediment surface in a ferruginous, oxic, or euxinic ocean or in an oxic or anoxic atmosphere subsequently becomes buried and, ultimately, lithified into the rock record. What this thesis examines, first and foremost, is the geochemical reactions that occur during the period of time between deposition and lithogenesis and how they may influence the preservation of these primary signatures in the sediment. These early reactions, cumulatively referred to as "diagenesis", have the potential to alter that geochemical signature which was acquired at the surface. If these reactions are understood comprehensively, then the primary signature in the rock record

can be decoupled from the diagenetic signature and the true primary redox signal can be revealed.

Without access to the exact sedimentary conditions of the ancient ocean, modern environments analogous to past conditions need to be used to ascertain the sequence of diagenetic processes that can generate a preserved geochemical signature. However, care needs to be taken to when applying interpretations of modern environments to the past for a number of reasons: the same geochemical signature could have been generated by multiple processes, certain environmental characteristics (e.g. the pH, carbon fluxes and ionic composition of seawater) may not be comparable between the past and present, and chemical reactions may have altered the signature in the sediment between the timing of deposition and the formation of the rock.

In this project, I am examining the effect of early sedimentary diagenesis in a modern analogous environment on three commonly used paleoredox proxies: the δ^{98}Mo isotope system, the δ^{53}Cr isotope system and iron speciation measurements. Each of these has been used extensively to fingerprint paleoredox conditions in the geological record (Arnold, 2004; Planavsky et al., 2014; Sperling et al., 2015). The fundamental premise behind the use of these particular metals to explore paleoredox is introduced below. A more comprehensive introduction to each of these geochemical systems is given in **Chapters 4**, **5**, and **6** respectively.

1.2.1 Molybdenum and the δ^{98}Mo isotope system

Molybdenum (Mo) is a trace element which becomes more easily removed from solution in the presence of aqueous sulfide. As such, enrichments of Mo in shales have been used as an indicator of local euxinic conditions and a global decline in the abundance of Mo in shales has been interpreted as more widespread euxinic conditions in global oceans (Reinhard et al., 2013). The speed of Mo sequestration in sediments deposited below a euxinic water column means that the δ^{98}Mo of seawater is hypothesised to be directly transferred to the sediment, whilst sediments deposited under oxic conditions have a much lower δ^{98}Mo (Arnold, 2004; Kendall et al., 2017). Seawater δ^{98}Mo will change dependent on the relative balance of each of these sinks which can be tracked using the δ^{98}Mo of shales deposited underneath a euxinic water column. In summation, δ^{98}Mo in euxinic shales is hypothesised to track the fraction of euxinic conditions in the ocean and Mo enrichments in a particular sedimentary sequence can be used to track local euxinia.

1.2.2 Chromium and the δ^{53}Cr isotope system

Chromium (Cr) in nature typically exists in one of two oxidation states: an oxidised, soluble Cr(VI) form and a reduced, largely insoluble Cr(III) form. Higher sediment concentrations of Cr are thus inferred to form under anoxic water columns (promoting the formation of the insoluble Cr(III)), regardless of whether this water column contains ferrous iron or sulfide (Reinhard et al., 2013). The δ^{53}Cr proxy relies on the premise that Cr(III) can only be oxidised in terrestrial environments if a certain threshold of atmospheric oxygen is present (Planavsky et al., 2014). Since the most significant Cr isotopic fractionation is associated with reduction, sediments containing δ^{53}Cr which differ from bulk silicate earth values (-0.012‰) are inferred to have been deposited under an atmosphere containing some oxygen (Frei et al., 2009). Additionally, the balance of higher δ^{53}Cr anoxic sinks to lower δ^{53}Cr oxic sinks may provide some information on the balance of oxic and anoxic water masses in ancient oceans if paleoseawater δ^{53}Cr is recorded in independent record. In summation, the δ^{53}Cr proxy is proposed to be both a tracer of ocean anoxia and atmospheric oxygen.

1.2.3 Iron Speciation

The iron speciation proxy uses the mineralogy of iron in sediment to infer both anoxic and euxinic conditions in the water column (Poulton and Canfield, 2011). Under anoxic conditions, highly reactive iron minerals (e.g. iron carbonates, iron (oxyhydr)oxides and iron sulfides) form in the water column whereas under under euxinic conditions, predominantly iron sulfide minerals form in the water column; in both cases the minerals would become deposited in the sediment more rapidly than in an oxic environment (Lyons and Severmann, 2006). Where the fraction of highly reactive iron to total iron in the sediment exceeds 0.38, an anoxic water column is inferred. Furthermore, where the fraction of iron hosted in pyrite to the highly reactive iron exceeds 0.7, a euxinic water column is inferred. Iron speciation is one of the most widely used proxies to interpret the local redox conditions of a water column in sediments, which can aid in distinguishing between the global and local components of other paleoredox proxies (Planavsky et al., 2014; Sperling et al., 2015).

1.3 Early sedimentary diagenesis

To test these various paleoredox systems, an understanding of the redox reactions occurring in the sediment is necessary. A plethora of these reactions occur within sediments, many of which are driven or influenced by the breakdown of organic carbon. The reduction of oxygen is the most common half reaction coupled with the breakdown of organic matter as it is the

most energetically favourable terminal electron acceptor (TEA). In the modern atmosphere and ocean, oxygen is ubiquitous enough to always be in excess, therefore aerobic respiration is the dominant mechanism oxidising organic carbon (Equation 1.1).

$$C_6H_{12}O_6 + 6O_2 \rightarrow 6CO_2 + 6H_2O \tag{1.1}$$

Within sediment however, organic carbon can accumulate to the extent that the supply of oxygen is exhausted. Under these conditions, the breakdown of organic carbon can couple with less favourable terminal electron acceptors. A canonical order of usage called "the redox ladder" was initially proposed for environmentally available molecules (Figure 1.2) whereby one TEA will be used until depletion whereupon the next most energetically favourable TEA will be used (Froelich et al., 1979). Support for this mechanism came from the redox zonation observed in marine sediment cores. This redox ladder has since been shown to be more complex: variations in pH and Eh affect the relative favourability of different terminal electron acceptors (Bethke et al., 2011), cable bacteria can connect redox zones which are otherwise not adjacent to each other in a sedimentary profile (Meysman, 2018), and two different reduction metabolisms can coexist in the same sediment either in microenvironments or in coupled reactions (Hansel et al., 2015; Mortimer et al., 2011).

All of these reactions will influence how trace elements such as Mo and Cr are distributed in the sediment column. Changes in pH, Eh and major element cycling occurring as a result of diagenetic reactions can potentially break down previously deposited elements and cause them to be diffused elsewhere in the sediment column (Shaw et al., 1990). There is a growing body of work examining trace elements in modern sediments to understand how geochemical signals can be altered post depositionally (Liu et al., 2020; Scholz et al., 2013) but each environment is subject to different conditions and reactions, and thus many more sites are needed. In particular, there needs to be more sites where multiple redox proxies are tested in conjunction, as this will address the comparative benefits and drawbacks of each system.

1.4 Salt marsh pond sediments as potential analogues

All fieldwork for this thesis was conducted in East Anglian salt marshes in the UK. Aside from being an exotic destination for fieldwork, the sediments beneath saline ponds offer many of the geochemical characteristics of ancient ocean sediments and thus are an ideal location to test paleoredox proxies. Salt marsh ponds offer an easily accessible environment where sediment exists with a high organic carbon flux which is overlain by seawater. The high organic carbon flux means that the depth of oxygen penetration is minimal (<1 cm) and each electron acceptor is depleted more rapidly (thus constricting the redox transitions

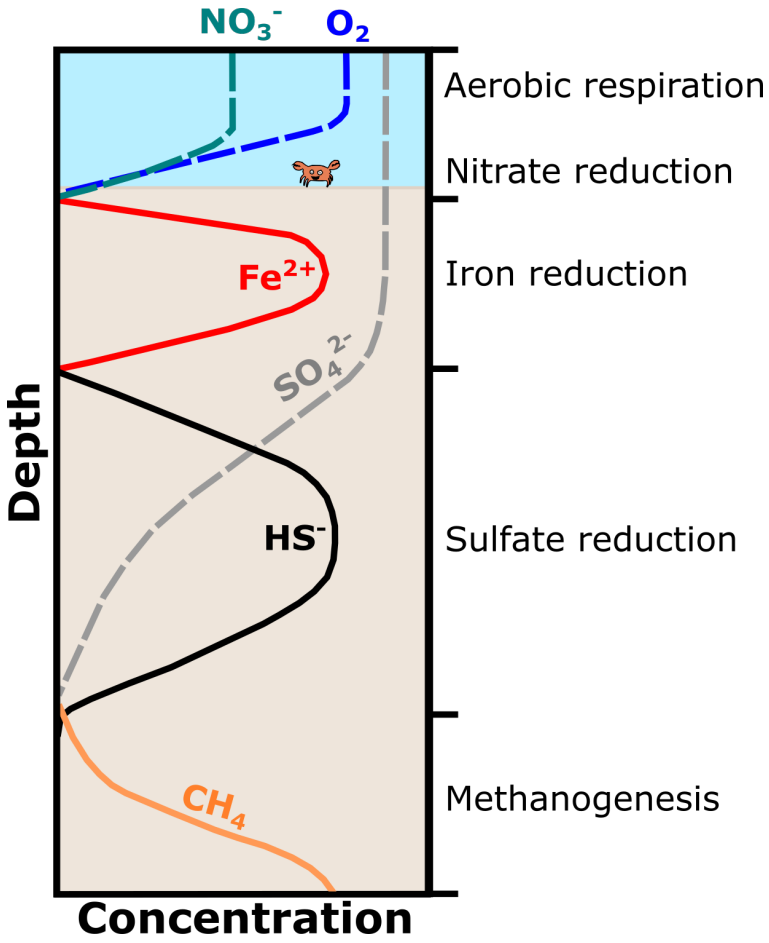

Fig. 1.2 - *Sediment column under the conventional redox ladder as electron acceptors are used in order of energy availability (Froelich et al., 1979). Dashed lines indicate electron acceptor for the redox reaction (reactant). Solid lines indicate the product of the redox reaction. Oxygen and nitrate are rapidly metabolised in the uppermost portion of the sediment and thus concentrations are highest in the water column. East Anglian salt marsh pond sediments do not always abide to this conventional redox ladder.*

vertically). These conditions make it an ideal environment to understand how paleoredox proxies are affected by a wide variety of anoxic redox conditions during early diagenesis.

These sediments have certain advantages over other potential modern analogues. Although open ocean sediments contain the same redox zones at depth, the lower organic carbon supply means that the depth of oxygen penetration and the width of each redox zone can extend for many metres, requiring the use of longer cores. Terrestrial lake settings could offer another potential analogue for past ancient oceans, however, lower ionic strength solutions would result in different types and rates of authigenic mineral precipitation, detrital sources and delivery would vary in comparison to marine settings, and other geochemical parameters such as a pH and alkalinity would be markedly different.

1.5 East Anglian salt marsh pond sediments

Salt marshes are highly productive coastal wetlands that serve a critical role in carbon sequestration and nutrient trapping (Barbier et al., 2011; McLeod et al., 2011; Valiela et al., 1978). Like other environments defined as "Blue Carbon", they sequester a disproportionately larger amount of carbon than their area would suggest. However, as a marginal environment poised between the terrestrial and marine realms, salt marshes are also extremely vulnerable to changes in environmental conditions such as anthropogenic eutrophication/drainage, climate change and sea level rise (Deegan et al., 2012; Kennish, 2001; Kirwan and Megonigal, 2013). For example, in the UK, up to 100 Ha of salt marsh land is estimated to be lost per year (Phelan et al., 2011). Understanding the geochemistry of these environments is therefore important if we wish to better predict how salt marshes may be affected by future environmental changes.

Salt marsh surfaces are highly heterogeneous; a largely vegetated platform is incised by a series of narrow, tidally fed creeks with varying cross sections (Allen, 2000; Lawrence et al., 2004). Saline ponds form where tidal drainage is most inefficient, forming pockmarks in the vegetated platform surface which seawater infills (Wilson et al., 2014). The low hydraulic conductivity of the sediment means that the ponds remain filled for the majority of the year and are sporadically flushed by tidal events which flood the vegetated platforms during high tides or storm surges (Santos et al., 2009). The formation mechanism of these ponds is uncertain, although it has been proposed that either physical processes (e.g. algal debris or heterogeneous development of the salt marsh) or biogeochemical processes (e.g. build-up of salinity in standing water or decay of deposited algal matter) are responsible for the initial formation of primary (well-rounded) ponds and senescence of creeks isolated by vegetation forms secondary (elongate-shaped) ponds—both of which can be present in the same salt

marsh (Pethick, 1974; Redfield, 1972; Wilson et al., 2014). As brackish water sits on the surface of these ponds, vegetation is prevented from colonising, resulting in a set of feedbacks which allow these ponds to remain semi-permanent and respond to sea level change and other larger perturbations (Wilson et al., 2014).

Huge quantities of organic carbon, both allochthonous (supplied by rivers and the oceans from elsewhere) and autochthonous (grown *in situ*) are supplied to the muddy sediment. As a consequence, the sediment beneath these ponds, and indeed throughout the salt marsh beneath the rhizosphere, is largely anoxic (Mills et al., 2016). In the ponds, the presence of a standing water column (1–50 cm) and the lack of surface vegetation limits the supply of oxygen into the sediment. In the absence of processes which would disturb the sediment (e.g. bioturbation or a rhizosphere), aerobic respiration is limited to a small boundary layer at the sediment surface (<1 cm) (Nealson, 1997). A rather unusual phenomenon discovered in these localities is that sediments beneath certain ponds contained dissolved ferrous iron (Fe^{2+}) in the porewater whilst the sediments beneath other ponds, sometimes less than 10 m away, contained dissolved sulfide (S^{2-}). The distribution and behaviour of these two different types of sediment and how this affects the chemistry of trace elements used as paleoredox proxies in these sediments will be the main focus of this thesis.

1.6 Thesis Roadmap

Chapter 1 – Introduction Chapter 1 provides a brief account of the redox evolution of the Earth's surface and the paleoredox proxies which are being tested in this thesis. The salt marsh system is introduced as an analogue for past redox conditions.

Chapter 2 – Controls on the Spatial Distribution of Pond Sediment Geochemistry in East Anglian Salt Marshes Chapter 2 provides an introduction to the fundamental geochemical processes occurring in iron-rich and sulfide-rich pond sediments in the East Anglian Salt marshes. Various hypotheses are posited for why these geochemical conditions co-exist in the spatial distribution that is observed.

Chapter 3 – Method Development for Trace Element Analysis using ICP-MS and for Chromium Isotope Analysis on the Thermal Ionisation Mass spectrometer (TIMS) Chapter 3 introduces the analytical methods which were developed for trace element concentration determination in porewaters and sediment and the development of the $\delta^{53}Cr$ methodology by TIMS.

Chapter 4 – The Geochemical Behaviour of Molybdenum in Salt Marsh Pond Sediments Chapter 4 looks at the δ^{98}Mo system under the varying redox conditions present in the salt marsh pond sediment. The work in this chapter provides evidence for diagenetic overprinting of sedimentary δ^{98}Mo during early diagenesis.

Chapter 5 – The Geochemical Behaviour of Chromium in Salt Marsh Pond Sediments Chapter 5 looks at the δ^{53}Cr system in salt marsh pond sediments where in spite of the anoxic conditions, δ^{53}Cr looks similar to oxic sediment. This chapter explores the small differences in δ^{53}Cr between the sulfide-rich and iron-rich pond sediment and how diagenesis influences δ^{53}Cr.

Chapter 6 – Potential for Diagenesis in the Proterozoic Rock Record Chapter 6 examines how early diagenetic overprinting may have consequences for paleoredox proxies in the geological record. A model shows how diagenetic overprinting can mimic a "euxinic" signal in the geological record. The model is tested on the 4000+ iron speciation measurements compiled by Sperling et al. (2015).

Chapter 7 – Conclusion Chapter 7 concludes the thesis by summarising the developments in our understanding of diagenesis in pond sediments and the effect of diagenesis on the three paleoredox proxies. The implications for the geological record are highlighted.

Chapter 2

Controls on the Spatial Distribution of Pond Sediment Geochemistry in East Anglian Salt Marshes

The work presented in this chapter has been published under the title **'Creek Dynamics Determine Pond Subsurface Geochemical Heterogeneity in East Anglian (UK) Salt Marshes'** in *Frontiers in Earth Science* (Hutchings et al., 2019). The sediment cores were collected by myself and many of the co-authors on this paper. Spatial mapping, data analysis and interpretation of the results were my own work. Co-authors and two reviewers provided comments on the published manuscript.

2.1 Introduction

2.1.1 Chapter outline

This chapter provides an in-depth description of the chemistry at the field site where I tested the applicability of the δ^{98}Mo (**Chapter 4**) and the δ^{53}Cr (**Chapter 5**) isotope systems in a modern sedimentary environment. In addition, the work in this chapter ties together work that the Turchyn group had been conducting since 2013; I provide a mechanism to describe the dichotomous pond sediment geochemistry which is observed in East Anglian salt marshes. Parallels can be drawn between the geochemistry in these locations and the geochemical conditions in mid-Proterozoic ocean sediments (**Chapter 6**).

2.1.2 East Anglian salt marshes: a geochemical dichotomy in pond sediments

As discussed in **Chapter 1**, East Anglian salt marsh pond sediment geochemistry is characterised either by sediment which has high dissolved ferrous iron in the porewater, or by sediment which has high dissolved hydrogen sulfide in the porewater. For brevity, I will ascribe the terms "iron-rich" pond sediment and "sulfide-rich" pond sediment for these two systems respectively from here onwards. All sampled pond sediments prior to this project had been described as one of these two categories, and multiple projects had been undertaken to look at some of the processes controlling redox changes in each type of sediment (Antler et al., 2019; Lin et al., 2020; Mills, 2014; Mills et al., 2016; Wilkening, 2017; Wilkening et al., 2019).

Still, some fundamental questions remained unanswered—what actually controls whether the sediment beneath a pond iss destined to become iron-rich or sulfide-rich? This is particularly poignant, as iron-rich pond sediment could be separated by less than 5 metres to a sulfide-rich pond sediment, yet two iron-rich sediments would be nearly identical between Norfolk and Essex—salt marshes over 100 km apart. A further question is, could sediment or porewater geochemistry, unidirectionally or reversibly, transform from one geochemical state to the other? The answers to these questions are fundamental to better understand the controls and interconnections between the iron, sulfur and carbon cycles within these salt marsh systems.

The work in this chapter first defines the major redox reactions in both iron-rich and sulfide-rich pond sediment. I used a wide array of sediment cores collected by other members of the research group and myself over the period from 2013–2018 to understand and explain larger patterns in the dataset of sediment cores.

The second part of this chapter looks at the spatial distribution of iron-rich and sulfide-rich pond sediment in East Anglian salt marshes. The heterogeneous structure of salt marshes means that ponds at different locations on the vegetated platform will be subject to different environmental conditions such as the frequency of tidal flooding events, the age and depth of the pond, the strength and nature of groundwater flows, differences in vegetation, and differences in the supply of organic carbon and nutrients. A clear spatial pattern would imply that differences in some combination of environmental conditions could be controlling the geochemistry of the pond sediment.

Following the results of this spatial survey, I then tested three potential hypotheses as controlling factors in determining the observed pond distribution: (1) the depth of the water column above the sediment, (2) the distribution of organic carbon in surface sediments and (3), the presence and nature of groundwater fluxes.

2.2 Methods

2.2.1 Field sites

For this study, I looked at two different salt marsh systems across East Anglia: a series of salt marshes across the North coast of Norfolk, UK and an isolated salt marsh at Abbotts Hall Farm, Essex, UK (Figure 2.1). Both salt marshes contain iron-rich and sulfide-rich pond sediment, implying some commonality (most likely geological provenance) between the two sites.

On the Norfolk coastline, protection offered by migrating barrier islands, spits and intertidal sand flats have allowed salt marsh systems to form since the start of the Holocene (Pethick, 1980). The muds, silts and sands of the intratidal zone overlay glacial gravel deposits which sit upon a predominantly chalk lithology visible in outcrops at Hunstanton (Chroston et al., 1999). In Norfolk, the field locations examined are three developed areas of stable, upper salt marsh near the small towns of Blakeney, Warham, and Stiffkey (Figure 2.1b). The upper marsh sediment is Romano-British in age (2000+ years) and consists of greyish-brown, silty sands and clayey silts, likely accumulated by vegetative capture of finer grained sediment, which sits upon a northwards dipping boulder clay (Pethick, 1980; Pye et al., 1990). The source of the salt marsh sediment is expected to be from the erosion of proximal cliffs, such as the Crag formation and outcropping chalk formations along the coast near Hunstanton (McCave, 1987).

Abbotts Hall Farm is a nature reserve owned by Essex Wildlife Trust on a tidally dominated estuarine portion of the River Blackwater. Area 3 (Figure 2.1g) lies on the edge of this tributary (defined as fringed-estuarine) where low energy environments are protected from direct wave action (Allen, 2000). The surface geology comprises of London clay and glacial deposits of chalky boulder clay, sand and gravel (Bristow et al., 1985). The salt marsh sediment consists of medium and fine-grained silts (Emmerson et al., 1997) reflecting a combination of tidally supplied eroded material and upstream tributaries. Salt marshes formed on the mudflats of the river were historically undergoing large scale losses due to sea level rise (Burd, 1992); as such, the site has been an area of coastal managed realignment strategy involving the breaching of an existing seawall, thus many of the fringe salt marshes are very young (<100 years) (Hughes et al., 2009). This is reflected by the shallow depths (<40 cm) required to reach the gravelly layer underlying the salt marsh sediments.

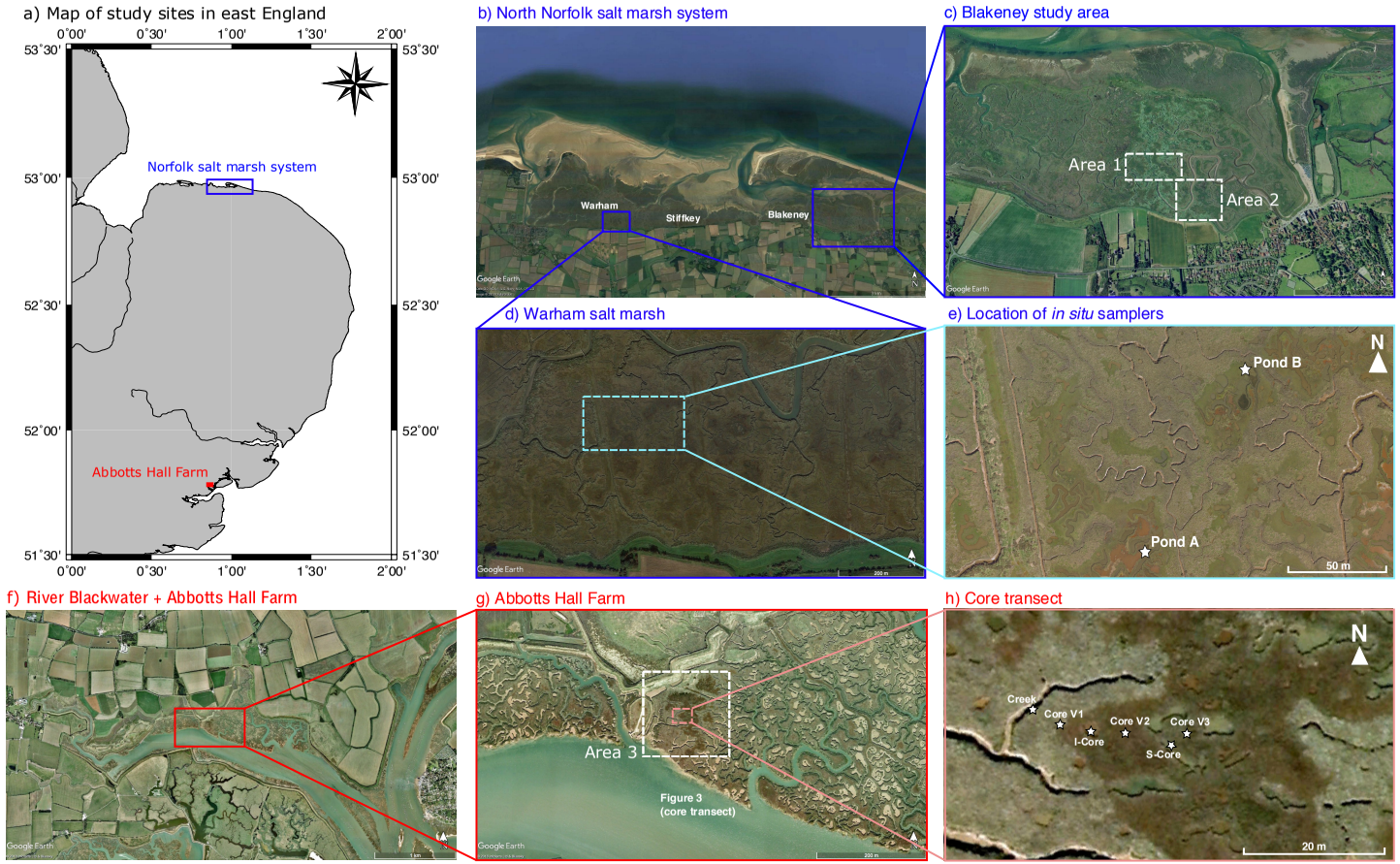

Fig. 2.1 - *a) Map of east England showing the Norfolk salt marsh system and Abbotts Hall Farm nature reserve (Essex Wildlife Trust). b) Google Earth satellite imagery (24-09-17) of the Norfolk salt marsh system comprising Warham marshes, Stiffkey marshes and Blakeney marshes. The blue box denotes the location of Figure 2.1d. c) Satellite imagery (31-12-1999) of Blakeney salt marsh. Area 1 and 2 correspond to the mapped areas in Figure 2.7 and 2.8 respectively. d) Google Earth satellite imagery (10-01-2019) of the Warham salt marsh. Light blue box indicates location of Figure 2.1e. e) Location of in situ samplers (Pond A and B). f) Satellite imagery (06-11-2006) of the River Blackwater and the location of Abbotts Hall Farm Nature reserve. Red box denotes the location of Figure 2.1g. g) Satellite imagery (06-11-1999) of Abbotts Hall Farm salt marsh system. Area 3 corresponds to mapped area in Figure 2.9. h) Positions of cores taken in a linear transect and the position of the core taken through the creek wall. (Image credits: Google Earth, © 2018 Infoterra Ltd & Bluesky and Image © 2018 DigitalGlobe)*

2.2.2 Porewater collection

Push core liners made of polyvinyl chloride (PVC) were used to extract vertical columns of sediment from ponds at irregular intervals over the period 2013–2018 by many members of the Turchyn research group. Porewater was extracted from the cores either in the field or within 24 hours of being collected using Rhizons (syringe-based samplers with an inert polymer membrane). Samples for each core were taken at variable depth resolutions (between 1 and 4 cm). Typically, between 2 to 10 mL of porewater was extracted from each depth sampled, depending on the sediment porosity and what was needed for analysis. Aliquots of porewater (50–2000 μL) for ferrous iron analysis were fixed with 100 μL ferrozine reagent; the precise amount of porewater depended on the amount of iron present. Aliquots (50–2000 μL) for aqueous sulfide were fixed with excess quantities of either—dependent on sulfide concentration or researcher—5% or 20% zinc acetate.

2.2.3 Analytical methods

All analytical measurements were carried out at the University of Cambridge. Dissolved iron concentrations (Fe^{2+}) were determined spectrophotometrically (Thermo Aquamate UV-Vis) according to the method described by Stookey (1970) with an error of 0.4%. Dissolved sulfide concentrations were measured spectrophotometrically using the methylene blue method with an error of 2% and a detection limit of 1 μM (Cline, 1969). Samples were diluted with ultrapure water to fit within a calibrated range. Major anions (sulfate and chloride) were measured by ion chromatography (Thermo Scientific Dionex ICS5000+) with an error up to 2% based on repeat analysis of standards. Samples measured for alkalinity were filtered using a cellulose nitrate membrane syringe filter (0.2 μM, 47 mm). Alkalinity was determined using the inflection point method by titrating 1–1.2 mL aliquots of filtered samples with 0.0166 M analytical grade hydrochloric acid (HCl). The pH was measured at 25°C on the NBS scale using an Orion 3 Star meter with ROSS micro-electrode (ORION 8220 BNWP PerpHect ROSS).

Samples for sulfur isotope analysis were separated into vials and a supersaturated barium chloride solution was added, precipitating barite ($BaSO_4$). The barite was cleaned using 10% HCl, triple washed with ultrapure water, and dried. The $\delta^{34}S_{SO_4}$ was determined through combustion on a Flash Element Analyser (Thermo Scientific) coupled with continuous helium flow to a Delta V Plus mass spectrometer. Samples were corrected to NBS-127 barite standards ($\delta^{34}S$ = 20.3‰) which were run before and after sets of 20 samples. Based on blind replicates and repeat running of the standard, the data had precision of 0.2‰ (1σ).

Sulfur isotopic compositions are reported in standard delta notation as per mil (‰) deviations from the Vienna Cañon Diablo Troilite (VCDT).

2.2.4 Mapping of ponds

In the absence of high-resolution satellite imagery of the Norfolk Salt Marshes, a method to aerially map and classify ponds was necessary. A drone (Phantom 3 Standard) was used to create an aerial survey at a height of 150 m in May 2018. The orthophotos were assembled using the MapsMadeEasy website and the projection used for uploading to QGIS was WGS 84 31N. I was unable to drone map for Area 3, in Abbotts Hall, so I used Google Earth satellite imagery of the area which fortunately provided a high enough resolution image.

Two ground-truth campaigns—in May and July 2018—were undertaken to characterise pond sediment types from the drone images. I initially attempted to characterise ponds directly from the drone-imagery, but this proved impossible given the variable surface colours and the small scale of other distinguishing features (e.g. worm burrow casts). The variability of surface sediment colours was a particular problem seasonally, where transient pulses of sulfide generation at the surface can stain the surface sediment black in Spring and Autumn. This can result in pond sediment where the colour of the surface varies across the sediment surface (Figure 2.2) and with depth.

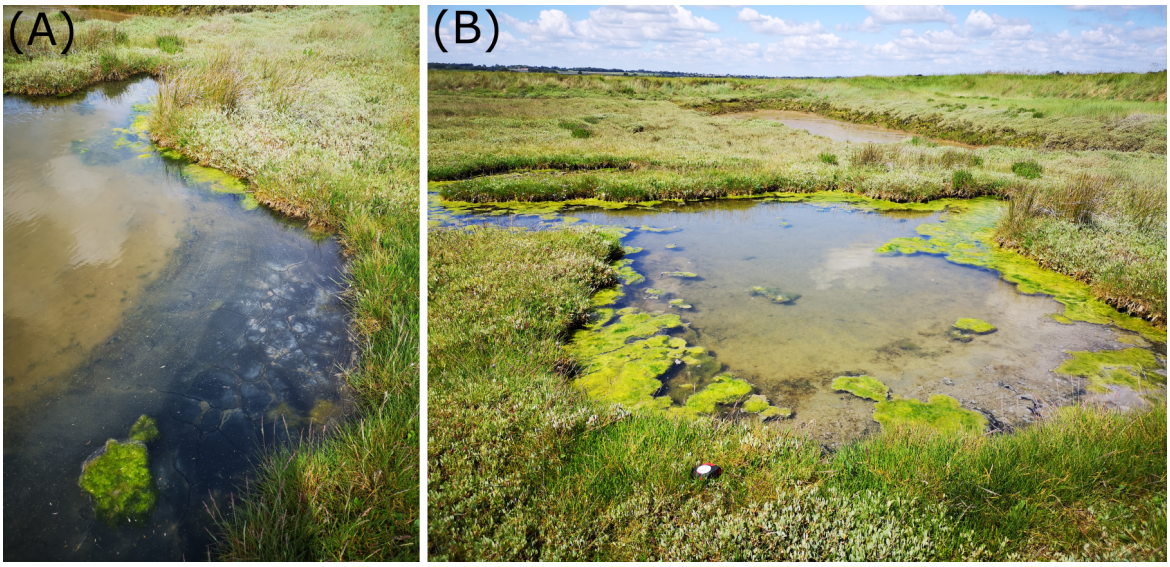

Fig. 2.2 - *Spatial variation in surface sediment colour. (A) The presence of algal blooms at the periphery of ponds causes sulfate reduction to become temporarily dominant over iron reduction, staining the surface sediment black (likely iron sulfides). (B) Evidence of algal blooms growing from the outside inwards.*

I therefore decided that in-field categorisation was more applicable. Following years of sediment core collection, our research group had found that there was a series of characteristics which could rapidly define a pond from observation/brief sediment handling (Table 2.1, Figure 2.3). Unfortunately, there was no single obvious characteristic that I considered which could diagnostically define the geochemistry in a pond sediment in the field. A plausible method was offered in van de Velde et al. (2020) where a silver wire could be inserted into the pond sediment to identify the presence of dissolved sulfide (AgS would rapidly form, coating the wire in a black precipitate (Fike et al., 2017)).

I constructed a classification scheme based on a combination of factors we had observed in the different pond sediments over time (Figure 2.4). More diagnostic features such as the presence of sulfide oxidising bacteria, the colour of the surface sediment, and the presence of worm casts at the sediment surface could quickly categorise the majority of pond sediments. Some ponds, however, contained sediment of which the geochemistry was more ambiguous. For cases such as this, in the absence of geochemical measurements, physical handling of the sediment was the only way to distinguish between the two ponds. Sulfide pond sediment has a higher porosity and a higher organic carbon content and thus feels softer to the touch (van de Velde et al., 2020).

Using this classification scheme, I was able to classify 350 ponds using the characteristic flowchart (Figure 2.4). For each pond visible in the aerial images, I would classify it as an iron-rich pond sediment, a sulfide-rich pond sediment or as an 'intermediate' between iron-rich and sulfide-rich. The third category was necessary given that some ponds contained attributes of both iron-rich and sulfide-rich sediments. This technique relied on classifying each pond as a discrete object based on the findings from Mills (2014) that showed a single sediment core was reflective of the entire pond chemistry. Rare (<5%) of ponds—particularly those which were elongate—contained localised patches of both iron-rich sediment and sulfide-rich sediment; for simplicity, ponds such as these were classified as intermediate. At each pond, I measured the depth of the overlying water column using a tape measure. I also recorded the following characteristics for 267 of the 350 ponds for statistical analysis of certain features: the presence of algae in the water column (Figure 2.3e), signs of burrowing macrofauna (Figure 2.3a,b), the presence of sulfide oxidising bacteria (Figure 2.3d) and signs of desiccation cracks (Figure 2.3f).

2.2.5 *In situ* sampling

In order to monitor geochemical changes in individual pond sediments over time, *in situ* samplers were designed to allow repeated sampling of pond sediment pore fluids without disturbing the sediment. These samplers were designed prior to my PhD and consist of plastic

Sediment characteristic	Pond sediment type		
	Iron	**Sulfide**	**Intermediate**
Sediment texture	Noticeably harder. Less easy to disturb while handling.	Soft, porous sediment – fluffy and easy to disturb.	Variable.
Sediment smell	No distinguishable smell when sediment is handled.	Very strong sulfide smell when sediment is handled.	Variable.
Sediment colour	Often reddish, in varying shades. Some black.	Grey–black.	Grey–black.
Sediment surface	Worm casts common[1].	No worm casts present. Sulfide oxidising bacteria present (*Beggiatoa* sp.)[2]	Worm casts common.
Water surface	Occasional iron oxide[3] mineral films.	White-pale grey film seen on the surface[4]. Bubbles seen from sediment and on the surface. Algal matter common at the edges[5].	Some bubbles seen on surface. Occasional dull white films.

Table 2.1 - *Typical characteristics associated with each type of pond classification. Characteristics are not defining of a classification and instead a composite method is used to classify ponds (Figure 2.4).* [1]*Worm casts were commonly 2–5 cm in length and present in varying numbers on the sediment surface (Figure 2.3a,b).* [2]*Sulfur oxidising bacteria seen in Figure 2.3c. These are typically distinguished by distinct white or yellow patches on the sediment surface.* [3]*Resinous iron oxide films present temporarily on the pond water surface and more commonly seen in creeks and standing water patches on the salt marsh vegetation (Figure 2.3d).* [4]*A pale grey or white sheen can be seen at certain times of the day in the form of stringy white lines on the water surface (Figure 2.3c).* [5]*Algal matter observed in ponds can vary in morphology and quantity (Figure 2.3e).*

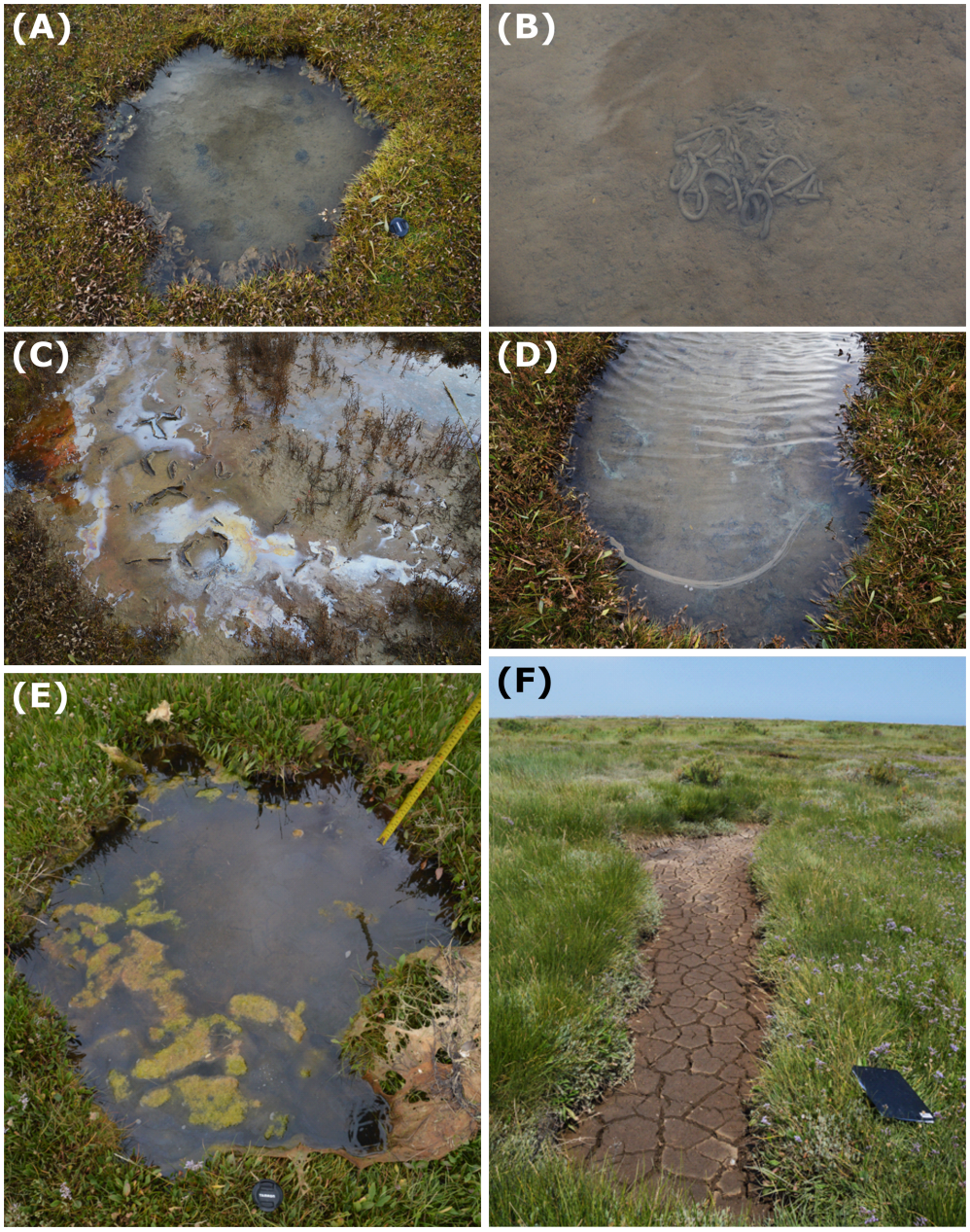

Fig. 2.3 - *Photos showing the common characteristics used to define different pond sediments. (a) Presence of worm casts on the surface of the pond sediment indicates bioirrigation ongoing underneath by macrofauna such as polychaete worms (Nereis spp.) and lugworm (Arenicola spp.) (a close-up of a typical worm cast is shown in (b)). (c) Mineral films occurring at the water surface is assumed to be comprised of predominantly iron (oxyhydr)oxides which have been oxidised in the water column. (d) Presence of sulfide-oxidising bacteria (e.g. Beggiatoceae) on the sediment surface indicated by yellow, white and grey staining. A bacteria film mixed with wind-derived dust is present on the water surface. (e) Algal material present growing in the water column—this often forms around the edges of a pond first before reaching the centre, presumably as it attaches to the pond edge (Figure 2.2). Detrital seaweed is observed on the edge of the pond. (f) Desiccation cracks formed in the pond sediment surface that extend up to 20 cm into the sediment.*

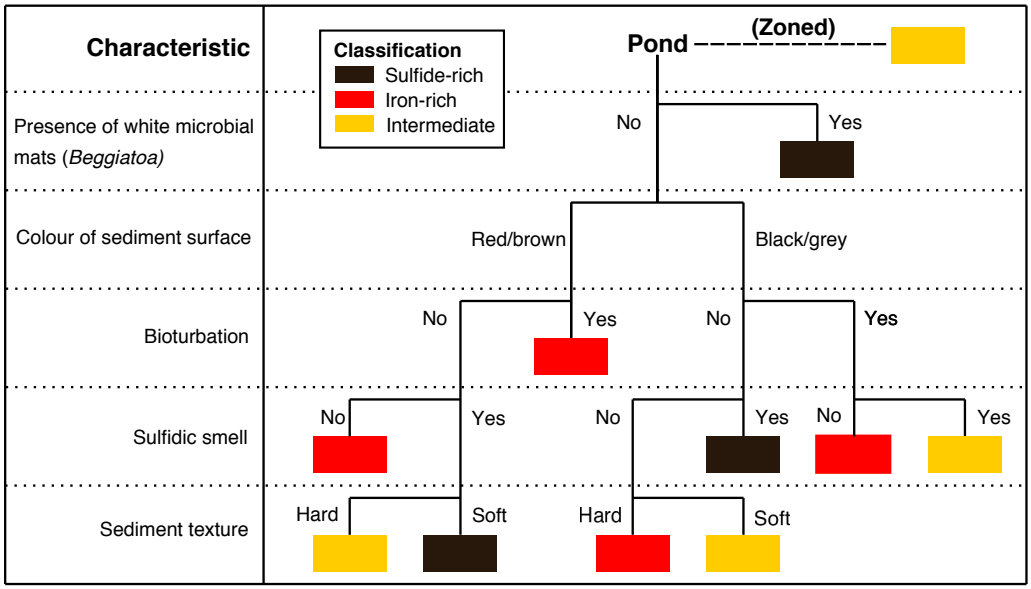

Fig. 2.4 - *Typical method of characterisation of an pond sediments based on features visible and/or easily testable from the surface (see Table 2.1 for description of characteristics). Flowchart is constructed in order of most diagnostic and most easily characterised (e.g. the presence of Beggiatoaceae and surface colour are far quicker to differentiate than the sediment texture). The presence of white microbial mats, presumed to be Beggiatoaceae and resulting oxidise sulfur products present on the sediment surface, was decided to be sufficient enough evidence that sulfate reducing conditions were present in these ponds (Figure 2.3d). The colour of the sediment surface was typically well differentiated; ponds were either a very dark grey colour or had a red/brown tint to them (similar to iron oxide colouration). If the pond sediment surface was a different colour to this or was a shade between the classifications, this category would be ignored for the classification. The presence of bioturbation was ascertained by worm casts seen on the sediment surface (Figure 2.3a,b). The presence of a single worm cast was deemed sufficient to assign a positive result to this category. The sulfidic smell property relates to a strong sulfidic odour when the sediment was removed from the water and handled. Sediment texture was determined by handling of the top 5 cm of sediment. When touched, certain sediments were clearly very soft and fluffy at the surface, whilst others had a stiffer clay texture. These would be defined as soft and hard respectively. Some characteristics were occasionally present but in spatially isolated zones on the pond (e.g. signs of bioturbation on one side of the pond and white microbial mats on the other). These were defined as 'zoned' on the diagram and ponds of this nature were classified as intermediate. This method is preferred to geochemical analysis as it is quicker than sampling and allows for rapid characterisation of the salt marsh system.*

frames to which Rhizon filters are attached at 2-cm intervals starting from the sediment-water interface to a depth of 34 cm (Wilkening, 2017). Outlets from the Rhizons were connected to sampling ports via airtight, double-walled, (<60 cm) tubes (polyethylene inner and PVC outer, ID = 1mm) to the surface to which 10 mL syringes were attached for extraction.

Two *in situ* samplers were installed in the sediments of ponds at Warham (termed Pond A and Pond B) in January 2017 (Figure 2.1d,e). Pond A appeared to contain sulfide-rich pond sediment (using the classification scheme shown in Figure 2.4)—whilst the other, Pond B, an elongate pond, was targeted since it contained sediment which showed characteristics of both iron-rich and sulfide-rich conditions. Samples of pore fluids from sediment in both ponds were collected in March, April, May, July prior to my PhD and I collected the samples in November 2017 and May 2018. During each sampling, the stagnant fluid in the tubing (roughly 0.6 mL for 60 cm of 1 mm ID tubing) was first removed by extracting and discarding 1–2 mL of pore fluid from each outlet. Another 4–5 mL of pore fluid was then extracted for geochemical analysis. All depths were sampled simultaneously.

2.2.6 Sediment core transect at Abbotts Hall Farm, Essex

To test for the presence of subsurface ground water flows, I took six sediment core samples from the Abbotts Hall salt marsh system along a linear transect of roughly 25 m from the centre of the salt marsh platform to the creek in May 2018 (Figure 2.1h). A horizontal core (internal diameter = 6 cm) was extracted at 20 cm depth into the creek wall in a south-easterly direction (named C-Core). Vegetated cores (V1, V2 and V3) were taken from the vegetated platform surface in areas between the ponds. An iron-rich pond core (I-Core) and sulfide rich pond core (S-Core) were taken in ponds displaying the designated geochemical behaviour (Figure 2.4). Porewater in all cores was tested for ferrous iron concentration, $\delta^{34}S_{SO_4}$ and major anion concentrations.

2.2.7 Carbon content analysis

In May 2018, sediment was extracting from the surface of 30 ponds in Abbotts Hall (Area 3 on Figure 2.1g) using a 1 mL syringe with a cut edge. Sediments were dried and crushed by pestle and mortar to homogenise the sediment. Roughly 3 µg of sediment was weighed into tin capsules with care being taken to remove any obvious roots or large pieces of organic material. Total carbon content were measured using a Costech element analyser coupled via continuous flow to a Delta V mass spectrometer in the Godwin Laboratory for Paleoclimate research. Five samples were tested for the presence of carbonate minerals using a duplicate washed in 0.1 M HCl and subsequently triple washed with ultrapure water. As there were no

carbonate minerals found, total carbon content is assumed to come from the organic carbon fraction.

2.3 Results

2.3.1 Porewater geochemistry in sediment cores taken from 2013-2018

In this section, I first present a full geochemical dataset from two sediment cores which reflect typical iron-rich and sulfide-rich pond sediment geochemical characteristics. I then present a larger dataset of cores where only Fe^{2+} concentrations and $\delta^{34}S_{SO_4}$ are reported to give an indication of the variability within the iron-rich and sulfide-rich pond sediment classifications. Also included in this dataset are sediment cores taken through the vegetated platform.

Porewater data collected from an iron-rich core taken from Stiffkey, August 2015, and a sulfide-rich core taken from Blakeney, August 2015 differ in many geochemical parameters (Figure 2.5). In the iron-rich pond sediment porewater there were ferrous iron (Fe^{2+}) concentrations up to 2 mM, little change in the $\delta^{34}S_{SO_4}$, near-zero aqueous sulfide, near seawater $[SO_4]/[Cl]$ ratios, lower overall pH and low alkalinity (Figure 2.5, *red*). In contrast, in the sulfide-rich pond sediment there was no measurable Fe^{2+}, an increase in $\delta^{34}S_{SO_4}$ up to 40‰ higher than seawater, sulfide concentrations above 4 mM, lower $[SO_4]/[Cl]$ ratios relative to seawater, higher pH and higher alkalinity (Figure 2.5, *black*). The concentration of both chloride and sulfate in the porewaters of both sediment cores are lower than that of typical seawater. In particular, the surface 20 cm of the iron-rich pond contains very low porewater chloride concentrations (200–400 mM, 30-60% lower than seawater) (Figure 2.5e,f). The porewater characteristics of these two cores reflect the typical geochemical conditions expected in iron-rich pond sediments and sulfide-rich pond sediments.

To test if there were any differences in pond sediment geochemistry beyond this bimodal classification, I compiled the porewater results of all the sediment cores collected in the research group from 2013–2018 (Figure 2.6). It should be noted that depths within the sediment cannot be accurately compared between the sampled ponds because water depth was not always recorded in ponds where sediment cores were taken, and there is no elevation data for these salt marsh platforms.

Dissolved Fe^{2+} was consistently present (up to 2.3 mM concentration) in iron-rich pond sediment porewaters, whereas Fe^{2+} concentrations were almost always negligible in sulfide-rich pond sediment porewaters. There were variations in the general pattern of Fe^{2+} concentrations within pond sediments broadly classified as ‘iron-rich’. In some sediment

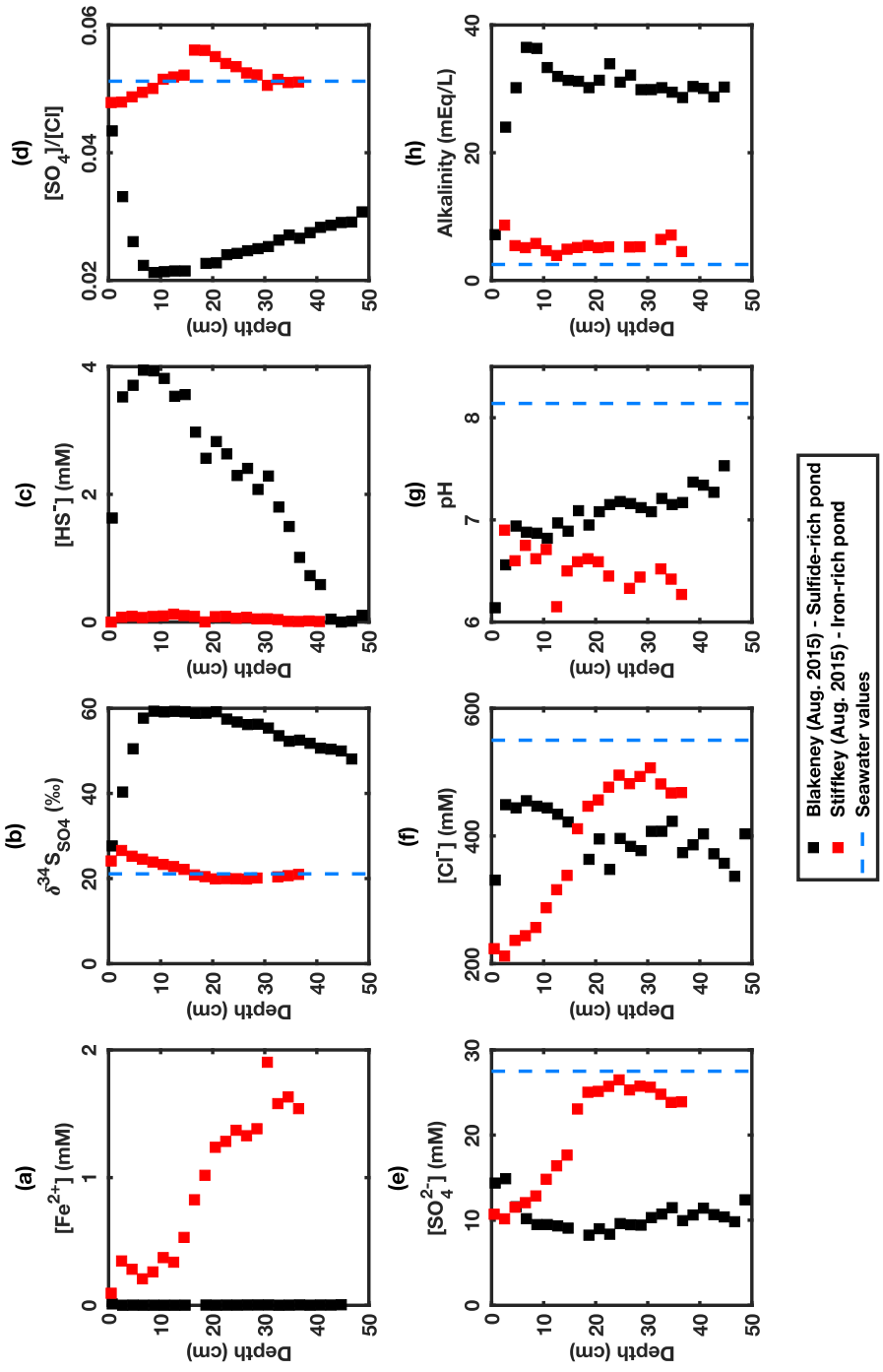

Fig. 2.5 - *Geochemical characteristics of porewater extracted from an iron-rich core from Stiffkey in August 2015 (shown in red) and a sulfide-rich core from Blakeney in August 2015 (shown in black). (a) Aqueous Fe^{2+} concentrations (mM) (b) $\delta^{34}S_{SO_4}$ (‰) (c) Aqueous sulfide concentrations (mM) (d) $[SO_4]/[Cl]$ ratio (e) Aqueous sulfate concentrations (mM) (f) Aqueous chloride concentrations (mM) (g) pH values (h) Alkalinity (mEq/L). Dashed blue lines represent typical seawater values (seawater concentrations of Fe^{2+} and HS^- are negligible).*

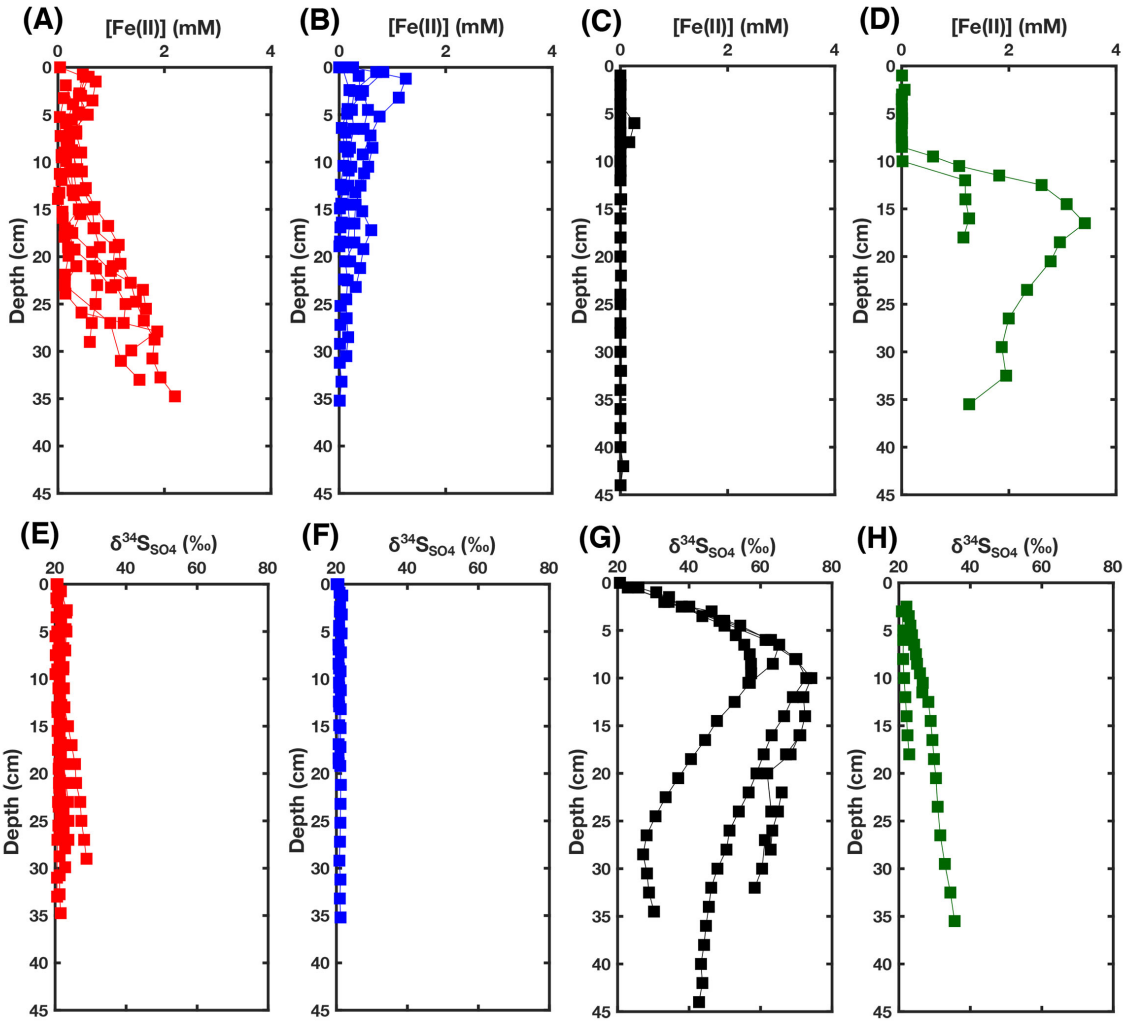

Fig. 2.6 - *Porewater compilation of sediment cores extracted from salt marsh ponds between 2013 and 2018. (a) Fe^{2+} concentrations and (e) $\delta^{34}S_{SO_4}$ for iron-rich pond sediment which shows a significant increase in Fe^{2+} concentration below 15 cm depth (see discussion for explanation). (b) Fe^{2+} concentrations and (f) $\delta^{34}S_{SO_4}$ for iron-rich pond sediment which shows a decrease in Fe^{2+} concentration below 15 cm depth (see discussion for explanation).(c) Fe^{2+} concentrations and (g) $\delta^{34}S_{SO_4}$ for porewater in sulfide-rich pond sediment. (d) Fe^{2+} concentrations and (h) $\delta^{34}S_{SO_4}$ for porewater in sediment cores extracted from the vegetated salt marsh platform.*

cores, porewater Fe^{2+} concentrations increased with depth, sometimes reaching as high as 2 mM at 35 cm depth (Figure 2.6a). In such cores, lower Fe^{2+} concentrations are observed from 5–15 cm; a zone where iron and manganese oxides visibly stain the sediment orange in some places. Conversely, in the other subset of 'iron-rich sediment cores' there was a decrease in Fe^{2+} concentration with depth (Figure 2.6b). Vegetated cores contained negligible ferrous iron up 10 cm below the surface (this coincides with the depth of root penetration). Below this rooting zone, porewater ferrous iron concentrations increase up to 3 mM—the highest observed in any of the cores (Figure 2.6d).

Both types of iron-rich core have porewater $\delta^{34}S_{SO_4}$ which exhibit a minor increase with depth or have a constant $\delta^{34}S_{SO_4}$ near that of seawater (Figure 2.6e,f). In sulfide-rich cores, $\delta^{34}S_{SO_4}$ reaches a maximum up to 70‰ by 15–25 cm depth below the sediment-water interface (Figure 2.6g). In vegetated cores, there is an increase of approximately 5–15‰ $\delta^{34}S_{SO_4}$ from 0–35 cm (Figure 2.6h).

2.3.2 Mapping of pond distributions

Two areas from the Blakeney salt marsh system were mapped using an aerial drone survey and an area in the Abbotts Hall salt marsh system was mapped using Google Earth satellite imagery (Figure 2.1f,g). Area 1, from Blakeney (Figure 2.7) consists of two groups of ponds separated by a tidal creek. Ponds containing sulfide-rich sediment tend to be situated further from large creek networks than ponds containing iron-rich sediment. The presence of sulfide-rich ponds is often accompanied by a region of standing water on the surrounding vegetated platform (visible in Figure 2.7a). Ponds of a similar geochemical and geomorphological nature appear to cluster in groups. Intermediate ponds, displaying neither or both criteria for iron-rich or sulfide-rich ponds, often lie at the boundary between iron-rich and sulfide-rich pond clusters. There are also clear differences in the vegetation over the marsh with "lawn" vegetation (e.g. *Puccinellia maritima*, *Salicornia* spp.) located at the centre of platforms and larger shrubs (e.g. *Spartina anglica*) located at the periphery (closer to creeks) (French and Spencer, 1993).

Area 2 was the most inland area sampled, slightly north of the Norfolk coastal path at Blakeney (Figure 2.8). Ponds with sulfide-rich sediment in this area tend to concentrate at the point furthest inland and iron-rich or intermediate ponds are located more towards the littoral zone. Drone imagery shows vegetation debris on the vegetated platform with sulfide-rich ponds (south in Figure 2.8a) and larger vegetation around the edges of sulfide-rich ponds. Proximity to larger creeks appears to favour the presence of ponds with iron rich sediment (north in Figure 2.8a).

At Abbotts Hall, there is a similar pattern of salt marsh ponds located further from creeks being more sulfide-rich (Figure 2.9), albeit less distinct than in Areas 1 and 2. Iron-rich and sulfide-rich pond sediment distribution does not seem to correlate with the type of vegetation observed on satellite imagery. An artificial drainage ditch (linear creek in NE of area) is proximal to an area where most of the pond sediments have been categorised as 'intermediate'.

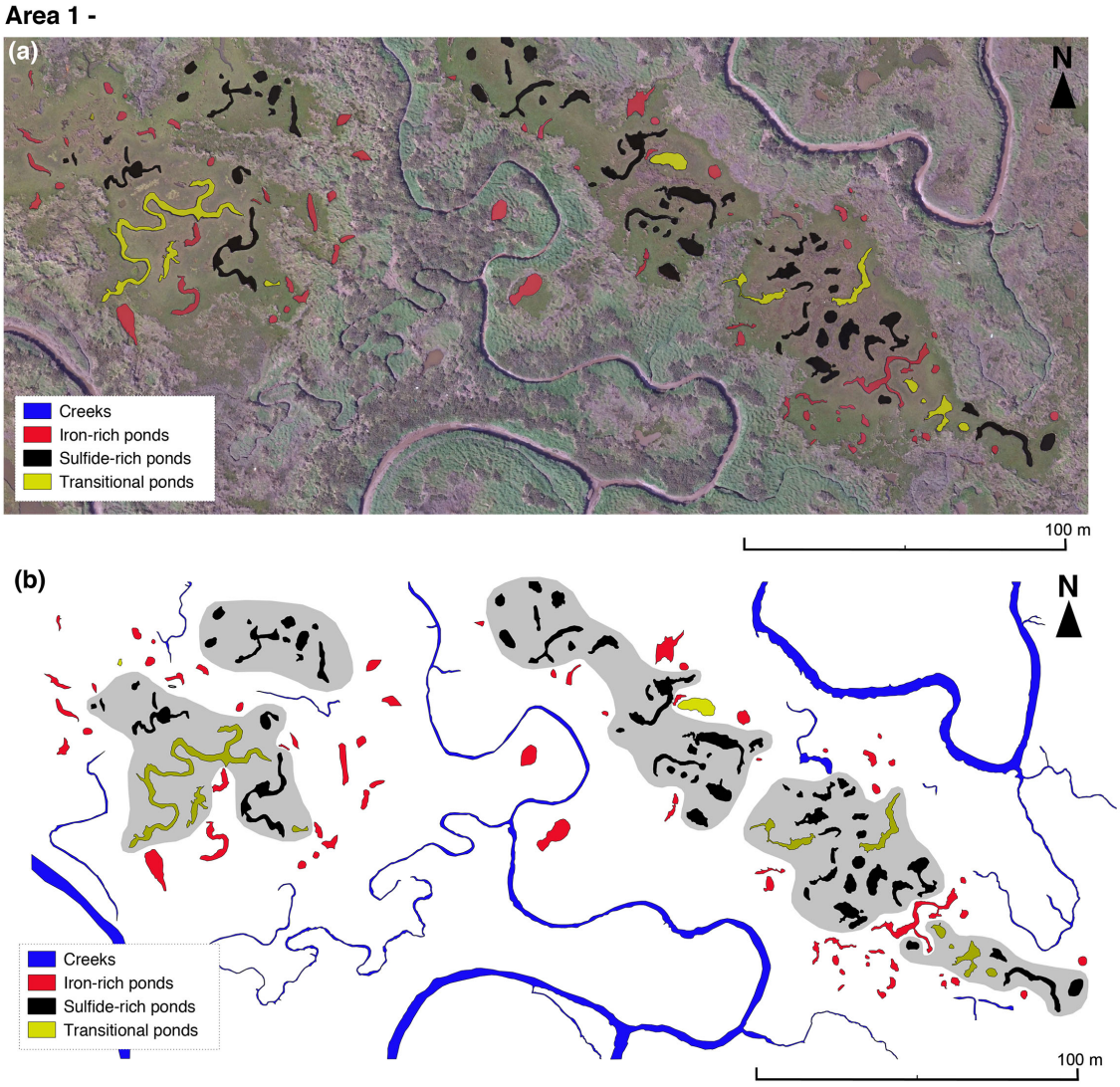

Fig. 2.7 - *Pond sediment classification in area 1 of the salt marsh in Blakeney. (a) Drone imagery taken on 03/05/18 of two aggregates in Blakeney salt marsh area 1 (See Figure 2.1c) overlain by geochemical classification observed over period from May and July 2018. I changed the classification of only two ponds between May and July 2018—both were changed from sulfide-rich to intermediate. (b) Geochemical classification of ponds sediments. Hypothetical, hand-drawn zones of sulfide-rich pond clustering shown in grey.*

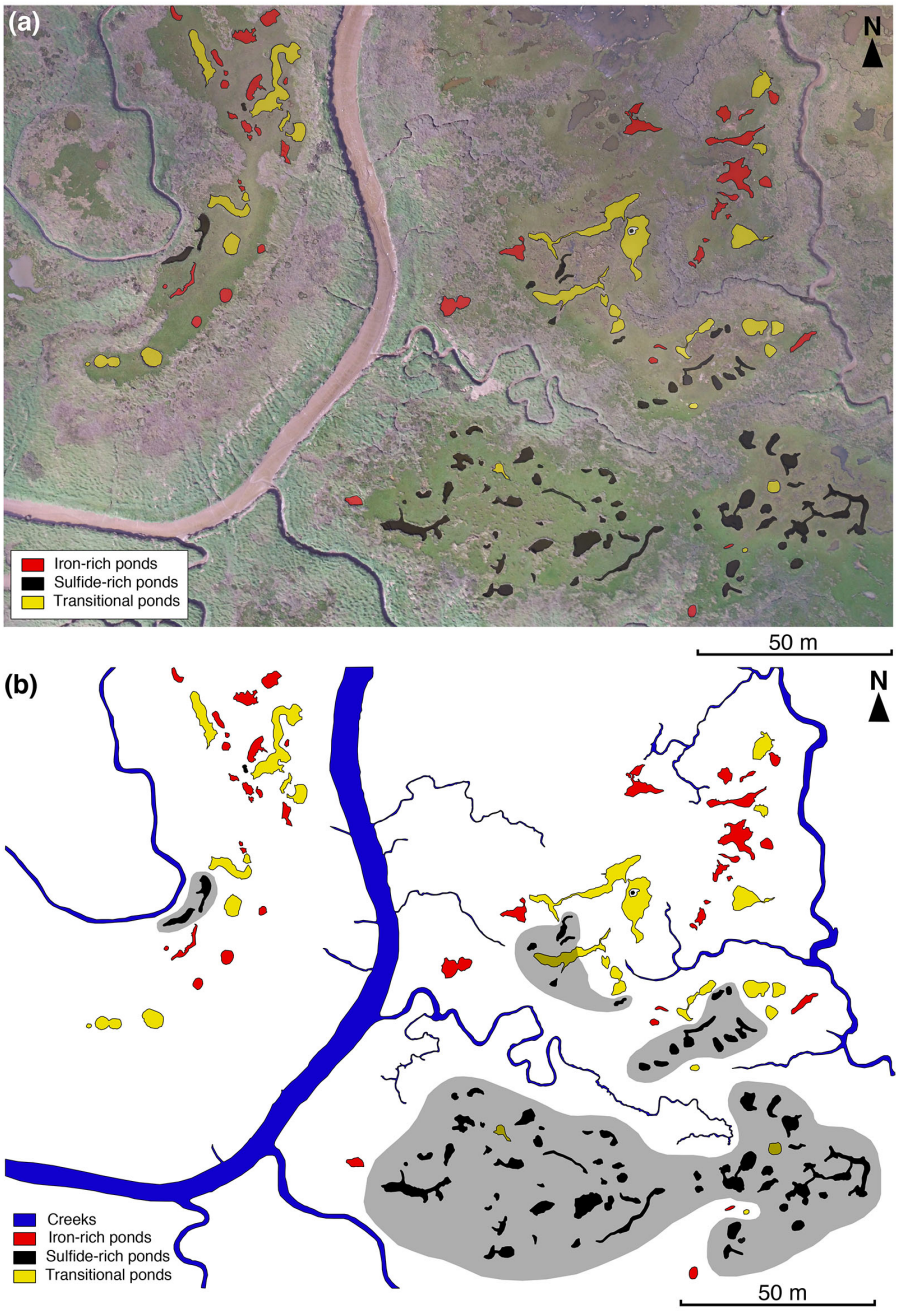

Fig. 2.8 - *Pond sediment classification in area 2 of the salt marsh in Blakeney. (a) Drone imagery taken on 03/05/18 of an aggregate in Blakeney salt marsh area 2 (See Figure 2.1c) overlain by geochemical classification observed over period from May 2018. (b) Geochemical classification with hypothetical, hand-drawn zones of sulfide-rich pond clustering shown in grey.*

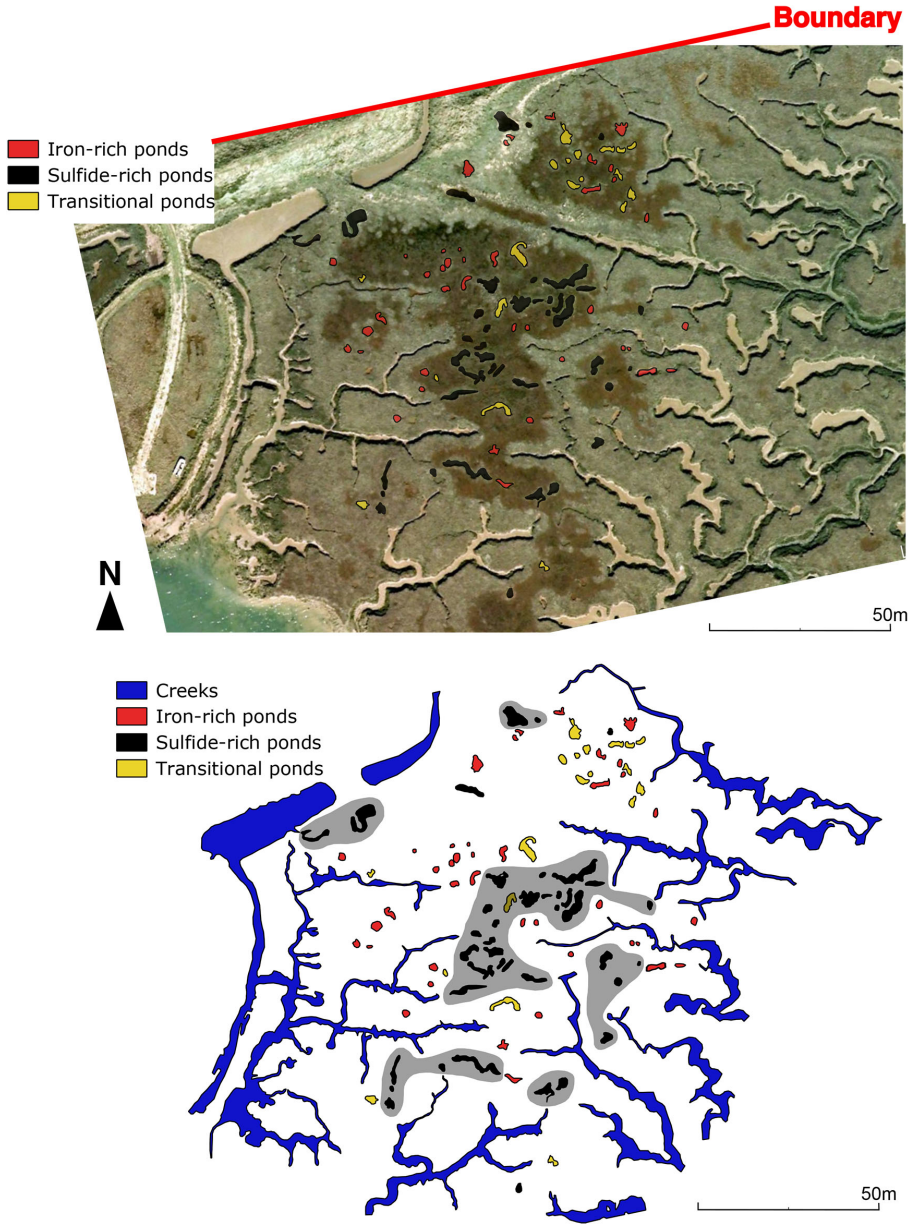

Fig. 2.9 - *Pond sediment classification of Abbotts Hall Farm salt marsh system. (a) Google Earth imagery (06/11/2006) of the salt marsh system in Abbotts Hall (Area 3) (See Figure 2.1g) overlain by geochemical classification observed in June 2018. (b) Geochemical classification with hypothetical, hand-drawn zones of sulfide-rich pond clustering shown in grey. Boundary depicted indicates the limit of the salt marsh.*

2.3.3 Pond characteristics and water depths

There is a correlation between water depth and the type of pond sediment geochemistry (Figure 2.10b–e); the average pond water depth overlying sulfidic pond sediments is deeper than that of iron-rich pond sediments (Area 1 - mean iron-rich pond water depth = 20.2 ± 5.0 cm (n=60), mean sulfide-rich pond water depth = 24.1 ± 4.7 cm (n = 50) (two sample t-test, $p < 0.05$); Area 2 – mean iron-rich pond water depth = 19.1 ± 5.6 cm (n = 40), mean sulfide-rich pond water = 22.4 ± 5.5 cm (n = 64) (two sample t-test , $p<0.05$); Area 3 – mean iron-rich pond water depth = 11.8 ± 4.0 cm (n = 40), mean sulfide-rich pond water depth = 15.2 ± 4.6 cm (n = 40) (two sample t-test, $p<0.05$)).

Figure 2.10a shows the number of ponds which present certain features notable from the pond surface (described in Table 2.1). Desiccation cracks, evidence of a transient drying effect, were found to be less prevalent in sulfide-rich ponds compared to iron-rich and intermediate ponds. This is consistent with the observation that sulfide-rich ponds in general have greater water depths and thus would dry out less frequently. The presence of algae in the water column is common in sulfide-rich (90%) and intermediate ponds (80%) and yet is only present in 30% of iron ponds. Intermediate ponds contain any combination of characteristics; in particular, cases where both algae and bioturbation were present was common (>70%).

2.3.4 *In situ* sampling from March 2017 – May 2018

Ferrous iron concentrations were negligible in both ponds over the sampling period (data not shown). Pond A (a sulfide-rich pond) shows small seasonal variations in $\delta^{34}S_{SO_4}$ of porewater sulfate with higher $\delta^{34}S_{SO_4}$ observed in the summer and autumn months (Figure 2.11a). These variations are particularly pronounced in the upper 15 cm. Changes in $\delta^{34}S_{SO_4}$ in Pond B (an intermediate pond) are far greater (Figure 2.11b); in March 2017, $\delta^{34}S_{SO_4}$ is constant with depth and only slightly elevated from the values seen in a 'typical' iron-rich pond. Over time, the $\delta^{34}S_{SO_4}$ of the shallow portion of the sediment (0–15 cm) increases to a maximum of 55‰ in July 2017 before returning to lower values in November 2017. In contrast, the deeper portion of the sediment (>15 cm) shows a consistent increase in $\delta^{34}S_{SO_4}$ through time—up from 24‰ in March 2017 to 35‰ in May 2018.

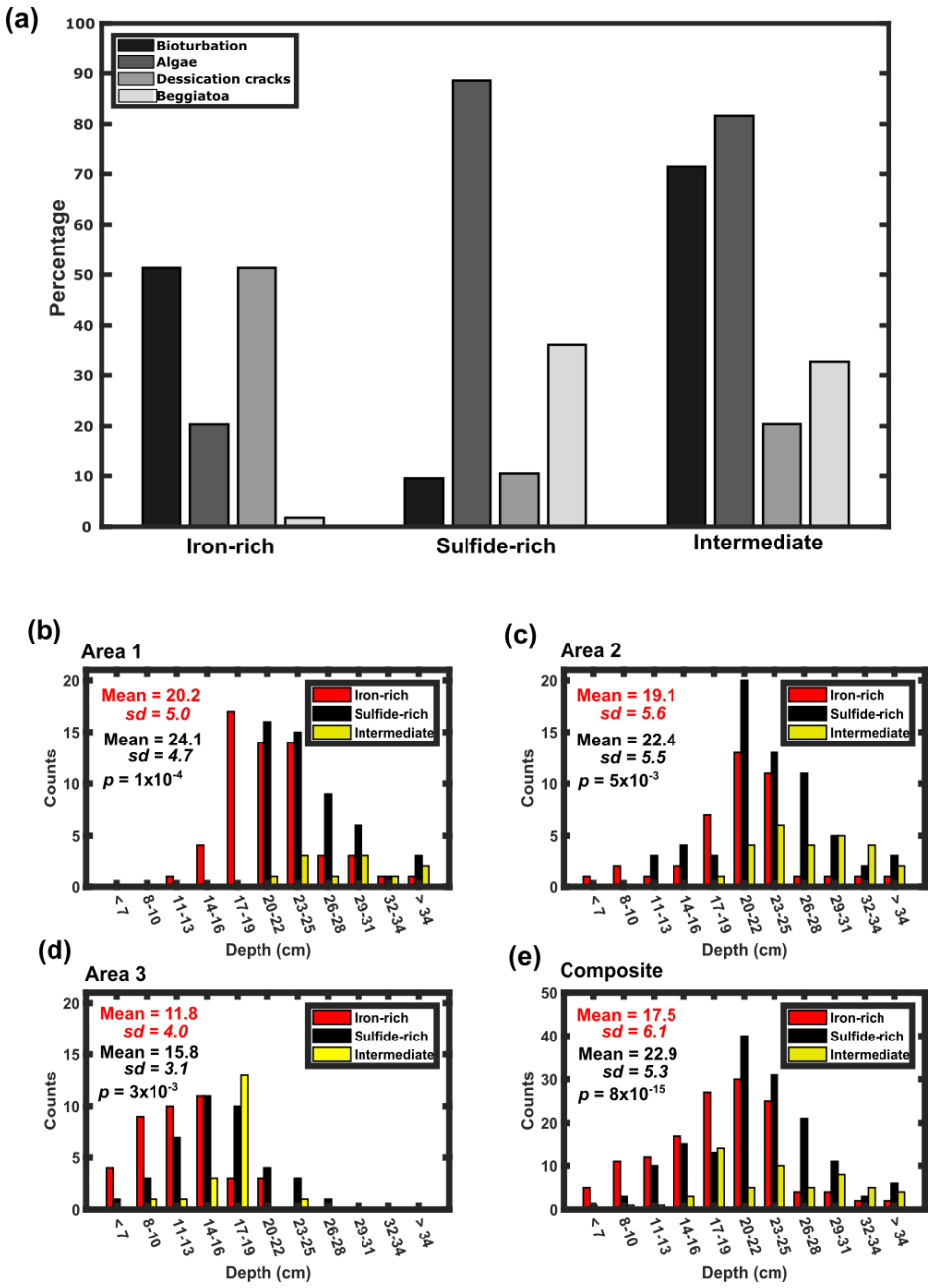

Fig. 2.10 - *Characteristics and water depth of salt marsh ponds in Blakeney and Abbotts Hall (a) Percentage of ponds which showed evidence of bioturbation, algae, desiccation cracks and sulfide oxidising bacteria (e.g. Beggiatoaceae) for each classification of pond. Data comes from all three mapped areas of salt marsh pond sediment. (b) Water depth measurements taken in Area 1 for each type of pond (17/05/18). P-value taken from t-tests testing the null hypothesis that there is no difference in water depth between pond classfications. (c) Water depth measurements taken in Area 2 for each type of pond (17/05/18). (d) Water depth measurements taken in Area 3 for each type of pond (19/06/18). (e) Composite made of all depth measurements taken from Area's 1, 2 and 3.*

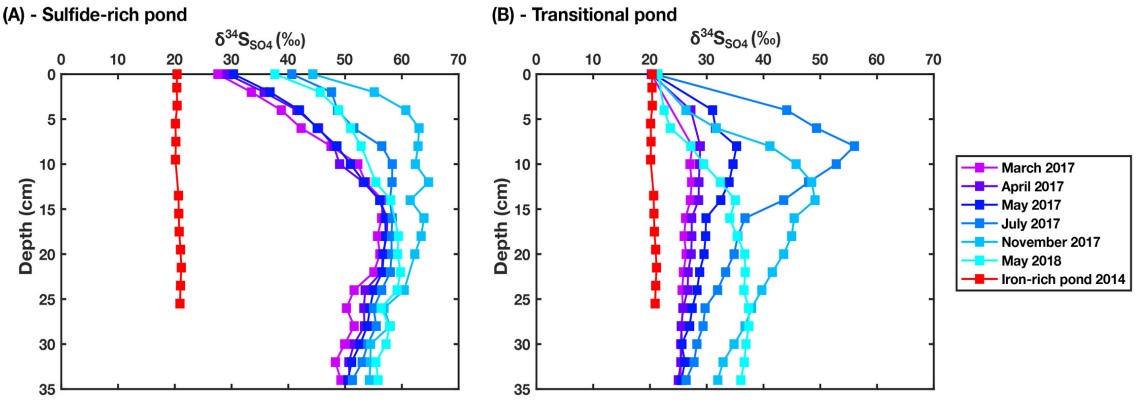

Fig. 2.11 - *Porewater geochemistry of two pond sediments over a 14-month period. (a) $\delta^{34}S_{SO_4}$ measured in porewater samples over a 14-month period for pond A (sulfide-rich pond). Data from an iron-rich pond sampled in 2014 is added for comparison. Analytical uncertainty is 0.2‰. (b) $\delta^{34}S_{SO_4}$ measured in porewaters over a 14-month period for pond B (intermediate pond). Data from an iron-rich pond from 2014 is added for comparison. Analytical uncertainty is 0.2‰.*

2.4 Discussion

2.4.1 Salt marsh pond sediment chemistry

There are multiple geochemical, mineralogical, and geomicrobiological methods of understanding the microbial reactions occurring in a sedimentary environment. Characterisation of the bacterial community present is comprehensive but requires an understanding of how this relates to the chemistry of the environment (Pett-Ridge and Firestone, 2005). Omics—the study of all the metabolic reactants, intermediaries and products in a system to infer microbial reactions—can potentially offer nuanced insight into microbial processes. However, it is difficult to scale the microbial data that is collected to an integrated collection of biogeochemical processes; the huge number of individual reactions in an environmental system makes interpretations non-unique and imprecise (Schimel, 2016). A more recent development is that of biosensors: microbes which have been bioengineered to emit a measurable response to certain environmental conditions (Masiello et al., 2013). Though in its infancy, this promises a new method of monitoring integrated redox changes in an environment.

The alternative method our research group has employed to understand redox reactions in an environment is to use the porewater and sediment concentrations and isotope ratios to infer the biotic and abiotic reactions occurring in the sediment. In essence, this involves measuring the concentration of the reactants (e.g. SO_4^{2-}) or the products (e.g. Fe^{2+}) of a microbial reaction. These measurements are the net integrated concentrations of all the

reactions occurring in the sedimentary environment, and therefore do not necessarily reflect the reactant/product resulting from an individual geochemical reaction. Geochemical analysis of porewater can nevertheless provide insight into how elemental cycles interact with both biotic and abiotic processes in the sedimentary environment.

In this discussion, I will first describe the fundamental reactions and questions regarding iron-rich pond geochemistry, sulfide-rich pond geochemistry and the possibility of intermediate pond geochemistry. I will then discuss what could possibly cause the different pond geochemistry types and whether a transition in pond chemistry could occur. Using the maps of those pond chemistries, I will then offer potential mechanisms which control their spatial distribution on a salt marsh platform.

2.4.2 Iron-rich pond sediment chemistry

Iron-rich pond sediments are characterised by high Fe^{2+} concentrations in the porewater well in excess of almost all known marine environments. For example, Lake Sulawesi—an often-cited modern ferruginous environment—contains porewater Fe^{2+} only up to 45 μM, nearly two orders of magnitude lower than in these salt marshes (Vuillemin et al., 2016). These high concentrations are most likely produced from the reduction of Fe^{3+}-containing minerals (e.g. ferrihydrite or goethite), either through bacterial iron reduction (e.g. for ferrihydrite in (Equation 2.1) or abiotic reduction coupled to sulfide oxidation (Equation 2.2). Once formed, the generated $Fe^{2+}_{(aq)}$ would either be reoxidised back to Fe^{3+} which would predominantly form insoluble minerals or it would be sequestered into the sediment phase as an Fe^{2+}-containing mineral—the most likely of which are iron monosulfides (Equation 2.3) or pyrite (Equation 2.4). The former process—that of Fe^{2+} oxidation—requires an electron acceptor (most likely O_2, but potentially also nitrate or Mn-oxides) to couple with the Fe^{2+}/Fe^{3+} half-reaction. While this process readily occurs at the sediment-water interface, staining the surface red or brown (Figure 2.2), oxygen diffusing into the sediment is quickly depleted within the uppermost centimetre. Therefore, a mechanism is required to explain how such high levels of iron reduction can be regenerated indefinitely at depth in the pond sediment.

$$4Fe(OH)_3 + 7H^+ + CH_2O \rightarrow HCO_3^- + 4Fe^{2+} + 10H_2O \tag{2.1}$$

$$HS^- + 2Fe(OH)_3 + 5H^+ \rightarrow 2Fe^{2+} + S^0 + 6H_2O \tag{2.2}$$

$$Fe^{2+} + HS^- \rightarrow FeS + H^+ \tag{2.3}$$

$$FeS + H_2S \rightarrow FeS_2 + H_2 \tag{2.4}$$

The most likely mechanism stems from the observation that roughly half of iron-rich ponds contain worm-casts at the sediment surface (Figure 2.3a,b), a result of delightful species such as polychaete worms (*Nereis* spp.) and lugworm (*Arenicola* spp.) burrowing in the sediment below (Antler et al., 2019). The amount of worm casts in iron rich ponds and worm density in sediment varies substantially, although the 5–15 cm depth increment has been reported to contain the highest density of worms (Antler et al., 2019). This burrowing effect—termed bioirrigation—introduces a mechanical pathway for oxic waters into an otherwise diffusion-dominated, anoxic system, allowing for reoxidation of aqueous Fe^{2+} to Fe^{3+}-containing minerals (Volkenborn et al., 2007). Evidence for this comes from the orange iron minerals surrounding the linings of burrows which are most likely some poorly crystalline Fe^{3+}-containing mineral such as ferrihydrite(Figure 2.12). This is further supported in the dissolved Fe^{2+} profiles of iron-rich pond sediments, where lower Fe^{2+} concentrations are observed at 5–15cm depth—the zone which coincides with maximum bioirrigation (Figure 2.6a).

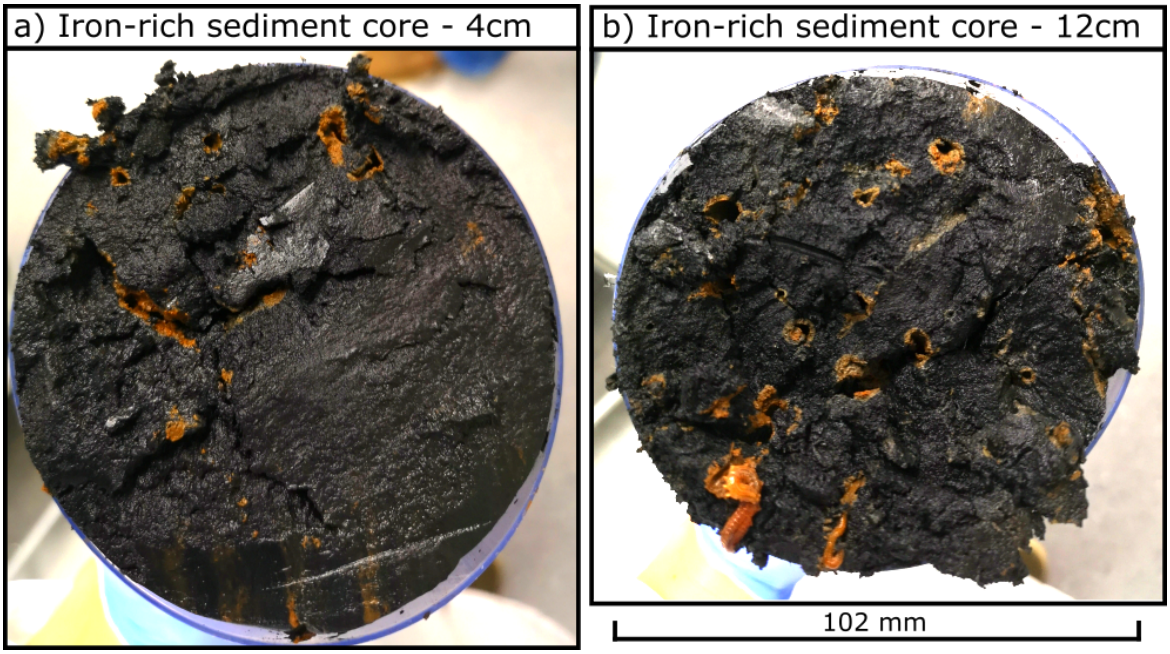

Fig. 2.12 - *Evidence of bioturbation at (a) 4 cm depth and (b) 12 cm depth in a sediment core collected in May 2019. Brightness has been adjusted to highlight the orange (likely ferrihydrite/amorphous iron oxides) burrow linings. Two polychaete worms are present in (b).*

Beneath this bioturbated zone, ferrous iron concentrations in porewater either increase from 15 cm to 35 cm in some cores (Figure 2.6a) or continue to decrease to negligible concentrations below 15 cm (Figure 2.6b). No major difference is observed in the corresponding $\delta^{34}S_{SO_4}$ (Figure 2.6e,f). This discrepancy among porewater profiles of ferrous iron could be due to varying extents of bioirrigation or through different iron minerals present at depth which would influence the rate of iron reduction, with amorphous phases being more rapidly reduced (Lovley and Chapelle, 1995). Another potential explanation for the increase in $Fe^{2+}_{(aq)}$ below 15 cm in certain cores is iron reduction coupled with deep sulfide oxidation (Hansel et al., 2015; Mortimer et al., 2011). This would be undetectable in sulfide or sulfate concentrations or $\delta^{34}S_{SO_4}$ if it were near quantitative, implying some kind of 'cryptic' sulfur cycling may be present (Blonder et al., 2017; Holmkvist et al., 2011; Mills et al., 2016). Indeed, the presence of a cryptic sulfur cycle has been suggested by the $\delta^{18}O$ of the porewater sulfate in these salt marsh sediments (Mills et al., 2016).

Iron-rich pond chemistry is therefore characterised by iron reduction coupled with subsequent reoxidation of that Fe^{2+} by dissolved oxygen mechanically brought deep into the sediment by bioirrigation. Although transiently available aqueous sulfide, produced through microbial sulfate reduction in microenvironments, could titrate some of the reduced iron into iron-sulfide phases (Antler et al., 2019), the ongoing regeneration of Fe^{3+} minerals generates favourable conditions for iron reduction over other microbial metabolisms, resulting in high ferrous iron concentrations within the sedimentary porewater. Reoxidation of Fe^{2+} can explain why pH does not increase with depth in the sediment, as would be expected with the acid-consuming behaviour of iron reduction, as iron reduction and oxidation have equal but opposing effects on pH (Soetaert et al., 2007). Therefore, the decrease in pH observed must reflect other reactions in the subsurface; a tentative suggestion may be methanogenesis at depth or sulfate reduction occurring in microenvironments.

2.4.3 Sulfide-rich pond sediment chemistry

Sulfide-rich pond sediments are characterised by high concentrations of porewater sulfide, diminished sulfate concentrations and an increase in the $\delta^{34}S_{SO_4}$ of the porewater sulfate (Figure 2.5). All of these attributes can be explained by microbial sulfate reduction (MSR) (Equation 2.5). During MSR, bacteria preferentially utilise sulfate with the lighter ^{32}S isotope over the heavier ^{34}S isotope. This leads to an isotopically lower sulfide pool and a residual porewater sulfate pool with a higher $\delta^{34}S_{SO_4}$.

$$2CH_2O + {SO_4}^{2-} \rightarrow H_2S + 2HCO_3^- \tag{2.5}$$

Higher alkalinity (up to 35 mEq/L) can be readily explained by MSR while an increase in pH cannot (Figure 2.5). It is most likely that reactions such as carbonate precipitation, or the reaction of iron monosulfides with hydrogen sulfide, cumulatively counteract the pH decrease often associated with MSR. The high sulfide concentrations are toxic to burrowing macrofauna, precluding the bioirrigation which characterises the iron-rich pond sediment. As a consequence, deeper sediment is relatively less disturbed and more homogenous and there is no means for oxygen to penetrate deeper into the sediment.

The maximum porewater $\delta^{34}S_{SO_4}$ and depth of the maximum varies among different sulfide-rich pond sediments, from 50‰ and 75‰ (Figure 2.6g). These variations suggest that there are differences in the amount of microbial sulfate reduction compared to the sulfate reservoir or how close to isotopic equilibrium this reduction is occurring (Johnston et al., 2007). Variations in temperature, sulfate concentration and carbon quantity/type would all influence these parameters. Sulfide-rich pond sediments have been suggested to release some methane, while iron-rich pond sediments do not (Mills et al., 2016).

2.4.4 Intermediate pond sediment chemistry

This broad dichotomy of pond sediment geochemistry arises due to the titration reaction between sulfide and ferrous iron or iron monosulfides (Equation 2.3) which means that only one of the species (the one in excess) can be present in significant quantities. The pond sediment 'type' therefore reflects environmental conditions which favour production of either reduced iron or aqueous sulfide. While the canonical redox ladder suggests that electron acceptors are used in a specific order with Fe^{3+} being exhausted before sulfate is used (Froelich et al., 1979), the microbial use of electron acceptors becomes much more complex at circumneutral pH conditions. A convergence in the useable free energies for iron-reducing bacteria, sulfate-reducing bacteria and even methanogenic bacteria means that even subtle changes in pH or Eh can switch the dominant metabolism at marine pH conditions (Bethke et al., 2011). This can produce transient events where sulfide can be generated in the presence of algae in the uppermost 10 cm of sediment (Figure 2.13). Sulfate reduction and iron reduction can also coexist in the same sediment at the same time—albeit with one reduction mechanism at significantly lower rates than the other—either as heterogeneous microenvironments, else in redox coupled reactions (Hansel et al., 2015; Mills et al., 2016; Mortimer et al., 2011).

A consequence of this is that certain pond sediments can have either low concentrations of dissolved iron or aqueous sulfide if the time-integrated products of iron reduction and sulfate reduction are roughly even. Under these circumstances, there may be sulfide present in low enough quantities to be tolerated by burrowing macrofauna or there may be low

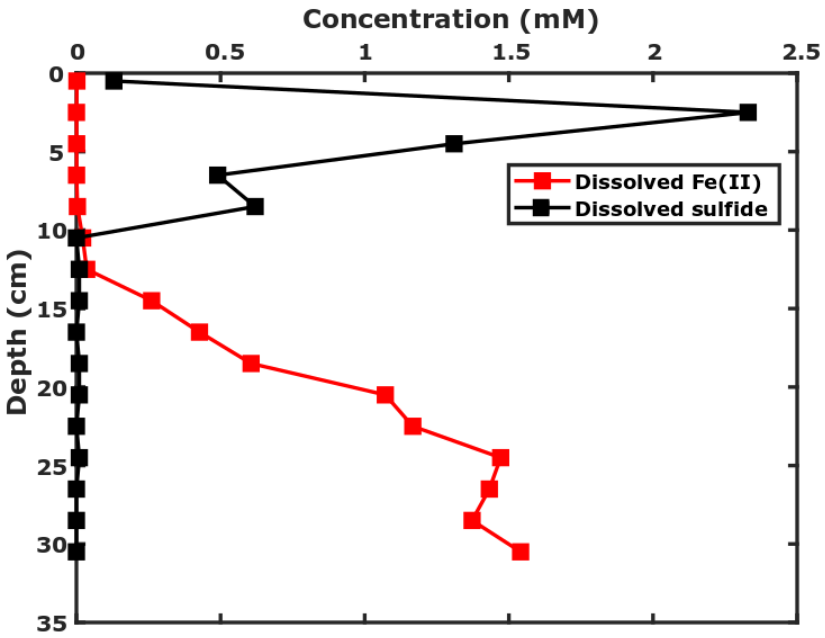

Fig. 2.13 - *Evidence of transient sulfide production at the sediment-water surface of an iron-rich pond sediment. This sediment core was extracted from pond sediment overlain by macroalgae in the water column (the surface sediment was stained black from sulfide production). An example of this is visibly shown in Figure 2.2.*

enough Fe^{2+} concentrations to allow for periodic pulses of sulfide generation (Figure 2.13). These conditions, close to the geochemical "switch-point" between iron-rich and sulfide-rich classifications can produce surface features of both ponds and thus would be classified as intermediate-pond sediments according to my classification scheme (Figure 2.4). Alternately, there may be certain parts of the ponds that are undergoing sulfate reduction—typically near the edge where algae accumulate in the water column (Figure 2.2)—and other parts undergoing iron reduction (classified as "zoned" in Figure 2.4).

2.4.5 Spatial distribution of salt marsh pond sediment chemistry

There has been much debate whether iron-rich or sulfide-rich geochemistry in the sediments is the stable phase, whether pond sediment chemistry could change with time and, if so, what could cause such a change (Antler et al., 2019; van de Velde et al., 2020). Antler et al. (2019) suggested that sulfide-rich geochemistry is a meta-stable phase in the pond sediment which, upon introduction of bioirrigation to the system, could transform into more stable iron-rich geochemistry. van de Velde et al. (2020) instead suggested that the redox dichotomy occurs as a result of small differences in solid-phase input that, through non-linear feedback effects, dictates whether a pond becomes iron-rich or sulfide-rich. A controlling factor could potentially be constrained if there is a clear spatial distribution pattern over a marsh platform of the two types of pond sediment. Of the 350 mapped ponds, I classified 140 as iron-rich, 154 as sulfide-rich and 56 as intermediate. Whilst this suggests a similar number of iron- and sulfide-rich ponds in salt marsh systems, there were no sulfide-rich ponds in some localities (e.g. the Stiffkey salt marsh) and the relative proportions of the three types of pond varied from area to area.

The position of creeks on the salt marsh platform appears to play a first order control on determining the distribution of the two types of pond sediment. Sulfide-rich pond sediments are more likely to be located away from larger creek networks than iron-rich pond sediments. This result is consistent across two sites; Area 1, in Blakeney (Figure 2.7), Norfolk; and in Area 3, Abbotts Hall, Essex (Figure 2.9). Given the spatial separation of over a hundred kilometres between these sites, this is unlikely to be a local phenomenon and instead is a result of more widespread, pervasive, processes. I suspect that Area 2, where iron-rich pond sediments seem to become more common towards the littoral zone, is an extension of the same process but the relationship is based on the distance inland instead of proximity to a creek (Figure 2.8).

This observed spatial distribution precludes temperature as a control on the type of pond chemistry as diurnal changes would be far larger than any spatial differences in temperature across the platform. Bioirrigation differences, as has been suggested in van de Velde et al.

(2020), are also unlikely to vary in this way, unless the delivery of macrofauna is in some way related to the tidal creeks. I therefore propose three controls can cause the observed distribution: (1) a difference in the surface hydrology (both physically and as an input/output of chemical species), (2) a difference in the groundwater regime in the salt marsh and/or, (3) differences in the age, and therefore, depths of the ponds across the platform.

2.4.6 Potential switching of pond sediment geochemistry

Results from *in situ* samplers installed in the sediment of a suspected intermediate pond suggest that iron-rich pond sediment can transition to sulfide-rich pond sediment over relatively short (yearly) timescales. The gradual increase in $\delta^{34}S_{SO_4}$ in pond B (intermediate sediment) from March 2017 to May 2018, particularly at >20 cm depth, implies progressively increased rates of sulfate reduction with time (Figure 2.11b). In comparison, the *in situ* sampling of the sulfide-rich pond sediment nearby shows only minor variations seasonally (Figure 2.11a). Further evidence of rapid geochemical transition is observed in a core taken in June 2019 which shows evidence of transient production of sulfide occurring in the upper most 10 cm of iron-rich sediment (Figure 2.13) and in a deeper (60 cm) core extracted from sulfide-rich pond sediment in Warham salt marsh where sulfate reduction is on top of a zone of iron reduction (Figure 2.14). This is the opposite direction to the canonical redox ladder, where Fe^{3+} should be preferentially used as an electron acceptor before sulfate. This deeper core is interpreted to reflect a pond which has historically undergone the iron-rich to sulfide-rich transition. It is unknown currently how deep the sulfate reduction zone penetrates into the iron-rich salt marsh sediment and how age of the pond relates to the depth of the sulfate reduction zone.

The reverse geochemical transition—that of sulfide-rich to iron-rich geochemistry—has not been observed directly in this salt marsh system. This is most likely due to the stability of the iron sulfide minerals under anoxic conditions which prevent liberation of Fe^{2+} ions for iron oxidation. A mechanical introduction of oxygen to the system could facilitate this transition by oxidising iron sulfides, such as bioirrigation in the iron-rich pond sediment, but the presence of aqueous sulfide is toxic to burrowing eukaryotes, preventing bioirrigation from occurring. A more likely mechanism exists when large desiccation cracks form during transient drying out events in the summer. Penetrating up to 20 cm in depth, these cracks could potentially reoxidise enough iron to reestablish the iron redox system once again (Figure 2.3f).

Given the clear spatial distribution observed in Figure 2.7, Figure 2.8 and Figure 2.9, it can be assumed that the environmental changes that cause creek migration are necessarily slower than the rate of geochemical transition. If this were not the case, I would expect

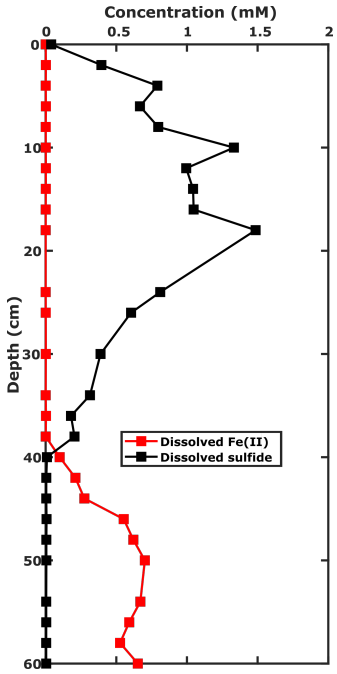

Fig. 2.14 - *Dissolved iron and sulfide concentrations in a 61-cm deep sediment core extracted from a sulfide-rich pond in Warham. Details for the methods in collecting this core described in section 3.2.2.*

to see distributions more reflective of past creek positions or following a more random distribution. Creek migration rates are surprisingly slow on salt marsh platforms, mostly limited by the creeks ability to export the eroded sediment (Allen, 2000), therefore this only places a limited time constraint on the process of geochemical change. An indication of more rapid geochemical transformation rates is hinted by in the North-East corner of the Abbotts Hall site, where an artificially dug linear creek is associated with a cluster (north of the creek) of intermediate ponds (Figure 2.9).

Almost all ponds appear to exist on lawn vegetation as opposed to within the taller vegetation closer to the creeks. This is likely because standing water, and subsequent formation of these ponds, is more likely to exist in the lower energy zone where lawn vegetation is present. I have not established if the vegetation type of the adjacent platform surrounding a pond affects pond sediment geochemistry.

2.4.7 Potential hypotheses for controls on pond sediment chemistry

It seems most likely that all pond sediment will initially contain pond sediment abundant with Fe^{3+}-containing minerals. The surrounding geological landscape contains the glauconitic Crag formation and iron-rich chalk formations at Hunstanton, providing an iron-rich source

of sediment to be trapped in the marsh (Hamblin et al., 1997) given the major provenance source to Norfolk salt marshes is from erosion of proximal cliffs (McCave, 1987). This is corroborated by the high iron concentrations in the vegetated platform (up to 10 wt% of dry sediment). Iron reduction is again common in the vegetated platform and likely behaves similarly to iron-rich pond chemistry, with the addition of plant roots delivering oxygen in the sediment in addition to burrowing macrofauna (Figure 2.6d).

Sulfate, too, should be in significant quantities on the salt marsh. Tidal inundation events can supply large quantities of seawater to the ponds at regular (>monthly) intervals (Figure 2.15). The high concentrations of sulfate in seawater means that sulfate delivery will be far in excess of sulfate consumption rates.

Given these conditions, I offer three potential hypotheses for why pond sediment geochemistry could change from iron-rich to sulfide-rich and potentially vice versa. These are as follows: (1) Variations in the depth of the ponds over the salt marsh platform, (2) Variations in the amount of carbon and/or nutrients delivered to ponds over the salt marsh platform and, (3) variations in the composition and extent of the groundwater fluxes to ponds over the salt marsh platform.

Variations in depth of the ponds

The mean water depth of the sulfide-rich ponds is greater than for iron-rich ponds in all three areas ($p < 0.05$) (Figure 2.10b–e). There is, however, no threshold value where it can be said that if a pond is deeper, it will have a sulfide-rich subsurface geochemistry. Variations in the oxygen concentration in the pond water will be predominantly controlled by wind strength and *in situ* photosynthesis; controls largely independent of water depth. I therefore suggest the relationship between water depth and sediment geochemistry is unlikely related to any physical role that deeper water in the pond might play. One exception is if a deeper pond is sufficiently unmixed by the wind that water column stratification could occur. If this occurs, the bottom part of the water column could become anoxic if effluxes of reductants from the sediment strip dissolved O_2 from the water column.

An explanation for the observed relationship between pond classification and water column depth is that the older the pond is, the more likely it is to be sulfide-rich. The change in water column depth with time $\frac{dZ}{dT}$ reflects a variety of factors, namely, the depth of the hollow into the vegetated platform the pond sits in (D_{Max}), and the relative fluxes (A) of evaporation, ground water drainage and precipitation (Equation 2.6).

$$\frac{dZ}{dT} = D_{Max} - A_{Evaporation} - A_{Drainage} + A_{Precipitation} \tag{2.6}$$

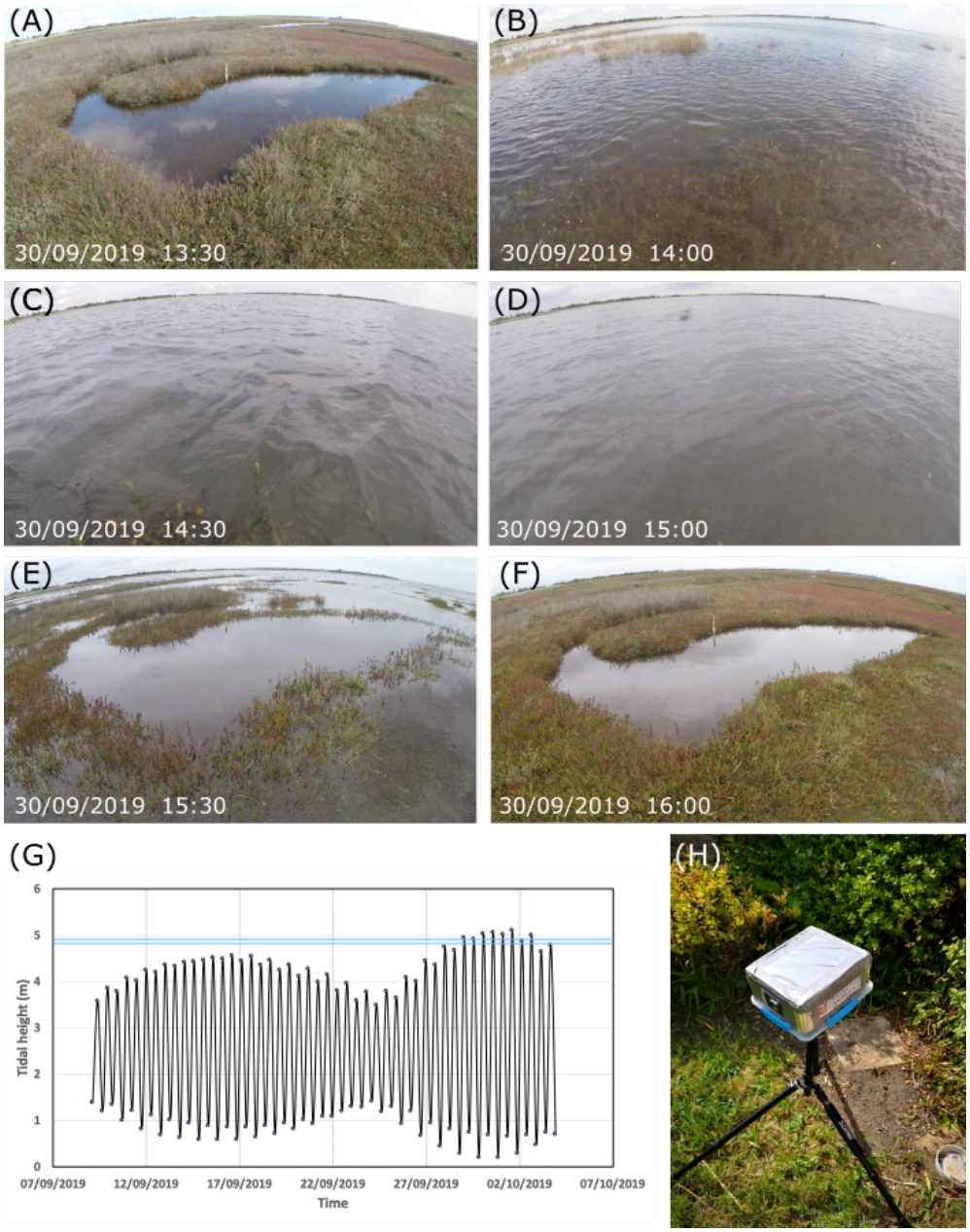

Fig. 2.15 - *Results of a remote timelapse study conducted in September 2019. Subfigures A-F show a typical flooding event that occurs during high tide. Note the whole event starts and finishes with 150 minutes. (G) Tidal heights for high and low tide taken from Clacton-on-Sea station (reference: tidetimes.org.uk) over the period. The light blue lines correspond to the low and high estimates of the tidal height needed to flood the platform. This is based off of two flooding events which were captured in the month period (29/09/2019 13:00 and 20/09/2019 13:30) (the second high-tide times were not recorded since they occurred in the evening). (H) The remote sensing camera consisted of a GoPro camera attached to a CamDo Blink rig which turned the camera on and off for 4 weeks to save battery. A packet of couscous in a permeable bag was used to prevent excess moisture in the container. This study showed that flooding events occurred in regular successions during Spring tides, and that rough tide heights of 4.9 m were necessary to flood the platform.*

D_{Max} is a term which foremost reflects the age of the pond. As salt marshes accrete via vegetative capture of sediment, areas devoid of vegetation accrete at slower rates (Spivak et al., 2017). Consequently, the depth of the pond somewhat reflects the height of the salt marsh upon its formation (complicated by rates of organic matter degradation affecting the porosity of the sediment (Spivak et al., 2017; van Huissteden and van de Plassche, 1998). The fluxes of evaporation, drainage and precipitation all scale with the surface area of the pond, though not necessarily in a linear way. My results lead me to conclude that the age component is the factor which controls the relationship between water depth and pond sediment classification observed in Figure 2.10 and that variations in the water column depth should play a more minor role. A better measure would have been to measure both water column depth and D_{Max} as this would isolate the age component of the pond and solely give information on the water column.

One important distinction to make is when ponds are very shallow or very deep. In ponds where the water depth is very shallow (<10 cm), iron-rich pond sediments are much more common. Desiccation cracks forming after complete evaporation of the water column would create a physical mechanism for atmospheric oxygen to enter deeper into the sediment, allowing for reoxidation of reduced iron mineral species. Desiccation cracks are both more common in the iron-rich pond sediments (Figure 2.10a) and are more likely in ponds where the water column is more susceptible to total evaporation. Therefore, at very shallow depths, the propensity for complete evaporation of pond water keeps pond sediments in an iron-rich state. Where water column depth is particular deep (>30 cm), the chances of total water column evaporation decreases. In such cases, this may favour the presence of *in situ* algal growth, increasing the carbon flux into these deeper pond sediments. These conditions favour sulfate reduction and may provide a mechanism for the increased appearance of deeper ponds being sulfide-rich.

Variations in surface carbon/ nutrient delivery to ponds

Given that the terminal electron acceptors of iron reduction and sulfate reduction (Fe^{3+} and SO_4^{2-} respectively) should be largely in excess in these salt marsh systems, the dominant redox reaction will instead be controlled by changes in the electron donor (organic carbon) and the pH/Eh of the system. If a higher amount of organic carbon is deposited on iron-rich pond sediment, Fe^{3+}-containing minerals would become temporarily depleted, favouring the onset of microbial sulfate reduction in the sediment. This onset of microbial sulfate reduction has been simulated in batch incubations of otherwise iron-rich pond sediments spiked with lactate in Mills et al. (2016) and we observe temporary production of sulfide in iron-rich ponds around the periphery of the pond surface—where algal blooms have formed

(Figure 2.2). The ease of switching between redox reactions in these salt marsh sediments is a manifestation of the similar free energies of the terminal electron acceptors at marine pH (∼8) (Bethke et al., 2011).

An increase in organic carbon loading to sediment can explain a geochemical switch as follows: During periods of temporary concurrent sulfate reduction and iron reduction, the produced reduced Fe^{2+} and dissolved sulfide will react to form iron monosulfides. If organic carbon again becomes limiting, sulfate reduction ceases, and the iron reduction/oxidation is able to continue. If, however, carbon content is high enough to stimulate sulfate reduction to the point that more integrated sulfide has been produced than iron, then dissolved sulfide will become the excessive aqueous phase. This would generate the feedback that burrowing macrofauna would be prohibited by the presence of toxic sulfide, iron cannot be recycled, and hence an indefinite geochemical switch would occur.

The organic carbon content in the upper 5 cm in sediment in ponds at Abbotts Hall (Area 3) follows the iron-rich and sulfide-rich distribution which would be expected. Sulfide ponds have a significantly greater organic carbon content in the upper 5 cm ($p < 0.05$) (one outlier was excluded from this test which was 2SD from the mean). Additionally, ponds near the creeks have a lower organic carbon content (Figure 2.16). Despite evidence that carbon can clearly switch the geochemical redox system (Koretsky et al., 2003; Mills et al., 2016), a mechanism is required to explain the carbon or nutrient (to stimulate carbon production) distributions. I hypothesise that if a pond is proximal to the creeks, it is susceptible to more flooding events and thus any organic carbon, present as dissolved organic carbon, *in situ* vegetation or marine algae, would be flushed more regularly than ponds located centrally (Spivak et al., 2017). The ponds in the centre of the platform therefore sustain conditions for *in situ* macroalgal growth better than ponds on the platform periphery. Additionally, the drag imparted by the rough, vegetated surfaces mean that particulate organic carbon is more likely to be deposited in the centre of the platform, as the water loses energy during the ebb flow back to the creeks. This explanation is consistent with the more inland area which would be less affected by routine flooding events (Figure 2.8).

There is clearly a need to better understand the quantity and type of organic carbon delivery to these ponds, and the metabolic pathways for carbon during sedimentary diagenesis. A more rigorous approach would be to characterise the different pools of organic and inorganic carbon, since some unknown portion of the organic carbon would have been metabolised before measurement. Anecdotally, I have always found that ponds surrounded by taller vegetation (e.g. *Spartina anglica*) are more likely to contain sulfide-rich sediment, which may reflect more efficient capture of allochthonous carbon during tidal inundation

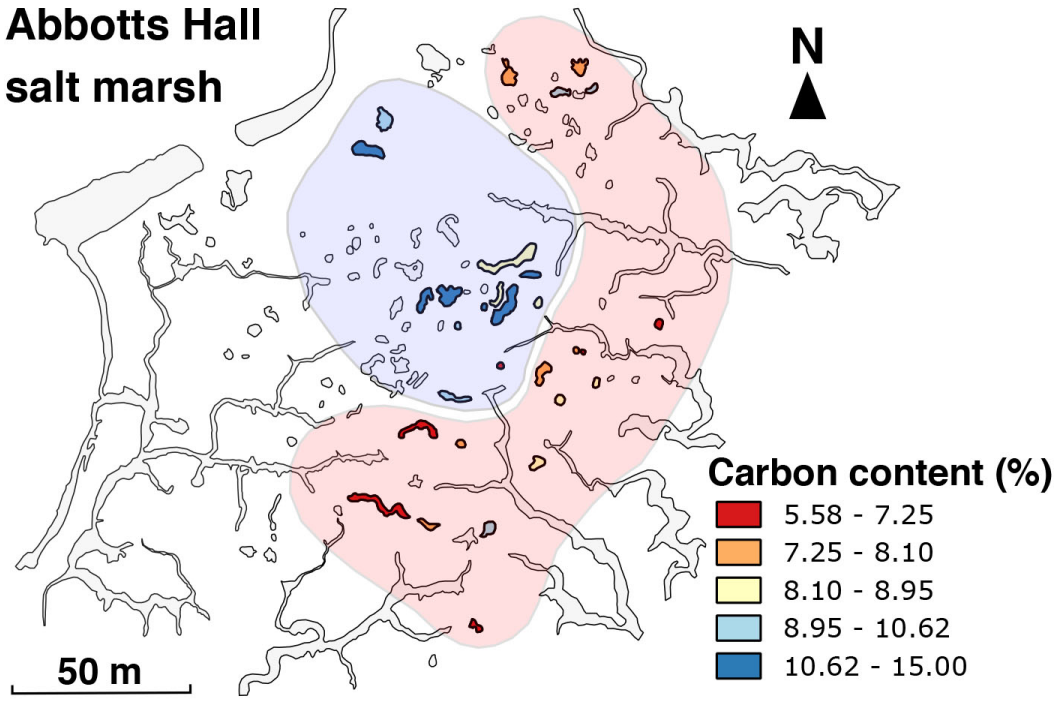

Fig. 2.16 - *Distribution of organic carbon content (%) in the top 5 cm of pond sediment across Abbotts Hall Farm salt marsh. Hand-drawn zones of 'high' and 'low' organic carbon content are shown to represent the overall relationship.*

events. Factors such as these need to be explored more thoroughly to constrain the role of carbon in the geochemistry of these marshes.

Variations in composition and extent of the groundwater fluxes to ponds over the salt marsh platform

The final hypothesis to explain the spatial distribution in the pond geochemistry is that subsurface groundwater flow may play a role in distributing reactants, such as ferrous iron, heterogeneously across the salt marsh platform.

The large variation in ferrous iron concentrations across the core transect in the vegetated platform suggests some subsurface groundwater flow is occurring (Figure 2.17). The depth of the ferrous iron maxima does not correlate with distance from the creek and instead appears to vary randomly. Hydrological flow paths in salt marshes are complex to predict; a catchment area is typically dictated over long timescales by hydrological equilibrium attained by the flood and ebb tides (Allen, 2000). It therefore seems likely that the spatial distribution of sulfide-rich and iron-rich pond sediments is not controlled primarily by subsurface flows.

In a core extracted horizontally into the creek wall, there is a 3 mM decrease in ferrous iron over the 5 cm boundary layer (Figure 2.18). The chloride and $[SO_4]/[Cl]$ data suggests this is hydrological mixing and not simply a zone of iron reduction. Ferrous iron must therefore be effluxing from the salt marsh platform into creek water over time, corroborated by measurable Fe(II) concentrations in creek waters (Table 2.2). Burrowing by crabs appears to increase this zone of transport further than would be expected by simple diffusion. The absolute flux is small compared to the amount of iron in the salt marsh sediment, so this is unlikely to alter the total inventory of sedimentary iron on the salt marsh platform significantly over time.

Chloride concentrations in the vegetated cores vary largely at the surface (Figure 2.17b), implying significant variations in the balance of tidal inundation events, evaporation and precipitation across 10 m distances. The likelihood of evaporation/precipitation differences over such a short distance seems improbable, therefore this observation lends support for tidal inundation events being heterogeneous across some parts of the salt marsh platform which may cause heterogeneous detrital carbon distribution.

2.4.8 Potential mechanism for pond sediment distribution

The mechanism which dictates whether pond sediment becomes iron-rich or sulfide rich is likely some combination of the three effects described above which, together, create conditions favourable for a certain dominant redox condition. This process is undoubtedly

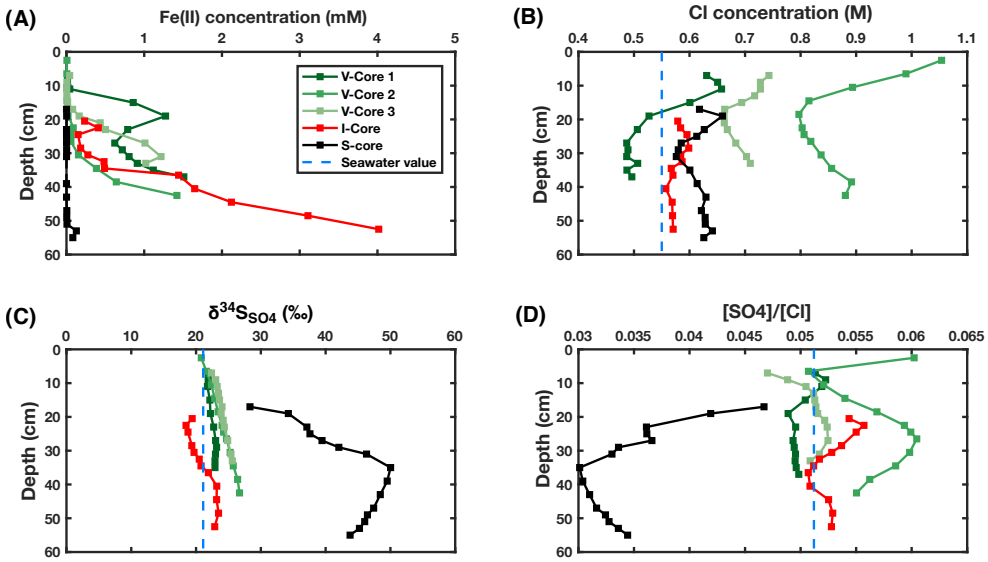

Fig. 2.17 - *Porewater geochemistry of sediment cores taken across a core transect (Figure 2.1h). (A) Dissolved Fe^{2+} concentrations (B) Chloride concentrations (C) Porewater $\delta^{34}S_{SO_4}$ (D) Porewater SO_4/Cl ratio. The depths are corrected for the pond sediment depth below the vegetated surface.*

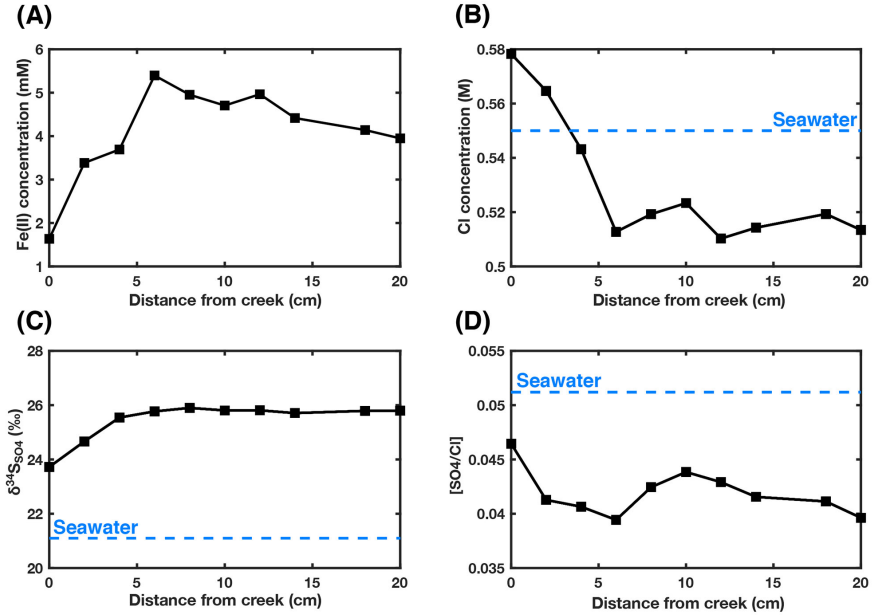

Fig. 2.18 - *Porewater geochemistry of a sediment core horizontally extracted from creek wall (see Figure 2.1h for location). Depth is 20 cm from the surface of the salt marsh. (a) Fe^{2+} concentrations (M) (b) Cl concentrations (M) (c) Porewater $\delta^{34}S_{SO_4}$ (d) $[SO_4]/[Cl^-]$. Blue dashed line corresponds with seawater values. Location shown in Figure 2.1.*

Creek no.	Fe(II) Concentration (mM)
1	0.008
2	0.021
3	0.000
4	0.017
5	0.005
6	0.005
7	0.000
8	0.001
9	0.000

Table 2.2 *Ferrous iron concentrations taken from 15 mL of creek water in 9 separate creeks from Abbotts Hall salt marsh which were immediately fixed with 100 µL of ferrozine solution and analysed via the methods in Stookey (1970).*

influenced by non-linear feedbacks related to bioirrigation, however, bioirrigation alone cannot explain the observed spatial distribution (Antler et al., 2019; van de Velde et al., 2020). In the following section, I discuss a plausible mechanism which can control the observed spatial distribution of pond sediments (Figure 2.19).

The baseline sediment of the marsh platform contains an abundance of Fe^{3+} minerals which becomes the principle terminal electron acceptor for bacterial iron reduction. All pond sediments will therefore initially contain dissolved Fe^{2+} in the porewater. Over time, the sediment beneath each pond may undergo one of two broad fates.

First, the pond sediment could sustain high levels of iron reduction coupled with dissolved Fe^{2+} reoxidation induced by bioirrigation. Carbon input to that pond must be lower than the inventory of readily reducible Fe^{3+}-minerals to prevent high levels of sulfate reduction occurring, which would produce hydrogen sulfide and remove some of the reduced Fe^{2+} as iron sulfide species. Thus, ponds where detrital carbon inputs and *in situ* algae formation are low will be more likely to contain iron-rich sediment for prolonged periods of time. This favours ponds at the periphery of the salt marsh platform which are younger and shallower, and more susceptible to "tidal flushing" events that would export algae produced in the pond. The formation of desiccation cracks during summer months would provide a mechanism to reoxidise any iron sulfide minerals that had formed during transient sulfate reduction; again, this process is favoured by the shallower ponds that exist on the platform periphery.

The second fate that can befall pond sediment is that the pond sediment changes from iron-rich geochemistry to sulfide-rich geochemistry. The known mechanism which can enforce this change is the introduction of organic carbon to the pond sediment to the extent that sulfate reduction becomes significantly competitive (Mills et al., 2016). The argument

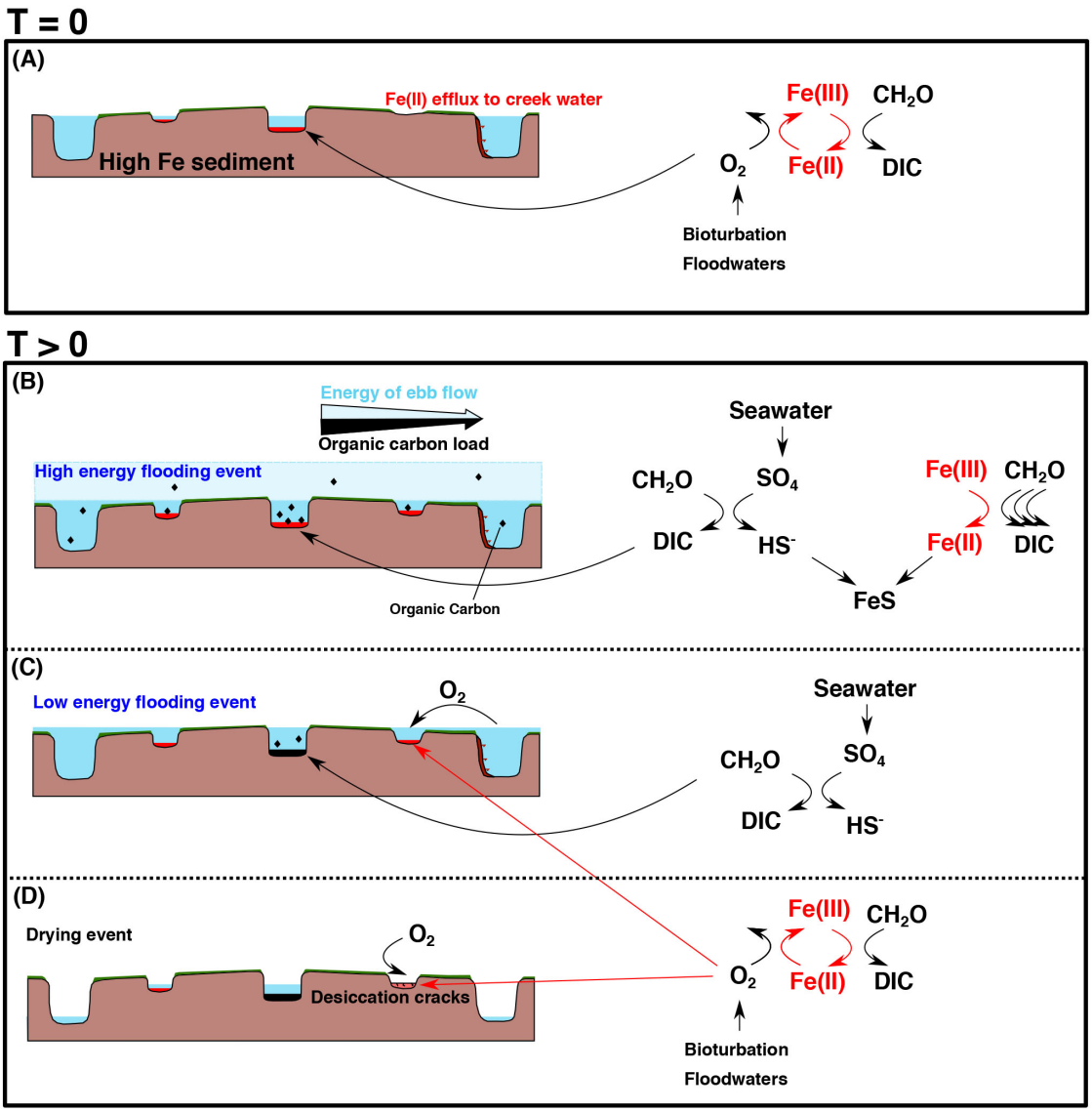

Fig. 2.19 - *Schematic of potential mechanisms driving pond chemistry heterogeneity over a salt marsh platform. Vertical scale is exaggerated (likely elevation differences are within a metre). Panel A represents an earlier stage of development ((Time)T = 0) in a salt marsh platform whereas panels B, C and D represent changes over time ((Time)T > 0) (e.g. the effects of deeper, older ponds and the potential transitioning of pond sediment geochemistry). (A) Due to the high iron content of the sediment, all ponds are hypothesised to contain iron-rich pond sediment geochemistry. Fe(II) efflux to creek demonstrates the unknown diffusive flux at the creek wall boundary (Figure 2.18). (B) Periods of extremely high flooding (storm events or very high tides) from tidal creeks. All ponds are flushed with seawater and detrital organic carbon will be deposited heterogeneously. (C) Low energy flooding events which may only flood ponds closer to the creeks introduces oxic water and removes algae growing in the pond water (Spivak et al., 2017). (D) Periods of excessive dry weather on the salt marsh platform (as observed in July 2018). Differential water head is attained due to the low hydraulic conductivity of the clay-rich sediment. See text for full explanation of mechanism.*

opposing this, as stated in Antler et al. (2019), is that a large enough source of labile carbon is environmentally unfeasible. In response, I would argue the change does not actually require all carbon to present in one event, as the formation of iron sulfide species essentially removes some of the iron from being able to be reoxidised, decreasing the pool of bioavailable iron in the sediment (Figure 2.20). Continued burrowing would be able to reoxidise some of these iron-sulfide minerals in the same way as it would reoxidise dissolved Fe^{2+} but would be less effective as iron sulfide minerals would not diffuse to these regions as readily as dissolved Fe^{2+} would. This time-integrated transition of Fe^{3+}-minerals to iron sulfide minerals would lower the effective "switch-point" necessary to change the sediment to sulfide-rich. This switch-point is the point at which sulfide produced from sulfate reduction is in excess of ferrous iron produced from iron reduction. At that point, burrowing is inhibited by the toxicity of sulfide, and this negative feedback makes the sulfide-rich pond stable.

Fig. 2.20 - *Photo of black iron-sulfide minerals staining the sediment away from the lining of burrows. The immediate lining of burrows is stained brown, reflecting precipitation of iron (oxyhydr)oxides.*

Following this logic, older pond sediments are more likely to become sulfide-rich simply because more organic carbon would have reached the sediment-water interface with time. Therefore, more of the Fe^{3+}-minerals will have been converted to iron-sulfide, and the switch-point is more likely to have been reached. Older ponds are more likely to located centrally on a salt marsh platform; drainage efficiency decreases with distance from the

creeks, and so primary pond formation will start at the furthest point. Consequently, age can explain the primary spatial distribution of pond sediments.

To shift a sulfide-rich sediment back into an iron-rich sediment, a perturbing mechanism is necessary to introduce oxygen deep into the sediment to reoxidise iron sulfide minerals—an example of this would be desiccation in the summer months. A negative feedback is therefore generated where the deeper, older ponds in the centre of the platform are less likely to have complete evaporation of the overlying water column and are therefore more likely to remain sulfide-rich. It is unknown what effect larger-scale drying events, such as in May-June 2018 where almost all pond sediments where dried out, has on the distribution of pond geochemistry.

Not all ponds follow this spatial behaviour; there are clear cases where sulfide-rich pond sediments are located close to creeks and vice versa. In view of this, it is likely that other processes, aside from carbon loading with age, influence the spatial distribution: spatially heterogeneous groundwater flows could periodically supply or strip pond sediments of ferrous iron and favour one metabolism over the other, certain ponds with tall vegetation may be disproportionately efficient at capturing detrital organic carbon during tidal inundation events, and some water columns may have more suitable water chemistry (e.g. temperature, macronutrients and micronutrients) which favour rapid and pervasive algal growth. Finally, I highlight the fact that new ponds are generated every year; shallow ponds can form in the centre of the platform and deeper ponds, through senescence of creek tributaries can form adjacent to creeks. External factors—including human disturbance such as myself, with a plastic tube—can also generate new ponds in areas where they perhaps would not have been in naturally (Figure 2.21).

One conclusion which can be drawn from this study is that these salt marsh systems are complicated. Measuring a single pond is like measuring a single—albeit fascinating—geochemical reactor; it behaves due to a specific set of conditions which may not reflect the wider formation processes of ponds on the marsh. I have attempted a more holistic approach with this study and have found that a broad relationship can be drawn when considering the age and carbon-loading of a pond sediment. This may explain why ponds on the marshes at Stiffkey appear to only contain iron-rich sediment—perhaps the carbon inputs to ponds are lower here, or the ponds are relatively younger? Another pertinent question is whether this dichotomy of pond sediment chemistry only arises when the total iron content in the salt marsh sediment is sufficiently high. If so, are these salt marshes particularly important or unimportant in terms of the fate of blue carbon? An understanding of the behaviour of carbon on various UK salt marshes will surely answer this question.

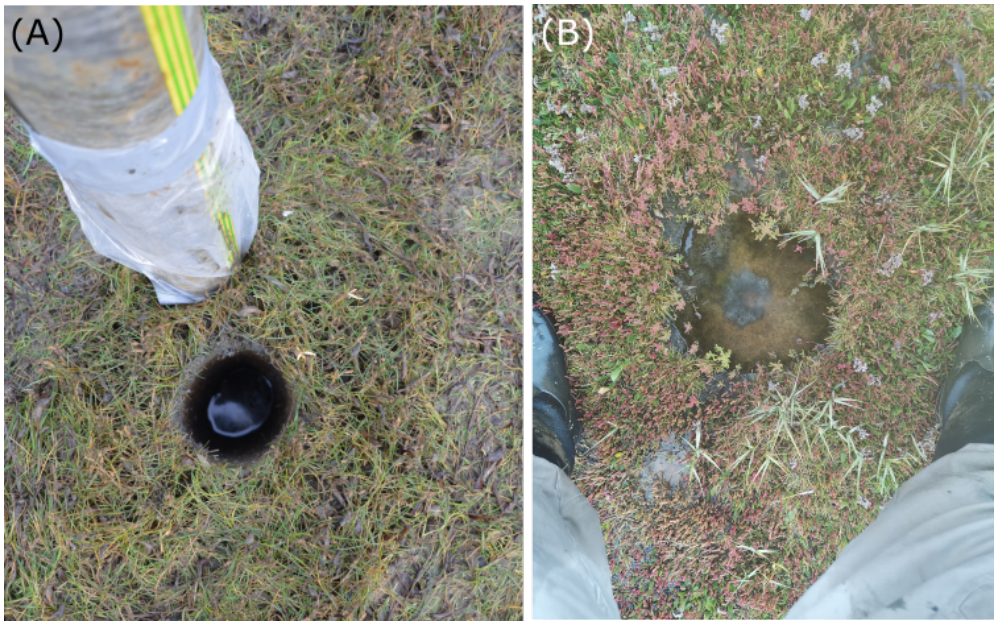

Fig. 2.21 - *The formation of a new proto-pond at Abbotts Hall Farm salt marsh, Essex. (A) A vegetated core taken in November 2018 was extracted leaving a cavity in the salt marsh surface. (A) Over time, this pond expanded through erosion/further flooding events and grew to over twice the diameter in 10 months. It is unknown what effect this anthropogenic intrusion had on global CO_2 emissions.*

2.5 Conclusion

Sulfide-rich and iron-rich sediments are found throughout the East Anglian salt marshes. The distribution of the types of pond sediment and the *in situ* sampler data suggest that pond sediment geochemistry can be transformed from iron-rich to sulfide-rich over as short a timescale as a few years. Drone-based mapping of the salt marshes has shown that ponds containing sulfide-rich sediments tend to be congregated in the centre of a salt marsh aggregate of ponds, further away from larger creek networks. I hypothesise that this is due to a combination of factors, including delivery of organic carbon across the salt marsh platform, the age of the pond, variation in physical characteristics based on the position of the pond (i.e. water depth and the propensity for total evaporation), and a possible sub-surface groundwater flow distributing reactants based on position on the salt marsh. This study suggests that some combination of these effects will result in chemical heterogeneity of salt marsh pond sediment geochemistry and that single mechanism appears dominant. This work implies that artificial drainage ditches, common in agricultural reclamation of East Anglian salt marshes, could alter the geochemistry of these pond sediments on short timescales. This

has consequences for the carbon budget, and for nutrient and trace metal capture within salt marsh ecosystems.

2.6 Implications for further chapters

The work in this chapter has introduced and elaborated on the fundamental redox processes present in East Anglian salt marshes whilst highlighting the important of constraining the individual redox conditions for each pond of interest.

This acts as a foundation through which to test various hypotheses of widely used paleoredox tracers for iron-rich (or ferruginous) sediments and sulfide-rich (or euxinic) sediments. A particularly important factor which has not previously been addressed is what effect will be had on these paleoredox proxies if the sediment geochemistry switches from one redox state to another. Will this diagenetic history be sustained, over-written or some combination of the two in the sediment?

Chapter 3

Method Development for Trace Element Analysis using ICP-MS and for Chromium Isotope Analysis on the Thermal Ionisation Mass spectrometer (TIMS)

3.1 Introduction

3.1.1 Chapter outline

Methods for analysing the major elements in salt marsh pore fluids, as well as the concentration of sulfide and iron and the sulfur isotopic composition of sulfate ($\delta^{34}S_{SO_4}$) were already well developed at the University of Cambridge prior to my arrival. The methods for measuring trace metal concentrations were distinctly more limited—for both salt marsh sediments and porewaters—with only one project previously looking at these environments in this context (Traynor, 2016). During my PhD, I aimed to better understand the geochemistry of molybdenum (Mo) and chromium (Cr) in these environments. For each of these elements, a reliable method of measuring both the concentrations and stable isotope ratios was necessary.

The first part of this chapter focusses on the sample collection and accurate determination of trace metal concentrations in porewater and aqua regia leachates of the pond sediment. This was necessary for two reasons: Firstly, accurate concentration measurements are required for the sample preparation (in particular, correct addition of the double spike) in measuring the stable isotopic composition of Mo and Cr. Secondly, since the behaviour of different

elements are often interlinked in a sedimentary environment, measuring a suite of elements helps understand these relationships better. This is particularly true of iron and manganese; the speciation of these elements strongly affects the behaviour of many other trace metals due to adsorption, co-precipitation and altering the geochemical conditions of the porewater (e.g. pH) (Goldberg et al., 2009; Shaw et al., 1990).

The second stage of my project was making stable isotope measurements of Mo and Cr. The Mo isotope methodology was developed at Royal Holloway, University of London (RHUL) prior to the work in this thesis and these methods are provided in detail in **Chapter 4** alongside the Mo isotope data. There was no methodology developed at the University of Cambridge for making chromium isotope measurements at the beginning of my PhD. Therefore, a significant part of this chapter will describe the development of a method for purifying and analysing chromium isotope ratios on a Thermal Ionisation Mass Spectrometer (TIMS).

3.2 Sample collection

A method for core collection was in place before my thesis began; this methodology is described in Mills et al. (2016). I list below the modifications and rationale behind the chosen method of sediment core collection and core processing for trace element analysis. Most importantly, due to the low concentrations of trace metals, modifications were necessary to minimise contamination.

3.2.1 Sediment core collection

As carbon is deposited at the sediment surface, redox variations are distributed vertically through the sediment, as described by the classical redox ladder, with more energetically favourable electron acceptors being used successively until depletion (Froelich et al., 1979). In open marine systems, the low flux of carbon to sediments means that single redox zones (e.g. the sulfate reduction zone) can extend for many metres, requiring long drilled or gravity cores to capture variations in redox conditions (Schulz et al., 1994). In salt marsh sediments however, the large delivery of carbon causes the boundaries between redox zones to become condensed since electron acceptors are much more efficiently depleted with depth (Berner, 1981).

These shallow and rapid variations in redox conditions mean that push coring is a viable method of sampling in these salt marshes. This method involves pushing a PVC core liner into the sediment slowly, using one's hand to support the bottom (after digging through the

mud) and carefully lifting the entire tube. Immediately after extraction, the overlying water is siphoned off, and the entire core is wrapped in tape/cling film to keep it as airtight as possible to prevent drying out of the sediment and to preserve the redox conditions in the sediment. This technique has been used in this project to extract sediment cores between 30–40 cm data reported in **Chapters 4 and 5**. Deeper sediment cores (>60 cm) can be extracted using a method I call the 'vacuum method'. This method involves very slowly inserting the core liner into sediment (to prevent compaction), replacing any air-filled space at the top of the core with pond water, and then forming an airtight seal at the top of the core before extraction. This technique has two benefits: (1) the limited expansion of the overlying pond water means sediment cannot fall out of the base of the core during extraction and (2), pond water preserves the loose sediment structure at the top of the sediment core. I chose not to use this method for trace metal work as the presence of overlying pond water may mix down the boundary of the inner-core wall. Mixing of overlying seawater with the sediment would be particularly concerning when measuring Mo in the sulfide-rich sediment, as the seawater concentration of Mo is an order of magnitude higher than in porewaters (Nakagawa et al., 2012).

Large quantities of porewater are required to separate a sufficient sample size of any trace metal for isotopic analysis. A large diameter core liner (102 mm) was therefore used for the sole purpose of collecting porewater for isotopic analysis in each study. The plastic core liners were pre-cleaned by: (1) wiping the outside with soap to remove any residual organics and (2) wiping thoroughly with a Kimwipe with MQ water. Previous coring by the lab group has simply covered the predrilled holes with electrical tape. Although likely an unnecessary precaution, I opted to wrap the core in cling film before taping the holes to prevent any chemicals from the tape glue contaminating porewater samples. A smaller core placed within 30 cm of the larger core was used to collect porewater to analyse geochemistry other than trace metals. Porewater chemistry in ponds has been observed to be spatially homogenous over this scale so the chemistry is assumed be directly correlative (Mills, 2014).

3.2.2 Porewater extraction

Rhizons were used to extract sediment porewaters for this project. This method of porewater extraction is preferred to sediment centrifugation as it better preserves anoxic conditions during extraction. Rhizons were precleaned with the following steps: (1) they were first stored in MQ overnight to remove any sediment or dust, (2), rinsed with 1 mM distilled HCl for 2 hours, (3) flushed with MQ using a syringe and (4), dried overnight in a laminar hood. Cr, Mo and U blanks from Rhizons after cleaning were below detection limit on ICP-MS.

During extraction, Rhizons were inserted horizontally into the sediment at roughly 2 cm intervals. Negative pressure was created inside the syringe which forces porewater through the permeable membrane (0.22 μm pore size) at the end of the Rhizon into the syringe.

Typical porewater yields were between 15–20 mL for each 2 cm depth increment. Based on porosity measurements with depth (Figure 3.1), this sampling resolution corresponds to an extraction of 17–38% of the porewater volume at each depth increment. At these extraction volumes, drawdown from other depth increments should be limited (Seeberg-Elverfeldt et al., 2005). As a precaution, syringes from all depths were allowed to fill to 5 mL before more sample was pulled at any depth increment to prevent over-extraction at the top of the core, where porosity is highest.

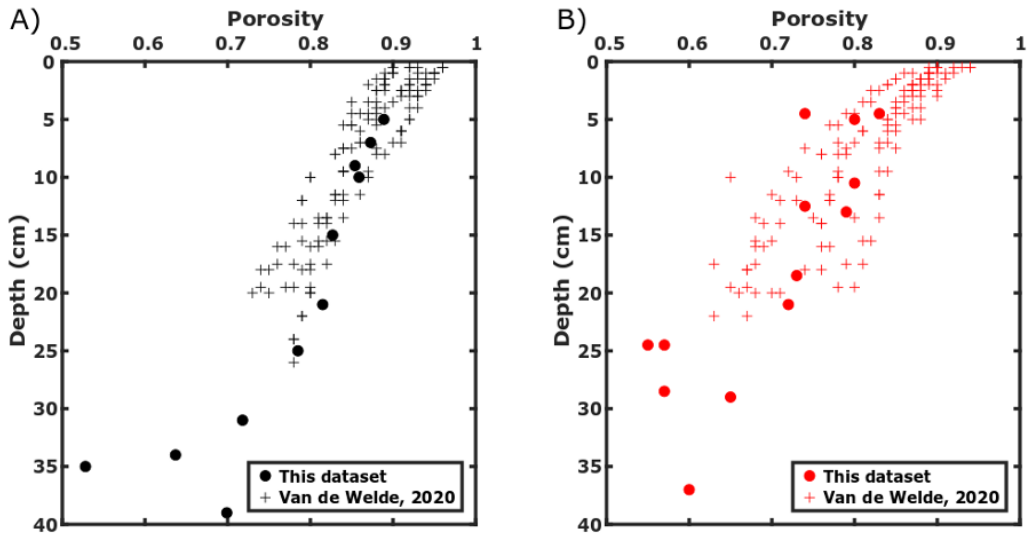

Fig. 3.1 - *Porosity measurements made for (A) sulfide-rich pond sediments and (B) iron-rich pond sediments for a variety of cores used in this thesis. Porosity measurements made in 2015, 2016 and 2018 are included from van de Velde et al. (2020) for comparison. Water density is assumed to be 1.035 g cm^{-3} and sediment density is assumed to be 1.90 g cm^{-3} and 2.00 g cm^{-3} based on density measurements in sulfide-rich sediments and iron-rich pond sediments respectively (van de Velde et al., 2020). This is considerably lower than typical marine sediment dry weight estimates (~2.60 g cm^{-3}) due to the high organic matter content in the salt marsh sediments.*

3.2.3 Sediment extraction

Sediments were sampled prior to porewater extraction to prevent porewater mixing altering the sediment geochemistry. Sediments were removed from pre-drilled holes using syringes with cut-edges (Figure 3.2). These were weighed into 7 mL container vials for processing.

All sediments were digested within two hours after extraction to prevent any further reaction with remaining porewater.

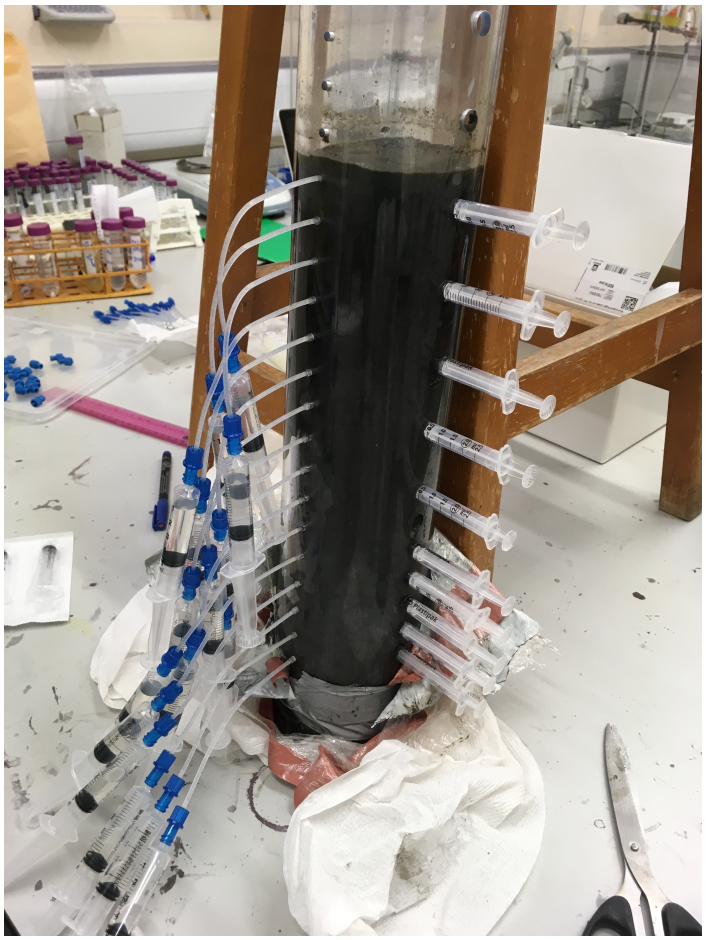

Fig. 3.2 - *Photo showing collection of sediment and porewater from a salt marsh sediment core. Rhizons connected to plastic syringes are on the left hand side of the photo. Syringes with a cut end are inserted at regular intervals on the right hand side of the photo. Suction draws sediment from the core into the syringe.*

3.3 Analysis of trace metals in saline porewaters and aqua regia leaches

This section describes the method developed to accurately measure the aqueous concentration of a suite of trace metals in porewaters and aqua regia leaches prior to isotopic analysis. While isotope dilution—a more accurate concentration measurement (**Appendix C**)—was the principal method used to report Mo and Cr concentrations in **Chapters 4 and 5** respectively,

I required an independent method of measuring trace element concentrations in my samples for two reasons.

Firstly, I wished to measure other trace elements in tandem with Mo and Cr. As element cycles are often interlinked and interdependent, complimentary concentration profiles of multiple elements reveal otherwise unknown diagenetic processes. For example, Cr in sediments is typically a mixture of detrital and authigenic mineral phases. In the absence of mineralogical mapping, a good estimate of the ratio of detrital : authigenic phases can be made by measuring the Ti concentration in sediment and calculating the detrital Cr input by correcting to a constant detrital Cr/Ti ratio (Gueguen et al., 2016). The elements of interest to this project, listed in Table 3.1, comprise a selection of redox sensitive species (Cr, V, U, Fe, Mn), species that react with other element cycles (Mo, Co, Ni) and species that exist in detrital minerals and therefore act as a check for authigenic vs detrital sources (Al, Ti).

The second reason I required accurate concentration measurements prior to isotopic analysis relates to the double-spike method used in the isotopic determination of δ^{98}Mo and δ^{53}Cr. For both isotope systems, an enriched isotopic double-spike solution is added to the sample prior to purification and instrumental analysis to correct for mass fractionation processes occurring during the experimental procedure (see **Appendix A** for full discussion). The error of the isotope measurement is dependent on the molar ratio of the double-spike solution to the sample such that there is an optimal ratio where errors are the minimum (Rudge et al., 2009). To target this molar ratio, an accurate concentration measurement of both the double spike concentration and sample concentration (commonly referred to as a "concentration check") is required.

The analysis of porewaters is far more analytically challenging than the aqua regia digests due to the lower trace element concentrations. I therefore describe the entire process of porewater analysis first before highlighting the modifications and differences in measuring trace elements in the aqua regia digests.

3.3.1 Trace metal determinations in porewaters

Benefits of ICP-MS in trace element analysis

The high salinity matrix of the salt marsh porewaters complicates the measurement of trace elements. High sodium (seawater = ~11,000 ppm Na) concentrations need to be diluted substantially in order to minimise blocking of the sample and skimmer cones and to minimise matrix effects during instrumental analysis on the inductively-coupled plasma mass spectrometer (ICP-MS) (Dass, 2007). If the dilution is too large, however, the trace element concentrations can fall below the detection limit of the instrument. This is a particular

Element	Seawater concentration (nMol/L)	Seawater concentration (ppb)	Reference	Behaviour
Chromium	1.2–6.5	0.06–0.34	(Moos et al., 2020)	Nutrient-like
Molybdenum	107	10.3	(Nakagawa et al., 2012)	Conservative
Uranium	13.9	3.3	(Ku et al., 1977)	Conservative
Vanadium	34–45	1.7–2.3	(Emerson and Huested, 1991)	Nutrient-like
Iron	0–1.5	0–0.084	(Tagliabue et al., 2012; Worsfold et al., 2014)	Nutrient
Manganese	0–4.5	0–0.220	(Klinkhammer and Bender, 1980)	Surface-enriched
Nickel	0.5–8	0.029–0.840	(Middag et al., 2020)	Nutrient
Cobalt	0–0.09	0–0.005	(Hawco et al., 2018)	Nutrient
Aluminium	18.5–278	0.5–7.5	(Hydes, 1977)	Scavenged
Titanium	2–300	0.096–14.360	(Orians et al., 1990)	Scavenged

Table 3.1 - *Reported concentration ranges for trace elements of interest for this project. Note that Cobalt, Manganese and Iron will be considerably higher in the porewaters and Aluminium and Titanium will comprise a particulate fraction which has passed through filters typically. These values were used as first approximations when creating artificial standards.*

problem for elements such as Cr and V, which exist at very low concentrations in seawater. A list of the elements of interest and their concentration in seawater is given in Table 3.1.

Concentration measurements at the University of Cambridge for trace metal cations could be conducted on either the inductively-coupled plasma optical emission spectrometer (ICP-OES Agilent) (detection limit = 1 ppb) or on the ICP-MS (Thermo Scientific Element 2) (detection limit = 20 ppt). Though the ICP-OES is less susceptible to matrix effects and instrumental issues arising from high salinities, the concentration of elements such as U and Cr are below the limit of detection at even a tenfold dilution. I therefore used the ICP-MS, which is capable of measuring most trace elements in porewaters, even at 100-fold dilutions.

Fundamentals of ICP-MS

The ICP-MS converts nebulised aqueous samples into a plasma using an electromagnetic coil. The elements in the sample (along with the constituents of the carrier gas) become positively charged ions in the high temperature, charged conditions; the overall charge of the plasma is maintained by free electrons.

A sample cone and a skimmer cone create an interface which accelerates and focuses the plasma beam to the mass spectrometer itself by the use of a pressure and temperature differential. A series of lenses further focuses the ion beam with the aim of removing larger polyatomic interferences. A large magnet deflects the ions based on atomic mass to separate detection cups which can then be calibrated to measure the concentration of specific elements.

Sample preparation for ICP-MS

The low elemental concentrations of targeted elements in the salt marsh porewater samples means that the signal-to-noise ratio of a sample becomes a particularly important factor during analysis. The noise corresponds to the background number of counts, in the absence of a sample, that the detector measures. The largest component that contributes to noise comes from potential contamination in the acid matrix that the samples and standards are diluted in. The signal refers to the counts per second that are measured when a sample ion beam hits the detector. To minimise error on each concentration measurement, effort must be taken to both maximise the signal and minimise the noise. A minimum threshold for this is the Limit of Detection value (LOD) which is typically three times the standard deviation of the blank measurement, though uncertainty on the concentration measurement will decrease as this signal is maximised or blank is minimised.

To maximise the signal counts, a 100-fold dilution from seawater ($\sim$110 ppm Na) was found to be the maximum dilution possible to still keep Cr above the detection limit (Figure

3.3b). For elements such as Uranium, where the blank is low and the signal in seawater is high, concentrations can be run at both 1:100 and 1:1000 with little variation in the results (Figure 3.3a, $r^2 = 0.975$).

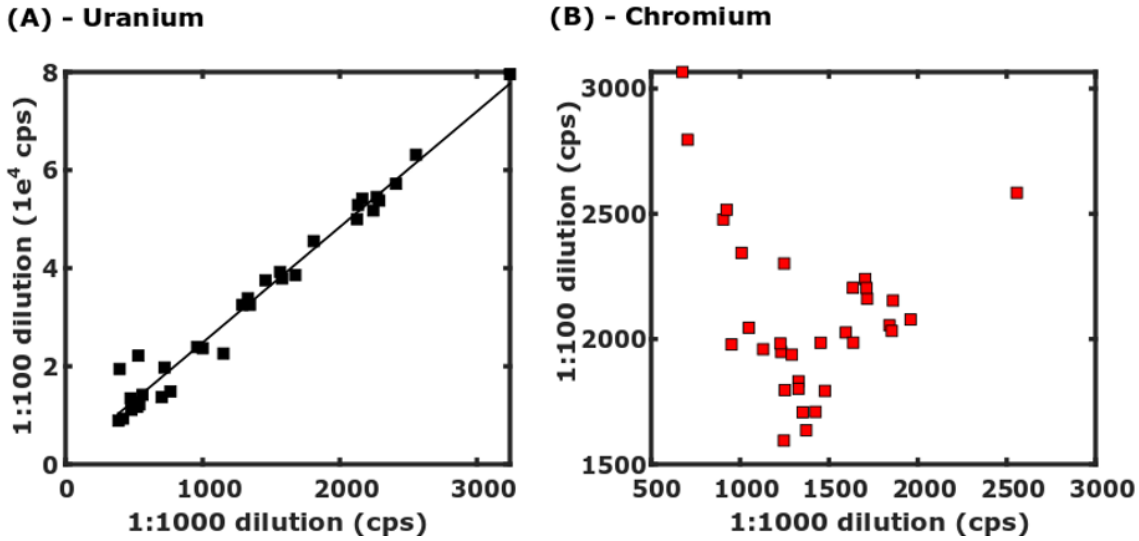

Fig. 3.3 - *Effect of dilution on the measurements of Cr and U on ICP-MS. (A) The mass of uranium has few interferences and a low contamination blank. As such, despite the low signal (∼500-3000 cps) there is little difference in the measurement between a 100-fold and 1000-fold dilution. (B) The larger contamination blank and polyatomic interferences associated with Cr means that 1000-fold dilutions are affected by too much noise for an accurate concentration measurement.*

The contamination blank can be minimised by clean lab practices and using an ultraclean acid matrix in all samples and standards. For all samples and standards run on ICP-MS, a double-distilled 0.1M HNO_3 matrix was used. This was chosen as the cleanest possible acid while still being a sufficiently low pH solution to keep all cations in solution. All plasticware which the sample could come into contact with (aside from the syringe) was HCl/HNO_3 acid cleaned.

As a test to see if measurements on porewaters were above the limit of detection, I ran repeats of acid blanks, 100-fold diluted seawater, 100-fold diluted iron-rich porewater and 100-fold diluted sulfide-rich porewater using the ICP-MS (Table 3.2). My results suggest that certain elements (e.g. Cr, Mo and Fe) are more susceptible to accumulating in reagents due to their abundance in laboratory conditions and thus have a higher acid blank. Only Fe in seawater and sulfide-rich porewater, Ni in all porewater samples and Co in seawater were below the limit of detection. Elements such as Cr, Fe and Co are considerably more concentrated in porewaters than in typical seawater samples, permitting measurement by this method. For all further analyses in this thesis, all acid blanks were tested prior to any run and

if the sample signal was not greater than 3 times the standard deviation of the acid blank, the samples were re-diluted in fresh acid.

Running samples in a $\sim$110 ppm sodium concentration matrix introduces multiple problems during instrument analysis: First, there may be a higher portion of interferences on elements of interest. Second, small variations in the matrix introduces large differences in the ionic strength of the solution. Lastly, the intensity of the ion beam as a result of these high dissolved solid matrices can cause detectors to become saturated. The next section looks at the steps developed to mitigate the effects of these problems.

Interference minimisation

An interference in mass spectrometry is where the signal of the element of interest is convolved with the signal produced by another chemical species over the same mass window. This can occur if the mass range of the isotopes of two ions (e.g. ^{54}Cr and ^{54}Fe) overlap—although almost all elements have at least one isotopic window which can be measured that is interference free. An alternate, and more common, form of interference is a polyatomic interference—where the sum of the masses of two ions that are common in the sample matrix combine to create a mass which interferes with an element of interest (e.g. the ^{52}Cr ion has large potential interference issues with the ^{40}Ar^{12}C polyatomic ion). Any combined sum of ^{40}Ar, ^{12}C, ^{16}O, ^{1}H and ^{14}N are potentially important polyatomic interferences to monitor as these elements are most abundant in the plasma. Polyatomic masses with three or more ions are possible (e.g. ^{40}Ar^{12}C^{1}H) but are significantly less significant. Additionally, doubly charged ions can interfere with elements of interest; since the recorded parameter is the mass/charge ratio, a mass exactly twice as large as an element of interest with a 2+ charge will be measured in the same mass window (e.g. ^{206}Pb^{++} can interfere with ^{103}Rh^{+}).

The most efficient way to prevent interferences is to optimise the mass-peak separation for an ion—defined as the mass resolution. There are three resolution modes on the ICP-MS: low, medium and, high. Measuring an element in high resolution means you can clearly separate the peaks from any proximal mass interferences; however, the produced signal decreases by an order of magnitude between low and medium resolution, and again between medium and high resolution. For many of the elements in which I am interested, medium resolution offers the "goldilocks" resolution where peaks are sufficiently separated whilst still providing enough signal to measure precise concentrations. To improve separation of the peaks, in particular for ^{52}Cr and ^{56}Fe which both lie on the left-hand side of the ^{40}Ar^{12}C and ^{40}Ar^{16}O peaks respectively, I tuned in both low and medium resolution until there was no overlap between the element and the interference peak. Each peak was checked manually before any samples were measured and the approximate signal values were compared to

Element	Acid blank CPS (n=3)	Range in 110 ppm iron-rich porewaters CPS (n=5)	Range in 110 ppm iron-rich porewaters CPS (n=5)	110 ppm seawater CPS (n=2)
Chromium	213±32	10840 – 12150	15609 – 18609	618±141
Molybdenum	472±201	16180 – 47505	2796 – 3536	22063±1224
Uranium	5±2	5260 – 14061	4638 – 17625	20876±2164
Vanadium	5±5	812 – 1040	3016 – 3524	979±1
Iron	2926±2109	$1.3x10^6$ – $1.2x10^7$	5279 – 16841	6174±75
Cobalt	17±15	308 – 582	515 – 703	12±3
Nickel	64±70	178 – 325	94 – 274	255±15

Table 3.2 - *Raw signals (CPS) measured for three repeats of 0.1 M HNO_3 used for dilutions and for two repeats of 100-fold diluted N. Atlantic seawater. Also compared are 5 porewater samples taken between 6 and 17 cm in an iron-rich and sulfide-rich pond sediment core. The counts for these represent the range of raw intensities measured of those 5 samples.*

a long-term standard (seawater or an enriched concentration standard) to check that the instrument was not measuring an interference peak.

Matrix effects

In ICP-MS, the measured signal of an ion can be enhanced or suppressed based on the nature of the matrix it is in. This could be due to changes in the efficiency of ionisation imparted by the presence of other elements, the build-up of salts on the sample cone clogging the sample beam or some space-charge effect occurring in the plasma. Higher ionic strength samples, such as the 110 ppm Na seawater solutions measured in this study, will have both large matrix effects and larger errors based on variations in the matrix (i.e. a 5% difference in Na concentration will cause larger absolute concentration changes in a high ionic strength than in a low ionic strength solution).

To homogenise matrices between porewater samples at different depths, which have up to 50% variations in salinity, all samples were individually diluted to constant Na concentrations (±0.5%) with 0.1 M distilled HNO_3. Sodium concentrations were determined by ICP-OES, along with other major elements. As other major cations behave conservatively in seawater, it is assumed that different sample matrices matched by Na concentrations will also have very similar concentrations of other major conservative cations with the caveat of iron and sulfur species.

I looked at three main ways of monitoring and calibrating samples for matrix effects: (1) standard addition to samples, (2) addition of a ^{115}In spike to monitor matrix differences and, (3) the use of a set of calibration standard in a similar matrix to the samples.

(1) – Standard addition The most rigorous and accurate method to correct for matrix effects is to add varying quantities of known concentration spike to the sample so that a linear relationship is observed (Figure 3.4). The gradient of this line indicates how the measured signal varies as a function of analyte concentration. The y-intercept of the line is the concentration of the solution of interest (i.e. the concentration with zero spike added). In the case of the sample measured in Figure 3.4, the concentration is calculated from the intercept to be 0.033 ppb Mo (intercept counts-per-second divided by the gradient). As a standard addition approach is a function of the matrix effects of that specific sample, if the concentration of the spike is precisely known, this method can provide the most accurate results. The drawbacks of this approach are that each sample has to be run multiple times with different amounts of spike, increasing instrument usage, consumables and time.

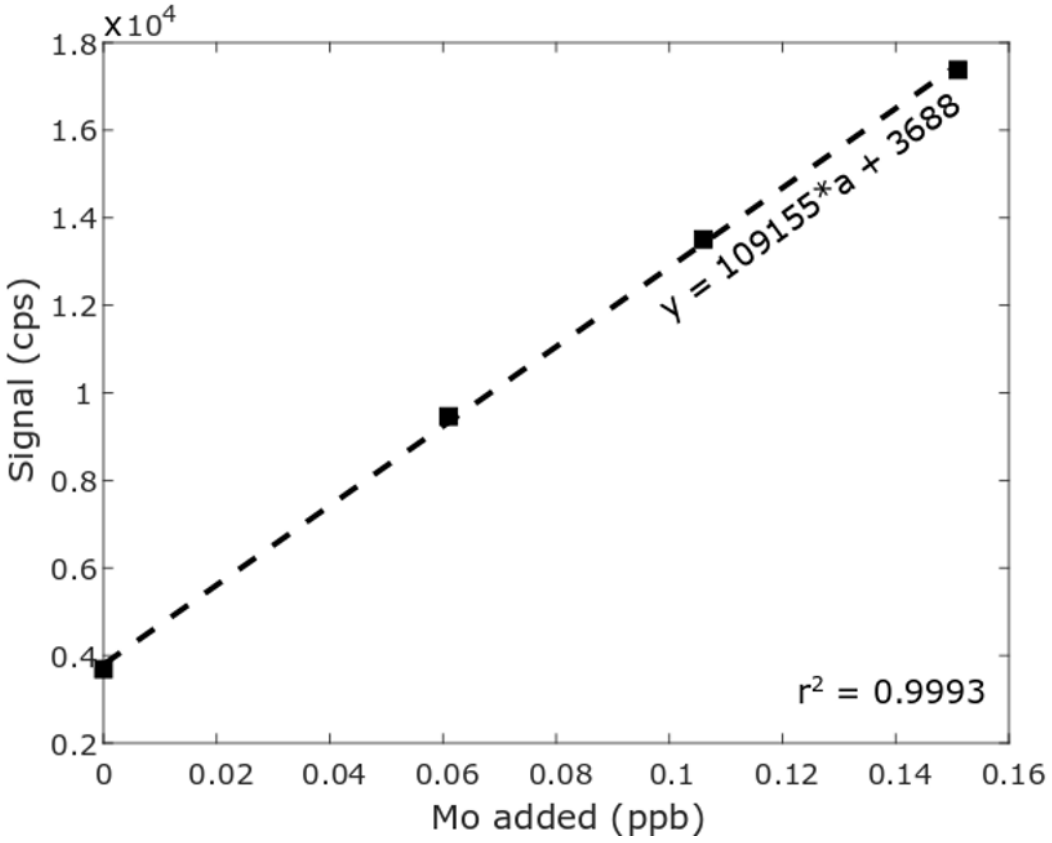

Fig. 3.4 - *A typical standard addition experiment used to calculate the concentration of an element in a unique matrix. In this case, four aliquots of the same sample are run with different amounts of spiked Mo solution while maintaining the same Na concentration. The gradient of the line (in this case = 109,155) shows how responsive the measured signal is to a change in analyte concentration. The y-intercept shows the signal produced by an unspiked aliquot of the sample, which is the concentration of the analyte in the sample. For samples with widely varying matrices, this can sometimes be the only way to measure individual samples.*

(2) – Addition of ^{115}In to samples An alternate method to monitor and correct for matrix effects is to add a constant aliquot of an element which responds to matrix effects but will not interfere with any of the measured signals—an example of which is ^{115}In. This method has the advantages of being quick, and corrects each individual sample based on the individual matrix. The disadvantage is that this method is sensitive to how precisely the aliquot of element is added, and elements may behave differently than ^{115}In in different matrices, which is not corrected for. I used a 0.25 ppb ^{115}In for all samples as a check for contamination; if a sample exhibited a particularly errant ^{115}In signal, I would remeasure the sample.

(3) – Calibration standards The most commonly used method to determine sample concentrations is the use of a set of calibration standards spiked with the varying concentrations of the elements of interest. For optimal accuracy, each standard should have a matrix as similar to that of the samples as possible, and the set of standards should span the expected elemental concentration range for the samples. The gradient of the standard calibration line can be used to calculate the concentration of all of the samples. This method has the advantage of being quicker and less exhaustive than the standard addition method, while still accounting for the matrix effect on each individual element of interest. It is important to accurately and precisely know the concentrations in the calibration standard set to get accurate measurements with low errors.

When creating the calibration standards, I had to consider that the porewaters collected from a sulfide-rich pond would have a different matrix from those collected from an iron-rich pond. While conservative elements, such as Mg, K, and Cl, would behave conservatively with constant Na concentration, the differences between the behaviour of Fe and S in these pond sediments would lead to large differences in the dissolved concentrations of Fe^{2+}, HS^- and SO_4^{2-}. To test if separate calibration standards would be necessary for porewater samples from the two different types of pond sediment, I ran standard-addition experiments for porewater samples relative to a seawater standard (Figure 3.5). A higher relative count difference, as a percentage difference from seawater, means more counts were emitted from the same analyte concentration in a sample due to matrix effects. Differences in the sulfide/sulfate concentration appeared to impart only small matrix effects on the measurement for all elements (<8% difference on calibration line) (Figure 3.5b). On the contrary, when ferrous iron concentrations were higher, more counts were measured on all elements. Chromium appeared to be affected the most by this effect, with 21% more counts in a 1.2 mM Fe^{2+} solution than in a seawater matrix (Figure 3.5a). These results suggested that although a seawater matrix was suitable for sulfide-rich porewaters, a separate set of calibration standards with a high Fe^{2+} matrix was necessary for iron-rich porewaters,

otherwise the concentrations of trace elements would be overestimated. For porewater measurements, I therefore used two sets of calibration standards: one set with a seawater matrix for sulfide-rich porewaters and pond waters and, one set with a high Fe^{2+} seawater matrix for iron-rich porewaters.

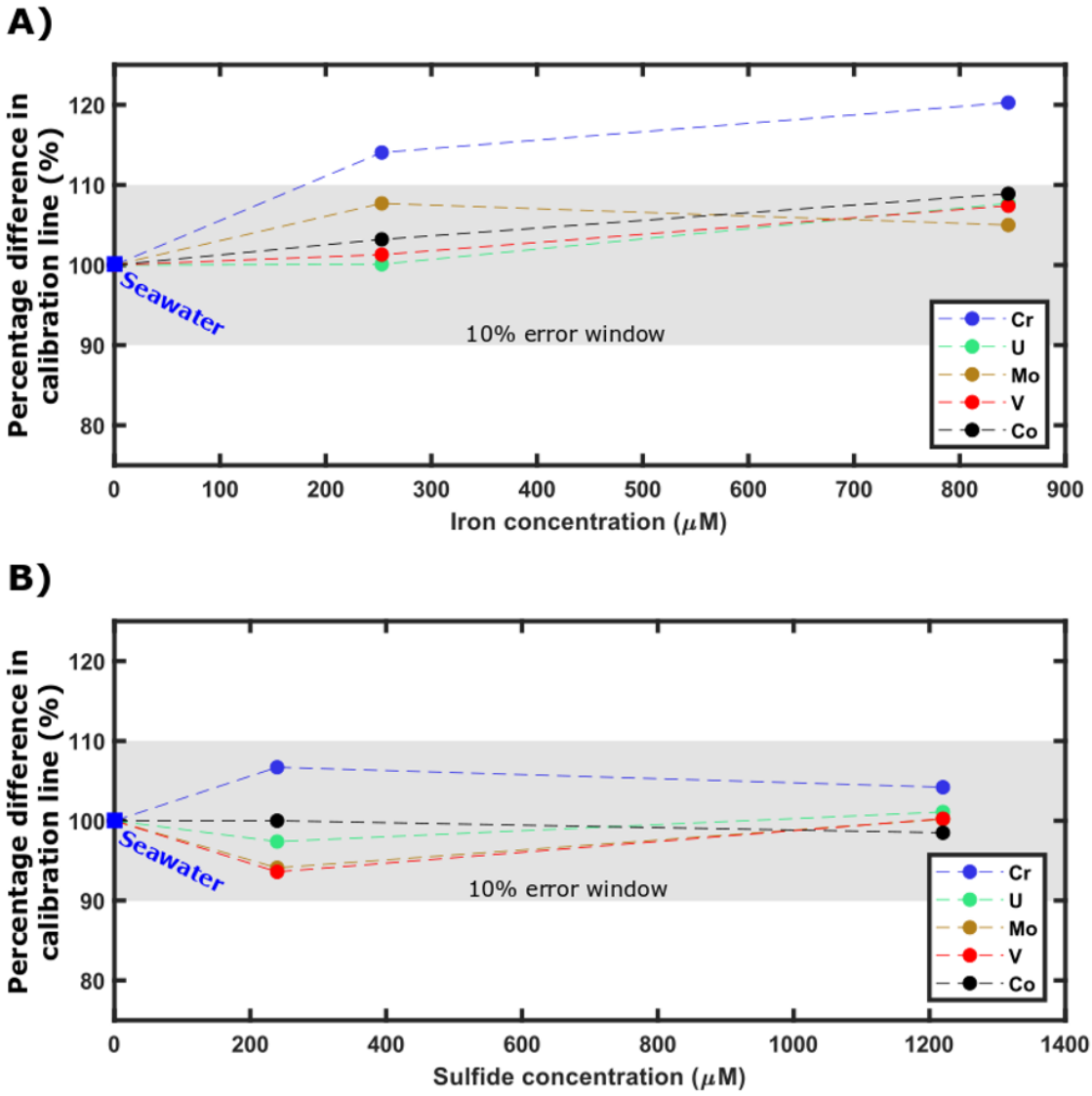

Fig. 3.5 - *Relative variations in emission intensity for Cr, U, Mo, V and Co for (A) iron-rich porewater and (B) sulfide-rich porewater relative to IAPSO seawater standard. A higher count difference corresponds to a higher intensity per unit concentration (i.e. more efficient emission of the element). A 10% error window is highlighted in grey. Iron and sulfide concentrations correspond to the concentrations before the dilution preparation for ICP-MS.*

The two calibration standard sets were made up in similar ways. A matrix (taken from IAPSO N. Atlantic seawater for the seawater standard and porewater from 12 cm in an

Element	Mo	U	Cr*	Ni	V	Co
Measured conc (nmol/L)	114.4±6.1	13.6±0.2	10.1	8.8±8.8	22.7±1.7	b.d.l.
Published values (nmol/L)	107	13.9	1.2–6.5	1.7–11.9	34–45	0.0

Table 3.3 - *Concentrations measured by ICP-MS using the calibration standards compared to published values. Seawater concentrations references shown in Table 3.1. b.d.l = Below Detection Limit. *only one sample was measured.*

iron-rich sediment core for the Fe^{2+}-rich standard) was repeatedly (n = 5) measured on the ICP-MS with standard addition of single element spikes to determine the exact elemental concentrations of the raw matrices. A large aliquot of matrix was spiked with single element standards for each element of interest. The standard set was then created by weighing different proportions of the spiked matrix with the unspiked matrix. With the exception of Ni in the iron-rich porewater standard (r^2 = 0.90), all elements had an r^2 exceeding 0.99 when measured. As a precaution, for every new core, I ran at least one sample with standard addition to validate the use of the calibration standard. In all cases, the sample standard addition calibration gradient agreed well with the calibration standards (<5% error).

The results from measuring North Atlantic seawater show support for the calibration standards for Mo, U, Ni and V (Table 3.3). Chromium in seawater is overestimated which is surprising given the accuracy of sediment digest concentrations. This is assumed to be contamination in the OSIL seawater sample which was accumulated during processing.

Choice of detector for concentration measurements

The ICP-MS uses three modes of detection: Counting mode, Analog mode and Faraday mode. Counting mode measures the raw number of times an ion hits the detector and is used for small ion beams. Analog mode uses a secondary electron multiplier to produce a cascade of electrons (through amplification of electrons through electrodes) which ultimately produce an electrical current which is measured. In Faraday mode, the current produced from neutralising the impacting ions is recorded in a Faraday cup. The sensitivity of this method is much lower, and large numbers of ions correspond to a very small amount of current.

The ICP-MS automatically switches between Counting, Analog and Faraday mode with increasing ion counts. A Faraday cross calibration is run before every sequence which calibrates the detectors using carrier gas Ar as the analyte so that the same signal is recorded regardless of detector mode. Turning down the radio frequency (RF) power to 20% means the Ar signal is at the perfect size to tune between all three modes. The Ar peak is then

manually aligned so that the detectors are calibrated. This is important given the wide range of intensities for the desired elements which are present in these porewater samples (10–10^8 cps).

Behaviour of Mo on ICP-MS

Multiple problems arose when trying to measure the concentration of Mo in porewaters by ICP-MS. Acid blank values tended to be significant (Table 3.2), possibly due to contamination of Mo in the acid or due to polyatomic interferences such as $^{40}Ar^{39}K^{16}O^{+}$ and $^{79}Br^{16}O^{+}$. This is not a large issue in seawater and iron-rich pond water matrices, where Mo concentrations typically exceed 10 ppb (Table 3.1, Table 3.2). In sulfide-rich porewater however, the concentration of Mo is significantly lower (<2 ppb) as a result of thiolation and removal of thiomolybdate species to the sediments (Erickson and Helz, 2000). After dilution, this puts many of the porewater samples below the instrumental limit of detection, depicted by sulfide-rich porewater samples falling on the LOD line in Figure 3.6.

Another issue which arose was the tendency for Mo concentrations in porewater samples to be underestimated compared to Mo concentrations calculated by isotope dilution. Seawater samples and concentration standards, on the other hand, were within error between the two methods (blue circles – Figure 3.6). Isotope dilution is a far more robust way of determining concentration, therefore I assume that the ICP-MS is underestimating Mo concentrations in iron-rich and vegetated porewaters. The reason for this is unclear, however I suspect that the complexation of Mo with organic ligands may be preventing efficient ionisation. This is supported from the observation that porewaters extracted from a vegetated core being the most susceptible to this "dampening" effect. I trialled adding concentrated hydrogen peroxide (H_2O_2) to samples in an attempt to oxidise any organics, however this resulted in no improvement of the concentration measurement. Given that concentration checks do not have to be completely accurate, and that I calculated final concentrations using isotope dilution, this does not affect the results in **Chapter 4**.

Behaviour of Cr on ICP-MS

Chromium concentration measurements on ICP-MS were also susceptible to multiple issues. Similar to Fe, the most abundant mass of Cr (^{52}Cr) lies on the left-hand side of a large argon interference ($^{40}Ar^{12}C$). All Cr measurements are therefore measured in medium resolution, and the focus lenses are carefully tuned to separate the Cr and $^{40}Ar^{12}C$ peak. Chromium measurements on ICP-MS appear to be particularly susceptible to instrumental drift, and thus bracketing standards are a requirement. I suspect this is due to ionic build up deposited on

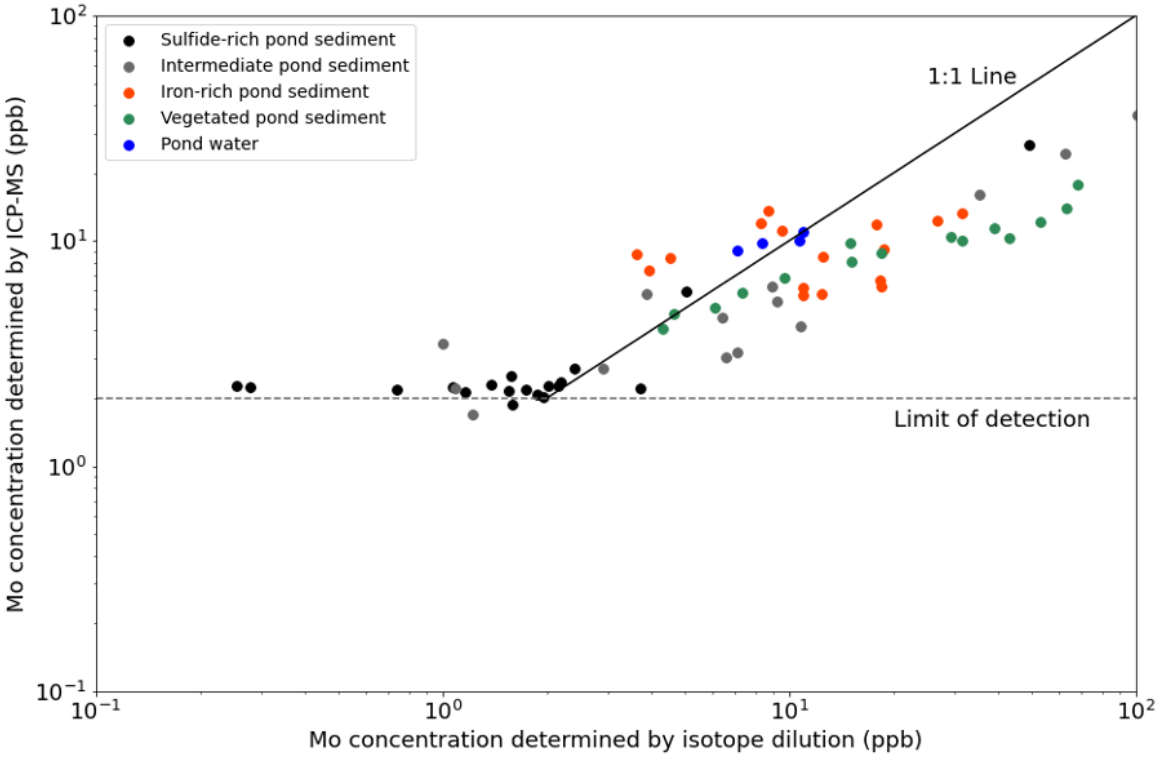

Fig. 3.6 - *Porewater molybdenum concentrations determined by isotope dilution and by ICP-MS (Element). Four sediment cores taken through different types of pond sediment are shown. Dashed line indicates the limit of detection (2 ppb); at this concentration, noise on the ICP-MS prevents lower concentration measurements. Samples which fall on the 1:1 line represent identical measurements on ICP-MS and by isotope dilution. Note the log scale on both axes.*

the cones throughout an instrumental run. As discussed above, the concentration of Cr is very low in seawater samples and only marginally higher in porewater samples. Concentration checks to correctly add chromium isotopic double spike are fortunately tolerant to a wide range in concentration, therefore ICP-MS provides an accurate enough measurement for this purpose.

3.3.2 Trace metal determination in aqua regia digests

Compared to porewater analysis, concentration checks on the aqua regia leachates are significantly more straightforward and accurate. All aqua regia leachates were diluted 10,000-fold to get within a concentration range measurable on the ICP-MS Element. Matrix matching is next to impossible as each digest will have a different proportion of ions, therefore a multi-element standard set containing Fe, Ti, Al, Ni, Co, V, Cr, Mo and U in 0.1 M HNO_3 is used for calibration. The addition of a 1 ppb ^{115}In spike to every sample, standard and bracketing standard was used to correct for variations in matrix effects—which never exceeded 10%.

Molybdenum and Chromium concentrations measured by isotope dilution and by ICP-MS are strongly correlated ($r^2 = 0.97$ and $r^2 = 0.98$), indicating that the issues involving porewater samples do not extend to these leachates. The high concentrations of Cr, Fe and V remove the issues of low signal observed in porewater samples. Based on repeat measurements of an iron-rich pond sediment sample (n = 5), long term precision was <3%.

3.3.3 Section conclusions

In summary, a method for trace element analysis on porewater samples using ICP-MS has been developed for certain elements (U, Mo, Cr, V, Ti, Al) at the University of Cambridge in both porewater and sediment digests. These developments have allowed for the measurement of lower elemental concentrations in the porewaters than in the previous Masters project (Traynor, 2016). In particular, the tenfold lower dilution and the separate calibration standards significantly improved the concentration measurements of trace metals.

Concentration measurements for sediment digests are reliable and accurate by ICP-MS. There is close agreement between isotope-dilution-derived and ICP-MS-derived measurements, supporting these measurements.

For concentration check purposes, Mo and Cr concentration measurements in porewaters are sufficient, however detection limit issues and unknown matrix effects means isotope dilution is the preferred method of measuring elemental concentrations. Elements such as U, Co, V, Ti and Al, which either have interference-free beams produce reproducible porewater concentrations within the expected range. Further work, most probably involving purification

of the samples by column chemistry, would be necessary to provide accurate concentration measurements of Mo and Cr in these saline, organic-rich porewaters.

3.4 Development of method to measure δ^{53}Cr using TIMS

This section describes the method development of a technique to measure δ^{53}Cr of sediment samples at the University of Cambridge using a Thermal Ionisation Mass Spectrometer (TIMS).

When reporting the Cr isotope composition using delta notation, the convention is to report the ^{53}Cr/^{52}Cr ratio of a sample compared to the ^{53}Cr/^{52}Cr ratio of a standard. I report to the SRM979 standard for all δ^{53}Cr measurements in this thesis (Equation 3.1). This is the most widely used standard reference material, although some research groups opt for the NIST3112a reference standard instead which has been reported as -0.07±0.04‰ relative to SRM979 (Schoenberg et al., 2008; Zhu et al., 2018).

$$\delta^{53}Cr = \left(\frac{\left(\frac{^{53}Cr}{^{52}Cr}\right)_{Sample}}{\left(\frac{^{53}Cr}{^{52}Cr}\right)_{SRM979}} - 1 \right) \times 1000 \tag{3.1}$$

3.4.1 Experimental methods

Teflon and plasticware cleaning methods

Samples are easy to contaminate with external sources of Cr during even simple chemical procedures since Cr exists in measurable quantities in both acids and in uncleaned plasticware. From sediment core collection to isotopic measurement, any contact with metal (which contains a high concentration of Cr) was minimised.

All Teflon containers went through the following cleaning steps: (1) triple rinse with MQ, (2) 50% HNO_3 leach overnight on a hotplate set at 100°C, (3) triple rinse with MQ, (4) 50% HCl leach overnight at 100°C, (5) double rinse with MQ, (6) ~1% distilled HNO_3 leach overnight at 100°C and (7), triple rinse with MQ. For Teflon vials which had contained organics (e.g. aqua regia digests of sediments), 200 μL of concentrated distilled HNO_3 was refluxed at 120°C for 24 hours in the containers before the normal Teflon wash sequence.

All other plastic ware (pipette tips, centrifuge tubes, LDPE bottles) was washed in cold 50% HNO_3 overnight. I found that heating the acid or leaving it in acid longer than overnight denatured the plastic. Whilst this did not actually add any blanks to samples, the denatured plastic became brittle and could not be used for centrifugation.

Isotope	^{50}Cr single spike powder	^{54}Cr single spike powder
^{50}Cr	99.70%	1.5%
^{52}Cr	0.25%	1.5%
^{53}Cr	0.02%	1.5%
^{54}Cr	0.03%	95.5%

Table 3.4 - *Isotopic composition of the single spike powders as reported by ISOFLEX.*

Reagents

All acid used in the column purification procedure was single distilled. The Cr blank on 6 M HCl and 5 M HNO_3 was 9 ng/L and 3 ng/L respectively (determined by ICP-MS).

Ultrapure H_2O_2 was purchased from Sigma Aldritch with a certified Cr blank of <50 ng/L. Ammonium persulfate (APS) ($(NH_4)_2S_2O_8$) BioXtra (>98.0%) was purchased from Merck. Ammonium persulfate solution degrades rapidly, hence it was always prepared on the day of usage; the APS salt was dissolved in MQ and used within three hours.

The anion exchange resin AG1-X8, 200–400 mesh size, was obtained from Eichrom in chloride form. The resin was transferred to a clean teflon bottle using a teflon spatula. Distilled water was added to the resin at a ratio of 4:1 and vigorously shaken. A noticeable white layer of degraded beads was visible at the water surface immediately. After 10–15 minutes, many of the beads had settled, and the overlying water was decanted to waste. The resin in the bottle then underwent the following procedure following Moos and Boyle (2019): (1) 3 distilled water rinses, (2) 1 M NaOH (∼1 hour), (3) 10 distilled water rinses, (4) 6 M HCl (∼7 days), (4) 5 distilled water rinses, (5) 6 M HCl (∼1 day) and (6), 5 distilled water rinses. The addition of a strong base, followed by a strong acid, should remove any species adsorbed to the beads. The Cr resin blank increases significantly if these resin batch cleaning steps (i.e. the previously detailed rinses and the removal of degraded beads) are omitted (Moos and Boyle, 2019). Resin was added to triple rinsed Bio-Rad Polyprep columns with 2 mL bed volume; the efficiency of the separation procedure strongly depends on the packing of the resin (discussed below), hence all column resin was checked and resuspended if there were any visible heterogeneities in the resin.

Double spike solution preparation

Enriched ^{50}Cr and ^{54}Cr metal powder standards were ordered from ISOFLEX with a certified isotopic composition shown in Table 3.4.

The single spike solutions were dissolved in 1 M HCl overnight at 100°C. Stronger oxidising acids (e.g. HNO_3) are less suitable for dissolving Cr metals as a thin oxidised layer

forms around the outside of the metal, inhibiting dissolution (Haber and Goldschmidt, 1906). The single spike solutions were evaporated and brought up in a 3% distilled HNO_3 matrix. Concentrations of the single spike solutions were measured on a MC-ICP-MS (Neptune) at RHUL against a Sigma Aldritch 1000 ppm Cr standard solution. The single spike solutions were then mixed into a double-spike solution at the optimal ratio described in Rudge et al. (2009). The double-spike solution was later calibrated using TIMS (See **Appendix A**).

Isotope reference standards

Two isotopic standards were prepared for isotopic analysis of Cr. The primary standard, SRM979, was bought in hydrated chromium nitrate form from the National Institute of Standards and Technology (NIST). The powder was dissolved in 3% distilled HNO_3.

NIST3112a was used as the secondary standard. Solution bottles (10 mL) with a certified Cr concentration of 10.009 mg/g suspended in HNO_3 were purchased from NIST. These were gravimetrically diluted in 3% distilled HNO_3 to $\sim$100 ppm and $\sim$1 ppm working standards.

3.4.2 Chromium purification procedure

Pre-column chemistry protocol

Before isotopic analysis by TIMS, Cr needed to be separated from any matrix ions which may cause potential interferences on any of the ^{50}Cr, ^{52}Cr, ^{53}Cr and ^{54}Cr ion beams. However, mass-dependent isotopic fractionation occurs during this Cr separation process, resulting in a change in the Cr isotopic composition of the sample if some Cr is lost during the column procedure (Ball and Bassett, 2000; Trinquier et al., 2008). Since Cr yields from the separation procedure are typically between 60–90%, there must be some portion of isotopically fractionated Cr which is lost during the separation procedure (Ball and Bassett, 2000; Frei and Rosing, 2005; Moos and Boyle, 2019; Trinquier et al., 2008). To correct for this effect, I used the addition of a ^{50}Cr–^{54}Cr double spike—a solution enriched with precisely known concentrations in ^{50}Cr and ^{54}Cr—to correct for mass dependent isotope fractionation occurring during both Cr separation and instrumental analysis (For a full description of the double spike deconvolution method, see **Appendix B**).

I measured the Cr concentration of samples by ICP-MS following the procedure in *Section 3.1.3* and dried down an aliquot of solution which contained 500 ng of Cr in Teflon. For sediments, this was typically between 0.1–1 mL of aqua regia leach solution.

The sample and standards were re-dissolved in a 1 M HCl matrix. The double spike, in exactly the same 1 M HCl matrix, was mixed with the sample at a targeted total [Cr] spike-to-sample ratio of 0.45. There is a tolerance of at least 30% on the concentration

measurement as the double spike deconvolution method produces identical δ^{53}Cr values between spike to sample ratios of 0.3–0.6 (**Appendix A**). The mix was left to equilibrate at 100°C for at least 24 hours to ensure sample/spike equilibration. This step was particularly troublesome while developing the method (See *Section 3.4.5*).

Cr column procedure

A wide range of different methods to separate Cr using column chemistry exist in the literature (Table 3.5). Most utilise the characteristic of Cr to behave as either an anion (CrO_4^{2-}) or a cation (Cr^{3+})—based on its oxidation state as Cr(VI) and Cr(III) respectively—in order to separate it from other matrix elements in a sample (Ball and Bassett, 2000).

I opted to base my column chemistry procedure on the method used in Moos and Boyle (2019) with some minor modifications. I chose this method because it produces analytically consistent results on small sample sizes and uses fairly low strength acids which do not include HF.

Instead of using an Fe clean-up column described in Moos and Boyle (2019) as the final step, I decided to use this column first in my separation procedure; this is because many of the salt marsh samples—both porewater and sediment leachates—contain high concentrations of dissolved iron which should be removed first to lower the ionic strength of the matrix added to the other columns in the procedure. Lowering the ionic strength of the sample means resin surfaces are more effective at binding ions which increases the efficiency of later columns at separating Cr.

Anion resin cleaning procedure

The method I adopted uses the same pre-cleaned resin AG1-X8, 200–400 mesh size column resin three times but under different chemical conditions. Between each column step, the resin is cleaned using the following method: (1) 5 mL 5 M HNO_3, (2) 3 x 3 mL MQ and (3) 80 mL 1 M HCl. In Step (1), the addition of nitrate (with a high selective preference of 65) is an efficient way of displacing any chromate or leftover matrix ions from the resin (Table 3.6). The combined MQ and HCl steps regenerate the resin back to chloride form. As the relative selectivity of the chloride ion is much lower than for the nitrate ion, 43 bed volumes of OH^- or Cl^- are necessary to fully regenerate the resin (Biorad, 2000). A significantly smaller cleaning process is used in Moos and Boyle (2019) which would not effectively regenerate the resin. Whilst this is unlikely to contribute a significant Cr blank, as the majority of the Cr would be removed by the addition of nitrate, it will mean the resin is less effective at separating chromium which may lead to lower yields. The longer cleaning steps allowed

Type of column separation	Method overview	References
Two/three column approach: anion and cation column(s).	Initial anion column (e.g. AG1-X8 resin) is used to separate Cr from matrix elements. Cr is eluted from the column resin by either (1) a lowering of pH or (2) the addition of some reductant (e.g. H_2O_2 under acidic conditions). Secondary cation column (e.g. AG50WX8) is used to separate Cr from other matrix elements (e.g. Al, Ti, Fe and V).	(Ball and Bassett, 2000; D'arcy et al., 2016; Frei and Rosing, 2005; Füger et al., 2019; Gueguen et al., 2016; Schoenberg et al., 2016)
Two-three column approach: Multiple anion column steps.	Two or three columns packed with anion exchange resin (e.g. AG1-X8). At least one column involves the addition of Cr(VI) to the column which is then reductively eluted. Typically, an iron clean-up column step is added to remove excess iron.	(Frei et al., 2009; Moos and Boyle, 2019)
Cation exchange column	One column packed with (AG50WX8 resin) is used to separate Cr from matrix elements.	(Birck and Allègre, 1988; Bonnand et al., 2011; Trinquier et al., 2008)
Anion exchange column	Cr(VI) is added to a column with anion exchange resin (AG1-X8). Matrix elements are removed by rinses in the column before Cr(VI) is reduced and eluted as Cr(III).	(Schoenberg et al., 2008)

Table 3.5 - *Summary of published methods to separate Cr from matrix ions for isotopic analysis.*

Counterion	Relative selectivity of AG1-X8 (anion) resin
NO_3^-	65
Cl^-	22
SO_4^{2-}	85
CrO_4^{2+}	85* (assumed to be similar to sulfate ion)

Table 3.6 - *Relative selectivities of ions on to the AG1-X8 anion resin (Biorad, 2000).*

me to reuse all the resin four times with no difference in the measured isotope composition; whereas other laboratories use fresh resin every time (Bruggmann, *personal communication*).

Column calibrations

The best way to determine the behavior and efficiency of column chemistry is to conduct column calibrations. This involves monitoring the concentrations of elements of interest—in this case Cr and its elemental interferences (Fe, V and Ti)—over the course of the column elution by splitting the eluted material from each column step into fractions. With high resolution sampling, there should be a clear peak where the elements of interest are eluted from the columns.

As the procedure involved stick/non-stick column chemistry and used standard 2 mL-bed Polyprep columns, I assumed that one column calibration would accurately reflect the behaviour of all further columns.

I used an aqua regia leachate as the starting solution as this reflects the complex matrices that I was seeking to separate Cr from. The same leachate was used throughout the calibration to simplify calculations. For each stage, I dried down the amount of leachate required to contain 500±7.8 ng of Cr—as determined by five replicates by ICP-MS—to add to the columns.

Column 1 - Iron clean up column Column 1 is principally used to remove the large quantities of dissolved iron in both the sediment digests and the iron-rich sediment porewaters. Previous studies which have measured samples with a high Fe content use a similar first column (Frei et al., 2009; Paulukat et al., 2015; Schoenberg et al., 2016). The sample-spike mixture was dried down and dissolved in 1 mL of 6 M HCl overnight at 80°C. The cooled sample was added to column resin which was cleaned and preconditioned with 12 mL of 6 M HCl. In this high chloride, low pH matrix, dissolved iron complexes with chloride ligands to form $FeCl_4$. This complex readily adheres to the resin whilst other cations pass through.

To fully push any remaining sample through the column, a further 4 mL of 6 M HCl was added. This column proved extremely effective (99.8%) at removing iron from a typical sample matrix (237 ppm Fe) (Figure 3.7). Only minor amounts of chromium are lost during the elution (<4%).

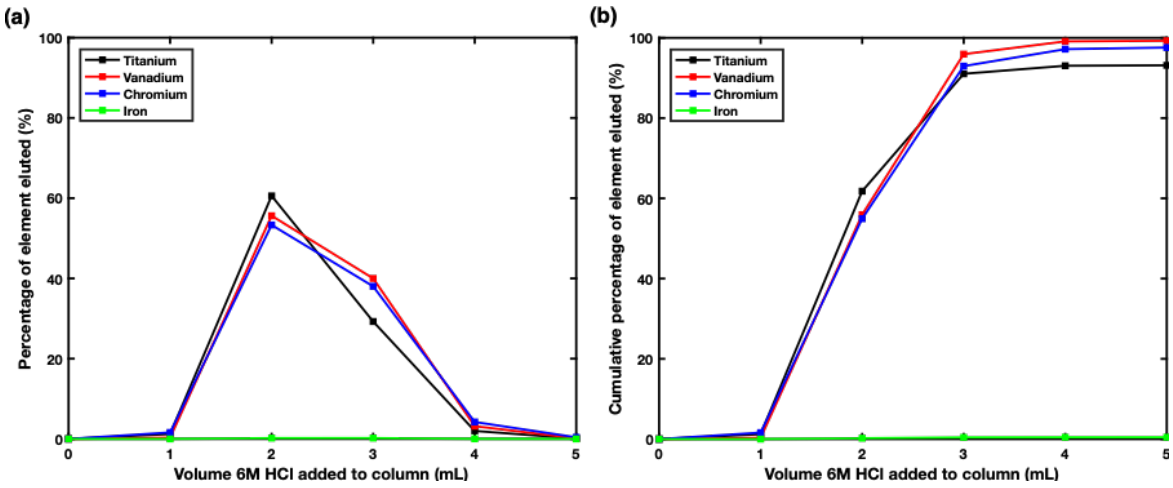

Fig. 3.7 - *(a) Column calibration of Cr, Fe, Ti and V for the first column at separate 1 mL collection intervals. Element concentrations in the eluent generated is given as a percentage of the concentration of the initial sample. (b) Cumulative percentage element concentrations (based on concentration of initial sample).*

Column 2 - Chromium purification column The eluent from the first column was dried down to completion. After cooling, the residue was dissolved in 30 μL of 6 M HCl and 8970 μL of MQ (0.02 M HCl matrix). A 1 mL aliquot of freshly prepared 0.2 M ammonium persulfate solution was then added. The mixture was quickly capped, shaken and placed on a hotplate at 120°C for one hour. Ammonium persulfate is an oxidising agent which effectively oxidises Cr(III) to Cr(VI) under low pH conditions. The dependencies of this oxidation reaction on solution pH, temperature and APS concentration are discussed in Moos and Boyle (2019) so I replicated the conditions of their procedure. The sample is removed after 1 hour and cooled whilst the precleaned columns were conditioned with 5 mL of 0.018 M HCl.

Samples were loaded carefully onto the column using a pipette. The Cr in the sample solution, now present as the anionic Cr(VI) species, can bind to the column with a high selectivity (similar to that of sulfate) along with other matrix anions. Matrix cations (e.g. Ti and V) do not bind to the resin and pass through to waste. The addition of a 3 mL MQ step, a 5 mL 0.2 M HCl step and a 6 mL MQ step rinsed any remaining V and Ti ions out while not considerably affecting the Cr bound to the resin. With a well-packed resin, leakage rates

during this stage are less than 10% of the total Cr added to the column (Figure 3.8). This loss of Cr is most likely Cr(III) which has not been effectively oxidised by the APS. Column packing appears very important during this stage; any minor heterogeneities in the resin can allow substantial amounts (>50%) of Cr to pass through in the first rinse stages (Figure 3.9).

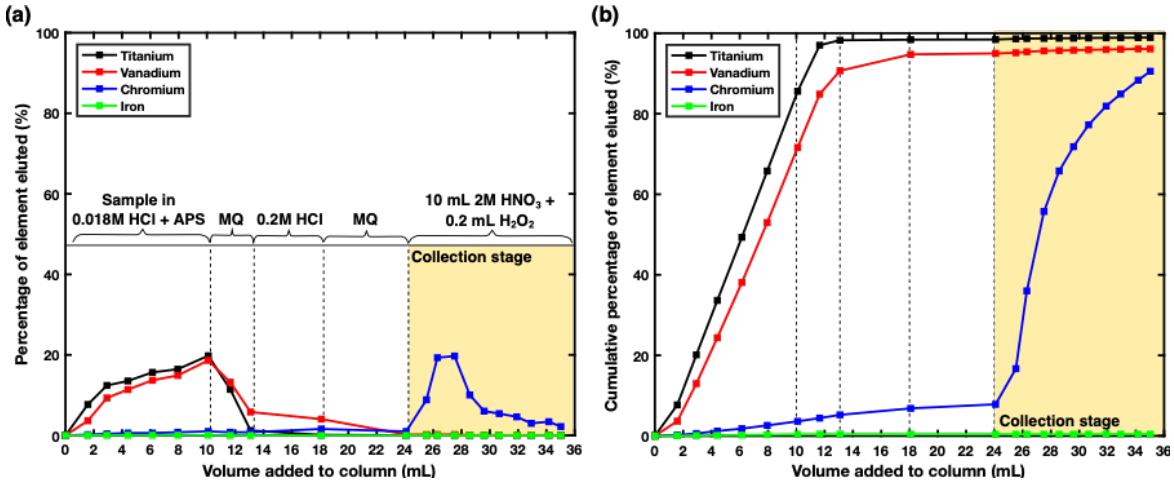

Fig. 3.8 - *(a) Column calibration of Cr, Fe, Ti and V for the second column at separate ∼1 mL collection intervals. Element concentrations in the eluent generated are given as a percentage of the concentration of the initial sample. Shaded golden window indicates the cumulative collected eluent used in column 3. (b) Cumulative total of the eluent collected during each step.*

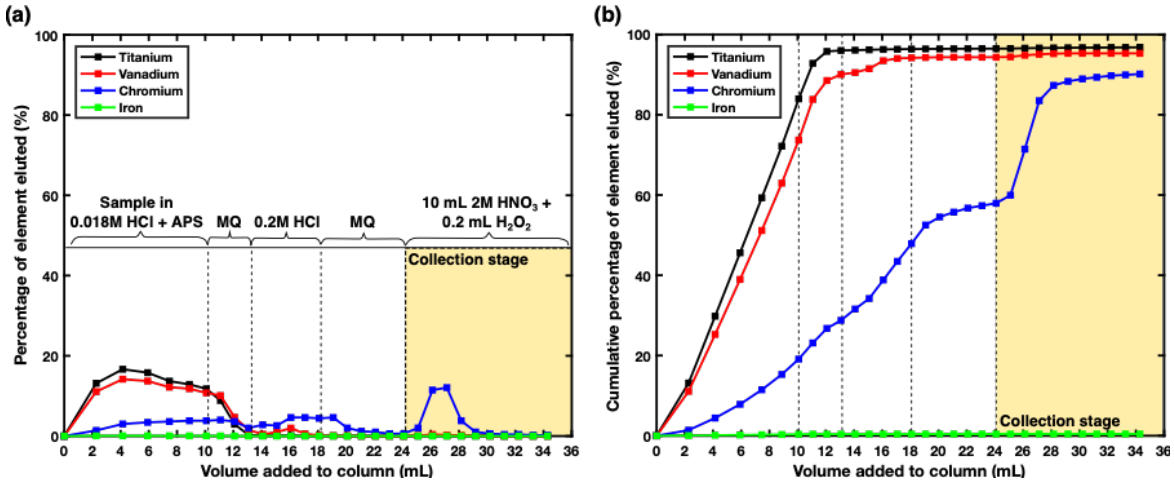

Fig. 3.9 - *The effect of poor resin packing on the separation of Cr. Description is the same as Figure 3.8.*

After the final rinse stage, Cr(VI), along with anions which were not removed in Column 1, is left attached to the resin. To elute the Cr from the resin, 10 mL of 2 M HNO_3 and 200

μL of H_2O_2 were pipetted onto the column simultaneously. In acidic conditions, H_2O_2 is an effective reductant of Cr(VI) (Pettine et al., 2002; Zink et al., 2010), thus Cr(VI) is reduced to Cr(III)—which is eluted from the column, as evidenced by a well-defined peak (Figure 3.8). The broad tail of this peak likely reflects a combination of ongoing Cr(VI) reduction and the high concentration of nitrate ions displacing Cr(VI) which escaped immediate reduction. The yield of Cr after the first two columns was roughly 80%.

The eluent collected from the second column was then dried down. A small amount of sulfuric acid remains in the residue, preventing complete evaporation on the hotplate (the boiling point of H_2SO_4 is 337°C). Though sulfur interferences are less important on TIMS than on MC-ICP-MS (Moos and Boyle, 2019), the presence of high sulfur concentrations can hinder filament loading and form large reservoir effects which generate erratic isotope ratio measurements (Ball and Bassett, 2000). Furthermore, the >10 μL of residue remaining would be extremely time consuming to load on to filaments. A third column is therefore necessary to separate chromium from this sulfuric acid matrix.

Column 3 - Secondary chromium purification column The third column in this procedure removes excess sulfate and other anions still present in the matrix. To ensure that any Cr being added to the column was in Cr(III) form, 110 μL of 1 M HCl and 50 μL of H_2O_2 were added to the dried down sample residue and left to react for 1 hour. This should ensure complete reduction of Cr(VI) to Cr(III) (Pettine et al., 2002). Afterwards, 10840 μL of MQ is added to form a dilute HCl matrix suitable for anion retention on to the column resin. The sample was carefully poured on to precleaned resin conditioned with 5 mL 0.018 M HCl and the eluent was completely collected. Three x 1 mL additions of 0.01 M HCl were added to fully push through the sample. A broad Cr elution peak is observed to come off over the entire collection window as Cr(III) can pass through the resin (Figure 3.10). The 15–20% loss of Cr in this step is assumed to be caused by residual Cr(III) left in the Teflon container during pouring of the sample mixture. After seeing these results, I modified the method by using the first 1 mL addition of 0.01 M HCl to rinse the leftover sample and pour that on to the resin. Sulfate and other anions are largely removed during this process, as is evident from the lack of sulfuric acid when the eluent is dried down.

Any leftover organic material, most likely from the column resin, was broken down overnight by 120 μL of aqua regia heated to 100°C. The digest was dried down to form a dry speck at the base of the Teflon. For most standards and samples, the speck is typically light blue or green in colour, though the absence of this colour has no bearing on the isotopic ratio measured.

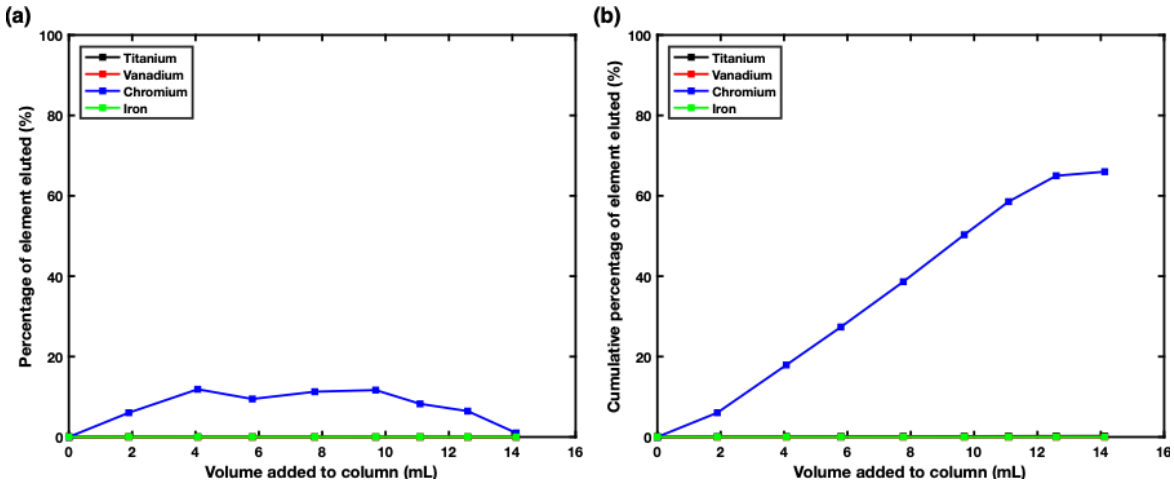

Fig. 3.10 - *(a) Column calibration of Cr, Fe, Ti and V for the first column at separate ∼1–2 mL collection intervals. (b) Cumulative total concentration of elements as a percentage of the initial amount in the aqua regia leachate.*

3.4.3 Preparation of samples for TIMS analysis

Fundamentals of TIMS

Thermal Ionisation Mass Spectrometry (TIMS) is one of the oldest methods for measuring isotope rations in easily ionisable materials (Fantle and Bullen, 2009). Samples are typically loaded onto a metal filament (typically W, Pt, Re or Ta) which is heated at low pressure. At a certain temperature, the element will first evaporate from the filament, and then an electron from the neutral species will "tunnel" onto the filament (this occurs due to the closeness of the filament and analytes Fermi levels) (Dass, 2007). An electrical potential gradient is used to accelerate the positive ions produced towards the electromagnet where the ion beams are deflected differently based on their mass-to-charge ratio. Faraday cups positioned at calibrated locations measure the current produced by the net charge of ions hitting the detector.

The work in this thesis was conducted on a Thermo Scientific Triton Plus thermal ionisation mass spectrometer (TIMS). The detector array consists of 9 Faraday cups with the central cup fixed in position.

Advantages and disadvantages of TIMS

Chromium isotope measurements can be made on MC-ICP-MS and TIMS. MC-ICP-MS analysis is much faster (<15 minutes per sample) and the use of a wet sample matrix means that reservoir effects during analysis are minimal. MC-ICP-MS can potentially measure

smaller sample sizes as long as the instrument is tuned correctly. These reasons explain why many research groups currently opt to measure δ^{53}Cr by MC-ICP-MS (Goring-Harford et al., 2018; Gueguen et al., 2016; Moos et al., 2020; Schoenberg et al., 2016).

Despite this, measuring δ^{53}Cr by TIMS offers certain advantages. Using MC-ICP-MS, the ^{52}Cr peak has to be measured on the left shoulder of the ^{40}Ar^{12}C peak, requiring careful instrument tuning. As TIMS does not use an argon carrier gas, there are no argon related interferences during analysis. Any interferences on Cr isotope beams only become a problem if the interference is ionised from the filament at the same temperature as Cr. Chromium peaks on TIMS are therefore much more stable, and less susceptible to Fe, V, Ti and S interferences. Importantly, matrix effects are less important in TIMS isotopic analysis. Whereas MC-ICP-MS can have substantial instrumental drift arising from variations in the plasma—requiring regular standard bracketing—drift correction is not necessary on TIMS. These reasons mean that with a large enough sample size, many of the sources of error are much lower on TIMS than on MC-ICP-MS, resulting in a more precise isotopic measurement.

Sample preparation for TIMS

All samples and standards measured for δ^{53}Cr were loaded onto zone-refined rhenium filaments. The filaments were mounted onto pre-cleaned filament posts and heated under vacuum conditions the day before use and stored in a dry desiccator hood. I used a single filament approach—where the filament acts as both the evaporation and ionisation filament—as this has been proven to work for Cr in most studies and is analytically simpler (Frei et al., 2009).

The use of a loading solution (a mixture of compounds used to aid emission of a specific element of interest) is necessary due to the high ionisation potential of Cr (6.77 eV). Loading solutions for Cr isotope analysis are numerous and varied, though the combination of colloidal silica and phosphoric acid and/or boric acid began early in the development history and has continued to be used in a majority of studies (Table 3.7) (Barnes et al., 1973; Frei et al., 2009; Füger et al., 2019). An ideal loading solution should promote the emission of large beam of Cr (>1 V) which is stable and can be run at low filament currents so as not to ionise potential interferences (e.g. Fe).

During method development, I trialled a range of reported loading solutions to test which created the most ideal conditions for Cr emission from the filament (Table 3.7). I found the method described in Trinquier et al. (2008) to be significantly better than other reported methods. A short description of this method is as follows. I first dissolved the standard/sample in 1.5 μL of 6 M HCl; to ensure efficient dissolution of the sample, the sample is mixed by pipette a few times. This Cr suspension was loaded onto outgassed filaments and dried at 0.4 A (10–15 minutes). When dry, an amount of loading solution

Loading method	Reference	Outcome
4 μg 10000 ppm Al, 250-300 μg (12.5%) H_3PO_4, 100 μg/μL Colloidal silica. All loading solutions mixed and dried down. Loaded onto the filament in 6 M HCl form.	(Fantle and Bullen, 2009)	High (>1600°C) ionisation temperatures required to emit samples. Produced beams of 0.5-1 V
4 μg 10000 ppm Al, 250-300 μg (12.5%) H_3PO_4, 100 μg/μL Colloidal silica. Sample loaded in 6 M HCl, each loading acid added sequentially and dried down.	(Fantle and Bullen, 2009)	High (>1600°C) ionisation temperatures required to emit samples. Produced beams of 0.5-1 V
4 μL of loading solution containing: "silica gel", 0.5 M H_3PO_4 and 0.5 M H_3BO_3 at a ratio of 4:1:0.5. Loading solution is loaded on top of the dried Cr salt.	(Bruggmann et al., 2019)	High (>1500°C) ionisation temperatures required to emit samples. Produced beams of 0.5-1 V.
Purified sample taken up in 1.5 μL of 6 M HCl. 350 μL of 4% colloidal silica, 250 μL of 5000 ppm Boric Acid and 175 μL 1000 ppm Al An amount proportional to the quantity of Cr in the sample (1.5 μL per 500 ng Cr) is loaded on to the dried Cr salt.	(Trinquier et al., 2008)	Emission temperature of 1150–1300°C Produced stable beams up to 20 V

Table 3.7 *Summary of loading methods tested for analysis of δ^{53}Cr using TIMS from published methods. The outcome of standards tested using these methods is described.*

(freshly made on the day of analyses) was added proportional to the amount of Cr in the sample (1.5 μL per 500 ng Cr). The loading solution was then left to fully evaporate at 0.7 A (∼5 minutes). The current was increased slowly until the filament glowed dull red for one second (∼1.8–2.2 A). The standard/sample typically looked a dark grey in colour. Some standards appeared to have localised patches of sample, although this made no difference to the efficiency of the run. Chromium loaded with this method was ionised at temperatures between 1150 and 1300°C and produced a stable ^{52}Cr beam of 5 V for at least 6 hours (Table 3.7). The only issue I encountered while measuring standards using this loading method was that beams could behave quite unstably during the heating procedure, presumably due to reservoir effects created through imperfect loading. Heating the filament to produce an ion beam of 10 V before lowering the intensity to 5 V was found to remove these instabilities, likely as those small reservoirs were burnt off. This loading method was used for all reported samples and standards in this thesis.

When I trialled the methods in Fantle and Bullen (2009) and Bruggmann et al. (2019), I found that very high ionisation temperatures (1500-1600°C) were necessary to emit a beam of 0.5–1 V (Table 3.7). This would be unsuitable for sample analysis as elemental interferences such as those from Fe would more efficiently ionise at these elevated temperatures. Additionally, the low intensity of the ion beams—in particular the smallest ^{53}Cr beam—would result in larger uncertainties in the isotope analysis. Altering the ratio of the components of the loading solution had little effect on the measurements. I initially suspected the issue might be from the uncharacterised "silica gel" described in Bruggmann et al. (2019) and Füger et al. (2019) so I trialled standards loaded with a range of silica concentrations from 0.1% to 40%. Below 1% silica concentrations, samples did not ionise effectively. Above 10%, the loading solution would become a brittle glass that would not adhere to the filament. A "sweetspot" of 4% silica concentration was found to be the best, though it did not lower the ionisation temperature. I also trialled the removal of boric acid from the method used in Bruggmann et al. (2019), to no avail. The presence of phosphoric acid may somehow be causing this difference in the loading methods, since the Trinquier et al. (2008) method omits this reagent.

3.4.4 Instrumental analysis of δ^{53}Cr

Cup configuration

Chromium isotopic analysis requires the simultaneous monitoring of the ^{50}Cr, ^{52}Cr, ^{53}Cr and ^{54}Cr beams alongside potential interferences (^{49}Ti, ^{51}V, ^{56}Fe). The closeness of these atomic masses mean that analysis can be run within the mass range on the Triton in static mode as opposed to dynamic mode. The cup configuration used is shown in Table 3.8. During my

L4	**L3**	**L2**	**L1**	**C**	**H1**	**H2**	**H3**	**H4**
	^{49}Ti	^{50}Cr	^{51}V	^{52}Cr	^{53}Cr	^{54}Cr		^{56}Fe

Table 3.8 *Cup configuration for Cr isotope acquisition on TIMS. At the ionisation temperatures reached during analysis, ^{49}Ti and ^{51}V were not emitted. For this reason, these beams were measured using the default machine parameters.*

project, I tested the reproducibility of the collection cups by shifting the ^{52}Cr beam to the L2 cup (^{49}Ti was therefore not monitored in this case). There was no significant difference between isotope ratios collected with this cup configuration.

Turrets filled with up to 21 filaments were loaded into the source the night before analysis to allow the pumps to decrease the HV source pressure to <2 x 10^{-7} bar. The turret was initialised (allowing the turret to rotate to all sample positions) before use so there would be no change in pressure during the sequence.

Instrumental procedure and heating protocol

Baseline and gain calibrations were made with the analyser gate shut every morning or at the start of a sequence run. While establishing this method, I ran every sample manually on the TIMS so that I could understand the behaviour during ionisation. After ∼50 standard runs, I found the behaviour of ionisation was reproducible enough to run an automated sequence (with defined heating parameters). A typical heating method for sample analysis is as follows: (1) filaments are heated to 1200°C at a rate of 100°C min^{-1}, (2) the filament is held at this temperature to allow the beam to stabilise (at this point, the intensity ranges between 1-10 V), (3) parameters are tuned on the instrument to create the highest intensity beam at that given filament temperature, (4) the filament is further heated at a rate of 20°C min^{-1} until 10 V of Cr is emitted, (5) the filament is held at this temperature to allow the beam to stabilise, (6) the filament is cooled until a stable intensity of 5 V is emitted and, (7) instrument parameters are tuned again and the peak centring of the beam is checked. At this point, the beam is typically stable between 4 and 6 V. Each sample acquisition comprises of 20 blocks of 20 cycles, providing 400 sets of simultaneous isotope values. Rarely, I observed variable isotope ratios in the first 100 measurements, so I exclude these from calculating the final isotope ratios.

3.4.5 Issues with method development

When initially setting up the method, I directly loaded mixed double-spike and standard solutions onto the filaments without column purification. This is a typical first step when developing an isotope method. As both the double spike and standards were in purified Cr solution, it seemed excessive to run them through the entire column procedure.

When measured, these double spike-standard mixtures exhibited mass independent fractionation to varying degrees. In particular, the $^{50}Cr/^{52}Cr$ ratio would behave erratically throughout the run, independently of the $^{53}Cr/^{52}Cr$ and $^{54}C/^{52}Cr$ ratios. An example of this effect is shown in a particularly problematic DS-SRM979 mixture in Figure 3.11. As would be expected, the deconvolved $\delta^{53}Cr$ varied largely over the run (since the ^{50}Cr beam is used in the deconvolution process) (Figure 3.11a). As this effect occurred early in the method development process, while I was testing out different loading methods, it was tricky to deconvolve this effect in samples where the mass independent variations were much more subtle. Interestingly, a research group at Princeton University were encountering a similar problem, with the ^{54}Cr beam behaving erratically instead. This problem has not been reported previously in $\delta^{53}Cr$ measurements in the literature. However, a similar effect had previously been seen for lead also on TIMS (Thirlwall, 2000).

Two possible explanations for this mass independent behaviour were considered: (1) there was a specific interference on the ^{50}Cr beam and/or, (2) the double spike solution and standard were not sufficiently mixing/equilibrating. A mass scan of the samples found no signal being recorded on ^{48}Ti, ^{51}V or ^{56}Fe beams (more abundant isotopes of those elements) which discounted many of the typical interferences from affecting the ^{50}Cr signal. The possibility of other potential interferences was excluded using three tests. First, the systematic renewal of each reagent used in the loading procedure did not remove the effect on ^{50}Cr, suggesting no contamination was being introduced in the loading solutions. Second, a heated blank Re filament was run on the TIMS to assess the possibility of the ionisation of filament material—however, even at 1600°C, no beams at the measured masses were recorded. Finally, repeats of both standard SRM979 (n=7) and double spike (n=3) solutions behaved mass dependently when run separately.

Therefore, it was assumed that the double spike and standard were not fully equilibrating. This seemed surprising, given the low volume of mixed liquids (<0.5 mL combined), that both solutions were in the same matrix (3% HNO_3) and that equilibration time was similar to other measured isotope systems (overnight refluxing at 100°C). This effect had also not been described previously in the literature, and yet two research groups were encountering the same problem simultaneously. Poor equilibration of double spike-standard solutions is a particular issue for TIMS analysis, in comparison to MC-ICP-MS, due to the method

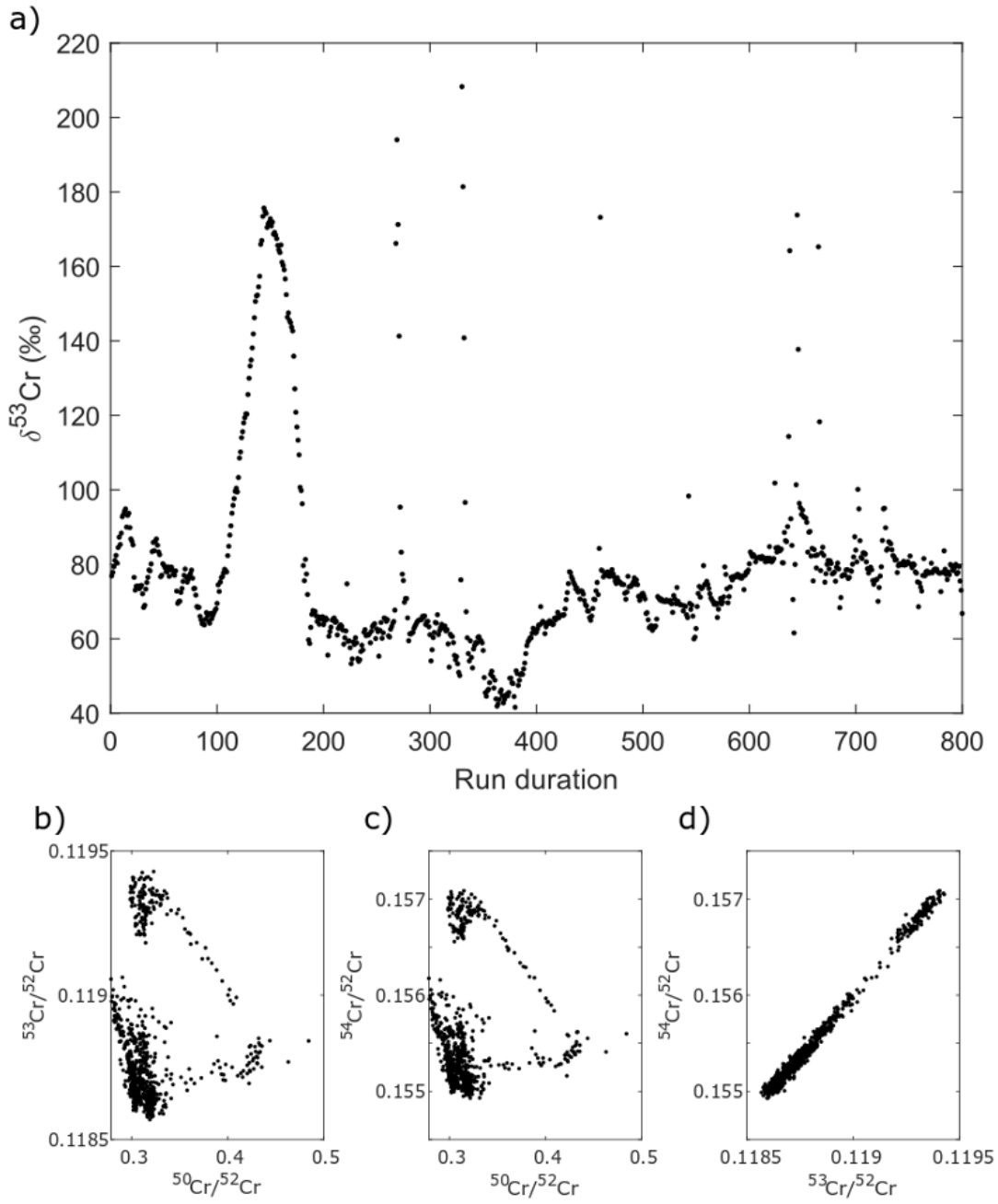

Fig. 3.11 - *Measurements of a standard SRM979 which exhibited large degrees of mass independent fractionation as a result of poor double-spike and standard equilibration. (a) Double spike corrected δ^{53}Cr value over the course of analysis showing large reservoir effects. Note the correct value of δ^{53}Cr for SRM979 is 0‰ (b) Cross plot between ^{53}Cr/^{52}Cr ratio and ^{50}Cr/^{52}Cr ratio. (c) Cross plot between ^{54}Cr/^{52}Cr ratio and ^{50}Cr/^{52}Cr ratio. (d) Cross plot between ^{53}Cr/^{52}Cr ratio and ^{54}Cr/^{52}Cr ratio—this shows evidence of only mass dependent fractionation.*

of loading. As the sample is loaded onto the filament in solid form, individual pockets or 'reservoirs' of Cr salt may be heterogeneously distributed across the filament surface. Some of these reservoirs will be more susceptible to evaporation—perhaps if activators such as boric acid are more concentrated in that space—and thus will evaporate first.

During the process of evaporation, mass dependent fractionation occurs as the lighter isotopes of Cr (^{50}Cr) are preferentially sputtered from the filament over the heavier isotopes (^{54}Cr). If the double-spike and standard are fully equilibrated, every reservoir will have the same mix of isotopes at the start, hence this mass dependent fractionation can be corrected for during double spike deconvolution, resulting in a constant δ^{53}Cr (Figure 3.12a). If however, the double spike solution and standard solution are not fully equilibrated, different reservoirs on the filament will have different initial isotopic compositions. When ionised, the combination of isotopes evaporated would therefore change based on the combination of reservoirs that are being sputtered from the filament. As a result, the δ^{53}Cr will vary erratically, with spikes of different δ^{53}Cr as reservoirs are burnt off (Figure 3.12b). Reservoir effects can still be important in fully equilibrated double spike-standard solutions if there are two or more very larger reservoirs that are at different stages of evaporation (as the measured ratios will be a combination of the two reservoirs). Care was therefore taken to create an even distribution of salt on the filament.

I tested a few different methods of ensuring sufficient spike-sample equilibration: (1) increasing the equilibration time to four days, (2) drying down the double spike-standard mixture and dissolving it in 1 M HCl, (3) drying down the entire loading solution and re-dissolving it in 6 M HCl and, (4) digesting the double spike-standard mixture in aqua regia before re-dissolving it in 1 M HCl. Though small improvements were seen, none of these alterations entirely removed the mass independent fractionation and the erratic δ^{53}Cr measurements. The only way which seemed to produce a stable, mass dependent, ^{50}Cr beam was to run the spiked standards through the entire column chemistry process used for samples. The reason for why this is necessary to effectively equilibrate the double spike and standard solutions is unclear. It is presumably some combination of the mechanical mixing caused by the movement of the solution through the resin beads and the process of Cr(III) in solution being oxidised by APS to Cr(VI) and then reduced again to Cr(III) during the separation procedure.

Although the separation procedure removed mass independent fractionation, there was still variation in the measured δ^{53}Cr of identical double spike-standard solutions (Figure 3.13 – *Orange squares*). These variations were most likely caused by a loss of isotopically fractionated Cr onto the column resin before the double spike and standard were fully equilibrated (this would not be corrected for during double spike deconvolution). Drying

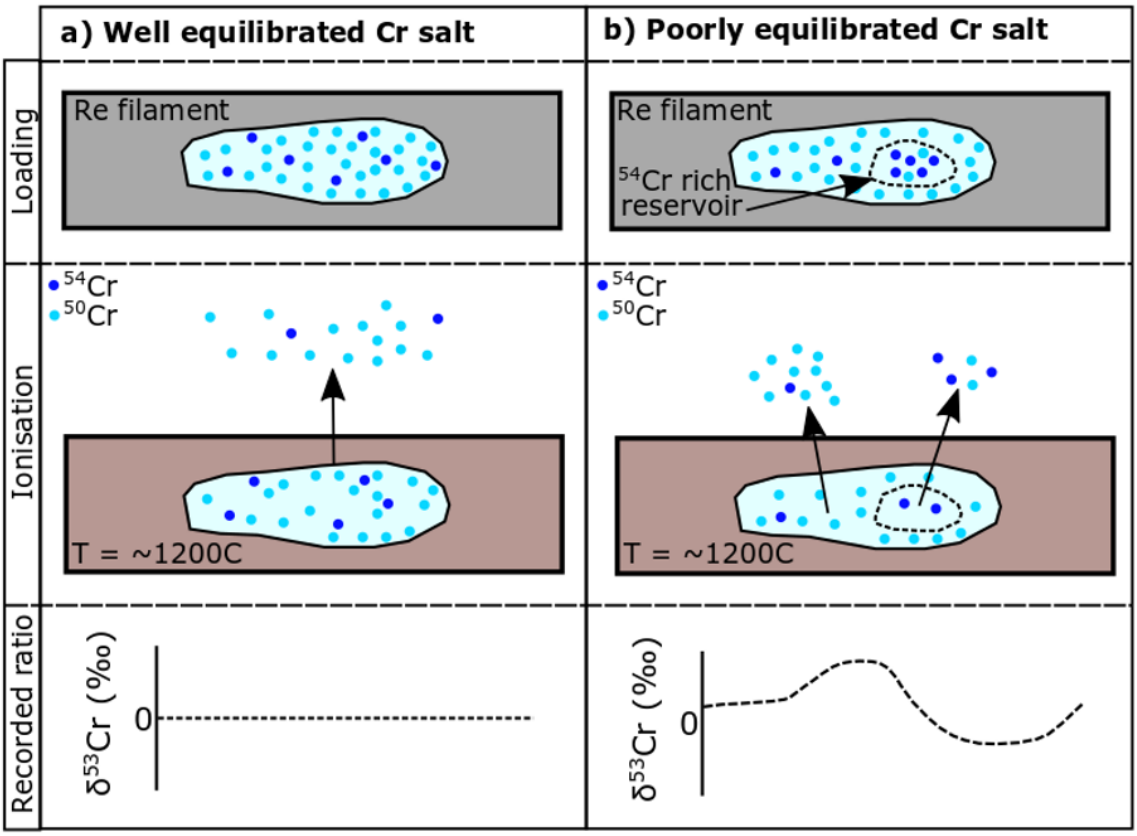

Fig. 3.12 - *Effect of good and poor equilibration between double spike and standard mixture on the ionisation from Re filament.* ^{54}Cr *and* ^{50}Cr *are used to represent heavy and light isotopes, respectively—*^{53}Cr *and* ^{52}Cr *would behave in a similar way. (a) In the case of well equilibrated solution, the Cr salt on the filament has a uniform isotope ratio, so the mass dependent variations can be corrected in the* $\delta^{53}Cr$ *ratio. (b) In the case of poorly equilibrated solution, small reservoirs of* ^{54}Cr *enriched and* ^{50}Cr *enriched areas can exist. As these reservoirs isotopically evolve at different times during ionisation, the resultant* $\delta^{53}Cr$ *ratio is erratic as reservoirs are burnt off at separate times.*

down the spike and standard individually, re-dissolving them in an identical 1 M HCl matrix, and mixing them on at 80°C for three days prior to loading appeared to remove the variations in the δ^{53}Cr values (Figure 3.13 – *Blue squares*). It is likely that equilibration in this matrix is efficient enough prior to the column procedure so that any fractionation can be corrected for during the double spike deconvolution process. I therefore adopted this method for all samples measured in this thesis. An example of the typical corrected isotope measurement and ratio cross-plots is shown in Figure 3.14.

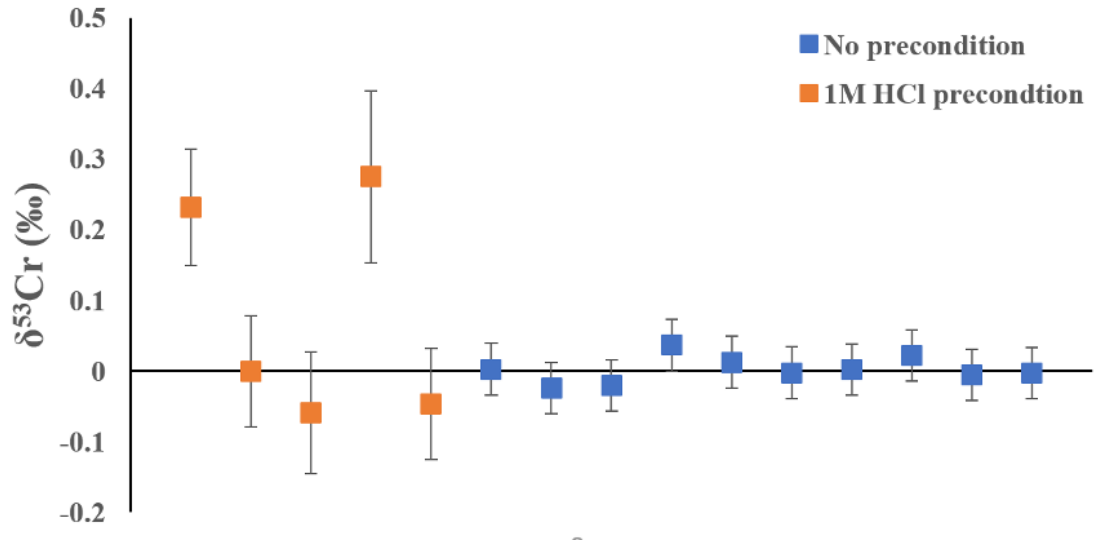

Fig. 3.13 - *δ^{53}Cr of standards (SRM979) passed through the entire column chemistry processed with and without a 1 M HCl precondition. 1 M HCl precondition refers to dissolving the double spike and standard individually in 1 M HCl and mixing in these matrices.*

3.4.6 Testing for potential interferences and background corrections

Despite the column separation procedure being very efficient at removing any V, Fe and Ti from the sample matrix (Figure 3.8), I tested the effect of potential elemental interferences on the δ^{53}Cr measurement. Two DS-SRM979 mixtures which had been through the column separation process were doped with ~200 ng of single element V, Fe and Ti ICP-MS standard solutions. These standards were first heated to typical sample temperatures (1150-1400°C) to replicate the temperature of measurements. The range of masses expected to encapsulate the interference peaks were scanned to ascertain if any of that element was being emitted.

No V or Ti was emitted in measurable quantities over the mass ranges (50–52) and (48–50) respectively. Presumably the loading solution in this method prevented emission of these elements at the ionisation temperature required for Cr emission. In a further test for V,

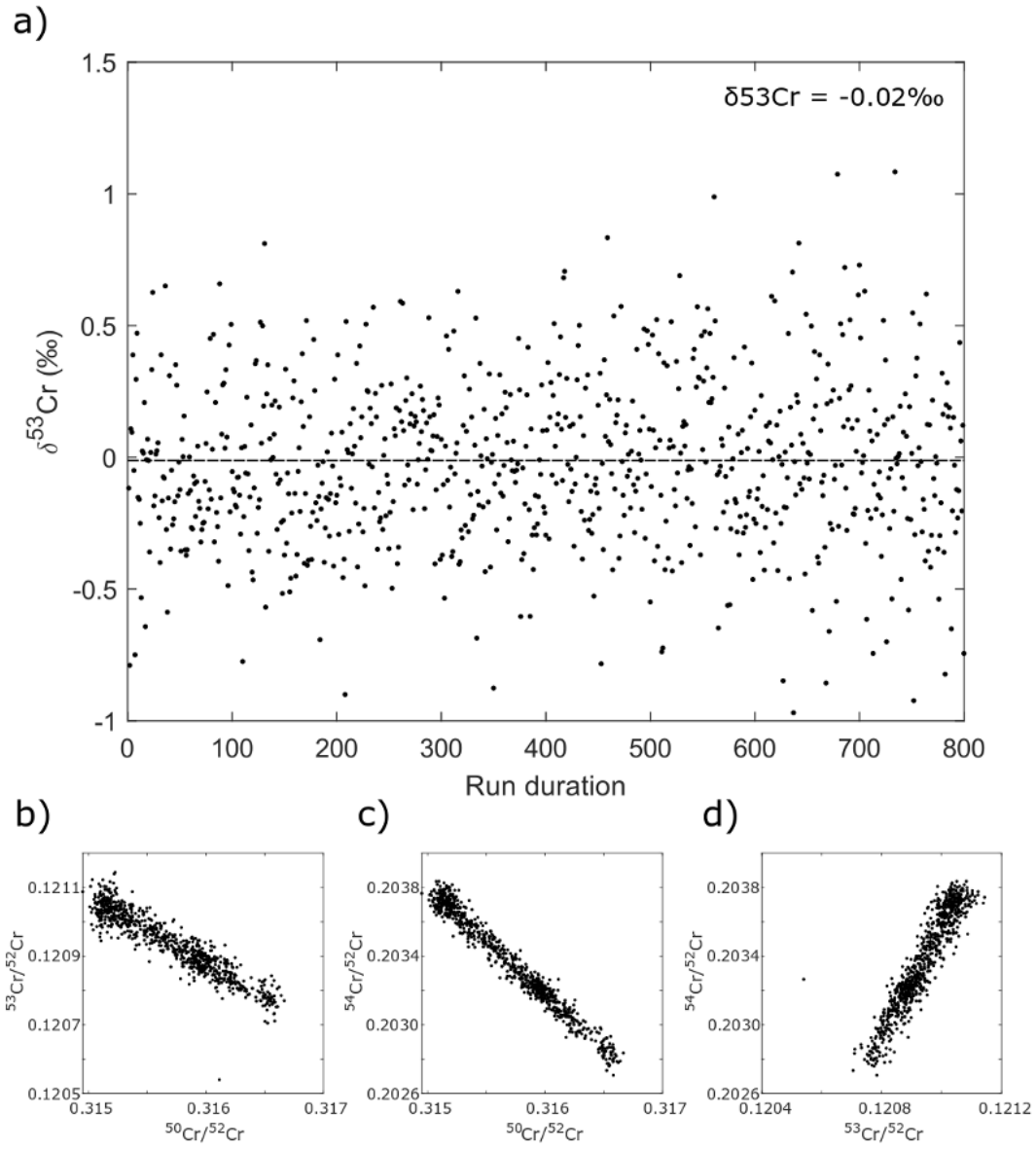

Fig. 3.14 - *Results from an SRM979 measurement run using the final preparation method. (a) Deconvoluted δ^{53}Cr measurements through the run. Note the correct value of δ^{53}Cr for SRM979 is 0‰ (b) Cross plot between the ^{53}Cr/^{52}Cr ratio and ^{50}Cr/^{52}Cr ratio. (c) Cross plot between ^{54}Cr/^{52}Cr ratio and ^{50}Cr/^{52}Cr ratio. (d) Cross plot between the ^{53}Cr/^{52}Cr ratio and ^{54}Cr/^{52}Cr ratio. All show mass dependent fractionation.*

Standard	δ^{53}**Cr (‰)**
SRM979	0.005 ± 0.012
SRM979 + 10 ng V	0.002 ± 0.012
SRM979 + 50 ng V	-0.000 ± 0.013
SRM979 + 100 ng V	0.006 ± 0.013

Table 3.9 - *δ^{53}Cr values of SRM979 standards spiked with varying amount of vanadium single element spikes.*

Standard	δ^{53}**Cr (‰)**
Repeat 1 - Uncorrected	-0.307 ± 0.010
Repeat 1 - Corrected	-0.012 ± 0.012
Repeat 2 - Uncorrected	-0.454 ± 0.012
Repeat 2 - Corrected	-0.001 ± 0.011

Table 3.10 - *Two repeats of SRM979 spiked with 100 ng of Fe. Uncorrected refers to raw ratios being used to determine δ^{53}Cr without corrected for iron concentrations. Corrected refers to the δ^{53}Cr value calculate after the correction outline in Equation 3.2*

the element most prone to passing through the column procedure for Cr separation (*Section 3.4.2.4*), I found that increasing spiked concentrations of V had no effect on the δ^{53}Cr value of the standard (Table 3.9).

A measurable Fe peak was observed at mass ~55.9; this peak was focussed and aligned to be measured alongside the Cr beams during routine analysis. The ^{56}Fe beam was subsequently monitored for all sample measurements since the ^{54}Fe beam would be present over the same mass range as the ^{54}Cr beam, adding a small intensity to the beam. A correction can be applied to remove the contribution of the ^{54}Cr beam caused by Fe (Equation 3.2).

$$\delta^{54}Cr_{Corr} = \delta^{54}Cr_{Raw} - \left(\delta^{56}Fe_{Meas} \times \frac{\delta^{54}Fe_{Nat}}{\delta^{56}Fe_{Nat}}\right) \tag{3.2}$$

I tested this correction on a sample containing 100 ng of spiked Fe and found it reproduced the δ^{53}Cr value well (Table 3.10).

Iron appears to be ionised more efficiently at higher temperatures. Efforts were therefore made to keep the temperature of ionisation as low as possible to prevent large uncertainties from the correction. For smaller sample sizes (<100 ng), higher temperatures are necessary to ionise all of the Cr from the filament, therefore the correction is larger (Figure 3.15).

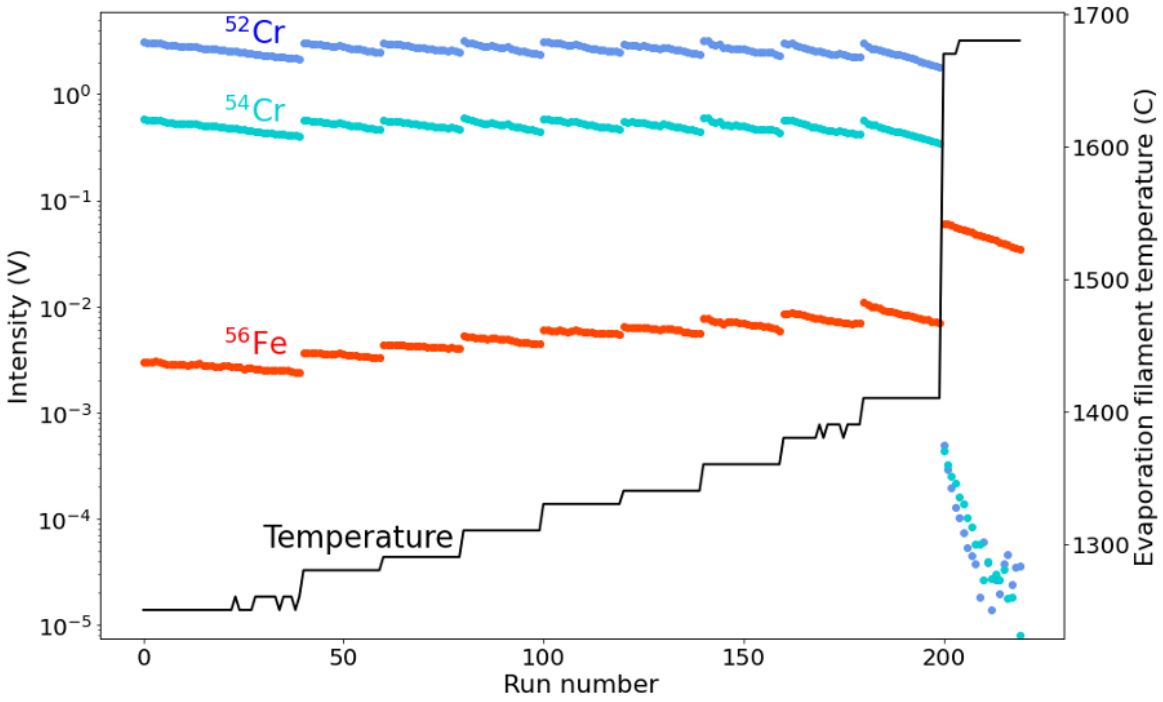

Fig. 3.15 - *Intensity of the ^{52}Cr, ^{54}Cr and ^{56}Fe beam over the measurement run of ~50 ng of SRM979 (the lowest sample sized measured). Temperature of the evaporation filament increases throughout the run to maintain a consistent ^{52}Cr beam. Note that the ^{54}Cr and ^{52}Cr beams stayed relatively constant until measurement 200 whilst the ^{56}Fe beam slowly increased. At measurement 200, all Cr is burnt off so the temperature markedly increases. Accompanying this is a large increase in the ^{56}Fe beam. The contribution of the ^{56}Fe beam is typically not as high as this in large sample sizes.*

Aliquot size SRM979 (ng)	**δ^{53}Cr (‰)**
500	0.006 ± 0.012
400	-0.007 ± 0.011
300	-0.008 ± 0.012
200	-0.005 ± 0.012
100	-0.010 ± 0.012
75	-0.020 ± 0.014
50	-0.029 ± 0.017

Table 3.11 - *δ^{53}Cr measurements of varying aliquots of SRM979. Note that the aliquot size refers to the amount of Cr mixed before processing and does not include the Cr added with the double spike solution.*

3.4.7 Detection limit of Cr measurements on TIMS

To test the feasibility of low chromium sample analysis by TIMS, I tested the detection limit of the analysis using between 50 ng and 500 ng of SRM979 standard. Even at 50 ng, a near-accurate isotope composition was measured (Table 3.11); a 3 V beam could be sustained for roughly one hour of analysis. However, there does seem to be a slight trend towards negative δ^{53}Cr values with decreasing sample size. This is most likely due to the ^{56}Fe correction applied (Equation 3.2) or due to contamination by the 0–5 ng Cr blank during processing.

3.4.8 Complete methodology and long term reproducibility of SRM979 and NIST3112a standards

This method of δ^{53}Cr analysis using TIMS relies on a modified combination of the column preparation method of Moos and Boyle (2019) and the loading method of Trinquier et al. (2008). A schematic outline of the full method is shown in Figure 3.16. This method produces reproducible and accurate δ^{53}Cr for both isotopic standards and aqua regia leachates of salt marsh pond sediments.

During each sequence, five SRM979 standards are run alongside sixteen samples. On every third turret, I also ran a NIST3112a standard. Figure 3.17 shows the long-term reproducibility of the δ^{53}Cr for these standards. The long-term value for SRM979 was 0.00±0.02‰ and for NIST3112a was -0.11±0.02‰. The offset between these two standards are within uncertainty of both Schoenberg et al. (2008) and Zhu et al. (2018).

3.4.9 Section conclusions

In this section, I described the development of the method to measure Cr isotopes using TIMS at the University of Cambridge. A modified version of the three-column approach used in Moos and Boyle (2019) was employed to separate Cr from other matrix ions. After testing a number of methods to load Cr onto filaments, I found the best approach was described in Trinquier et al. (2008) which provided large, stable Cr isotope beams during analysis. The largest problem during method development was that there was insufficient equilibration of the double-spike solution and the samples/standards. This was solved by redissolving the double-spike solution and sample/standards in 1 M HCl and mixing for three days at >100°C. Using this method, I was able to reproducibly measure SRM979 and NIST3112a isotopic reference standards to a sample size as small as 50 ng.

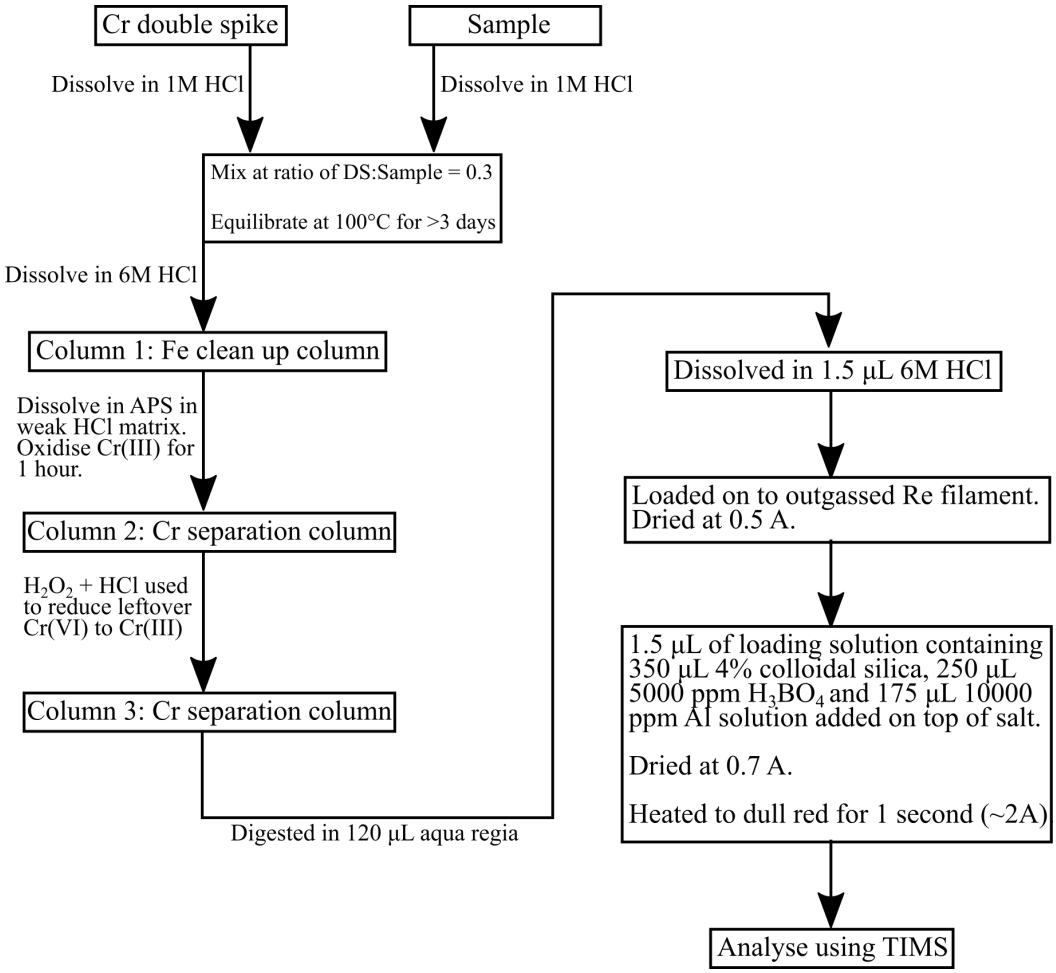

Fig. 3.16 - *Schematic showing the full methodology for chromium isotope analysis of samples and standards using TIMS. See text for full description of the methods*

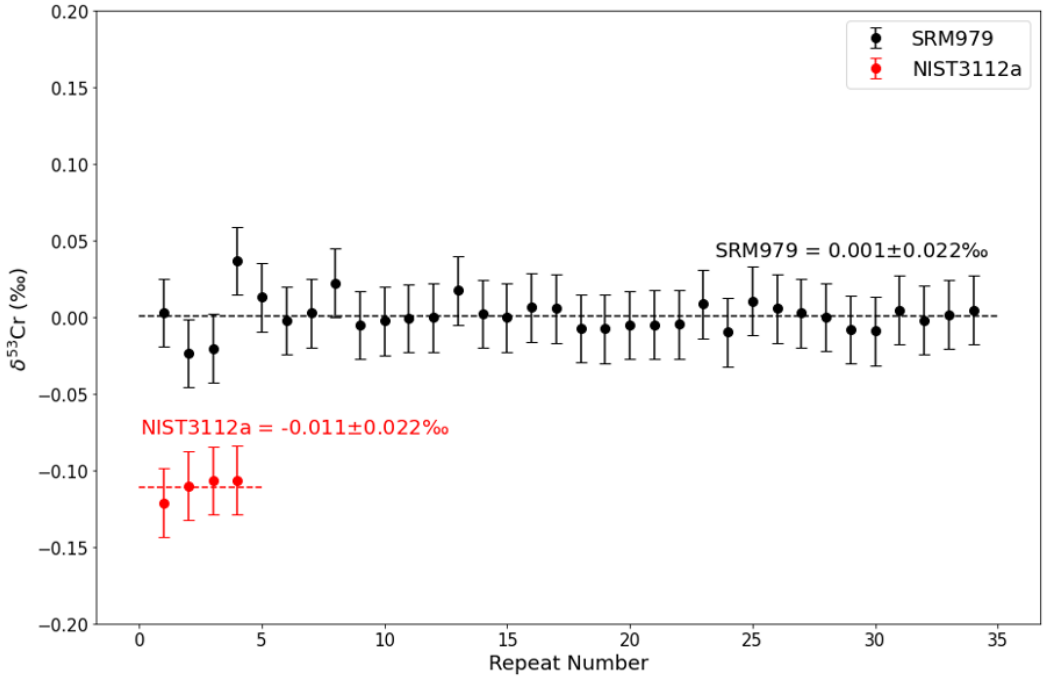

Fig. 3.17 - *Long term reproducibility of $\delta^{53}Cr$ for SRM979 and NIST3112a over the course of this project. Dashed line represents the mean $\delta^{53}Cr$ value of all measurements.*

3.5 Implications for further chapters

The method described in this chapter to measure the trace element concentration of porewater and sediments using ICP-MS was used to provide the preliminary concentration checks for isotope analysis and other trace metal (e.g. Fe, Mn, Ti and V) concentrations in **Chapter 4** and **Chapter 5**. The method described in this chapter for Cr isotope analysis was used to measure the δ^{53}Cr of salt marsh pond sediments in **Chapter 5**. I next examine the behaviour of the Mo and Cr in the two types of pond sediment present in East Anglian salt marshes in an attempt to better understand the behaviour of these elements in different redox conditions.

Chapter 4

The Geochemical Behaviour of Molybenum in Salt Marsh Pond Sediments

The work presented in this chapter has been published under the title **'Molybdenum Geochemistry in Salt Marsh Pond Sediments'** in *Geochimica et Cosmochimica Acta* (Hutchings et al., 2020). Alex Dickson developed the method to measure Mo isotopes at Royal HoIloway, University of London. I conducted all fieldwork, laboratory work, data interpretation and writing of the manuscript. Co-authors and three reviewers provided comments on the published manuscript.

4.1 Introduction

4.1.1 Chapter outline

The work in this chapter examines the behaviour of molybdenum (Mo) in East Anglian salt marsh pond sediments. I present a high-resolution record of Mo concentration data and isotope measurements in the pore water and sediment in three different pond sediment cores. I interpret this data using my understanding of the redox conditions in these environments outlined in **Chapter 2**. The work conducted in this chapter provides a more mechanistic understanding of the δ^{98}Mo isotope system with relation to redox conditions, which will aid in interpreting the geological record.

4.1.2 Molybdenum behaviour in aqueous environments

Molybdenum (Mo) (M_w = 95.95) is a redox sensitive trace metal which behaves differently under oxic and sulfide-containing aqueous conditions (Kendall et al., 2017). In the modern oxic ocean, Mo predominantly exists as the soluble molybdate ion (MoO_4^{2-}), which behaves conservatively with a residence time of 440 kyr (Miller et al., 2011). Molybdenum is much more efficiently scavenged under sulfide-containing aqueous conditions than under oxic/anoxic conditions in the absence of sulfide. Consequently, enrichments of sedimentary Mo in the rock record have been used to suggest water columns that are locally euxinic—containing free aqueous sulfide (Reinhard et al., 2013; Scott and Lyons, 2012).

4.1.3 The δ^{98}Mo isotope system

The δ^{98}Mo isotope system provides further constraint on redox conditions which has been used to understand paleoredox conditions in Earth history (Arnold, 2004; Dickson, 2017; Goto et al., 2020; Kendall et al., 2017) and to trace modern biogeochemical redox reactions (Skierszkan et al., 2019, 2017). The Mo isotope ratio is reported in delta notation relative to NIST-SRM-3134 + 0.25‰ (Equation 4.1) (Nägler et al., 2014).

$$\delta^{98}Mo = \left(\frac{\left(\frac{^{98}Mo}{^{95}Mo}\right)_{Sample}}{\left(\frac{^{98}Mo}{^{95}Mo}\right)_{SRM3134}} - 1 \right) \times 1000 + 0.25 \tag{4.1}$$

No known chemical reaction preferentially removes heavier Mo isotopes to the sedimentary phase, thus the δ^{98}Mo of sedimentary Mo is lower than the water from which it derives, while residual porewaters have been observed to have a higher δ^{98}Mo (Kendall et al., 2017; McManus et al., 2002; Nägler et al., 2011). As a consequence, seawater δ^{98}Mo (2.3‰) is higher than any surface sediment signature (Nakagawa et al., 2012; Nägler et al., 2011; Siebert et al., 2003). The process of Mo removal into sediments differs based on the geochemistry of the water column, sediment, and the porewater, and each process imparts a characteristic δ^{98}Mo into the sediment. These differences in sedimentary δ^{98}Mo allow us, in theory, to distinguish between sediments deposited under different redox conditions.

4.1.4 Molybdenum and δ^{98}Mo behaviour in the absence of sulfide

In sedimentary environments where an aqueous, or dissolved, sulfide fraction (comprising H_2S, HS^- and S^{2-}) is absent in both the overlying water column and in the porewater, molybdate ions adsorb to Fe and Mn oxides present at the sediment-water interface. Molybdenum

isotope fractionation occurs when a tetrahedral coordination of MoO_4^{2-} in solution changes to a distorted octahedral Mo-containing surface complex during adsorption (Wasylenki et al., 2011). Different Mo isotope fractionation factors (Δ^{98}Mo) are associated with adsorption to different Fe and Mn oxide minerals, the largest isotope fractionation being associated with adsorption onto Mn oxides ($\Delta^{98}Mo = \delta^{98}Mo_{Seawater} - \delta^{98}Mo_{Mn-Oxide}$ = 2.2–3.3‰) (Barling and Anbar, 2004; Wasylenki et al., 2011). Molybdenum isotopic fractionation during adsorption to Fe-minerals depends on the mineral in question, with Mo isotopic fractionation factors ranging from Δ^{98}Mo = 0.83‰ for magnetite (Fe_3O_4) up to Δ^{98}Mo = 2.19‰ for hematite (Fe_2O_3 (Goldberg et al., 2009). Variations in the mineralogy of the iron minerals have been posited as a potential driver for the range of δ^{98}Mo measured in bulk oxic sediments (Goldberg et al., 2012). While oxic environments cover most of the modern ocean floor (>80%), the slow rate of adsorption, combined with the propensity of Fe and Mn oxides to be reduced and release any adsorbed Mo during sediment burial under reducing conditions, means that oxic sediments play a disproportionately smaller role in removing Mo from the modern ocean than their area would suggest (Reinhard et al., 2013; Scott and Lyons, 2012; Shaw et al., 1990).

4.1.5 Molybdenum and δ^{98}Mo behaviour in the presence of sulfide

In the presence of aqueous sulfide, the molybdate ion (MoO_4^{2-}) is progressively thiolated to oxythiomolybdate species ($MoO_xS_{4-x}^{2-}$) and terminally to tetrathiomolybdate (MoS_4^{2-}) at a rate of reaction on the order of hours, days, weeks and months for each sequential reaction in Equation 4.2 respectively. At and above 11 μM $H_2S_{(aq)}$, tetrathiomolybdate becomes the dominant aqueous Mo species (Erickson and Helz, 2000).

$$MoO_4^{2-} \rightarrow MoO_3S^{2-} \rightarrow MoO_2S_2^{2-} \rightarrow MoOS_3^{2-} \rightarrow MoS_4^{2-} \tag{4.2}$$

While thiomolybdate species are more efficiently scavenged onto particles than molybdate species, the pathway of sequestration of the various thiomolybdate species (Equation 4.2) remains debated. Pyrite has been discounted as a major host for Mo in sediments, though Mo could potentially adsorb to other sulfide-containing minerals (Chappaz et al., 2014). Organic carbon and Mo have a strong empirical association (Algeo and Lyons, 2006; McManus et al., 2006), which has led some authors to suggest that thiomolybdate is scavenged into the sediment by organic matter (Dahl et al., 2017; Lyons et al., 2009). Other authors have suggested this link may not be causal, and have instead advocated that the formation of an iron-sulfur-molybdenum complex—which ultimately becomes sequestered as an $FeMoS_4$ species—is the main output of Mo in euxinic sediments (Helz et al., 2011; Helz and Vorlicek,

2019; Vorlicek et al., 2018). Regardless of the mechanism, the presence of aqueous sulfide in porewaters causes dissolved Mo to be near-quantitatively removed to sediments, hence bulk sediment δ^{98}Mo in sulfidic sediments tends to be higher than non-sulfidic sediments. Whilst it was initially thought that dissolved Mo was quantitatively captured in euxinic environments, it has since been shown that there is a limiting aqueous Mo concentration present dependent on pH, sulfide concentration and availability of free iron (Helz et al., 2011). As such, the δ^{98}Mo in sediment where aqueous sulfide is present in porewater can be up to 0.5‰ lower than the dissolved δ^{98}Mo (Nägler et al., 2011).

4.1.6 Motivation for study

We still lack a fundamental understanding of the specific reaction pathways which determine the sediment δ^{98}Mo in anoxic Fe/Mn dominated environments and in aqueous sulfide dominated anoxic environments. Factors such as periodic water column redox changes, particle reactivity in the water column and organic matter likely all play a role in the δ^{98}Mo of the sediment that is ultimately buried (Dahl et al., 2010; Helz et al., 2011; King et al., 2018; Scholz et al., 2018, 2013, 2017). In order to fully utilise the potential of the Mo isotope and concentration proxy, we must first understand the behaviour of Mo in well constrained redox environments.

For this study, I collected sediment cores from one pond identified as iron-rich, a second pond identified as sulfide-rich and a third pond suspected to be an intermediate between iron and sulfide pond chemistry. By using high resolution sediment and porewater measurements of Mo concentration and isotopic compositions coupled with measurements of redox active elements (e.g. Fe and S), I was able to understand both active geochemical processes (captured by the porewater) and time integrated geochemical processes (captured by the sediment). The objective was to determine how the behaviour of Mo is controlled by iron and sulfur cycles in marine and marginal marine sediments. My hypothesis was that Mo concentrations and isotopic composition would reveal the chemical and mineralogical reactions occurring in salt marsh pond sediment that are not evident in iron or sulfur measurements alone.

4.2 Methods

4.2.1 Field site and sample collection

Cores for this work were collected at Abbotts Hall Farm salt marsh, Essex, UK (see *Section 2.2.1* for site description). Ponds were selected based on the classification method outlined in **Chapter 2** (Figure 2.4). Pond sediment classified as iron-rich (sampled Nov. 2018), pond

sediment classified as sulfide-rich (sampled May 2018) and pond sediment classified as intermediate (sampled May 2018) (Figure 4.1). A wider core (ID = 102 mm) was used for all sediment analysis, porewater major cation, porewater trace metal analysis and Mo isotope measurements and a narrower core (ID = 65 mm) was used for porewater sulfur, iron, and anion analysis. Once cores were placed, each could be lifted in turn without disturbing the sediment or water within the other core.

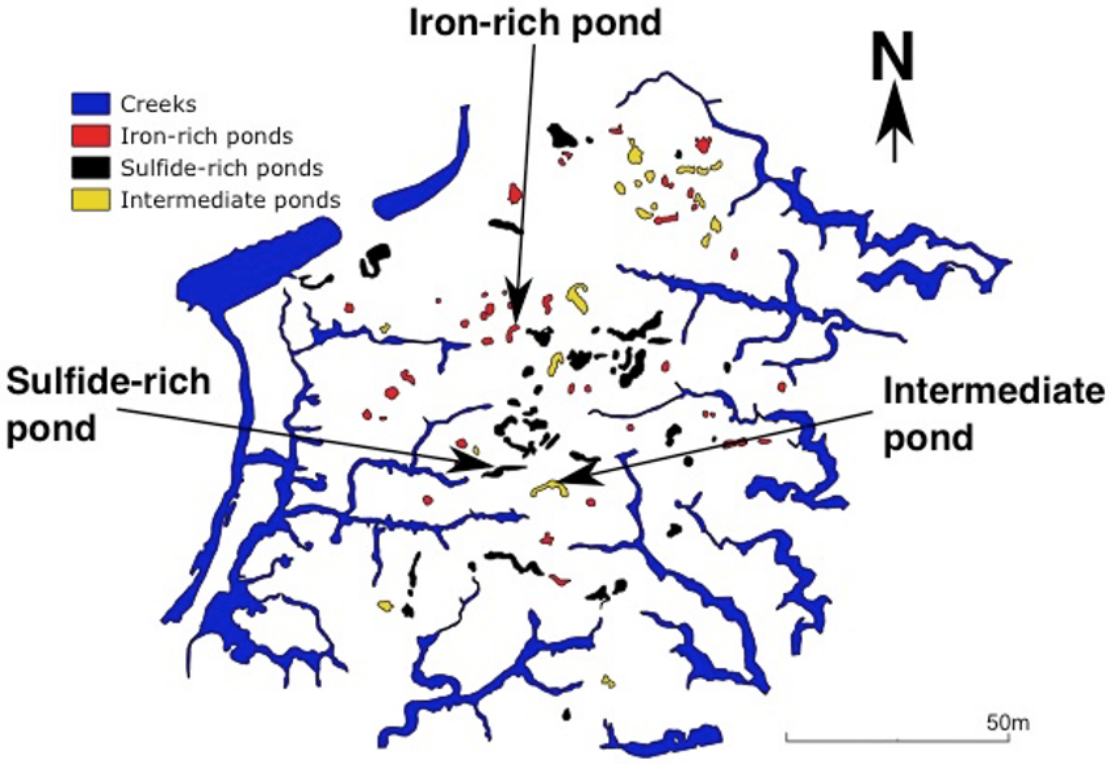

Fig. 4.1 - *Locations of three sediment cores taken in ponds on the salt marsh platform at Abbotts Hall Farm, Essex.*

Pond water overlying the pond sediment was collected from the three ponds during the November 2018 sampling. The pond water was sampled at a later period due to the extreme drying that occurred in the ponds during May 2018 sampling which resulting in a <2 cm water column. I assume that, given the regular tidal flushing of these ponds (at least monthly), only minor δ^{98}Mo distillation will occur over a year-timescale. The effect of the near-complete evaporation of the pond water on the porewater results in May 2018 is unknown. Acid cleaned 125 mL LDPE bottles were submerged and sealed under the pond

water to ensure no air bubbles. Pond water was filtered within 24 hours and acidified with 1 mL of concentrated HNO_3.

4.2.2 Porewater and sediment extraction

Roughly 15 mL of porewater was extracted for each sample from the core at 2 cm resolution using Rhizons attached to a 5 mL syringe. Sediments were sampled using 2 mL cut syringes at the opposite core edge prior to porewater extraction to prevent porewater mixing. All sediments were digested immediately after extraction to prevent any further reaction with remaining porewater.

4.2.3 Aqueous geochemical analyses

Dissolved iron, dissolved sulfide, major anions and sulfur isotopes were measured at the University of Cambridge as described in *Section 2.2.3*. Major cation concentrations were determined using ICP-OES (Agilent). Trace metal concentration analyses are described in *Section 3.3*. The porewater pH was measured using a Mettler Toledo with a Five Easy plus pH probe immediately upon extraction from the core to prevent CO_2 degassing.

4.2.4 Sedimentary analyses

Weighed 500 mg aliquots of wet sediment were digested in 4 mL of concentrated aqua regia for >24 hours at 115°C. Samples were centrifuged and the eluent was carefully pipetted for analysis. For three samples in the iron-rich core, the adsorbed Mo fraction was leached from 1 g of wet sediment using 20 mL of 0.1 M phosphate solution. This mixture was shaken for at least 24 hours, centrifuged, and the eluent was extracted. The remaining sediment was rinsed with a (<1 mM) NaCl solution, centrifuged, and the eluent was discarded. The sediment was left to dry overnight and weighed before being digested as per the method above. The phosphate concentration used in this leaching step is well in excess of experiments where >99% of Mo (as molybdate and thiomolybdate) was desorbed from goethite and >85% was desorbed from pyrite as phosphate ions compete with molybdate/thiomolybdate for surface sites on the mineral (Xu et al., 2006). Methods for determining sedimentary metal concentrations in the leachate are described in *Section 3.2.2*.

A sediment core was taken from the iron-rich and sulfide-rich pond in May 2019 to determine sediment mineralogy using X-Ray diffraction (XRD) at Royal Holloway, University of London (RHUL). It is assumed that the changes to the mineralogy of sediment are minimal over the course of a year, given the slow accretion of salt marsh sediment. Since

both the iron-rich pond sediment and sulfide-rich pond sediment did not appear to show any large change in porewater chemistry over this sampling period, it seems unlikely authigenic minerals would have changed significantly. Sediments were taken from a number of depths and immediately transferred to an anaerobic glove box. A thin layer of sediment was smeared on glass slides and left to dry under anaerobic conditions. Samples were measured by XRD within 30 minutes of being removed from the glovebox. XRD was conducted on a Philips PW1830 X-Ray diffractometer from 0-90 degrees. Mineral peaks were identified using Match! software and mineral abundances were calculated using Rietveld analysis.

4.2.5 Mo isotope and concentration determination

Mo was purified from the sample matrix using the single anion exchange technique of Pearce et al. (2009) as modified by Dickson et al. (2016) to separate Zn.

Sample preparation prior to column chemistry

The Mo concentration of all samples was measured by ICP-MS at the University of Cambridge (described in *Section 3.3*) to ascertain the required spiking aliquot. Samples were spiked with ^{100}Mo-^{97}Mo double spike for an optimal spike/sample ratio of 0.3 and refluxed overnight before being evaporated to dryness. For sediment digests, 0.2 mL of concentrated HCl was added to replace molybdenum nitrate salts (from the aqua regia digest matrix) with molybdenum chloride salts and evaporated to dryness. Salts remaining from porewater evaporation required redissolution in 3 mL of 4 M HCl for the same step. Samples were re-dissolved in 6 mL 1 M HF/ 0.5 M HCl, refluxed for two hours to ensure dissolution and centrifuged before being loading onto the columns. Centrifugation is required to prevent calcium fluoride deposits from contaminating the columns.

Resin cleaning

Biorad Polyprep (2 mL bed volume) columns loaded with precleaned anion exchange (AG1-X8) resin were used. To clean the column resin, I added in sequence: (1) 10 mL of 7.5M double-distilled HNO_3, (2) 6 mL of 4M double distilled HCl and, (3) 3 x 10 mL additions of 1M double-distilled HCl.

Column separation

Columns were preloaded with 2mL 1M HF/ 0.5M HCl before additions of the sample. Samples were poured directly onto the column resin carefully to avoid adding the calcium

fluoride residues at the base of the centrifuge tube. Major elements were eluted with (1) 8mL 1M HF/ 0.5M HCl and (2) 6mL 4M HCl. Zinc was eluted in 0.5M HF/ 0.1M HBr before collection of molybdenum with 8mL 3M HNO_3. Each sample was dried down and re-dissolved in 3% HNO3; this is the ideal matrix for MC-ICP-MS analysis.

MC-ICP-MS analysis

The δ^{98}Mo was determined by MC-ICP-MS (Thermo Neptune Plus) at RHUL. Concentrations checks were performed on the purified Mo solutions. All samples and standards were diluted to produce a ^{96}Mo signal of 3V to prevent variations of δ^{98}Mo with varying concentrations. Instrument parameters (e.g. cooling gas rates and lens positions) were tuned prior to the start of every run to ensure beam stability. Spiked NIST-3134 standards were run every three samples and a digested Open University (OU) solution Mo standard was run every ten samples. These standards were used to correct for any instrumental drift which occurred. The measurement on the OU standard was -0.12 ± 0.05‰ (2SD) based on 16 replicates which is in line with published values (Goldberg et al., 2013). For all runs, seawater was within analytical uncertainty of the accepted seawater value (2.34 ± 0.10‰) (Nägler et al., 2014) and procedural blanks were less than 1 ng. Reported Mo concentrations were calculated by isotope dilution using the ^{100}Mo-^{95}Mo ratio. Double-spike deconvolution was calculated using the same method as for Cr (**Appendix A**).

4.3 Results

4.3.1 Redox chemistry

Iron-rich pond sediment redox chemistry

Visible mineralogical changes (as seen in the colour of the sediment) in the iron-rich core coincide with differences in porewater and sedimentary concentrations of Fe and Mn (Figure 4.2, Figure 4.3). I divided the iron-rich core into four zones separated by these coloured boundaries (Figure 4.3). Dissolved sulfide is below detection limit in the iron-rich core and SO_4/Cl is marginally higher than in N. Atlantic seawater (Figure 4.2a). Dissolved ferrous iron is relatively constant in Zones I and II (∼1 mM), increases in Zone III to ∼1.8 mM, before decreasing to ∼0.2 mM from 20–30 cm (Zone IV) (Figure 4.2c). Sedimentary Fe contents are highest at the surface and generally increase with decreasing porewater Fe(II) with depth (Figure 4.2d). Iron mineralogy is a combination of ferrihydrite, pyrite, mackinawite, goethite, and—in Zone 4 only—hematite (Figure 4.4a, Table 4.1). Dissolved Mn is considerably

higher than in the other cores and increases from 0.02 mM to 0.14 mM by 27 cm depth (Figure 4.2e). Sedimentary Mn is roughly 1000 times lower than sedimentary Fe (Figure 4.2f) and is characterised as birnessite ($H_{2.72}Mn_{0.5}Na_{0.364}O_{2.544}$) (Table 4.1).

Sulfide-rich pond sediment redox chemistry

Instead of the coloured zoning seen in the iron-rich core, the sediment in the sulfide-rich and intermediate cores fades from black at the surface to dark grey at depth (Figure 4.3b). The sulfide and intermediate cores have comparable porewater sulfide concentrations with a peak at 5–10 cm between 5 and 9 mM and a decrease below this to ~1 mM at 35 cm (Figure 4.2b). The maximum porewater sulfide concentration is higher in the intermediate pond-sediment than in the sulfide-rich pond sediment (9 mM and 5 mM respectively). The SO_4/Cl ratio decreases from seawater until a constant ratio is reached in both the sulfide-rich core and intermediate core (Figure 4.2a). The constant SO_4/Cl is lower and deeper for the sulfide-rich pond (0.026) compared to the intermediate pond (0.032). Only trace amounts of ferrous iron were detected in both cores and dissolved manganese concentrations are much lower than in the iron-rich core (Figure 4.2c,e). Sedimentary Fe is roughly similar between the sulfide-rich and intermediate core; there is a consistent increase with depth from 5 mg/g to ~12 mg/g (Figure 4.2d). Almost all of the sedimentary iron present in the sulfide-rich pond sediment is present as a combination or pyrite and mackinawite (Figure 4.4b, Table 4.1). Similar to the iron-rich pond sediment, birnessite ($H_{2.72}Mn_{0.5}Na_{0.364}O_{2.544}$) is the main Mn hosting mineral.

4.3.2 Molybdenum concentration and isotopes

Iron-rich pond sediment

Both porewater Mo concentration and sedimentary Mo content decrease with depth in the iron-rich core (Figure 4.5b). A large increase in sedimentary Mo content at 5–12 cm and at 18–23 cm are observed with a noticeable increase in porewater Mo at the same depths. Phosphate-leached sediment—theoretically removing any Mo adsorbed to the sediment (Xu et al., 2006)—has a lower Mo content which decreases with depth from 1.1 μg/g at 0.5 cm to 0.6 μg/g at 28.5 cm. Porewater δ^{98}Mo is higher than sediment δ^{98}Mo at all depths (Figure 4.5a). Pond water δ^{98}Mo is within analytical uncertainty of seawater δ^{98}Mo and at all depths, porewater Mo fluctuates around this seawater value. Below 18 cm, porewater δ^{98}Mo anticorrelates with sedimentary δ^{98}Mo. Sedimentary δ^{98}Mo decreases from 1.65‰ (2.5 cm) to 0.28‰ (24.5 cm) and increases again below this depth to 1.11‰ (30.5 cm) (Figure 4.5a).

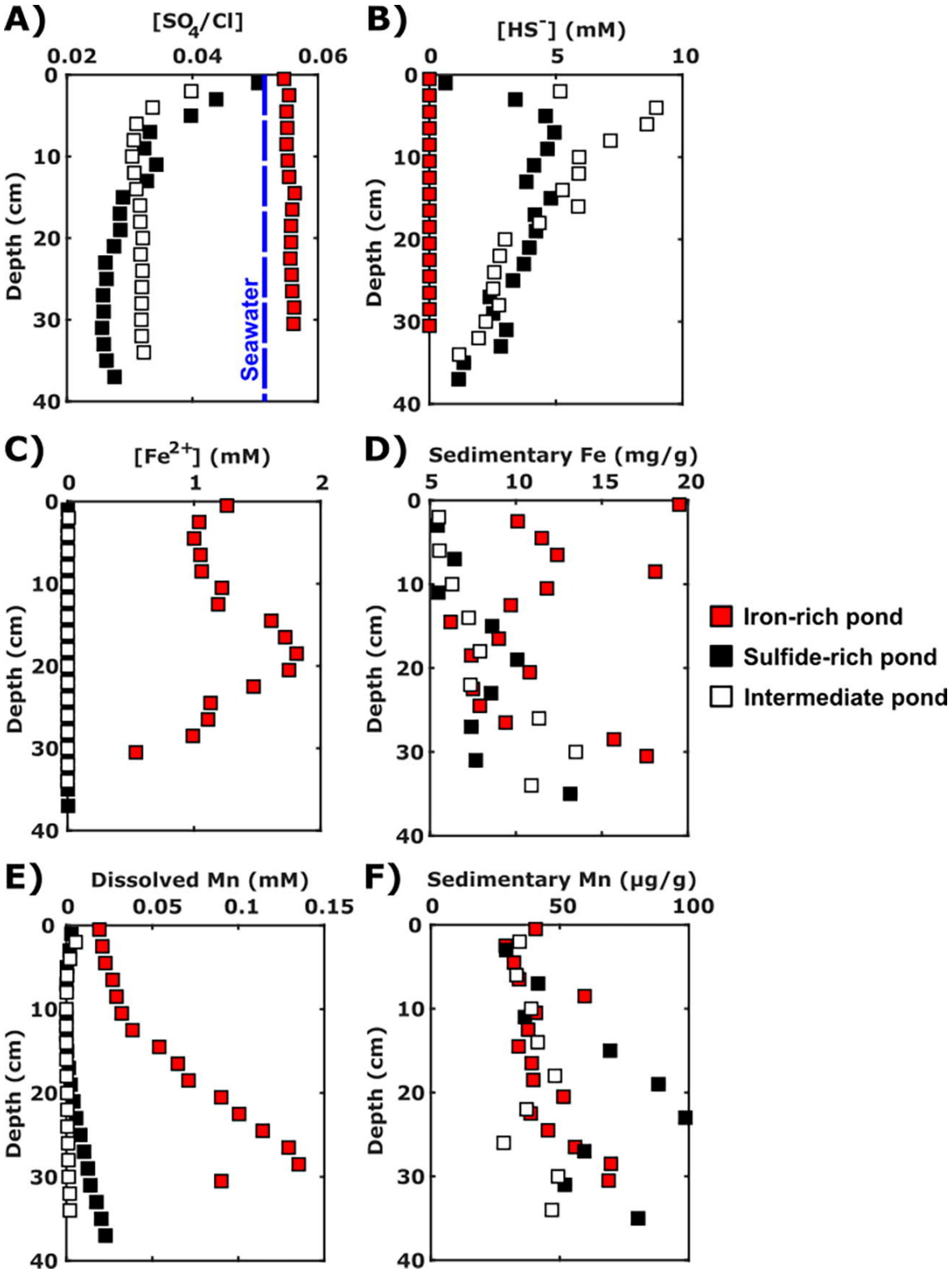

Fig. 4.2 - *Geochemical data for the iron-rich, sulfide-rich and intermediate cores: a) Dissolved SO_4/Cl ratios. Blue dashed line indicates typical seawater values. b) Dissolved sulfide concentrations. c) Dissolved Fe^{2+} concentrations. d) Sedimentary Fe content. e) Dissolved Mn in porewaters. f) Sedimentary Mn content. The analytical error bars for these analyses are smaller than the data symbols used.*

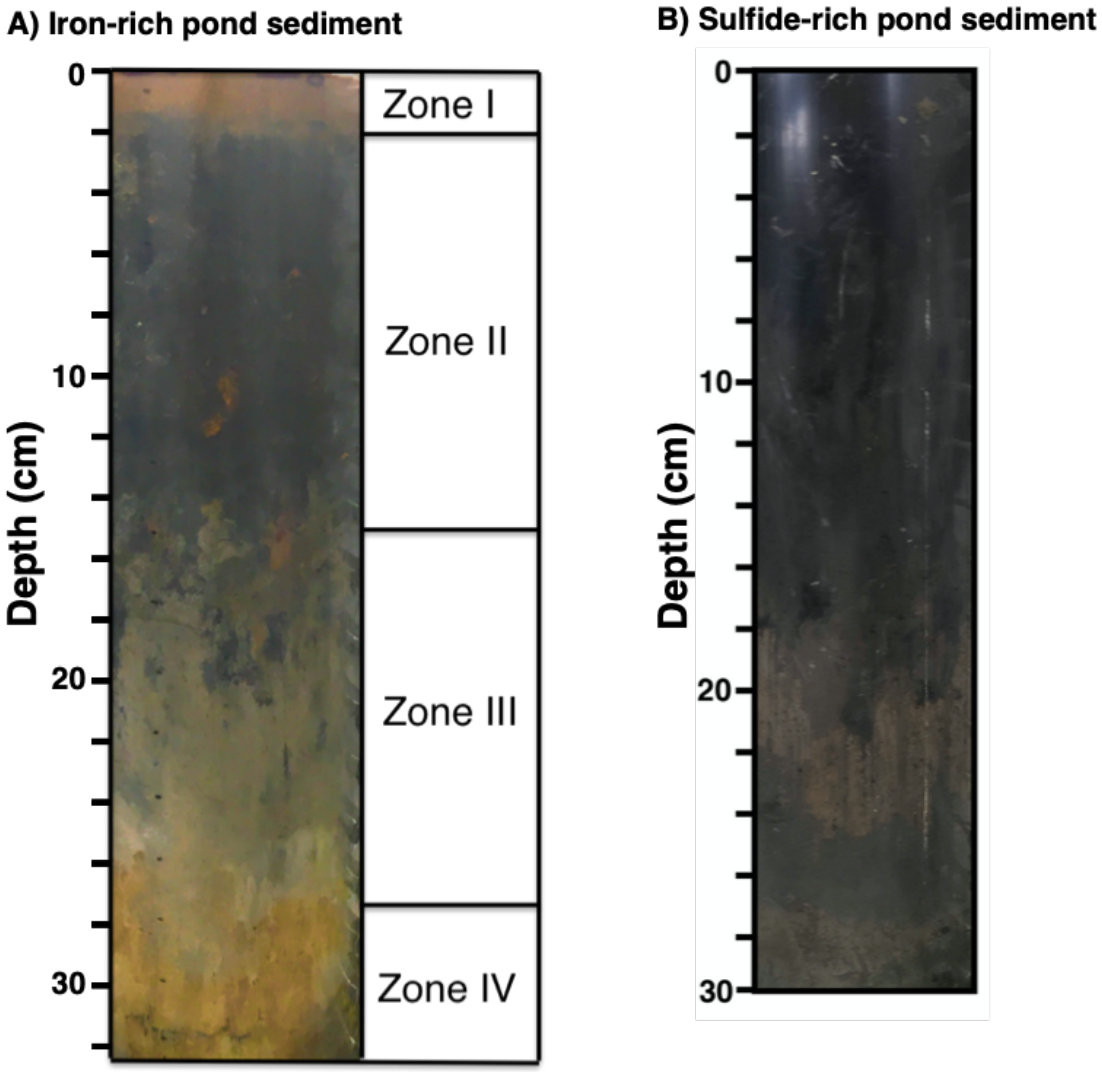

Fig. 4.3 - *a) Photo showing the visible redox zonations of the iron-rich pond sediment core before extraction of porewaters and sediment. b) Photo of the sulfide-rich pond sediment core before extraction of porewaters and sediments. The intermediate pond sediment was near-identical in appearance to the sulfide-rich pond sediment. Brightness has been increased in both photos to make the zones appear more clearly.*

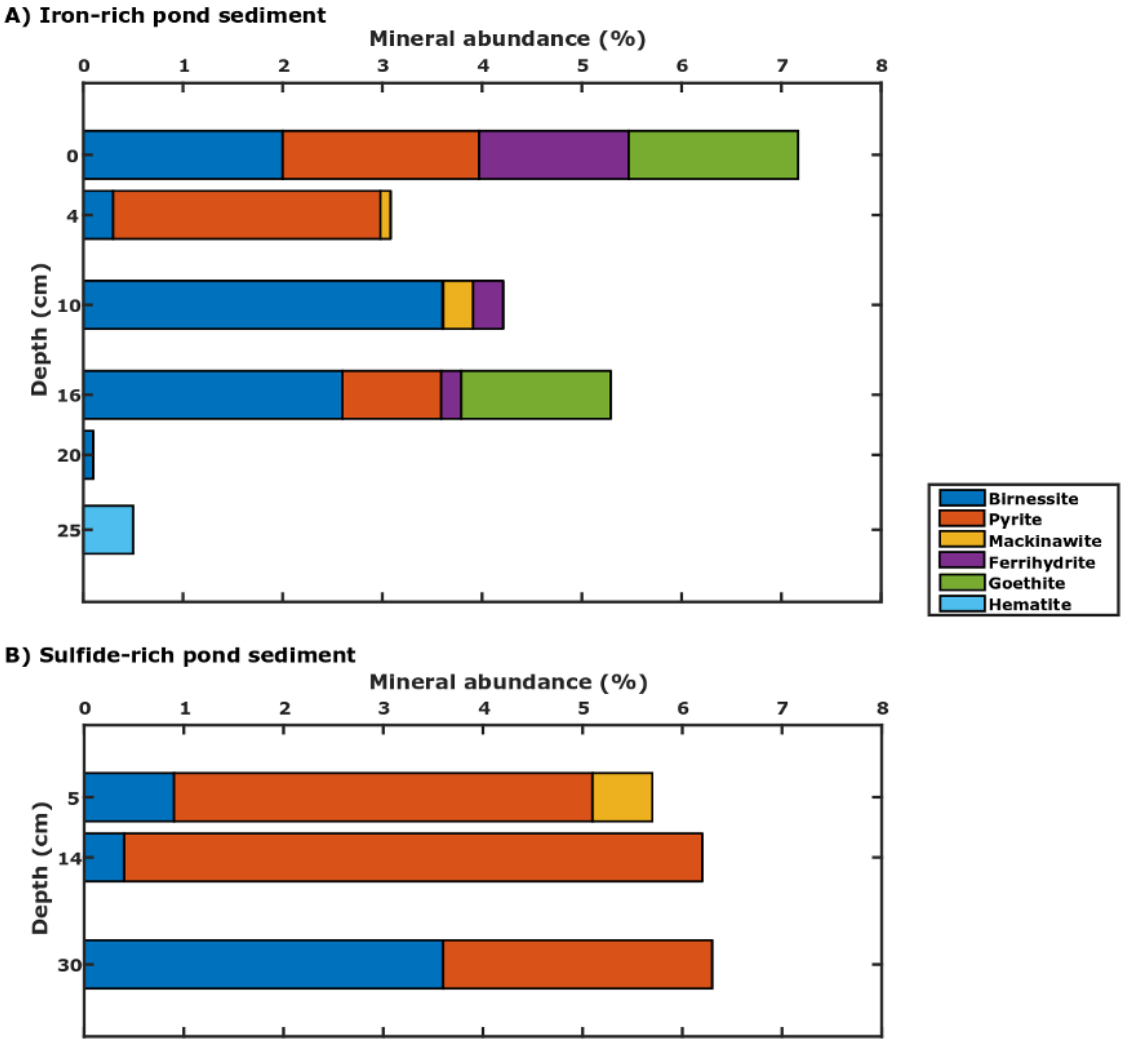

Fig. 4.4 - *Rietveld analysis of XRD mineralogical data for pond sediments analysed at various depths in the (a) iron-rich pond sediment and (b) sulfide-rich pond sediment. Only Fe and Mn oxides are shown here (full mineralogical assemblage is given in Table 4.1). Abundances are corrected for the removal of evaporitic salt minerals ($MgSO_4$ and KCl) which form during the drying out of residual porewater.*

Depth (cm)	DoC	Quartz	Halite	Illite	$MgSO_4$	Pyrite	Birn.	Mack.	Ferri.	Goet.	KCl	Hem.
Sulfide-rich pond												
5	26.72	45	32.4	16.1	2.7	2.7	0.6	0.4	0	0	0	0
14	26.53	51.3	22.6	21.3	0	4.5	0.3	0	0.01	0	0	0
30	29.62	54.5	5.9	33.8	0	2.5	3.4	0	0	0	0	0
Iron-rich pond												
0	21.57	37.1	28.6	28.9	0	1.4	1.4	0	1.1	1.2	0.2	0
4	29.32	38.4	29	30.3	0	1.9	0.2	0.1	0	0	0	0
10	26.51	43.8	22.7	30.3	0	0.01	2.8	0.2	0.2	0	0	0
16	33.77	48	18.5	29	0	0.8	2.1	0	0.2	1.2	0.3	0
20	40.16	63.7	10.5	25.7	0	0	0.1	0	0.01	0	0	0
25	39.9	78.8	0.1	20.7	0	0	0	0	0	0	0	0.5

Table 4.1 *Summary of identified minerals from XRD analysis. Estimated proportions for each depth point are conducted using Rietveld analysis for a best fit to the data and are given in percentage proportion. (Abbreviations: DoC = Degree of crystallinity, Birn. = Birnessite, Mack. = Mackinawite, Ferri. = Ferrihydrite, Goet. = Goethite and, Hem. = Hematite)*

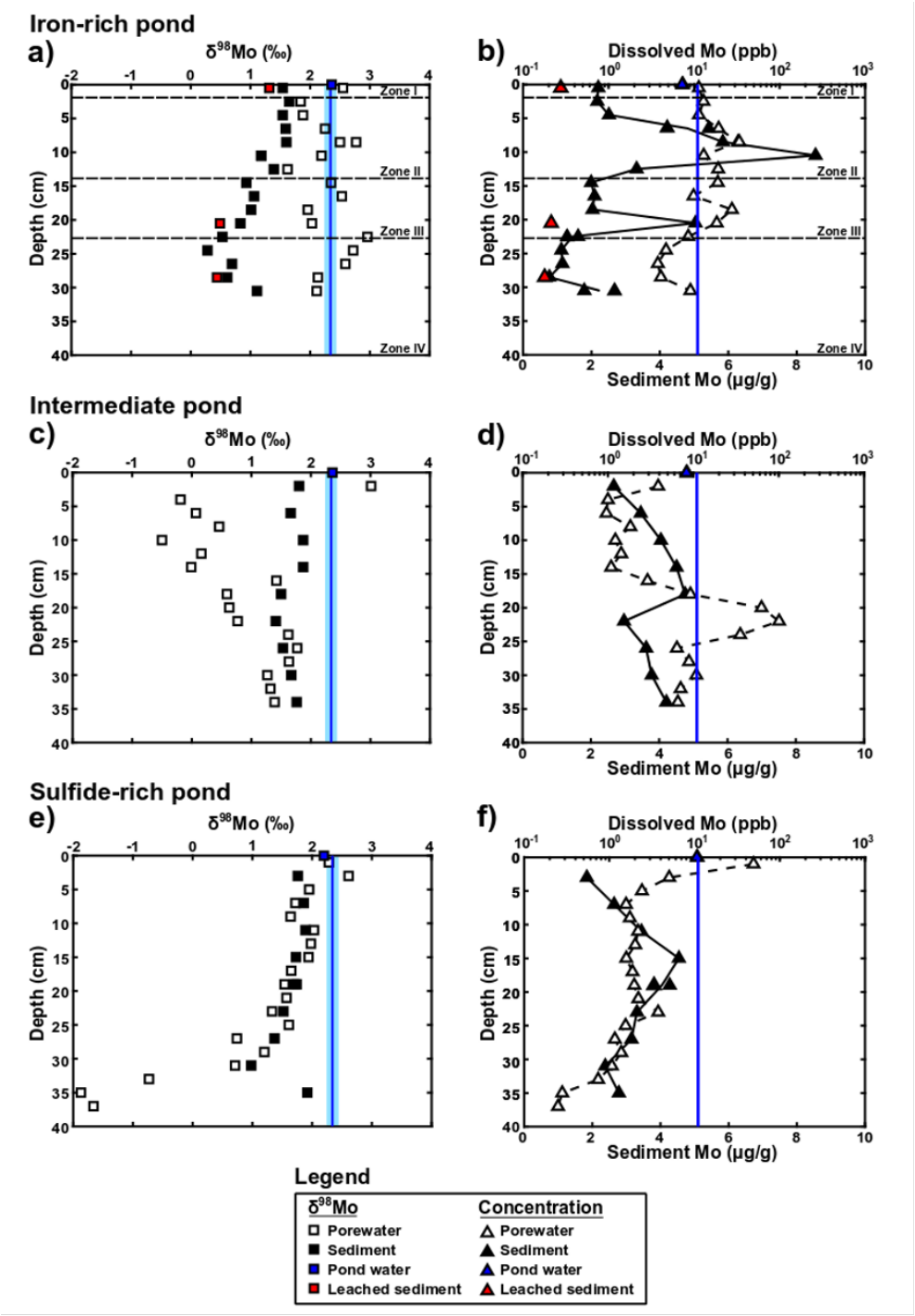

Fig. 4.5 - *Composite plot for all Mo concentration and isotope data from the iron-rich, sulfide-rich and intermediate pond sediments. For all plots, the solid blue line indicates typical seawater values and the shaded light blue line refers to the uncertainty on the seawater $\delta^{98}Mo$ value (±0.10‰) (Nägler et al., 2014). Uncertainty on $\delta^{98}Mo$ of the samples is ±0.06‰ which is within the area of the sample squares. Sediment and porewater $\delta^{98}Mo$ from the (a) iron-rich pond, (c) intermediate pond and, (e) sulfide-rich pond. Leached sediments were sediment samples treated with 0.1 M phosphate solution (red symbols). Sediment Mo content (bottom axis) and porewater Mo concentration (top axis) in the (b) iron-rich pond sediment, (d) intermediate pond sediment and, (f) sulfide-rich pond sediment.*

Sulfide-rich pond sediment

Porewater Mo concentration and δ^{98}Mo differs between the sulfide-rich core and the intermediate core despite both having high concentrations (up to 10 mM) of aqueous sulfide and similar porewater sulfide profiles. In the sulfide-rich core, porewater Mo concentration decreases from 40 ppb at the surface to <1 ppb at 35 cm (Figure 4.5f). Concurrently, porewater δ^{98}Mo also decreases from 2.2‰ to -2.0‰, a large range encapsulating the range of δ^{98}Mo in nearly all known environmental samples (Figure 4.5e).

In the intermediate core, porewater Mo concentration drops below 3 ppb and mean δ^{98}Mo is 0.00±0.50‰ between 4 and 14 cm (Figure 4.5c,d). From 15–25 cm, there is a large increase in porewater Mo concentration to ∼101 ppb (over 8x that of seawater). This increase is associated with an increase in porewater δ^{98}Mo to 0.5–1.5‰. Below this depth, porewater Mo concentration decreases to 8 ppb with a δ^{98}Mo of 1.4‰. There is a similar sedimentary content (4 μg/g) of Mo at 15–20 cm in both the sulfidic and intermediate cores. Sediment δ^{98}Mo ranges from 0.98–1.92‰ (mean = 1.64‰) and 1.41–1.87‰ (mean = 1.67‰) in the sulfide-rich core and intermediate core respectively (Figure 4.5c,e).

4.4 Discussion

In this discussion, I first consider the chemical reactions and Mo isotope fractionation in the iron-rich pond sediment. I then compare the geochemistry of the two ponds termed 'sulfide-rich' and 'intermediate', which contain comparable levels of porewater sulfide. If pond sediment chemistry is changing from initially iron-rich to sulfide-rich as previously hypothesised, there is a chance that the two different sulfide-containing pond sediments may capture different stages in this transition. Finally, I compare sediment δ^{98}Mo in the iron-rich pond sediment with the sulfide-rich pond sediment to understand the role of diagenesis on the sediment δ^{98}Mo.

4.4.1 Molybdenum behaviour in the iron-rich pond sediment

Four different redox zones are found in the iron-rich pond sediment; the colour in each zone is controlled by the mineralogy of iron in the sediment which, in turn, relates to the overall redox state in each of the zones (Figure 4.2, Figure 4.3). Differences in porewater and sediment Mo and their corresponding δ^{98}Mo track these redox zones closely (Figure 4.5a,b). At all sampled depths, porewater δ^{98}Mo is higher than sediment δ^{98}Mo.

Since dissolved sulfide concentrations are less than 1 μM in the iron-rich pond sediment, the dominant aqueous Mo species present in these iron-rich sedimentary porewaters will

be MoO_4^{2-} (Erickson and Helz, 2000). High dissolved Fe^{2+} concentrations prevent the accumulation of aqueous sulfide in these sediments as any sulfide generated through transient microbial sulfate reduction will be rapidly titrated by the excess dissolved iron to form iron sulfide species (Canfield et al., 1992). I surmise that Fe-oxides are likely to be the species which scavenge the majority of MoO_4^{2-}, despite the presence of Mn-oxides, because the sedimentary content of Fe is 500 times higher than Mn (Figure 4.2). Additionally, sedimentary δ^{98}Mo increases with decreased dissolved Mn concentrations (r^2 = 0.819)—the opposite direction to what would be expected if Mn oxides were influencing δ^{98}Mo (Figure 4.6) (Wasylenki et al., 2011). The following sections describe the potential reactions occurring in each of the sedimentary zones visible in Figure 4.3a.

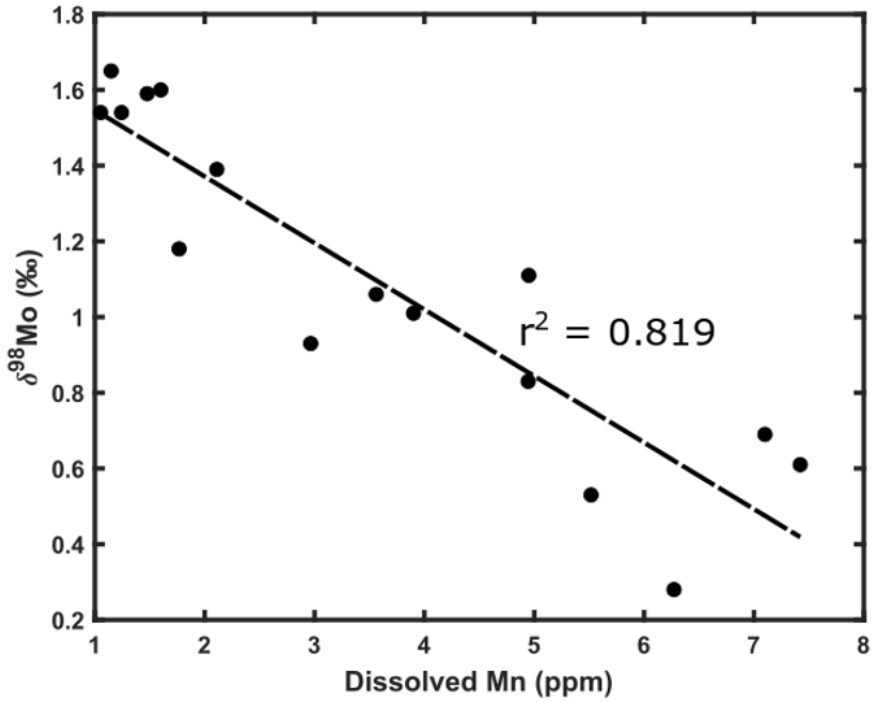

Fig. 4.6 - *Cross-plot of dissolved porewater Mn concentration (ppm) against the δ^{98}Mo of the sediment (‰). Dashed line shows a linear regression of the data. r^2 shown on the plot.*

Zone I: Surface sediment

At the sediment surface (0–2 cm depth), the reaction of ferrous iron with oxygen produces a reddish, iron oxide rich layer comprising minerals such as ferrihydrite and goethite (Zone I – Figure 4.3a, Figure 4.4a). The MoO_4^{2-} ion from seawater, in the overlying pond water, will be adsorbed as a polymolybdate complex onto these minerals at the sediment-water interface

(Wasylenki et al., 2011). Adsorption to Fe oxides is supported by the fact that the phosphate-stripped sediments (removing the adsorbed fraction from sediments) contain significantly (∼50%) less Mo than the same sample that was only digested in aqua regia. Furthermore, the $\Delta^{98}Mo_{PW-Sed}$ = 1.0‰ in Zone I is similar to the Mo isotope fractionation factor during adsorption of Mo to ferrihydrite (1.11 ± 0.15‰, (Goldberg et al., 2009)) and is similar to the offset recorded by surface ferruginous sediments underlying Peruvian seawater (between 0.82 to 1.04‰ lower than seawater δ^{98}Mo) (Scholz et al., 2017). Regular flushing of pond water with seawater prevents any increase in δ^{98}Mo of the pond water by isotopic distillation, so the pond water retains a δ^{98}Mo signature similar to that of seawater. I therefore expect the surface sediment δ^{98}Mo would have a consistent offset from pond water δ^{98}Mo through time.

Zone II: Bioirrigated portion of sediment

Mineralogical analysis (XRD) suggests that the sediment in Zone II, beneath Zone I, contains significant concentrations of pyrite and mackinawite (Figure 4.4a), staining the sediment black (Figure 4.3a). Iron redox cycling is facilitated in the sediment by the bioirrigation of burrowing macrofauna (See *Section 2.4.2* for a full description of the process); evidence for this cycling comes from the presence of amorphous iron (oxyhydr)oxides (e.g. ferrihydrite (Figure 4.4 – 10 cm)) around the lining of worm burrows (Figure 2.12). This process gives the geochemical impression that iron reduction is limited since porewater Fe^{2+} is lower in Zone II (Figure 4.2c). I propose that MoO_4^{2-} tracks this iron cycle as it would be recurrently desorbed and reabsorbed onto Fe^{3+}-containing minerals which are being reduced and then reoxidised respectively (Figure 4.7). This zone has a constant sediment δ^{98}Mo (∼1.4‰), similar to the surface sediment, implying that the molybdate ion adsorbed to the sediment phase is effectively 'well mixed'. This suggests that the residence time of the molybdate ion in the Zone II porewater is much shorter than the sedimentation rate, or other changes to the sedimentary redox zonation.

The higher sedimentary Mo observed in Zone II (Figure 4.5b) occurs as a result of this iron redox cycling. Below Zone II, the absence of bioirrigation means that there is no mechanism to reoxidise Fe^{2+} and therefore less Fe^{3+}-containing minerals are present to adsorb any desorbed molybdate. As desorption of molybdate is greater than adsorption of molybdate in Zone III, there will be a net transfer of molybdate from the sediment phase to the dissolved phase. This dissolved porewater molybdate will diffuse upwards into Zone II, where the greater presence of Fe^{3+}-containing minerals would re-adsorb it and thus concentrate sedimentary Mo. This is a more reasonable explanation for the peak of sedimentary Mo in Zone II than such a large change in the Mo capture rate at the sediment surface with

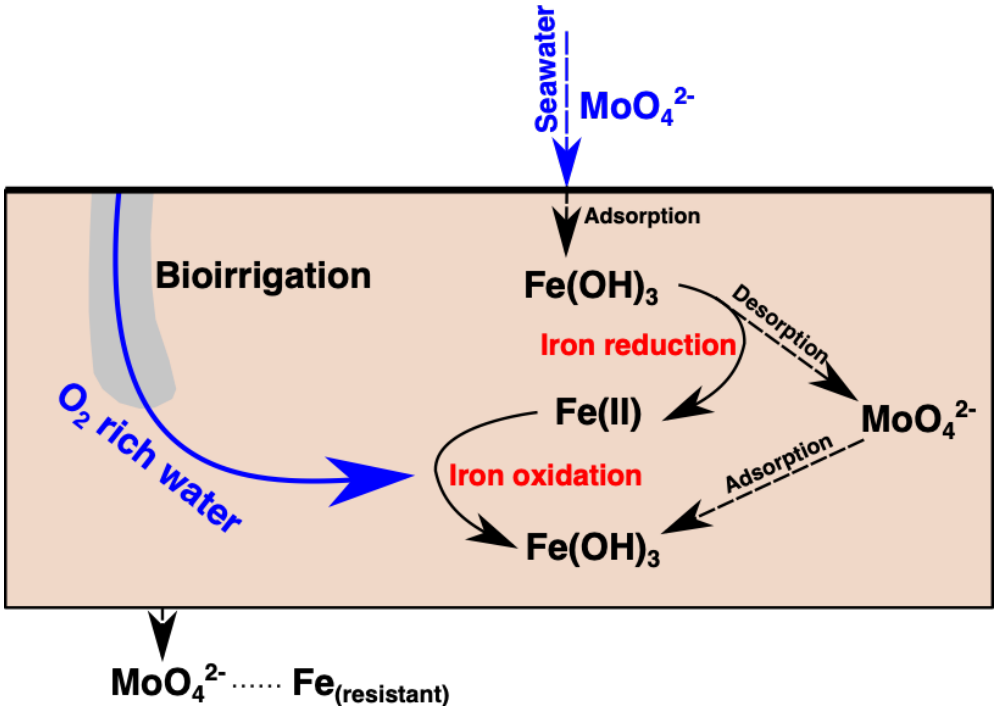

Fig. 4.7 - *Schematic of processes affecting Mo behaviour in Zone II of the iron-rich pond sediment. Molybdate is directly adsorbed from seawater onto iron and manganese oxides. When sedimentary Mo reaches Zone II, the molybdate ion will be desorbed and resorbed onto the Fe^{3+} minerals (e.g. $Fe(OH)_3$) as they are dissolved and re-precipitated respectively. This active iron cycling is set up due to bioirrigation caused by worms in the sediment sub-surface. Only molybdate adsorbed to species which are not bioavailable for iron reduction will be buried below Zone II into Zone III, hence sedimentary Mo content becomes enriched in Zone II.*

time. This process is particularly interesting since high sedimentary Mo contents are most commonly associated with euxinic conditions, although some combination of environmental conditions have been previously observed to produce increased Mo content in the absence of aqueous sulfide (Scholz et al., 2017). When corrected for porosity (Figure 3.1), the high sedimentary Mo content in Zone II—in the absence of aqueous sulfide—is comparable to the enrichments of Mo in geological samples recording euxinic environments. This porosity correction is necessary since the sediment contents reported in this chapter correspond to wet, unconsolidated sediments as opposed to the dry rock powders reported in rock record. I acknowledge that in order for these elevated sedimentary Mo contents in the salt marsh sediments to be preserved however, there would have to be some mechanism (such as an increase in the sedimentation rate) which would prevent sedimentary Mo from being affected by further iron cycling.

Zone III: Sediment beneath the zone of bioirrigation

In Zone III, the reduction of Fe^{3+}-containing minerals causes the release of adsorbed molybdate to the porewater, where it can subsequently diffuse away. This process is observed in the sharp decline of sedimentary Mo content between Zones II and III (Figure 4.5b). I suggest that the δ^{98}Mo of the remaining sediment is lower in this zone as the more labile, or microbially accessible, Fe^{3+} phases are first reduced, leaving behind Fe^{3+} phases which are more crystalline and resistant to bacterial iron reduction. There is a notable change in the Fe mineralogy with depth, from a ferrihydrite-goethite rich assemblage (less crystalline) at ~15 cm depth, to one dominated by hematite (more crystalline) at ~25 cm (Figure 4.4a). Less crystalline iron minerals, such as ferrihydrite ($\Delta^{98}Mo_{Fluid-Mineral}$ = 1.1‰) typically have higher δ^{98}Mo than more crystalline iron minerals, such as hematite ($\Delta^{98}Mo_{Fluid-Mineral}$ = 2.2‰) (Goldberg et al., 2009). The decrease in sediment δ^{98}Mo from Zone II to Zone III is therefore readily explained by this change in Fe mineralogy.

Zone IV: end of pond influenced sediment

The gravelly texture of Zone IV suggests that this may be the onset of the glacially derived material that underlies the silty muds characteristic of the salt marsh sediment at this location (Bristow et al., 1985). In this zone, the sediment δ^{98}Mo increases with depth whereas the porewater δ^{98}Mo decreases. These changes could be due to the presence of less crystalline Fe minerals (Goldberg et al., 2009), though this is not supported by XRD data (Figure 4.4a, Table 4.1). Porewater δ^{98}Mo may also be influenced by mixing with some groundwater flow below Zone IV. The presence of subsurface flows beneath salt marsh sediment has been

suspected but the nature of the fluid remains enigmatic (Antler et al., 2019; Hutchings et al., 2019; Mills et al., 2016).

4.4.2 Molybdenum behaviour in sulfide-rich pond sediment and intermediate pond sediment

Lower Mo concentrations in the porewaters of sulfide-rich ponds are explained by the rapid thiolation of molybdate species with aqueous sulfide and the subsequent scavenging of these thiolated species (Equation 4.2). Other than a near-surface difference, the deeper porewater aqueous sulfide concentrations are similar in both the intermediate and sulfide-rich pond sediments, meaning sulfide concentrations alone would not allow us to identify geochemical differences between these two pond sediments (Figure 4.2c).

Model to test the effect of an Fe-Mo-S mineral phase on porewater Mo concentrations

The chemical reactions sequestering Mo in sediment where aqueous sulfide is present in the porewater are debated (Helz and Vorlicek, 2019). One posited phase which could host Mo in such sediments is an Fe-Mo-S mineral with the empirical formula $FeMoS_4$ (*jordisite*), a phase which has been identified using X-ray absorption spectroscopy (Vorlicek et al., 2018). To test the likelihood of $FeMoS_4$ as a host phase, I used the model described in Helz et al. (2011) to predict porewater Mo concentrations if porewater Mo is assumed to be in equilibrium with FeS and an Fe-Mo-S mineral phase. The model uses measured values of ionic strength, Ca and Mg activity, total dissolved sulfide and the pH of the solution to predict dissolved Mo concentrations, as has been previously done in lake environments (Helz et al., 2011). This model is valid for these sedimentary environments if it is assumed that the rate of transport of Mo, thought to be mostly diffusive, is slower than the thermodynamics needed for the formation of of the Fe-Mo-S mineral phase.

Porewater Mo behaviour in sulfide-rich pond sediment

The model predicts porewater Mo concentrations similar to the measured values between 5 and 25 cm in the sulfide-rich pond sediment (Figure 4.8a). This match coincides with a portion of the sediment core where sediment δ^{98}Mo and porewater δ^{98}Mo are very similar (Figure 4.5e). If the model is correctly predicting that porewater Mo in this part of the sediment core is being controlled by solubility with an Fe-Mo-S mineral phase, then the similarity between the sediment and porewater δ^{98}Mo can be explained in one of two ways. First, if there is an Mo isotope fractionation factor associated with this chemical equilibrium,

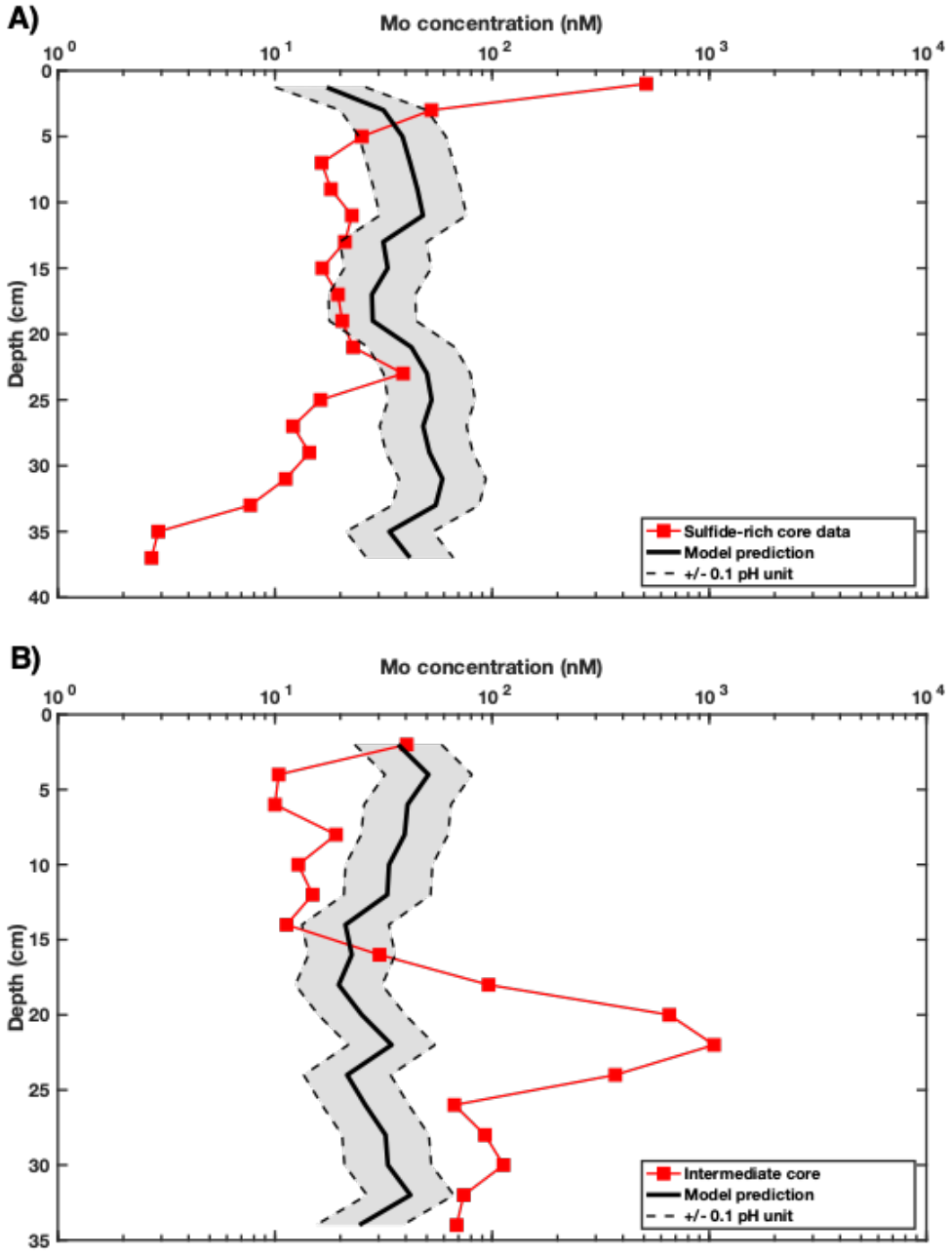

Fig. 4.8 - *a) Calculation of Mo concentration in porewaters using the model described in Helz et al. (2011) for aqueous systems in equilibrium with an Fe-Mo-S phase within (a) the sulfide-rich core and (b) the intermediate core. Ionic strength, Ca and Mg activities, pH and sulfide concentrations are used to predict porewater Mo concentrations. Error bars display model output assuming 0.1 pH uncertainty, since the pH determination had the largest source of measurement error in the model. For full model details, see Tables E.27 and E.28 and Helz et al. (2011).*

dissolved Mo in association with an Fe-Mo-S mineral phase could have a δ^{98}Mo value fortuitously similar to the bulk sediment δ^{98}Mo. This would require other Mo-hosting phases to be present in the sediment which were not interacting with the porewater Mo that would prevent the sediment δ^{98}Mo from changing significantly. An alternate explanation is that when dissolved Mo is controlled by association with an Fe-Mo-S mineral phase, any mechanism which operates between the sediment and dissolved phase does so with negligible equilibrium isotopic fractionation. For this to be true, equilibrium isotopic fractionation would have to be sufficiently slow to prevent an isotopic offset being generated between porewater and sediment. This, combined with rapid dissolution and re-precipitation of the Mo species at various nucleation points, could prevent significant net isotopic fractionation. While the specifics of this mechanism are not known, the data presented here suggests that that in environments where porewater δ^{98}Mo follows sediment δ^{98}Mo closely with depth, this may reflect a system where porewater Mo is in chemical and isotopic equilibrium with an Fe-Mo-S phase.

Since pH in the model has a disproportionately large role in determining Mo concentration, the model overestimates the amount of dissolved Mo present below 25 cm depth (Helz et al., 2011) (Figure 4.8a). The low concentrations ($\sim$0.5 ppb) of measured dissolved Mo below 25 cm depth have the lowest δ^{98}Mo measured in this study and may reflect the fluctuations of the depth of the redox boundary between iron reduction and sulfate reduction. Deeper sediments recovered from sulfide-rich ponds contain a boundary where aqueous sulfide becomes depleted and ferrous iron becomes present, presumably marking the end of the zone in which sulfate reduction outcompetes iron reduction (e.g. Figure 2.14). If this boundary depth changes during seasonal variations in the intensity of microbial sulfate reduction, the sulfide and ferrous iron concentration of porewater in this portion of the sedimentary column is likely to vary. The rapidity of these changes could produce intermediate thiomolybdates (MoO_3S^{2-}, $MoO_2S_2^{2-}$ and $MoOS_3^{2-}$) with lower δ^{98}Mo which could become scavenged and released later. This effect could temporarily produce porewater δ^{98}Mo lower than sediment δ^{98}Mo. The transient dissolution of such low concentrations of intermediate thiomolybdates would only minimally affect the recorded sedimentary δ^{98}Mo.

Porewater Mo behaviour in intermediate pond sediment

In the intermediate core at depths below 25 cm, similarity between porewater and sediment δ^{98}Mo suggests that porewater could be associated with an Fe-Mo-S-containing phase, similar to the sulfide-rich pond sediment (Figure 4.5c), however the model underestimates the dissolved Mo concentration (Figure 4.8b). This discrepancy may represent analytical errors on the measured pH which, as mentioned above, has a large effect on the predicted dissolved

Mo (Helz et al., 2011). There may also be ligands—not considered in the model—which stabilise thiomolybdate ions in the dissolved phase. At depths shallower than 25 cm the model completely fails to predict the dissolved Mo profile (Figure 4.8b). In particular, a peak in porewater Mo concentrations between 18–24 cm, over eight times seawater concentration, cannot be explained by solubility equilibrium with an Fe-Mo-S phase. I suggest that this peak of dissolved Mo reflects the release of adsorbed Mo during the sulfide-induced reductive breakdown of residual iron and manganese oxides which were formed when the pond sediment was initially iron-rich. The depth at which dissolved Mo concentrations are highest (23 cm) would therefore reflect the active dissolution zone. I expect that this dissolution front progresses downwards through the sediment as sulfide concentrations increase in the porewater from the surface sediment downwards with time. Upon release, the desorbed molybdate ion would be rapidly converted to thiomolybdate whilst concurrently diffusing away from the zone of peak dissolution. Consistent with this interpretation, δ^{98}Mo of the porewater at the depth where Mo concentrations are highest (0.63 ± 0.14‰) is similar to the sediment δ^{98}Mo signature recorded at the same depth (0.83‰) in the iron-rich pond sediment.

Removal of thiomolybdates through particle reactivity appears most effective from 5–15 cm in the intermediate core—the depth that coincides with the highest aqueous sulfide concentrations. As porewater Mo concentrations are below what is predicted for equilibrium with an Fe-Mo-S phase, I hypothesise that either the thermodynamic model for Fe-Mo-S breaks down at higher aqueous sulfide concentrations or some other species—possibly the iron-sulfide minerals present (Figure 4.4b) or organic matter—is helping to facilitate more effective sequestration of thiomolybdate. Two possible mechanisms could cause the low δ^{98}Mo in porewater located at this depth: (1) the dissolution of manganese oxides in the presence of aqueous sulfide which would release isotopically low (-0.7‰) molybdate or, (2) the formation of intermediate thiomolybdate species during a rapid change in sulfide concentrations. Since the porewater Mo concentrations are so low in this part of the sediment, even small changes in thiomolybdate speciation could cause a relatively large change in the δ^{98}Mo of the porewater. Regardless of the mechanism, the lower δ^{98}Mo of the porewater than that of the sediment suggests a temporal decoupling of the processes governing sediment and porewater isotopic compositions.

4.4.3 Bulk sediment Mo behaviour in pond sediments

Higher sedimentary Mo contents have been used to identify sulfidic environments in the geological record (Scott and Lyons, 2012). In this study, the total Mo content is not significantly different between iron-rich and sulfide-rich pond sediments (Figure 4.5b,d,f). This is because

ponds are relatively short-lived systems with seawater Mo being the only input. Therefore, even if there is a rapid uptake of Mo from the overlying pond water, there is not enough time to significantly capture Mo in the sulfide-rich sediments over their iron-rich counterparts. Whereas the iron-rich pond sediment contains a localised high content of sedimentary Mo from 5–15 cm due to active iron cycling (see above), sedimentary Mo is more constant with depth in the pond sediments containing aqueous sulfide. I hypothesise that this constancy is due to the redistribution of Mo as iron oxides are dissolved.

Sediment δ^{98}Mo in restricted basins with a water column containing >11μM dissolved H_2S, such as the Black Sea, have been shown to record the δ^{98}Mo of the input seawater flux (Neubert et al., 2008; Nägler et al., 2011). In these environments, where the water column above the sediment is restricted, isotopic distillation of the Mo in the water column causes water-column δ^{98}Mo to increase above typical seawater values (>2.8‰ in the Black Sea) and thus the sediment δ^{98}Mo evolves by Rayleigh fractionation to approach the initial seawater input value. For isotopic distillation of the water column to occur, the sequestration rate of Mo must therefore be greater than the rate in which fresh Mo (with a seawater δ^{98}Mo value) is replenished in the above water column. The short residence time (days–months) of the water column in the Norfolk ponds means that the seawater δ^{98}Mo is not recorded in the sediment δ^{98}Mo; instead, sediment δ^{98}Mo is more consistent with continental margin sediments where the overlying water column is less restricted (Poulson et al., 2006; Poulson-Brucker et al., 2009). The consistent replenishment of seawater to the pond prevents distillation of the pond water δ^{98}Mo signature (i.e. the replenishment rate is faster than the sequestration rate). The offset that is proposed to exist during sequestration of thiomolybdate species ($\sim$0.7‰) is therefore expressed, and the sediment δ^{98}Mo remains lower than the seawater δ^{98}Mo (Nägler et al., 2011). It is therefore likely, that the δ^{98}Mo of sediment in contact with aqueous sulfide lies on a continuum between 1.6‰ and 2.3‰, with lower δ^{98}Mo associated with more regular flushing of the overlying water (Brüske et al., 2020; Dickson et al., 2014; Dickson, 2017).

4.4.4 Early diagenetic overprinting of sediment δ^{98}Mo

The average sediment δ^{98}Mo is higher in the sulfide-rich (1.65‰) and intermediate sediment core (1.67‰) compared to the iron-rich sediment core (1.10‰). Given that all ponds in the salt marsh are hypothesised to have had initially iron-rich sediment chemistry, I suggest that the δ^{98}Mo of the pond sediment reflects the degree of diagenetic overprinting caused by exposure to aqueous sulfide contained in the porewater over time. As described above, when aqueous sulfide becomes present in porewaters, molybdate ions previously adsorbed to Fe-oxides are released as the iron minerals are reductively dissolved (creating localised peaks

in pore fluid Mo). As the desorbed molybdate diffuses away and is recaptured elsewhere in the sediment column, the low δ^{98}Mo associated with the adsorption of Mo to iron minerals is distributed across the sediment column. As the pond sediment ages, the presence of aqueous sulfide will continually capture Mo from pond water with a higher δ^{98}Mo than when the pond sediment contained no aqueous sulfide. The redistribution of sedimentary Mo during the breakdown of iron minerals acts as a mechanism to mix Mo throughout the sediment column and accelerates the isotopic overprinting process. This overprinting process will continue until the original lower pond sediment δ^{98}Mo present when the pond sediment was iron-rich is completely diluted by the Mo captured in the presence of aqueous sulfide (Figure 4.9). At this point, a constant sediment δ^{98}Mo profile with depth corresponding to the capture of thiomolybdate species (1.6–1.8‰) would be expected. This mechanism can explain the δ^{98}Mo measured in sediments in the sulfide-rich and intermediate cores. Above 15 cm, a constant δ^{98}Mo reflects the capture of thiomolybdate species. Below 15–20 cm in both sediment cores, the sediment δ^{98}Mo is lower by roughly 0.3–1‰. This likely reflects mixing between residual molybdate ions adsorbed to iron oxides and the newly added tetrathiomolybdates and intermediate thiomolybdate species.

These results suggest sedimentary δ^{98}Mo can be overprinted if the redox chemistry of the sedimentary system changes during early diagenesis. Original redox conditions which would be classified as 'ferruginous' are overprinted when porewaters become enriched in aqueous sulfide. The implication of this diagenetic change is that geochemical conditions recorded at the time of deposition are not preserved if there is an authigenic redistribution of the Mo and/or a change in the mechanism which captures dissolved Mo into sediment. East Anglian salt marsh ponds appear very susceptible to this geochemical transition, likely due to the close energy availability between sulfate reduction and iron reduction at circumneutral pH (Bethke et al., 2011).

4.5 Conclusions

These salt marsh systems provide a well characterised redox environment to study Mo behaviour. High resolution measurements of both porewater and sediment Mo are used to isolate individual mechanisms affecting Mo behaviour during diagenesis. Porewater Mo tracks diagenetic redox zones clearly in iron-rich pond sediments, and lower (0.5–1‰) sedimentary δ^{98}Mo signatures are recorded at depth. Bioirrigation in these ponds can enrich the sediment with Mo and extend the δ^{98}Mo signature acquired at the sediment-water interface to sediments as deep as the limit of bioirrigation.

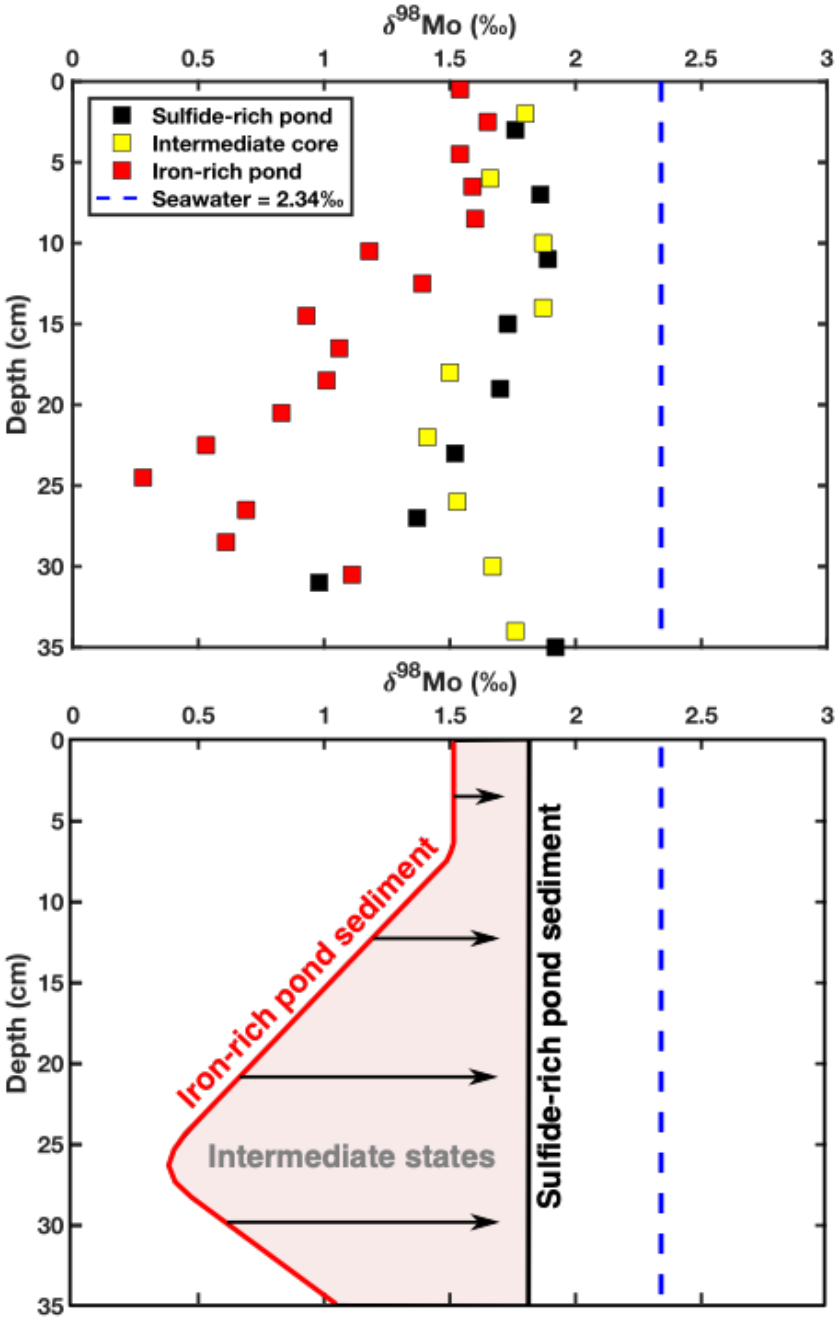

Fig. 4.9 - *Composite sediment $\delta^{98}Mo$ data and accompanying schematic showing the effect of diagenetic overprinting on the sedimentary $\delta^{98}Mo$ signature. a) Comparison of $\delta^{98}Mo$ in sediments from the three ponds. Blue dashed line represents seawater values. b) Schematic describing the temporal evolution of sediment $\delta^{98}Mo$ in pond sediments in East Anglian salt marshes. The sediment $\delta^{98}Mo$ profile follows the behaviour of iron-rich pond sediment (red solid line) until sulfate reduction becomes the dominant metabolism. At this point, the sediment $\delta^{98}Mo$ at all depths will become higher due to overprinting since sulfide-rich conditions sequester higher $\delta^{98}Mo$. Sediment $\delta^{98}Mo$ will therefore lie somewhere in the pink shaded zone (defined as intermediate states). Over time, overprinting of the sediment $\delta^{98}Mo$ will be complete, and a constant $\delta^{98}Mo$ will be expected around 1.7±0.1‰, a value typical of sediments with high aqueous sulfide in the porewater phase (Kendall et al., 2017).*

Differences in porewater Mo and its associated δ^{98}Mo reveal geochemical differences between two pond sediments with similar dissolved sulfide concentrations. In the intermediate pond sediment, porewater enrichments of Mo and decoupled porewater and sediment δ^{98}Mo suggest active redistribution of Mo as Fe and Mn oxides are broken down during diagenesis which releases the previously adsorbed molybdate ions. In sulfide-rich pond sediment, in the absence of reducible Fe and Mn oxides, the majority of Mo has already been sequestered as an Fe-Mo-S mineral phase so porewater Mo is controlled by solubility with this phase. This argument is supported by both predictions from the model described in Helz et al. (2011) and by similarities between sediment and porewater δ^{98}Mo occurring because of solubility equilibrium.

Sedimentary δ^{98}Mo is higher in pond sediments containing aqueous sulfide than in pond sediments containing ferrous iron. Given that iron-rich ponds transform to sulfide-rich ponds, differences in δ^{98}Mo must reflect overprinting of the sediment Mo. This effect is expected to be more rapid where residence time of Mo is shorter in the overlying water column. I suggest that soft sediment diagenesis needs to be considered when interpreting δ^{98}Mo in past and present systems.

4.6 Implications for further chapters

This chapter provides proof of concept that a high-resolution record of porewater and sediment in these pond sediments can elucidate how isotope systems behave under certain redox conditions. Rather than being directly influenced by redox conditions in the sediment, the behaviour of Mo instead depends on the redox cycling of Fe, Mn and S. As such, Mo appears to be capable of tracing the process of redox change in a sedimentary environment (i.e. the breakdown of iron oxides by sulfide) that has not been possible using solely sulfur-species measurements.

The behaviour of Cr (examined next in **Chapter 5**) differs from Mo in that Cr reacts directly to redox changes in the sedimentary environment and is largely associated with Fe mineralogy. As such, by understanding both Mo and Cr, I should be able to elucidate the behaviour of two of the most widely used paleoredox proxies in the same sedimentary environment.

Chapter 5

The Behaviour of Chromium in Salt Marsh Pond Sediments

5.1 Introduction

5.1.1 Chapter outline

In this chapter, I will explore the fate and behaviour of Cr in these salt marsh sediments, building on the knowledge I gained in Chapter 2 and Chapter 4. As the Cr isotopic composition of sedimentary rocks is increasingly being applied as a paleoredox proxy, interaction between the oceanic reservoir and sediments are of fundamental importance if we wish to infer the processes which govern the final Cr isotope signature recorded in sedimentary rocks. A particular lack of understanding hitherto is how δ^{53}Cr may be affected during early diagenesis, which may have implications for how we interpret the paleoredox record. All δ^{53}Cr values reported in this chapter were measured using the methods developed in **Chapter 3**.

5.1.2 Chromium isotope system

The introduction for this chapter will summarise the literature on the geochemistry of Cr, the uses of the Cr isotope system and the cycling of Cr in natural systems. When referring to an isotopic fractionation factor (ε) in this chapter, I am referring to the difference between the δ^{53}Cr of the product and the δ^{53}Cr of the reactant (Equation 5.1). This can be related to another commonly used term in isotope literature—(α) (Equation 5.2). This term expresses the magnitude of an isotopic effect with reference to the raw ^{53}Cr/^{52}Cr ratios of the product and the reactant (Equation 5.3).

$$\varepsilon = \delta^{53}Cr_{Product} - \delta^{53}Cr_{Reactant} \tag{5.1}$$

$$\varepsilon = (\alpha - 1) \times 1000 \tag{5.2}$$

$$\alpha = \frac{\left(\frac{^{53}Cr}{^{52}Cr}\right)_{Product}}{\left(\frac{^{53}Cr}{^{52}Cr}\right)_{Reactant}} \tag{5.3}$$

There have been two main applications of the Cr isotope system so far: (1) using δ^{53}Cr in the rock record to infer past paleoredox conditions and (2), using δ^{53}Cr to trace Cr reduction in contaminated areas. The major appeal for the Cr isotope proxy is that isotopic fractionation occurs predominantly due to changes in the redox conditions of the environment, whereas other mechanisms (adsorption and dissolution) have relatively minor roles in isotope fractionation. This means that Cr isotope ratios are a powerful tracer of the redox behaviour of Cr, and thus the paleoredox conditions of an environment.

5.1.3 Chromium oxidation states in aqueous environments

Chromium exists predominantly in two oxidation states, Cr(III) (charge = +3) and Cr(VI) (charge = +6), depending on the pH and Eh conditions of a system (Figure 5.1) (Rai et al., 1989). Oxidised Cr (Cr(VI)) is soluble in oxidising aqueous conditions and forms one of three species: chromate (CrO_4^{2-}), dichromate ($Cr_2O_7^{2-}$) or hydrogen chromate ($HCrO_4^-$) (Kitchen et al., 2012), the relative proportions of which depend on the pH conditions of the solution (Palmer and Pulis, 1994). In contrast, Cr(III) is present in reducing conditions as species such as Cr^{3+}, $Cr(OH)_2^+$ and $Cr(OH)_3$; these species are largely insoluble and are readily adsorbed to common environmental solid surfaces (e.g. iron minerals and organic matter) (Rai et al., 1987). A small amount of Cr(III) can be solubilised if ligands—most commonly organic ligands—form a complex with the Cr(III) ion (Puzon et al., 2005).

5.1.4 Cr isotope fractionation associated with redox and non-redox processes

Chromium isotope fractionation associated with Cr(VI) reduction

The reduction mechanism of Cr(VI) to Cr(III) involves the transfer of three electrons and a coordination change of the atomic structure of the molecule. The equilibrium Cr isotopic

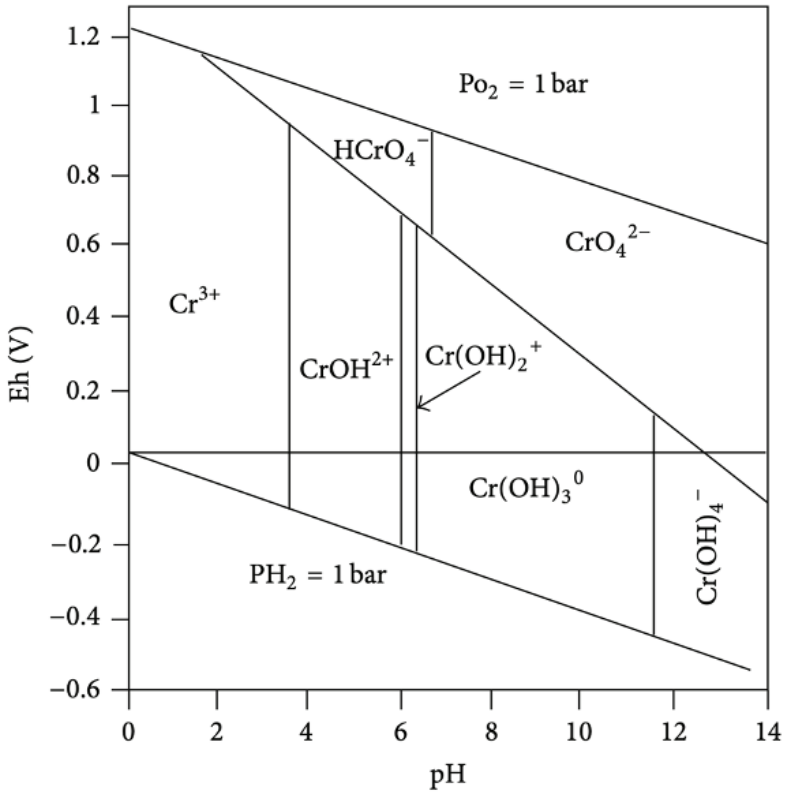

Fig. 5.1 - *Eh/pH diagram showing aqueous Cr speciation over a range of oxidation and pH conditions. This does not take into account the effect of environmental ligands other than the OH^- ion. Taken from Lukman et al. (2014).*

fractionation factor for Cr(VI) reduction, as determined through theoretical calculations, is large due to the stability of the Cr-O bonds in the (di)-(hydrogen)-chromate species (-6 to -7‰) (Schauble et al., 2004). However, for thermodynamic isotopic equilibrium, the forward and backward rates of the reaction must be equal but non-zero, thus the kinetic inhibition of the Cr(III) oxidation step makes equilibrium isotope fractionation largely unobtainable in environmental settings (Joe-Wong and Maher, 2020). Almost all changes in isotope fractionation observed during Cr(VI) reduction are therefore the result of kinetic isotopic fractionation—the process where a unidirectional chemical reaction subtly discriminates between the higher and lower mass isotopes. For Cr reduction, like the majority of elements, the lower mass ^{52}Cr forms slightly weaker Cr-O bonds in the chromate ion, thus these are preferentially broken over the ^{53}Cr-O bonds. Cr(III) products consequently have a lower δ^{53}Cr whilst the residual Cr(VI) has a higher δ^{53}Cr.

The direction of the kinetic isotope fractionation for Cr is the same as the theoretically predicted equilibrium isotope fractionation, but the magnitude is lower (Joe-Wong and Maher, 2020). There are however, large variations in the degree of Cr isotopic fractionation depending on the associated reductant (e.g. aqueous Fe(II) vs organic acids) which would suggest the mechanism of reduction differs among the various reductants (Table 5.1). In addition, the pH of the solution, the concentration of the Cr(VI) in the starting solution and the rate of reduction may all affect the observed isotope fractionation during Cr(VI) reduction (Døssing et al., 2011; Joe-Wong and Maher, 2020). Table 5.1 lists the intrinsic fractionation factors of the coupled reaction of Cr(VI) reduction with a variety of environmentally applicable reductants and conditions from the literature.

Chromium isotope fractionation associated with Cr(III) oxidation

The isotopic fractionation associated with the process of Cr(III) oxidation to Cr(VI) is less well characterised than that associated with the Cr(VI) reduction mechanism (Bain and Bullen, 2005; Zink et al., 2010). Isotope fractionation factors vary largely, with oxidised Cr(VI) typically having a higher δ^{53}Cr (Zink et al., 2010). This has been suggested as the reason for the low δ^{53}Cr measured in weathering profiles in terrestrial environments (D'arcy et al., 2016; Frei et al., 2014).

Effect of non-redox reactions on Cr isotope fractionation

Adsorption of Cr has been suggested to impart no isotope fractionation (Ellis et al., 2004). Recent studies have identified that a small isotopic fractionation is associated with dissolution of Cr from mineral lattices (Saad et al., 2017).

Reductant	ε (‰)	Reference
Magnetite	-3.5	(Ellis et al., 2002)
Organic rich sediments	-3.5	(Ellis et al., 2002)
$Fe(II)_{aq}$, pH = 4.0–5.3	-4.2	(Kitchen et al., 2012)
Fe(II) (1.15 mM), pH = 7	-3.6	(Døssing et al., 2011)
Fe(II) doped goethite (345 μM Fe(II))	-3.9	(Basu and Johnson, 2012)
FeS	-2.1	(Basu and Johnson, 2012)
Dissolved Fe(II) + Fe minerals	-1.8	(Bauer et al., 2018)
Assorted organic acids (humic, fulvic, mandelic)	-2.98 to -3.14	(Kitchen et al., 2012)
Pseudomonas fluorescens and *Shewanella oneidensis*	-1.58 to -4.90	(Zhang et al., 2018)
Multiple bacteria strains	-2.17 to -3.14	(Basu et al., 2014)

Table 5.1 *Table of fractionation factors (ε) for common environmental minerals and organic acids, and environmentally common bacteria.*

5.1.5 Uses of the chromium isotope system

The use of chromium as a paleoredox proxy

Since isotopic fractionation of Cr is primarily caused by redox conditions in an environment, the use of δ^{53}Cr in the rock record has been posited as a way of tracking redox conditions through time. Figure 5.2 illustrates the theory behind the use of δ^{53}Cr as a paleoredox proxy for atmospheric oxygen (Frei et al., 2009). Manganese oxides, only present above a specific threshold of atmospheric oxygen concentration, are assumed to be the major oxidant of Cr(III) in the terrestrial zone (Planavsky et al., 2014). If we consider conditions of the mid-Proterozoic—where there was atmospheric oxygen but anoxic, ferruginous oceans—during weathering, oxidation and transport to the ocean, removal of partially reduced Cr would cause the remaining Cr(VI) in rivers to have a higher δ^{53}Cr. When this high δ^{53}Cr dissolved Cr(VI) would have reached the ocean, the dissolved Fe^{2+} present would have quantitatively reduced and transferred Cr to marine sediments, preserving the isotopically fractionated signal acquired during transport. For this reason, Proterozoic banded iron formations and iron rich cherts were the first samples targeted for paleoseawater δ^{53}Cr over this period (Frei et al., 2009). In this interpretation, δ^{53}Cr the same as bulk silicate earth—such as during the Archaean—would be indicative of a lack of redox cycling on the planetary surface (as Cr(III) from silicates are mechanically brought to the seafloor). On the other hand, higher δ^{53}Cr values measured in rocks suggest the presence of partial reduction at the Earth's surface, removing low δ^{53}Cr material during transport—which is linked to an increase in atmospheric

oxygen. Chromium isotopes have been extensively used to estimate the timing of the rise of atmospheric oxygen during the great oxidation event (Babechuk et al., 2017; Frei et al., 2009), and the mid-Proterozoic (Crowe et al., 2013; Planavsky et al., 2014).

Contamination remediation

Industries including metal plating, chemical milling and compressor stations release significant quantities of Cr(VI) to the surrounding groundwater (Berna et al., 2010; Izbicki et al., 2012). Remediation of such sites is necessary as the soluble species of Cr(VI) are carcinogenic and toxic (Hausladen and Fendorf, 2017). As the Cr(III) ion is insoluble, and considerably less harmful than the Cr(VI) ion (Mertz, 1992), reduction is widely regarded as one of the most suitable remediation strategies, either through monitored attenuation with natural reductants or through the introduction of permeable reactive barriers (PRB) containing reductants (Szecsody et al., 2005).

Monitoring reduction in groundwater is required to understand the effectiveness of these remediation strategies. Measuring groundwater Cr concentration becomes problematic if natural sources of Cr mix with the contamination plume, obscuring the geochemical signal (Izbicki et al., 2012). Furthermore, measurements of Cr concentration do not give any information on the extent of reduction unless measurements are made at regular time intervals. The δ^{53}Cr of groundwater is a more suitable tracer of remediation techniques; variations in natural Cr concentrations can be constrained and effects of dilution can be deconvolved from the measure signal. Remediation monitoring in this way has been used at multiple contaminated sites (Berna et al., 2010; Izbicki et al., 2008, 2012). To further the effectiveness of Cr reduction monitoring using δ^{53}Cr, a better understanding is needed of the reduction mechanisms so that the effect of advective mixing between different Cr sources can be decoupled from solely Cr reduction effects. Furthermore, the effectiveness of reductants requires further refinement to understand when more aggressive remediation techniques are necessary for a site.

5.1.6 Environmental cycling of chromium

In the continental crust, chromium exists as Cr(III) hosted in oxide or silicate minerals or as primary minerals such as chromite ($FeCr_2O_4$) (Oze et al., 2004). The δ^{53}Cr of igneous silicate rocks is homogeneous, with a well-defined value of -0.12±0.1‰ (Schoenberg et al., 2008). Carbonate rocks provide a second terrestrial reservoir with much lower Cr concentrations, but typically with a positive δ^{53}Cr which is much more variable than the isotopic composition of Cr hosted in igneous rocks. Weathering of these rock reservoirs provides an input of Cr

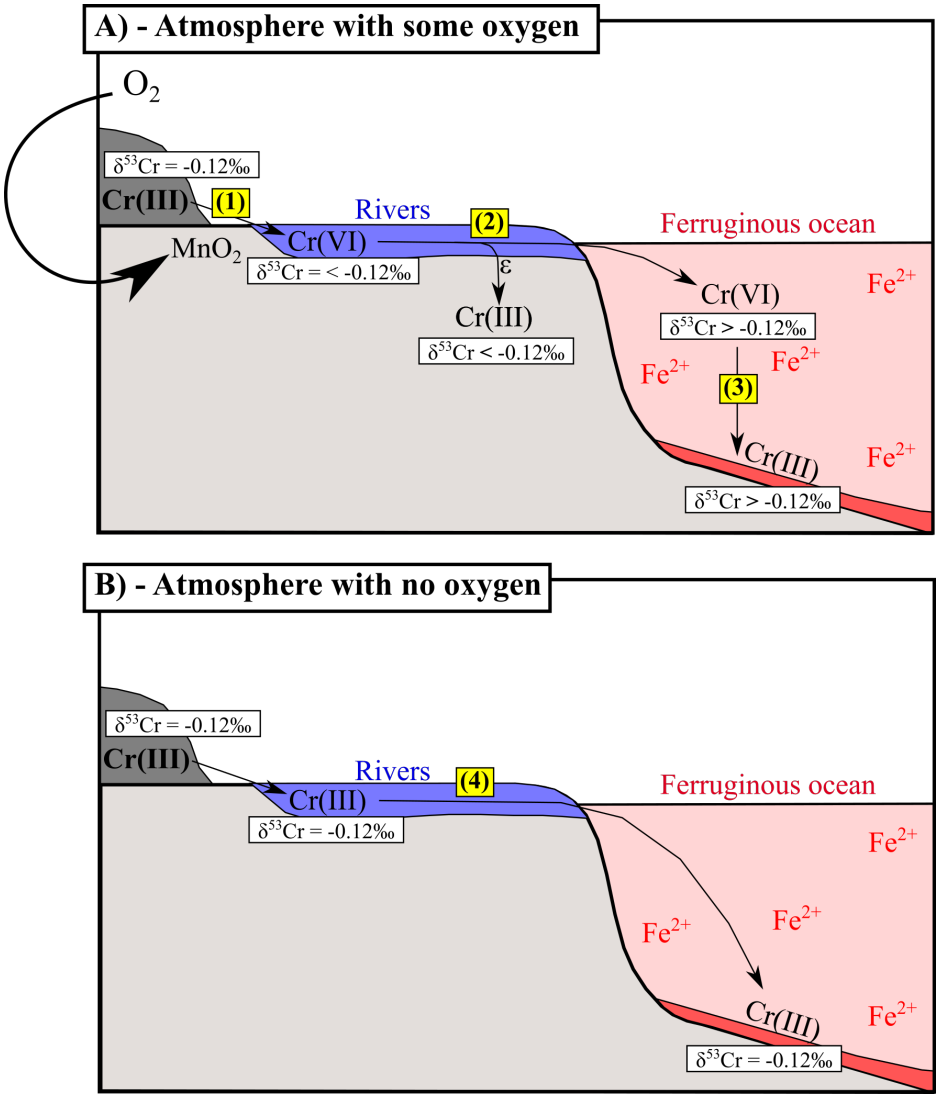

Fig. 5.2 *Theory behind the use of Cr as a paleoredox proxy for atmospheric oxygen. (A) Schematic showing environmental cycling under a mildly oxic atmosphere in the mid-Proterozoic. Process 1 – Weathering of Cr(III) and oxidation coupled to MnO_2 reduction produces Cr(VI) with a slightly higher $\delta^{53}Cr$. The presence of MnO_2 in a terrestrial weathering environment necessitates some threshold concentration of atmospheric oxygen (Planavsky et al., 2014). Process 2 – During transport (predominantly fluvial), partial reduction to Cr(III) causes low $\delta^{53}Cr$ to be deposited and a residual pool of higher $\delta^{53}Cr$ to exist as Cr(VI) in the river water which reaches the ocean. Process 3 – Upon entry to the ocean, Cr(VI) is quantitatively reduced to Cr(III) by the Fe^{2+}-rich conditions of the mid-Proterozoic, hence a higher $\delta^{53}Cr$ is recorded in marine sediments. (B) Schematic showing environmental cycling of Cr under an anoxic atmosphere. Process 4 – Small amounts of Cr(III) are mechanically weathered and transferred to the oceans. As a result, $\delta^{53}Cr$ in marine sediments under these conditions should equal bulk silicate earth values (-0.12‰).*

to rivers through dissolution and/or oxidation. Manganese oxides are the main oxidant of solubilised Cr(III) in the terrestrial zone (Oze et al., 2007) though it has been shown that H_2O_2 can potentially oxidise Cr(III) in anoxic, serpentinized environments (Oze et al., 2016).

Rivers deliver the majority (76–96%) of Cr to the oceans with dust, benthic, hydrothermal and groundwater sources comprising the remaining fractions (Bonnand et al., 2013; McClain and Maher, 2016). The Cr concentrations and associated δ^{53}Cr vary largely among different river systems as a result of lithology, distance and organic matter content ($\delta^{53}Cr_{Rivers}$ = -1.4‰ to +1.7‰) (D'arcy et al., 2016; McClain and Maher, 2016; Wei et al., 2020). In some estuaries, there has been evidence for conservative mixing between rivers and seawater (Goring-Harford et al., 2020), suggesting that rivers may directly transfer their δ^{53}Cr signatures to the ocean, whilst other studies suggest that alteration of δ^{53}Cr may occur during the fresh-water to salt-water transition (Sun et al., 2019).

Despite the differences in river water δ^{53}Cr, the δ^{53}Cr of the dissolved chromium in the ocean appears to be controlled by some other internal process. Initial measurements of oceanic δ^{53}Cr were only made recently due to the extremely low seawater Cr concentrations and showed conservative behaviour with depth in the Argentine Basin (Bonnand et al., 2013). Since these initial measurements, a number of studies suggest that there are large variations in both dissolved Cr concentration (1.2–6.5 nmol/kg) and in the δ^{53}Cr of seawater (+0.41‰ to +1.72‰)(Bonnand et al., 2013; Goring-Harford et al., 2020, 2018; Janssen et al., 2020; Moos and Boyle, 2019; Moos et al., 2020; Scheiderich et al., 2015) and that almost all samples lie on a logarithmic Cr concentration ln[Cr]/δ^{53}Cr relationship line (Figure 5.3) (Paulukat et al., 2016; Scheiderich et al., 2015). The fractionation factor (ε) can be graphically obtained by the following equation:

$$\delta^{53}Cr_{SW} = \varepsilon \ln[Cr] \tag{5.4}$$

These studies suggest that the behaviour of Cr in seawater appears to be controlled to first order by a process with a Cr isotope fractionation factor of -0.80±0.04‰; this fractionation remains consistent even in oxic estuaries (Sun et al., 2019). Deviations from this relationship typically occur only where there is significant freshwater dilution, such as in surface mixed layers (Frei et al., 2014; Scheiderich et al., 2015). Despite this consistent Cr isotope fractionation factor across global oceans, there is controversy over what process actually causes it. It was initially proposed to be the result of the reduction of Cr(VI) in oxygen minimum zones (OMZ). Studies conducted across OMZ boundaries, however, have reported no evidence of this Cr isotope fractionation associated with Cr(VI) reduction (Bruggmann et al., 2019). Another possibility could be the interaction of chromium with organic matter. Although Cr(VI) can be reduced on the surface of organic matter in the open

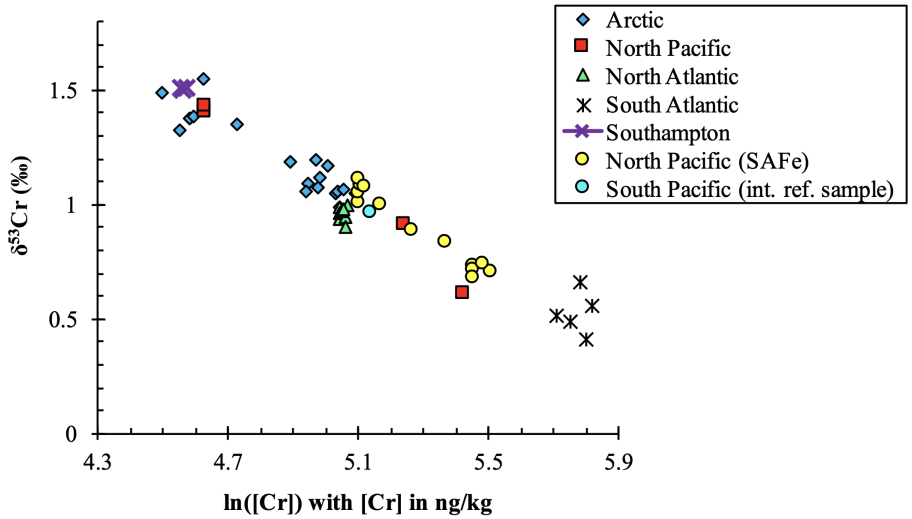

Fig. 5.3 *Relationship between Cr concentration and δ^{53}Cr in global oceans. Taken from Moos and Boyle (2019). Chromium concentration is given in the form ln[Cr] where [Cr] is chromium concentration*

ocean (Semeniuk et al., 2016), there is no proven case of Cr uptake in phytoplankton. At some locations, Cr displays nutrient-like characteristics, such as a degree of surface depletion (Moos and Boyle, 2019; Scheiderich et al., 2015), although other locations report chromium with conservative behaviour (Bonnand et al., 2013). Additionally, Cr does not show the increase from the N. Atlantic to Pacific that typical nutrient-like elements show.

This recently discovered variability of ocean δ^{53}Cr has created considerable complexities in whether sediments accurately record paleoseawater δ^{53}Cr on a global scale. Further complications arise when examining the mechanism behind how δ^{53}Cr is sequestered into sediments. These sedimentary sinks can be broadly divided into three categories: (1) the anoxic/suboxic sink, (2) the oxic sink and (3), the carbonate sink.

Suboxic and anoxic sediments

Reducing sediments typically contain the highest δ^{53}Cr (Bruggmann et al., 2019; Gueguen et al., 2016; Reinhard et al., 2013). Myriads of reductants exist in reducing environments (Fe^{2+}, H_2S, FeS), which ensure rapid drawdown of Cr from seawater to the extent that "quantitative capture" can potentially be reached. As such, the high δ^{53}Cr of seawater can theoretically be directly transferred into the sediments (Gueguen et al., 2016; Reinhard et al., 2013). In most cases however, there is at least some offset between seawater and sediment δ^{53}Cr, implying some non-quantitative capture of dissolved Cr (Goring-Harford et al., 2018). Some anoxic sediments have even been observed to contain δ^{53}Cr similar to

that of oxic sediments, such as in the Arabian sea (Schoenberg et al., 2008). Differences in the Cr speciation of seawater and diagenetic changes have been offered as suggestions for the measured δ^{53}Cr at these locations.

Oxic sediments

The lack of a mechanism to reduce dissolved Cr(VI) from oxic seawater means the majority of Cr hosted within sediments underlying an oxic water column will be residual Cr hosted in detrital components (e.g. silicate phases) and the authigenic Cr fraction will be minimal. The lack of any significant authigenic component means that δ^{53}Cr of most oxic, non-carbonate sediments is observed to be the same as Bulk Silicate Earth (-0.12‰) (Gueguen et al., 2016; Schoenberg et al., 2008). External factors, such as proximity to hydrothermal vents, where a plume of reductants can exist in the water column, can lead to a significant authigenic enrichment of Cr with a δ^{53}Cr more negative than BSE (Bauer et al., 2019).

The carbonate sink

Though the carbonate sink is less likely to be important on a global scale due to the very low Cr contents in carbonate minerals, carbonate reservoirs have been suggested as a record of paleoseawater δ^{53}Cr if the chromate ion replaces the carbonate ion in the mineral lattice with minimal fractionation (Farkaš et al., 2018; Holmden et al., 2016; Pereira et al., 2016). However, δ^{53}Cr has been observed to change with variations in rate of this substitution (Rodler et al., 2015), with Cr(VI) concentration of the surrounding solution (Tang et al., 2007) and with pH of the solution (Füger et al., 2019), all of which complicate the interpretation of such reservoirs.

5.1.7 This study

In this chapter, I sought to understand the processes controlling changes in δ^{53}Cr in East Anglian anoxic pond sediments using my understanding of the redox conditions. Few studies have attempted to address the effect of early diagenesis on the behaviour of δ^{53}Cr within sediments despite this being of fundamental importance to interpreting the Cr isotope record for paleoredox reconstructions. In addition, the work from this chapter is used in conjunction with the insight gained from δ^{98}Mo measurements in these pond sediments (**Chapter 4**) to suggest how these isotope systems could potentially be used to provide a better description of the redox conditions of an environment.

5.2 Methods

Sediment cores were collected from Blakeney salt marsh, Norfolk in February 2020 using the methods outlined in **Chapter 3**. There was persistent rainfall on the day of sampling.

5.2.1 Sediment and porewater extraction methods

Sediment samples were collected as described in *Section 3.2.3*. The sediments were digested in concentrated aqua regia for >48 hours at 125°C to ensure adequate leaching time. Despite incomplete digestion of the sediments, the silicate fraction of the sediment should have an isotopically distinct signature (-0.12‰) which can be corrected for using the Cr/Ti ratio (Equation 5.5) (Schoenberg et al., 2008). Authigenic Cr concentration and isotopic signature can therefore be back calculated (Gueguen et al., 2016). A subset of sediment samples was weighed before and after complete drying to measure porosity.

$$\delta^{53}Cr_{auth} = \frac{(\delta^{53}Cr_{bulk} - f_{det}\delta^{53}Cr_{det})}{(1 - f_{det})} \tag{5.5}$$

Porewaters were extracted using the methods described in *Section 3.2.2*.

5.2.2 Cr isotope separation and analysis

A variety of elements, including Cr, in sediment leachates were measured by ICP-MS (*Section 3.3.2*). After redissolution in 1M HCl, a correct addition of ^{54}Cr-^{50}Cr double spike in 1M HCl was added to individual samples and allowed to equilibrate for >2 days. Separation of Cr is described in *Section 3.4.2*. After separation, purified Cr was dried down, digested in 200 μL of concentrated distilled HNO_3 and dried down again. The samples were loaded on to outgassed Re filaments and run using TIMS (*Section 3.4*). Errors are reported based on the δ^{53}Cr of five SRM979 standards run alongside each set of 16 samples. Every other turret included a sample of NIST3112a as a secondary standard to test for long term reproducibility.

5.3 Results

Porewater iron and sulfide measurements are typical of the pond sediment classifications described in **Chapter 2**. Dissolved Fe^{2+} in the iron-rich pond sediment decreases from 0.6 to 0.3 mM over the top 5 cm, stays semi-constant at 0.2–0.4 mM from 5 cm to 25 cm depth, before sharply increasing to as high as 0.85 mM below 25 cm (Figure 5.4b). Dissolved HS^-

in the sulfide-rich pond sediment increases up to 4–5 mM from 5 to 20 cm and decreases below this point to 0.5 mM at 37 cm depth (Figure 5.4c). There was negligible dissolved Fe^{2+} in the sulfide-rich pond sediment and negligible HS^- in the iron-rich pond sediment.

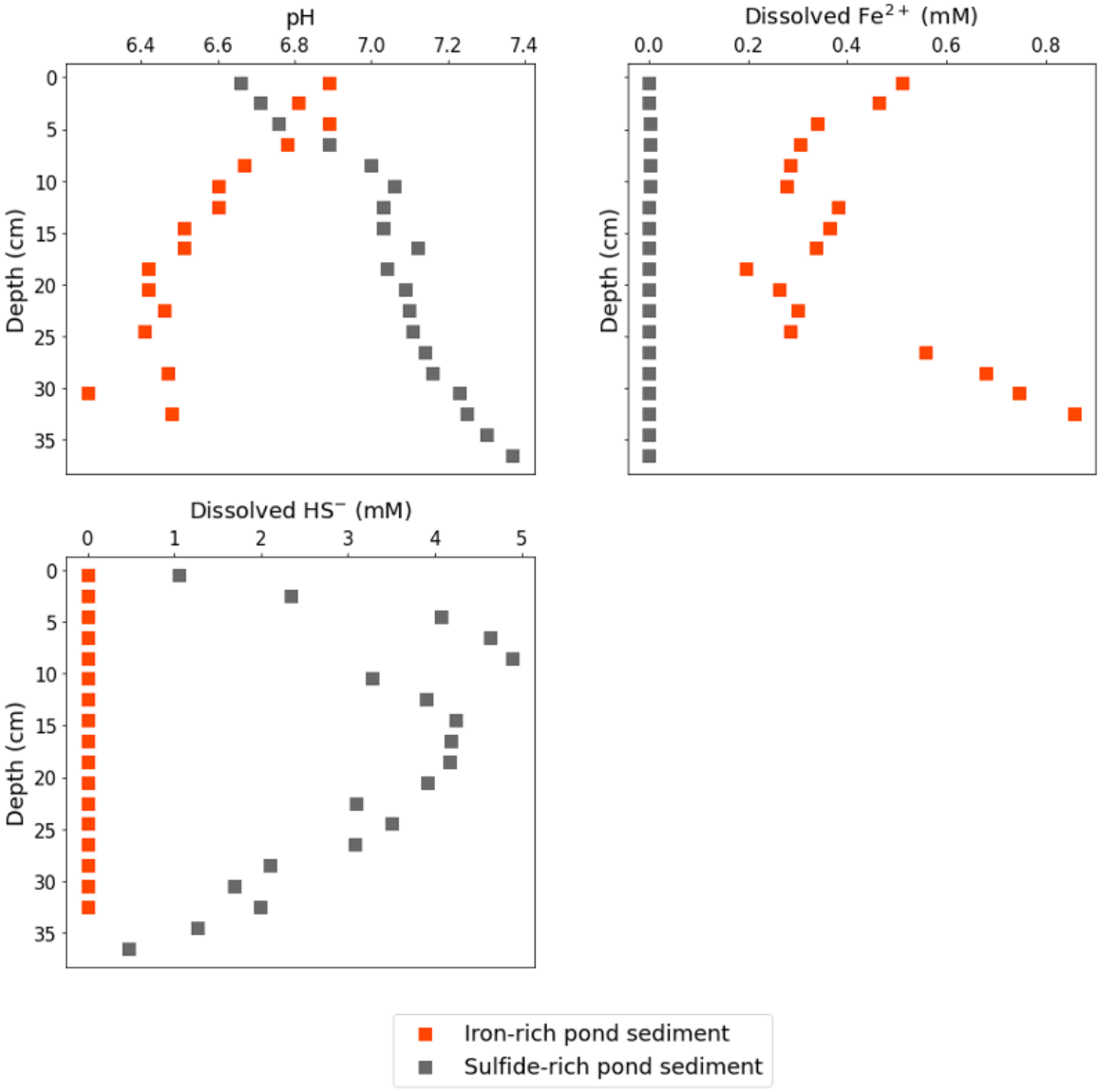

Fig. 5.4 - *Porewater chemistry of the iron-rich and sulfide-rich pond sediment at Blakeney: (a) pH, (b) dissolved Fe^{2+} concentration and, (c) dissolved HS^-.*

Bulk δ^{53}Cr measurements, calculated authigenic/detrital δ^{53}Cr and, porosity-corrected authigenic Cr concentrations are given in Table 5.2 and Table 5.3. Chromium in sediments is a mixture of allochthonous detrital material (Cr hosted in silicate minerals) and authigenic Cr that is forming *in situ*. A correction (Equation 5.5) can be applied to estimate the fraction of detrital material if a Cr/Ti ratio of 0.024 g/g and an isotopic signature of -0.12‰ (BSE) is

assumed (Gueguen et al., 2016; Schoenberg et al., 2008). The proportion of detrital material is in fair agreement with sequential extractions of Cr from these sediments conducted using the BCR method (Rauret et al., 1999) (**Appendix D**).

Correcting Cr concentrations to the dry sediment weight removes the effect of porosity differences throughout the sediment core and gives a better representation of the proportion of Cr present bound to the sediment. A polynomial relationship derived from four porosity measurements in each core was used to calculate the porosity with depth (Table 5.2 and Table 5.3). Authigenic δ^{53}Cr and porosity corrected Cr sediment concentrations are shown in Figure 5.5. All but two δ^{53}Cr measurements of sediments lie inside a narrow isotopic window between -0.07 and 0.08‰. Iron-rich pond sediment δ^{53}Cr is 0.035‰ higher than sulfide-rich sediment in the uppermost 15 cm of sediment, just outside analytical uncertainty. Below 15 cm, iron-rich pond sediment decreases to -0.05‰ at 32 cm depth. Sulfide-rich pond sediment δ^{53}Cr is marginally higher below 15 cm than above.

Figure 5.6 shows the same authigenic Cr data in comparison with a suite of other measured trace metals in the same sediment samples. Authigenic chromium concentrations are comparable between the cores in both the upper cm of sediment and below 15 cm depth. From 2–10 cm, authigenic Cr is higher in the iron-rich pond sediment by $\sim$10 μg/g. From 10–15 cm, authigenic Cr becomes higher in sulfide-rich pond sediment. The integrated total Cr between the two pond-sediments is comparable over 2–15 cm depth. Porosity corrected sedimentary Fe and V concentrations follow precisely the same trend in this upper 15 cm. Below 15 cm, authigenic Cr is similar between the two sites, varying between 45 and 60 μg/g.

5.4 Discussion

5.4.1 δ^{53}Cr in comparison to global oxic and anoxic sediments

Almost all samples measured in the East Anglian salt marsh sediments are indistinguishable from the composite of oxic sediments reported in Schoenberg et al. (2008) and Gueguen et al. (2016) (Figure 5.7). In comparison, sediments deposited beneath the anoxic Cariaco basin and a transect of sediments under oxic–anoxic water in the Peruvian margin have a notably higher δ^{53}Cr (ranging from 0.1–0.9‰) (Bruggmann et al., 2019; Reinhard et al., 2013). The measured range of seawater δ^{53}Cr lies between +0.41 and +1.72‰, higher than all of sediment samples measured in this study. Although I did not measure the overlying pondwater, it seems reasonable to assume that the input water would not have a δ^{53}Cr significantly lower than 0.41‰.

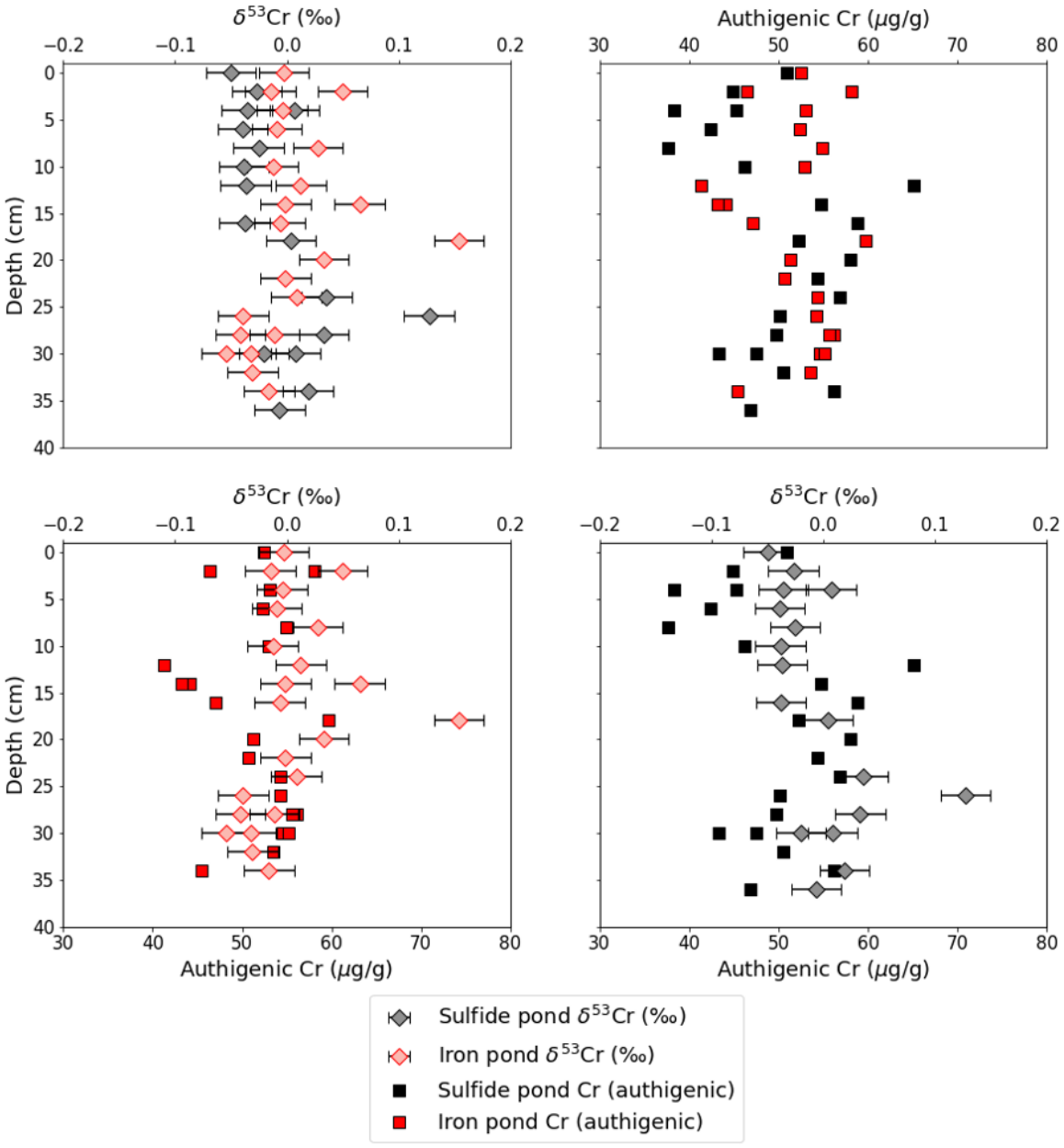

Fig. 5.5 - *Authigenic $\delta^{53}Cr$ and authigenic Cr sediment concentrations in iron-rich and sulfide-rich pond sediment. (a) authigenic $\delta^{53}Cr$, (b) authigenic Cr concentrations corrected for porosity, (c) overlaid $\delta^{53}Cr$ and concentration data for iron-rich pond sediment and (d), overlaid $\delta^{53}Cr$ and concentration data for sulfide-rich pond sediment.*

Depth (cm)	$\delta^{53}Cr_{bulk}$ (‰)	Cr_{bulk} (μg/g)	Ti (μg/g)	Cr_{det} (μg/g)	$\delta^{53}Cr_{auth}$ (‰)	Cr_{Auth} (μg/g)	Porosity	$Cr_{AuthSolid}$ (μg/g)
0	-0.07 ± *0.02*	6.00 ± *0.07*	71.4	1.7	-0.05	4.3	0.916	50.9
2	-0.06 ± *0.02*	6.05 ± *0.06*	74.3	1.8	-0.03	4.3	0.905	44.9
4	-0.06 ± *0.02*	5.96 ± *0.04*	79.0	1.9	-0.04	4.1	0.894	38.3
4*	-0.02 ± *0.02*	6.23 ± *0.08*	59.1	1.4	0.01	4.8	0.894	45.3
6	-0.06 ± *0.02*	7.11 ± *0.04*	89.2	2.1	-0.04	5.0	0.883	42.4
8	-0.05 ± *0.02*	6.31 ± *0.04*	62.2	1.5	-0.03	4.8	0.872	37.6
10	-0.06 ± *0.02*	8.75 ± *0.08*	96.4	2.3	-0.04	6.4	0.861	46.2
12	-0.06 ± *0.02*	13.46 ± *0.11*	153.5	3.7	-0.04	9.8	0.850	65.1
14		11.83 ± *0.36*	125.9	3.0		8.8	0.839	54.7
16	-0.06 ± *0.02*	13.73 ± *0.06*	150.4	3.6	-0.04	10.1	0.828	58.7
18	-0.02 ± *0.02*	12.32 ± *0.10*	114.6	2.8	0.00	9.6	0.817	52.2
20		13.92 ± *0.42*	110.9	2.7		11.3	0.806	58.0
22		14.92 ± *0.45*	157.5	3.8		11.1	0.795	54.3
24	-0.01 ± *0.02*	16.56 ± *0.17*	178.3	4.3	0.04	12.3	0.784	56.8
26	0.07 ± *0.02*	15.05 ± *0.17*	152.3	3.7	0.13	11.4	0.773	50.2
28	0.00 ± *0.02*	14.49 ± *0.19*	110.5	2.7	0.03	11.8	0.762	49.7
30	-0.04 ± *0.02*	15.28 ± *0.09*	143.5	3.4	-0.02	11.8	0.751	47.5
30*	-0.02 ± *0.02*	14.07 ± *0.15*	137.1	3.3	0.01	10.8	0.751	43.2
32		17.57 ± *0.53*	183.9	4.4		13.2	0.740	50.6
34	-0.01 ± *0.02*	18.84 ± *0.19*	150.7	3.6	0.02	15.2	0.729	56.1
36	-0.03 ± *0.02*	16.28 ± *0.08*	127.6	3.1	-0.01	13.2	0.718	46.8

Table 5.2 - *Sediment $\delta^{53}Cr$ and Cr concentrations in the sulfide-rich pond sediment from Blakeney. Corrections for authigenic chromium were calculated using Ti concentrations and Equation 5.5. $Cr_{AuthSolid}$ refers to the Cr concentration of the dry weight of the sediment calculated using a polynomial correction of porosity with depth. *refers to full procedural repeats of the sediment at that depth.*

Depth (cm)	$\delta^{53}Cr_{bulk}$ (‰)	Cr_{bulk} (μg/g)	Ti (μg/g)	Cr_{det} (μg/g)	$\delta^{53}Cr_{auth}$ (‰)	Cr_{Auth} (μg/g)	Porosity	$Cr_{AuthSolid}$ (μg/g)
0	-0.03 ± *0.02*	11.71 ± *0.19*	119.5	2.9	0.00	8.8	0.831	52.4
2	-0.04 ± *0.02*	13.52 ± *0.17*	137.5	3.3	-0.01	10.2	0.824	58.1
2*	0.00 ± *0.02*	11.04 ± *0.09*	119.9	2.9	0.05	8.2	0.824	46.4
4	-0.03 ± *0.02*	12.78 ± *0.20*	126.1	3.0	0.00	9.8	0.816	53.0
6	-0.04 ± *0.02*	13.24 ± *0.17*	132.2	3.2	-0.01	10.1	0.808	52.3
8	-0.01 ± *0.02*	14.97 ± *0.19*	162.7	3.9	0.03	11.1	0.798	54.9
10	-0.04 ± *0.02*	15.64 ± *0.28*	185.1	4.4	-0.01	11.2	0.788	52.9
12	-0.02 ± *0.02*	12.20 ± *0.16*	126.1	3.0	0.01	9.2	0.778	41.3
14	-0.03 ± *0.02*	13.14 ± *0.18*	118.7	2.8	0.00	10.3	0.767	44.1
14*	0.02 ± *0.02*	13.65 ± *0.13*	149.1	3.6	0.07	10.1	0.767	43.2
16	-0.03 ± *0.02*	14.79 ± *0.21*	135.9	3.3	-0.01	11.5	0.755	47.1
18	0.09 ± *0.02*	19.82 ± *0.22*	185.4	4.4	0.15	15.4	0.742	59.7
20	-0.01 ± *0.02*	19.19 ± *0.16*	221.3	5.3	0.03	13.9	0.729	51.3
22	-0.04 ± *0.02*	20.02 ± *0.27*	233.9	5.6	0.00	14.4	0.716	50.7
24	-0.02 ± *0.02*	19.76 ± *0.12*	147.7	3.5	0.01	16.2	0.701	54.3
26	-0.06 ± *0.02*	22.82 ± *0.19*	242.2	5.8	-0.04	17.0	0.686	54.2
28	-0.06 ± *0.02*	23.65 ± *0.24*	215.4	5.2	-0.04	18.5	0.671	56.1
28†	-0.04 ± *0.02*	24.75 ± *0.21*	268.7	6.4	-0.01	18.3	0.671	55.6
30	-0.05 ± *0.02*	24.32 ± *0.29*	228.2	5.5	-0.03	18.8	0.654	54.5
30*	-0.07 ± *0.02*	24.54 ± *0.33*	228.2	5.5	-0.05	19.1	0.654	55.2
32	-0.05 ± *0.02*	24.73 ± *0.23*	222.2	5.3	-0.03	19.4	0.637	53.5
34	-0.04 ± *0.02*	22.15 ± *0.22*	203.5	4.9	-0.02	17.3	0.620	45.4

Table 5.3 - *Sediment $\delta^{53}Cr$ and Cr concentrations in the iron-rich pond sediment from Blakeney. Corrections for authigenic chromium were calculated using Ti concentrations and Equation 5.5. $Cr_{AuthSolid}$ refers to the Cr concentration of the dry weight of the sediment calculated using a polynomial correction of porosity with depth. *refers to full procedural repeats of the sediment at that depth. †refers to the same sample reprocessed through column chemistry.*

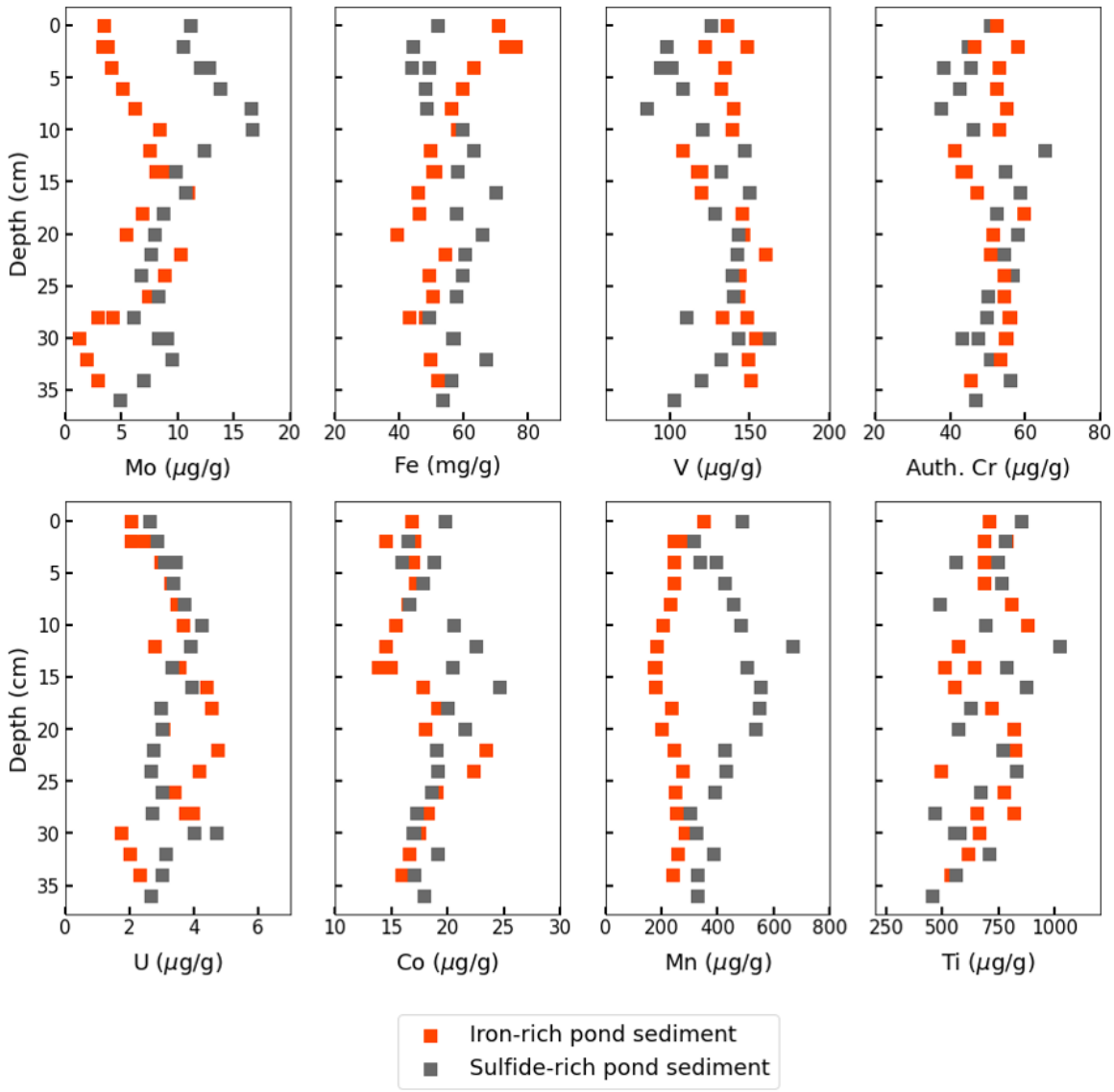

Fig. 5.6 - *Concentrations of (a) Mo, (b) Fe, (c) V, (d), Authigenic Cr (see Figure 5.5b), (e) U, (f) Co, (g) Mn, and (h) Ti in iron-rich and sulfide-rich pond sediments. Data is corrected for porosity measurements. For methods of analysis, see* ***Chapter 3****.*

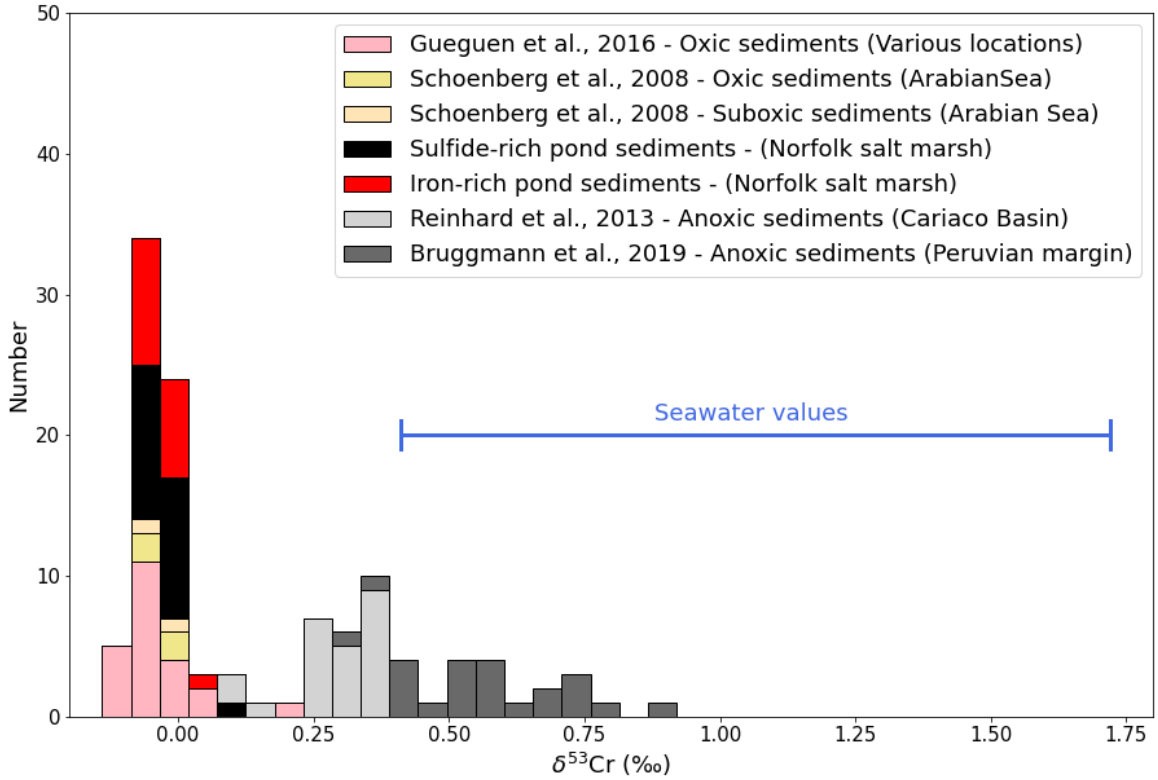

Fig. 5.7 - *Composite of $\delta^{53}Cr$ in global marine sediment samples compared to salt marsh pond sediments. These reflect a combination of surface sediments and multiple measurements taken through sediment cores. Range of seawater values reflects all global seawater samples ((Janssen et al., 2020) and references therein).*

Two possible reasons could explain why the δ^{53}Cr of these sediments are so much lower than other anoxic sediments and than the assumed seawater δ^{53}Cr; it could be a result of incomplete removal of Cr from the pond water in the ponds above, or it may reflect the depth of oxygen penetration into the sediment (termed the Non-Reactive Zone or NRZ). I will explore each of these theories in turn.

Multiple reductants capable of reducing Cr(VI) exist in the water column overlying pond sediments: organic reductants would be present due to *in situ* vegetative growth, $Fe^{2+}_{(aq)}$ would efflux from the sediment in the mornings/evenings and iron minerals could become temporarily suspended in the water column due to the disturbance of sediment by macrofauna. All of these reductants would produce Cr(III) with a lower δ^{53}Cr which could subsequently become shuttled to the sediment by adsorption to organic/inorganic particles (Table 5.1). If these reductants quantitatively stripped the pond water of Cr, the δ^{53}Cr of the sediment would isotopically evolve to match that of the pond water input δ^{53}Cr by Rayleigh distillation. Regular flushing of the tidal water in these salt marsh ponds however, supplies oxidised Cr (found in seawater) to the pond water column; this could create an isotopic offset between the sediment and overlying pond water (i.e. the environment behaves as an open system). Variations in δ^{53}Cr with depth in the upper portion of sediment may reflect small variations in the flushing time, with less regular flushing leading to a higher δ^{53}Cr of the sediment.

The second potential reason for the low sediment δ^{53}Cr could be the presence of an NRZ at the sediment-water interface (Bauer et al., 2018). If sediment is directly in contact with pond water, the δ^{53}Cr of the sediment would reflect the higher δ^{53}Cr of pond water (assumed to be seawater) minus the fractionation factor associated with Cr(VI) reduction (ε). The introduction of a non-reactive zone in the uppermost portion of sediment causes there to be a component of transport added to Cr(VI) reduction as Cr in the pond water must first diffuse through the sediment. As such, the δ^{53}Cr of the seawater trapped in the porewater becomes progressively higher with extent of reduction before it is able to diffuse out. This diminishes the isotope fractionation factor, and means that the δ^{53}Cr of the sediments will lie somewhere between $\delta^{53}Cr_{seawater}$ and $\delta^{53}Cr_{seawater}$ - ε (Clark and Johnson, 2008). The resultant δ^{53}Cr of the sediment may just fortuitously occur in the range of oxic sediments due to this effect.

5.4.2 Differences between the fate of Cr in the iron-rich and sulfide-rich pond sediment

The authigenic δ^{53}Cr and and Cr content of the sediment differs in the surface 15 cm between the two types of pond sediment. Given the close proximity of the two studied ponds,

the seawater input likely is of a similar composition and is resupplied to ponds at similar intervals (with the caveat that distance from creek may cause slight variations in resupply rate (**Chapter 2**)). The higher authigenic Cr content in the iron-rich pond sediment must therefore reflect a subtly different method of capture of dissolved pond water Cr than in the sulfide-rich pond.

In both types of pond sediment, there are a large amount of potential reductants (organic ligands, iron minerals etc.) present capable of reducing Cr(VI) from seawater with the Cr isotope fractionation factors outlined in Table 5.1 (**Process 1 and 4** – Figure 5.8). Table 5.1 summarises experimentally defined isotope fractionation factors with the various reductants and is thus a drastic simplification; variations in electron donor, microbial community and surrounding mineralogy can all alter the expressed Cr isotope fractionation factor (Basu et al., 2014; Zhang et al., 2018, 2019). Additionally, it seems very unlikely that the full isotopic offset would be expressed given the relatively fast sedimentation rates and seawater replenishment times at this site. Nevertheless, I suspect dissolved Fe^{2+} would be the most efficient reductant in iron-rich pond sediment due to the rapid kinetics of the reduction reaction and the high concentrations of Fe^{2+} present in the porewater. In sulfide-rich pond sediments, the absence of Fe^{2+} in the porewater results in iron sulfide minerals and organic ligands becoming more important reductants of Cr(VI) (Figure 5.8).

Based on the Cr isotope fractionation factors of expected reductants (Table 5.1), with equal authigenic uptake of seawater Cr(VI), I would expect δ^{53}Cr in iron-rich pond sediments to be lower than in sulfide-rich pond sediments—counter to what is observed. This discrepancy can be explained if iron-rich pond sediments more effectively strip seawater Cr(VI) from the pond water, possibly by a sedimentary efflux of Fe^{2+} during periods of anoxia in the early morning; this could cause an isotopic distillation of the water column that would, in turn, increase the δ^{53}Cr of the sediment. This is supported by the higher content of authigenic Cr at the sediment surface of the iron-rich pond compared to the sulfide-rich pond. The difference between δ^{53}Cr is so subtle however, that such an effect would likely be unnoticeable in the geological record.

The distribution of authigenic Cr over the sedimentary core in both ponds can be best explained in tandem with other elements present in the sediment (Figure 5.6). Sedimentary Fe concentrations are highest at the sediment-water interface of the iron-rich pond as Fe^{2+} diffuses upwards and reacts with O_2 dissolved in the pond water to form Fe oxides. Authigenic Cr mimics this behaviour, however it becomes concentrated further below the sediment-water interface. There is a very close coupling of sedimentary Cr and Fe content with depth (Figure 5.6b,d); this close relationship likely reflects a combination of the processes of Cr adsorption on to the precipitated Fe(III) (oxyhydr)oxides and co-precipitation of

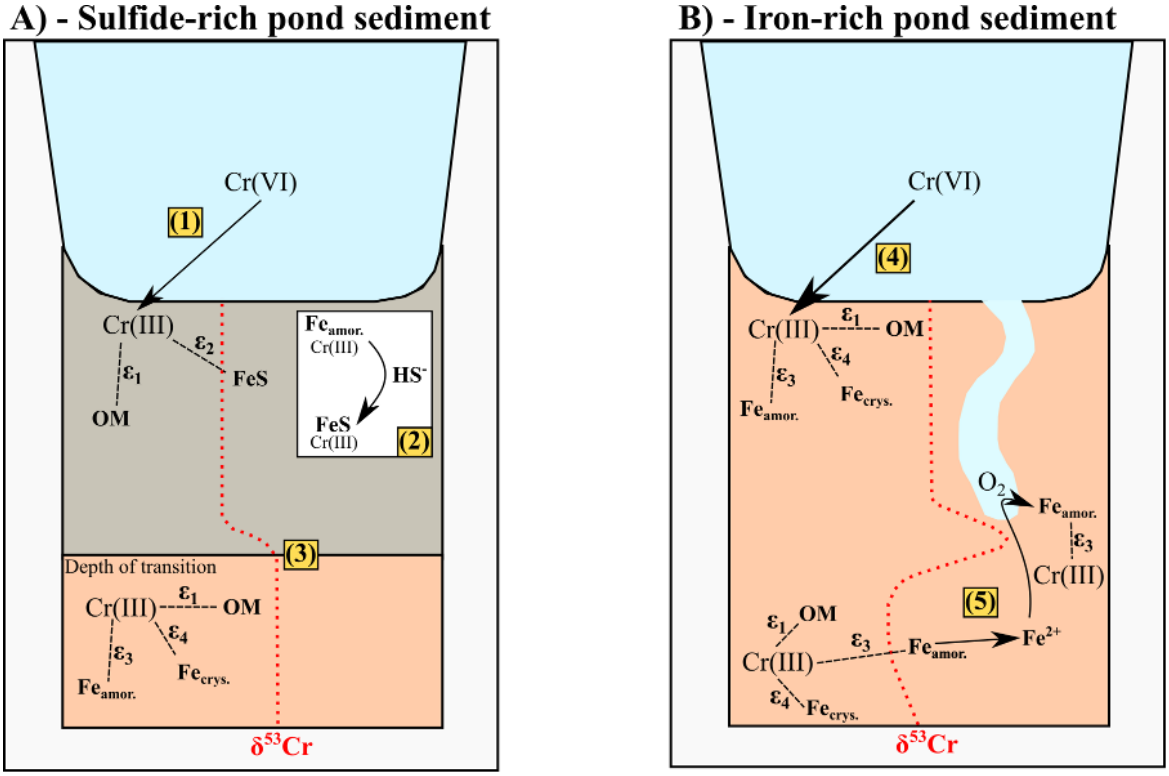

Fig. 5.8 - *Schematic of the diagenetic processes which control the behaviour of Cr in the (a) sulfide-rich and (b) iron-rich pond sediment. A)* ***Process 1*** *– Cr(VI) is reduced by organic matter and iron sulfide minerals with potential Cr isotope fractionation factors* ε_1 *and* ε_2 *respectively.* ***Process 2*** *– Any Fe-minerals, which are not already iron sulfides, that have been deposited would be broken down by the high concentration of aqueous sulfide in this part of the sediment. Chromium appears to follow the behaviour of liberated dissolved Fe which diffuses downwards in the sediment and forms iron sulfides.* ***Process 3*** *– The depth of transition refers to the point when the sediment was at the sediment-water interface and was an iron-rich pond; sediment deposited above this point would have always been under sulfide-rich conditions. Below this depth, the* $\delta^{53}Cr$ *is similar to that seen in the surface of the iron-rich pond sediment.* ***Process 4*** *– Cr(VI) is most likely reduced by organic matter, amorphous Fe-minerals and crystalline-Fe minerals with potential fractionation factors* ε_1, ε_3 *and* ε_4 *respectively. More rapid reduction causes a marginally higher uptake of Cr(VI) from the above water mass than the sulfide-rich pond and thus some isotopic distillation of the pond water* $\delta^{53}Cr$. ***Process 5*** *– Iron reduction below the zone of bioirrigation breaks down the amorphous Fe-minerals and thus changes the bulk* $\delta^{53}Cr$ *of the sediment (as Cr bound to OM and crystalline Fe minerals become proportionally larger). The released Fe and Cr are reprecipitated in the bioirrigated zone as amorphous Fe-minerals around the linings of burrows. The bulk* $\delta^{53}Cr$ *in this portion of sediment reflects a higher proportion of Cr bound to amorphous Fe-minerals.*

Cr(III)-Fe(III)-(oxyhydr)oxides. As described in detail in **Chapter 4**, in the iron-rich sediment, reduction of Fe(III) (oxyhydr)oxides is coupled with subsequent Fe^{2+} reoxidation due to the drawdown of O_2 rich seawater by bioirrigation. The rapid cycling of iron isotopically homogenises the δ^{53}Cr in this upper part of the sediment, in an identical mechanism to that observed in the δ^{98}Mo system.

In the sulfide-rich pond sediment, iron mineralogy appears to be diagenetically redistributed so that sediment at 2–10 cm is depleted in Fe and Cr. This is most easily explained by the breakdown of Fe-(oxyhydr)oxides by the reaction with aqueous sulfide (**Process 2** – Figure 5.8). Reprecipitation of Fe with sulfide may then occur where sulfide concentrations are highest (10–20 cm depth) as iron sulfide minerals. Chromium would similarly follow this movement of Fe, ultimately being captured onto the precipitated iron sulfide minerals. As with the iron-rich pond, the sediment δ^{53}Cr becomes mixed during this process.

5.4.3 Potential depth of pond geochemistry change

As described in **Chapters 2** and **4**, there is evidence for the potential of iron-rich pond sediment to become transformed into sulfide-rich pond sediment by a series of non-linear, positive feedbacks. The reverse transformation, on the other hand, has yet to be observed in these salt marsh sediments. Based on this model for the salt marsh geochemistry, all pond sediments will have once contained iron-rich geochemistry.

The similarities between the sulfide-rich pond sediment δ^{53}Cr/Cr concentration below 20 cm and the iron-rich pond sediment δ^{53}Cr/Cr concentration above 15 cm could be explained by similar methods of Cr(VI) reduction and capture. One hypothesis for this is that when the portion of sulfide-rich sediment at 20 cm was at the sediment-water interface, the pond sediment would have contained dissolved Fe^{2+} instead. Some switch-point was reached, converting the geochemistry to that of sulfide-rich sediment, and subsequently all Cr has been captured from seawater under sulfide-rich conditions (**Process 3** – Figure 5.8). This interpretation is corroborated by the similar concentrations of Fe, Mo, V, Co and Cr from 20–30 cm. In particular, the similarity in sedimentary content of Mo at 20-cm depth between the sediment cores implies that aqueous sulfide was not present in either pond sediment during the time period when that part of the sediment was at the surface.

A rough estimate can be placed on the timing of this transition using the sedimentation rates calculated for Blakeney salt marsh. If we assume 18-cm as the depth of transition and a sedimentation rate of 0.3 cm yr^{-1} (van de Velde et al., 2020), this places the conversion at ~60 years ago.

5.4.4 Diagenetic alteration of δ^{53}Cr during iron reduction?

In the iron-rich pond sediment, the minor decrease of δ^{53}Cr from 20–35 cm is outside of analytical uncertainty and may potentially reflect a small amount of diagenetic alteration of the δ^{53}Cr signal. This portion of sediment lies beneath the typical zone of bioirrigation, and thus is characterised by iron reduction (supported by increased concentrations of Fe^{2+} in the porewater). If iron reduction breaks down Fe-(oxyhydr)oxides onto which Cr is adsorbed or coprecipitated, the Cr will become liberated and can potentially be redistributed within the sedimentary column. Any effect of this must be minor, as authigenic Cr concentrations do not change significantly within this portion of sediment. It is reasonable however, to posit that poorly crystalline Fe-(oxyhydr)oxides would be reduced first, which may then release small amounts of authigenic Cr into the porewater for redistribution. This implies that Cr associated with poorly crystalline Fe minerals has a higher δ^{53}Cr and that whatever combination of reductants are left in the sediment contains Cr with a lower δ^{53}Cr. The remobilised higher δ^{53}Cr appears to be precipitated (possibly as iron (oxyhydr)oxides on burrow linings) in a lens of sediment at 15–20 cm where bioirrigation is still active and O_2-rich water is brought in with burrows (**Process 5** -Figure 5.8). This argument is supported by the mass balance of δ^{53}Cr in the 10–35cm in the iron-rich pond sediment which ends up statistically indistinguishable from the uppermost 10-cm of sediment ($\int_{0cm}^{10cm} \delta^{53}Cr_{auth}$ =0.004, $\int_{10cm}^{35cm} \delta^{53}Cr_{auth}$ =0.007). Further corroboration is observed in these sediment cores, where sedimentary Mo is depleted in the lowest part of the sediment core (below 25 cm), while an increase in sedimentary Mo is observed from 15–25 cm depth (Figure 5.6a). This would reflect molybdate adsorbed to iron-oxyhydroxides which was released and re-adsorbed in the bioirrigated zone (*Section 4.4.1*).

This potential diagenetic alteration of the δ^{53}Cr isotopic signature of the sediment is almost identical in nature to the progressive lowering of the sedimentary δ^{98}Mo in the same depth portion of the iron-rich pond sediment (**Chapter 4**). In both cases, the changing proportions of reductants with different isotopic fractionation factors influences the bulk isotopic composition of the sediment. The scale of the change in the δ^{53}Cr is markedly smaller than what was observed in the δ^{98}Mo system however, and such a change would almost certainly be indistinguishable in the rock record. This is probably because the bulk of authigenic Cr can be in solid-state solution with Fe(III) in the minerals, whereas the molybdate ions were almost all adsorbed to the Fe(III)-(oxyhydr)oxide surface (and thus were more susceptible to diagenetic breakdown).

5.4.5 The use of a coupled δ^{53}Cr and δ^{98}Mo system

The combination of δ^{53}Cr and δ^{98}Mo has the potential to be a powerful paleoredox tool (Figure 5.9). As discussed throughout this thesis, δ^{53}Cr is a tracer of anoxic versus oxic conditions whilst δ^{98}Mo is a tracer of euxinic conditions which, in conjunction, could reveal a precise interpretation of the paleoredox conditions of a sedimentary environment. My work suggests the importance of a regularly-flushed oxic water column above anoxic sediments in determining the δ^{53}Cr which would be preserved. Therefore, a possible interpretation using these two isotope proxies is that when δ^{53}Cr is similar to that found in oxic sediments and sediment δ^{98}Mo has non-oxic sediment values, this could indicate the presence of an oxic water column above anoxic sediments. This could potentially be a more nuanced way to distinguish sedimentary rocks which are deposited under a euxinic or ferruginous water column.

The similarity between δ^{53}Cr in the iron-rich and sulfide-rich pond sediment precludes the ability to identify diagenetic alteration of the signal caused by sulfidisation of iron minerals and thus independent proxies would be necessary to ascertain if sediment had become overprinted. This study has shown how multiple paleoredox proxies can be calibrated in tandem with each other to build up a better representation of the redox characteristics of a depositional environment.

5.5 Conclusion

These results suggest that the presence of an oxic water column prohibits capture of the seawater δ^{53}Cr signal, even if the sediments contain high concentrations of strong reductants such as Fe^{2+}_{aq}. In fact, the δ^{53}Cr of these sediments more closely approximates the signal associated with oxic sediments. I attribute this to either a non-reactive zone at the sediment surface, or to the regular replenishment of Cr in the overlying water column which outpaces the rate of Cr sequestration.

The two types of pond sediment have a similar range of δ^{53}Cr with depth. Subtle variations reveal that the iron-rich pond sediment may more efficiently capture Cr from the overlying water and that at 20 cm in the sulfide-rich pond sediment, there is evidence for the pond sediment once being iron-rich. The behaviour of iron mineralogy appears to strongly affect the distribution of authigenic chromium in both the iron-rich and sulfide-rich pond, likely due to co-precipitation or adsorption processes. A full schematic of the expected diagenetic processes is shown in Figure 5.8.

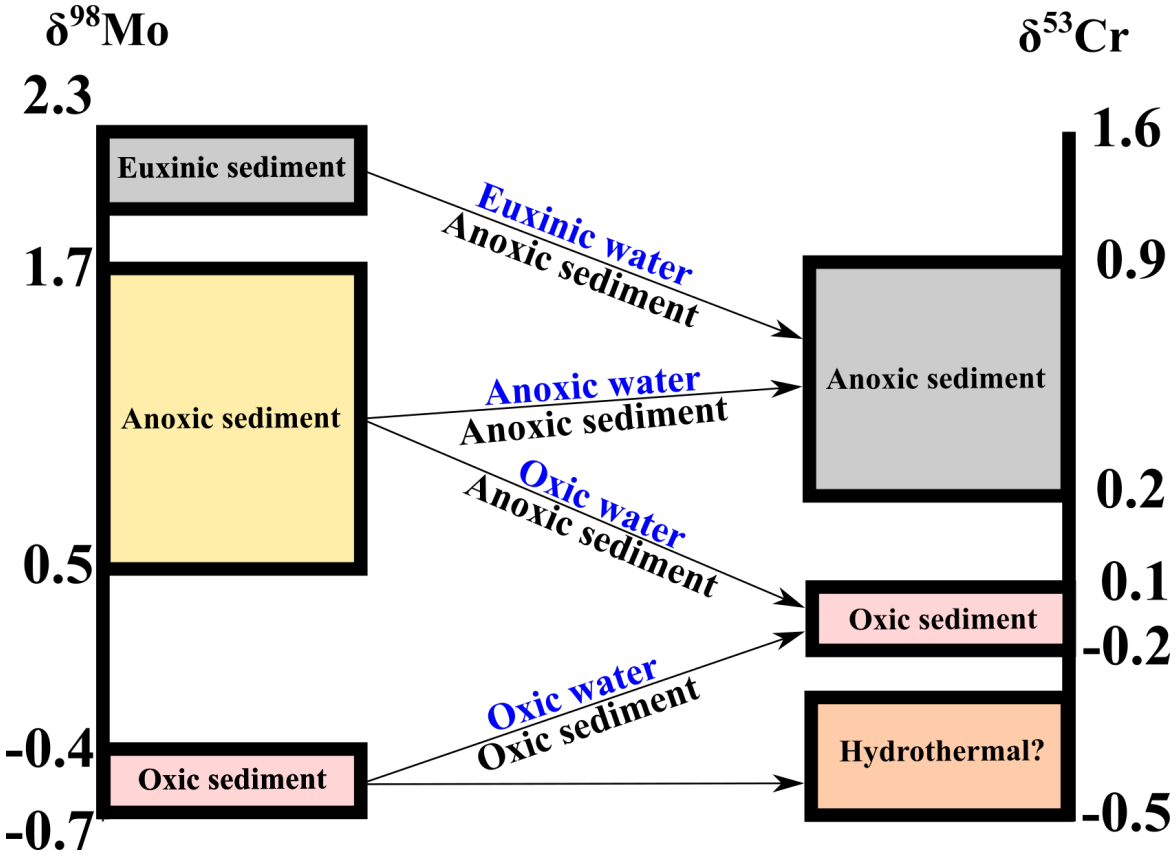

Fig. 5.9 - *Hypothetical model of understanding the water and sediment conditions of an environment using coupled $\delta^{98}Mo$ and $\delta^{53}Cr$ signatures. Boxes correspond to the approximate range of signatures used in the current classification of redox environments. Importantly, environments where $\delta^{53}Cr$ is similar to that of oxic sediment and the $\delta^{98}Mo$ of anoxic sediment may correspond to an oxic water column overlying anoxic sediments. "Hydrothermal?" box refers to the isotopically lower $\delta^{53}Cr$ in sediments reported by Bauer et al. (2019)*

In comparison to the δ^{98}Mo system, δ^{53}Cr is less strongly affected by the changes in redox conditions observed in these salt marsh sediments. Since Cr is less associated with aqueous sulfide than Mo, a systematic change from ferrous iron to aqueous sulfide in the porewater would not significantly affect the deposited δ^{53}Cr signal, although some portion of authigenic Cr may become redistributed. There is however some evidence to show that if iron reduction occurs deep in the sediment, this can change the relative proportion of a certain reductant (and accompanied isotopic fractionation) which may shift the sediment bulk signal at that depth.

This study further emphasises the need to understand local conditions in order to interpret δ^{53}Cr signals in the rock record. In particular, an understanding of the overlying water conditions, range of reductants present and the potential for iron reduction needs to be ascertained to reconstruct any paleoredox conditions. This study does highlight the potential for a scheme to use coupled δ^{98}Mo and δ^{53}Cr measurements in tandem to understand the redox characteristics of a depositional environment. The introduction of other redox sensitive species such as Re and U would likely add further specificity to this classification scheme.

5.6 Implications for further chapters

This chapter provides independent support for many of the diagenetic reactions identified in **Chapter 4**. Iron mineralogy appears to play a vitally important role in diagenetic reactions of many paleoredox proxies, hence **Chapter 6** looks at one of the most widely used proxies: iron speciation measurements in sediments. Inferring that the processes observed in these salt marsh sediments are applicable to that of mid-Proterozoic ocean sediments, I attempt to re-evaluate redox conditions from a diagenetic standpoint.

Chapter 6

Potential for Diagenesis in the Proterozoic Rock Record

6.1 Introduction

6.1.1 Chapter outline

The work from the previous two chapters examines the behaviour of two widely used paleoredox proxies under iron-rich and sulfide-rich anoxic sedimentary conditions. I found that certain diagenetic reactions could redistribute and change the geochemical signal of the sediment with respect to these proxies. In particular, the potential for aqueous sulfide in the porewater to alter the dominant iron mineralogy of the sediment post-depositionally has implications for what is ultimately preserved. This chapter extends the application of this work to the mid-Proterozoic sedimentary geological record. The iron-rich and sulfide-rich conditions observed in pond sediments are germane to the ferruginous and euxinic depositional conditions of the mid-Proterozoic oceans respectively. The effect of diagenetic reactions on iron speciation, one of the most widely used paleoredox proxies for this time period, is examined. Modelling work shows that the effect of diagenesis can be observed in iron speciation measurements in the rock record. The work in this chapter provides a new way of looking at the geological record through the lens of diagenetic reactions. It ties together many of the conclusions from the previous chapters and highlights an under-discussed process in paleoredox science.

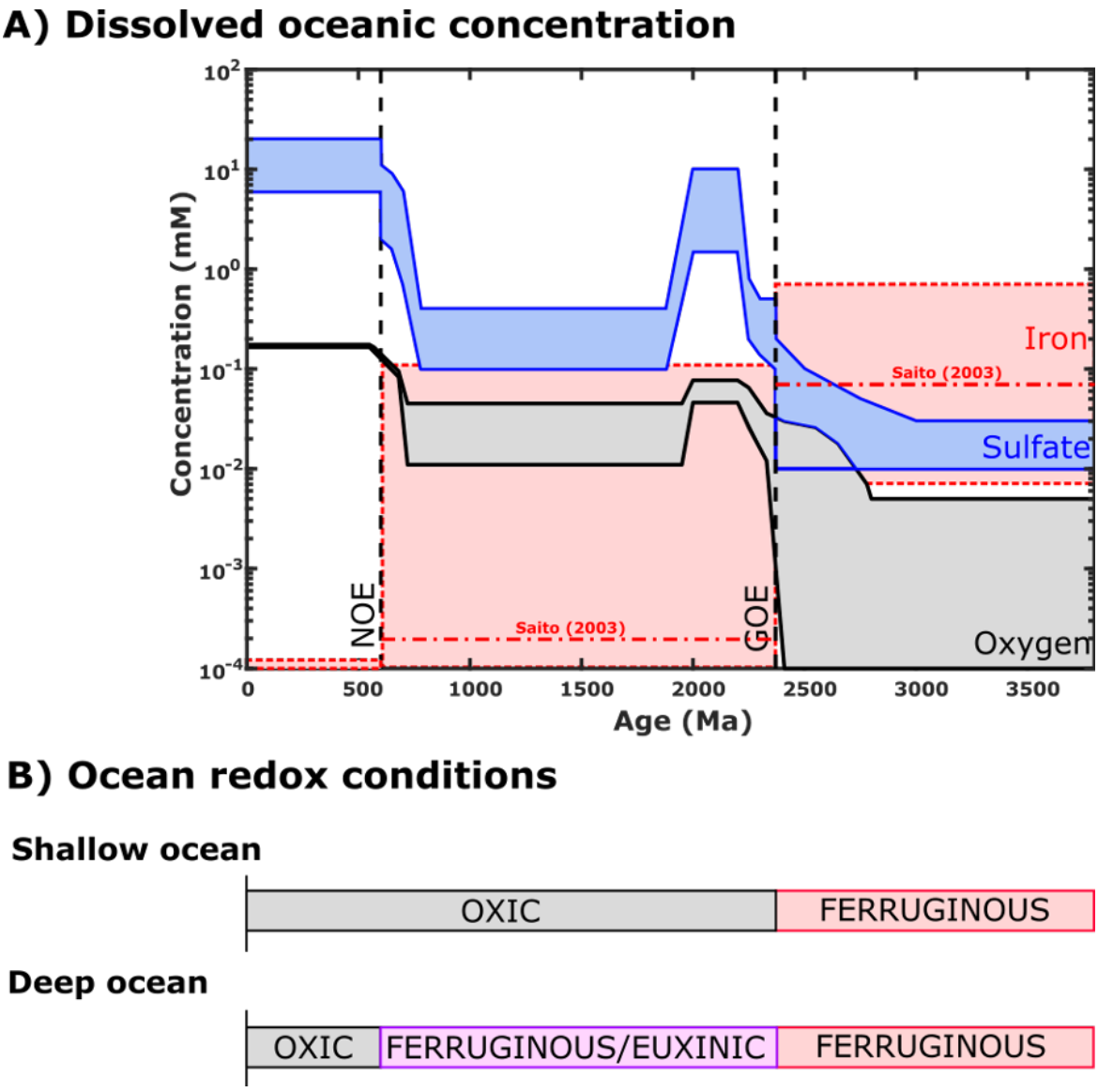

Fig. 6.1 - *(A) Relative concentrations of sulfate, iron and oxygen in Earth's oceans over geological time (note log scale on the y-axis) (Canfield and Farquhar, 2009; Fakhraee et al., 2019; Saito et al., 2003). Dissolved iron concentrations for Archaean based on estimates from Saito et al. (2003) with an order-of-magnitude uncertainty envelope. Dissolved iron concentrations are assumed to be lower and more variable in the Proterozoic relative to the Archaean and therefore a "best guess" uses a wider range of estimates (Derry, 2015), Modern oceanic iron concentrations are 0-1.5 nM which is below the limits of this diagram (Tagliabue et al., 2012). GOE and NOE refer to estimated timings of the Great Oxidation Event and Neoproterozoic Oxidation Event, respectively. (B) Literature estimates of the presence of oxic, ferruginous, and euxinic conditions in the shallow and deep ocean. Note that the period between the GOE and NOE contains evidence for both ferruginous conditions and euxinic conditions, sometimes co-existing.*

6.1.2 Redox evolution of Earth's oceans

The relative extent of euxinic and ferruginous conditions in the ocean has changed considerably over Earth history (Figure 6.1) (Lyons et al., 2014). Ferruginous conditions are thought to have been widespread in the Archean and Paleoproterozoic (>2.4 Ga) oceans based on the presence and δ^{57}Fe of banded iron formations (BIFs), low marine sulfate concentrations and the abundant evidence for a lack of atmospheric oxygen (Bekker et al., 2010; Fakhraee et al., 2019; Rouxel et al., 2005). Similarly, there is support for fully oxygenated oceans since the late Neoproterozoic, with the possibility of transient anoxia in the Phanerozoic, often associated with mass extinctions (Dickson, 2017). Ocean chemistry is less resolved in the mid-Proterozoic (1.8–0.8 Ga)—the period which lies between the two most significant atmospheric oxidation events—the Great Oxidation Event (GOE) and the Neoproterozoic Oxidation Event (NOE). Constraining redox conditions during this time is important since the hypothesised first appearance of eukaryotes and their initial diversification occurred within this interval (Guilbaud et al., 2015; Javaux et al., 2004; Knoll et al., 2006). Ocean chemistry in the mid-Proterozoic was initially assumed to be fully oxic shortly after the GOE (Holland, 1984) then suggested to be fully euxinic (Canfield, 1998), but has since been proposed to be spatially and temporally both ferruginous and euxinic (Planavsky et al., 2011; Sperling et al., 2015). The current understanding of this co-existence is that euxinic conditions were confined to 'wedges' near the continental shelf break and ferruginous conditions were present in much of the deep ocean (Poulton and Canfield, 2011; Poulton et al., 2010). The relative fraction of seafloor overlain by a euxinic water column in the Proterozoic remains controversial, with estimates from geochemical proxies varying between 1 and 100% (Canfield, 1998; Gilleaudeau et al., 2019; Reinhard et al., 2013; Sperling et al., 2015).

6.1.3 The iron speciation paleoredox proxy

In **Chapter 4**, I examined the molybdenum isotopic composition (δ^{98}Mo) of sediments—one of the most commonly used proxies to fingerprint ferruginous versus euxinic conditions in the geological record. Other proxies, such as iron speciation of the sediment, trace metal enrichments in shales (Reinhard et al., 2013), and the uranium isotopic composition (δ^{238}U) of carbonate minerals (Gilleaudeau et al., 2019) have also been used to address this same problem. Of these proxies, iron speciation of the sediment has been by far the most widely used due to the wide coverage of iron in marine sediments and the longevity of this method (Guilbaud et al., 2015; Planavsky et al., 2011; Poulton and Canfield, 2011; Sperling et al., 2015) (Figure 6.2).

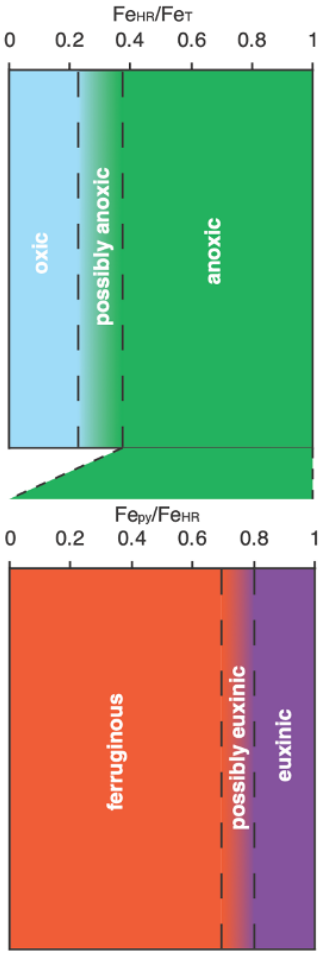

Fig. 6.2 - *Iron speciation classification scheme. The ratio of highly reactive iron (Fe_{HR}) over the total iron (Fe_T) can be used to infer an oxic vs anoxic water column above the sediment. Further speciation can be made by measuring the pyrite-hosted-iron (Fe_{PY}) relative to the Fe_{HR} which reveals euxinic versus ferruginous environments. Figure taken from Poulton and Canfield (2011)*

In an anoxic water column, highly-reactive iron minerals (Fe_{HR}) (comprising iron carbonate, iron (oxyhydr)oxide and pyrite minerals) accumulate in sediments to a greater extent than in an oxic water column. Sedimentary rocks where the ratio of Fe_{HR} to the total iron (Fe_T) exceeds 0.38 are inferred to have been deposited under an anoxic water column. Further iron speciation is also thought to be able to discriminate between sediments deposited under a euxinic versus a ferruginous water column; when the ratio of iron hosted in pyrite (Fe_{PY}) to Fe_{HR} exceeds 0.7–0.8, sediments are assumed to have been deposited in a euxinic water column (Anderson and Raiswell, 2004; März et al., 2008).

6.1.4 Potential new model for euxinic conditions overprint ferruginous sediments

Estimates of the fraction of seawater euxinia may differ among various proxies if post-depositional alteration mimics the geochemical signal imparted under euxinic conditions. Here, I will explore the idea that sediments which have been exposed—even transiently—to dissolved sulfide during early diagenesis will record a geochemical signature indicative of euxinic conditions, regardless of whether the water column itself had dissolved sulfide in it. This would imply that previous estimates of marine euxinia are too high and that euxinia is over-represented in the geological record.

This geochemical overprinting occurs due to the reaction of reactive iron minerals (predominantly iron (oxyhydr)oxides and iron carbonate minerals) with dissolved sulfide in porewater: this reaction forms iron sulfide minerals, and terminally, pyrite (Egger et al., 2016; Liu et al., 2020; Neretin et al., 2004; Raiswell and Canfield, 1996). This changes the preserved iron mineralogy and, in diffusion-limited sediment columns, redistributes the concentration and isotopic composition of metals, much of which is subsequently used to fingerprint euxinic conditions in the geological record. The key point is that the conversion of reactive iron minerals to pyrite occurs rapidly (<1000 years) for most iron-containing minerals, with the exception of iron contained in sheet-silicate minerals (Canfield et al., 1992; Raiswell and Canfield, 1996). The dissolved sulfide required for this reaction can be found in sedimentary porewater under two circumstances: (1), if there is an overlying euxinic water column from which dissolved sulfide diffuses into sediment (similar to the Black Sea today) or (2), if there is *in situ* generation of dissolved sulfide within the sediment column, typically by microbial sulfate reduction.

Once sedimentary iron minerals are converted to iron sulfide minerals, which are stable under anoxic conditions, it is unlikely they can be converted back in the absence of dissolved oxygen. Subaerial exposure of sedimentary rocks can allow this back reaction (Ahm et al.,

2017), but the mechanism to do this in an otherwise anoxic ocean is unclear. This suggests that this 'sulfidisation' effect is most significant where dissolved oxygen is low, there is widespread delivery of reactive iron minerals to global sediments, and the sediment is poised between iron-reducing and sulfate-reducing conditions.

The process of overprinting primary sedimentary mineralogy due to post-depositional exposure to dissolved sulfide has been observed in some modern marine sedimentary environments (Egger et al., 2016; Neretin et al., 2004; Scholz et al., 2013). Most modern marine sedimentary environments, however, contain low concentrations of highly-reactive iron minerals, which are efficiently trapped in estuaries and marginal marine environments (Poulton and Raiswell, 2002). In the geological past, when highly reactive iron minerals were deposited in sediment throughout the ocean, this process of overprinting could have been far more pervasive. Here, I will explore the effect of post depositional exposure to sulfide on iron speciation measurements before discussing how this process may also affect other proxies such as the trace metal and the molybdenum isotope composition in sediments.

6.2 Examination of the iron speciation proxy to diagenetic alteration

6.2.1 Evidence of diagenesis from Fe_{HR}/Fe_T and Fe_{PY}/Fe_{HR} ratios

A simple diagenetic model based on the dataset of iron-speciation measurements (n=4300) compiled in Sperling et al. (2015) is compiled to illustrate the effect of aqueous sulfide altering previously deposited iron mineralogy (Figure 6.3). This dataset comprises of iron speciation measurements made on shales from the Archean to the Neo-Proterozoic.

Theoretically, diagenesis could shift a sample with an Fe_{PY}/Fe_{HR} value of zero close to a value of one if dissolved porewater sulfide reacts with all available highly reactive iron and converts it to iron sulfide minerals. As Fe_{PY} is one component of the Fe_{HR} pool, this diagenetic exchange of a generic highly reactive iron mineral for pyrite would not shift the accompanying Fe_{HR}/Fe_T. Evidence of this effect is shown in the sediments underlying the oxic/hypoxic waters of the Bornholm Basin, whereby newly deposited sediments are characterised by an Fe_{PY}/Fe_{HR} value of 0.2–0.6 which increases with time as it becomes buried (up to an Fe_{PY}/Fe_{HR} value of 0.9 after 5000 years) (Figure 6.4). This is striking considering there is no evidence of euxinic conditions in the water column at this site, and therefore this increase in Fe_{PY}/Fe_{HR} must only reflect the diagenetic conversion of iron mineralogy (Liu et al., 2020). The Fe_{HR}/Fe_T slightly decreases over this depth range, most likely reflecting the ripening of iron mineralogy over time as opposed to any change in the

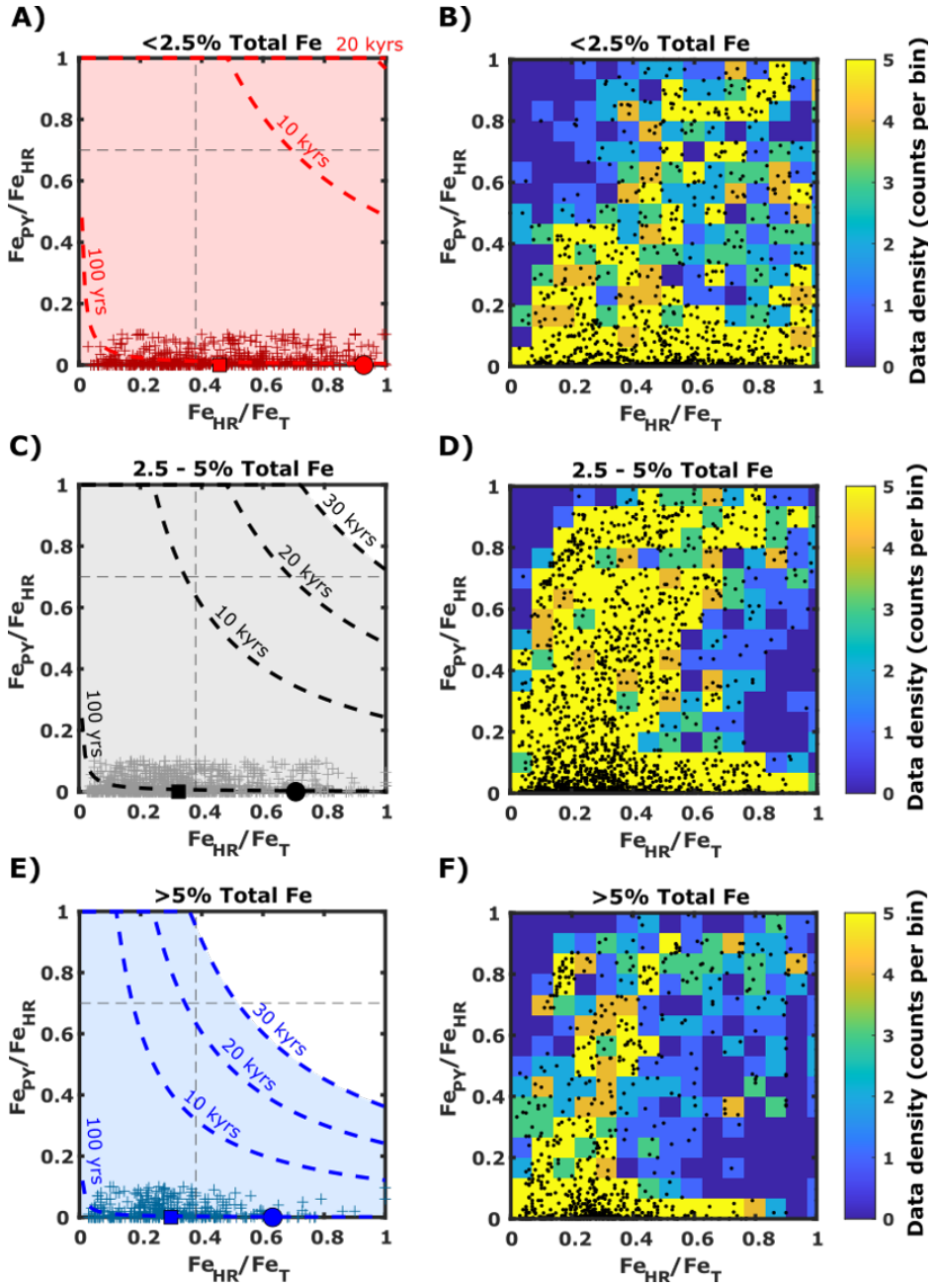

Fig. 6.3 - *The potential effect of diagenetic sulfidisation on iron speciation classification for: (A) a low Fe_T scenario (0–2.5% Fe_T), (C) an intermediate Fe_T scenario (2.5–5.0% Fe_T) and, (E) a high Fe_T scenario (>5% Fe_T). Crosses represent published iron speciation data points from Sperling et al. (2015) with Fe_{PY}/Fe_{HR} ratios<0.1 (thus representing sediments deposited in a past environment where there was no dissolved sulfide, and hence no Fe_{PY}). The mean of these data points (filled square) plus two standard deviation (filled circle) is shown. The dashed lines represent modelled changes to Fe_{PY}/Fe_{HR} based on a constant addition of sulfide (200 pMol cm^{-3} d^{-1}) after 100 yr, 10 Kyr, 20 Kyr and 30 Kyr (Egger et al., 2016). Total iron (Fe_T) is binned at 2.5%, 5% and 10% in (A), (C) and (E) respectively. Samples which plot inside the shaded area can be explained by diagenetic sulfidization up to 30,000 years of sulfide exposure. Grey dashed lines indicate classic iron-speciation classification boundaries (Canfield et al., 1992; März et al., 2008). Data density plots for the iron speciation dataset compiled by Sperling et al. (2015) for (B) 0–2.5wt% Fe_T, (D) 2.5–5wt% Fe_T and, (E) >5wt% Fe_T.*

efficacy of removal of highly reactive iron from the water column with time (Cornell and Schwertmann, 2003).

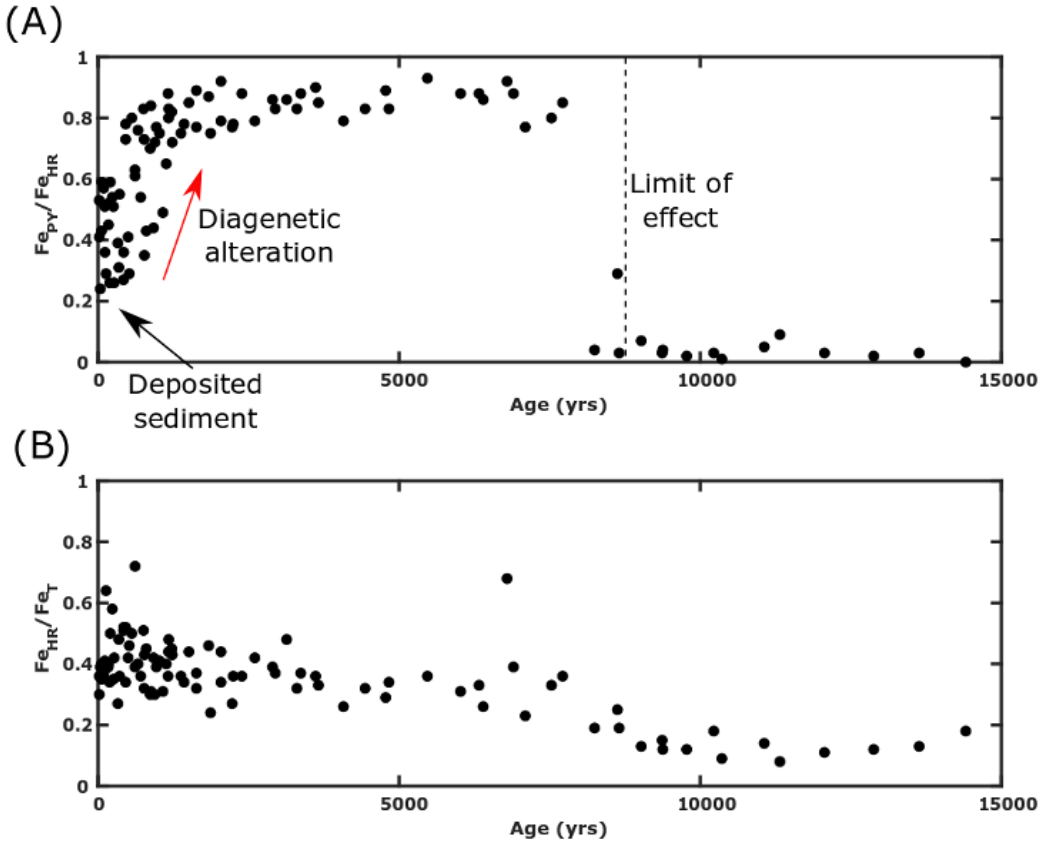

Fig. 6.4 - *Sediment age plotted against (a) Fe_{PY}/Fe_{HR} and (b) Fe_{HR}/Fe_T ratios. Sediment age was calculated by multiplying sediment depth by the sedimentation rate given in Liu et al. (2020). Sediments are deposited at sediment-water interface with a low (<0.4) Fe_{PY}/Fe_{HR} ratio, but upon burial into the sulfide production zone, become diagenetically altered to high >0.8 Fe_{PY}/Fe_{HR} ratios.*

To represent this diagenetic effect on Figure 6.3, for a given Fe_{HR}/Fe_T deposited at the sediment water interface, a vertical line can be drawn upwards on the Fe_{PY}/Fe_{HR} axis which reflects this conversion of highly-reactive iron to pyrite. There may be some potential decrease in Fe_{HR}/Fe_T if iron minerals age to become more crystalline with time (Cornell and Schwertmann, 2003), thus decreasing the numerator, but there is not an environmentally plausible method for the Fe_{HR}/Fe_T to shift towards the right post-depositionally other than longer term conversion of unreactive iron to pyrite (thus increasing Fe_{PY}). I would argue that the timescale for this would be larger than the timescale of the diagenetic model runs used in this study (Raiswell and Canfield, 1996).

6.2.2 Site specific models including a kinetic component

A more realistic framework than this Fe_{HR}/Fe_T threshold is one which considers site specific factors. A model which introduces a constant concentration of sulfide to a sediment parcel (Equation 6.1) over time is therefore more applicable (dashed lines – Figure 6.3).

$$Fe_{PY(D)} = Fe_{HR}\frac{[HS]}{2}T \tag{6.1}$$

The amount of diagenetically produced $Fe_{PY(D)}$ is a function of the concentration of Fe_{HR}, the amount of sulfide introduced to the system $[HS]$ and, the amount of time T over which dissolved sulfide is introduced. Two moles of dissolved sulfide are necessary to convert one mole of iron to pyrite, hence the division of the $[HS]$ in the equation. The dissolved sulfide is assumed to react and convert all Fe_{HR} to Fe_{PY} which assumes that the reaction rate is faster than the diffusion rate of sulfide; this is a fair assumption given the long timescales (1000+ years) that the model is run for (Raiswell and Canfield, 1996). For shorter time scales, this may not be as applicable, and kinetics of the reaction should be included. I used a 200 pMol cm^{-3} day^{-1} flux in Figure 6.3 in accordance with estimates from the Black Sea (corresponding to porewater sulfide concentrations of 1.5 mM), though site specific rates would be more applicable (Egger et al., 2016).

This model shows that higher absolute contents of Fe_{HR} (high Fe_{HR}/Fe_T samples) require larger amounts of sulfide to change Fe_{PY}/Fe_{HR} during diagenesis (Figure 6.3). In sediments with low Fe_T, virtually any measurement in an iron speciation crossplot can be generated by limited, local dissolved sulfide exposure whereas in sediments with high Fe_T, the deposited sediment is more buffered to the effect of sulfidisation due to the higher overall amount of Fe_{HR} at a given Fe_{HR}/Fe_T. The shaded zones in Figure 6.3 correspond to the space in an iron speciation cross plot where Fe_{PY}/Fe_{HR} can be explained by up to 30 kyrs of exposure to dissolved sulfide in the porewater. These are conservative estimates for the timescale of chemical reaction during burial-diagenesis; a sedimentation rate of 10 metres-per-million years corresponds to sediment exposed to dissolved sulfide over 30 cm of burial. For comparison, in the Black Sea, diagenetic sulfidisation over the last 15 kyr has overprinted close to 1 metre of sediment (Egger et al., 2016). Measurements which plot in the non-shaded upper ('euxinic') box can be assumed to have been deposited with at least some component of water column euxinia. It is clear that at higher Fe_T contents, iron speciation becomes a more reliable indicator of water column euxinia (Figure 6.3E). This is supported by the dataset of Sperling et al. (2015), where the portion of the iron speciation plot with high Fe_{HR}/Fe_T and medium (0.2–0.6) Fe_{PY}/Fe_{HR} (that which would reflect diagenetic overprinting) becomes sparser with increasing iron content.

Longer exposure times would continue to trend towards a vertical line as all iron mineralogy is ultimately converted to pyrite. Either a lower amount of initial highly reactive iron, or exposure to larger amounts of dissolved sulfide could result in a faster rate of complete pyritisation (Figure 6.5). This scenario of complete pyritisation is perhaps unlikely, given microenvironments in marine sediments or kinetic limitations. In order to preserve an iron speciation signal in the rock record, a point would need to be reached—depending on the sedimentation rate and whether a sedimentary column was advective or diffusive—where the sediment would no longer be in contact with sulfide, and this would be the preserved signal in the sedimentary rock.

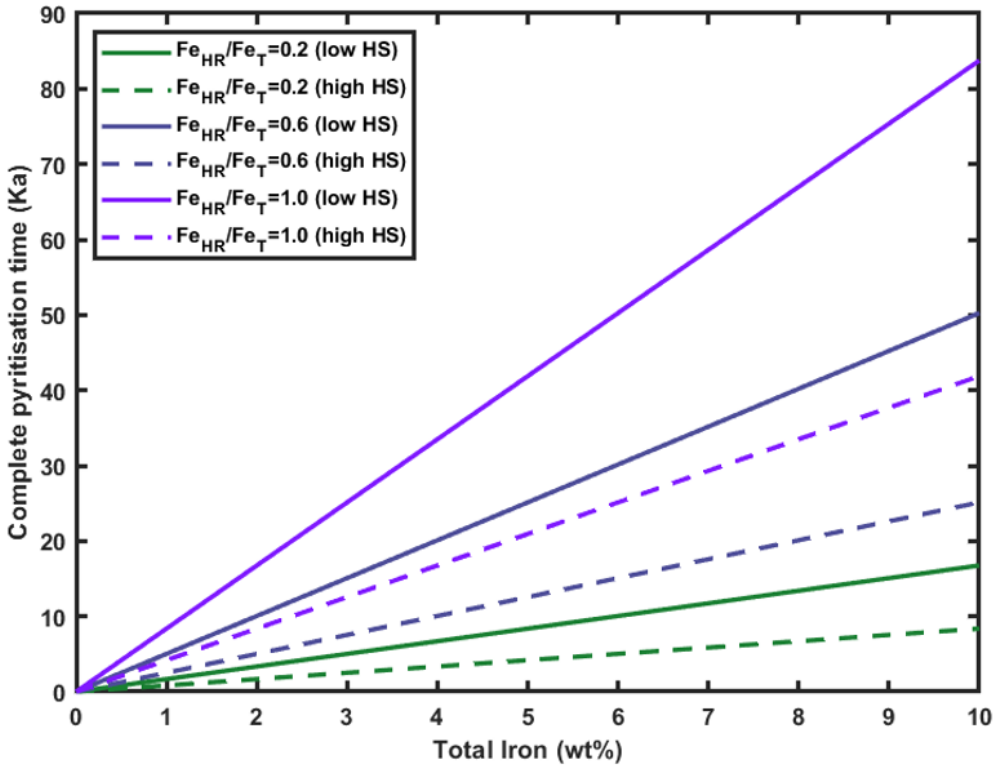

Fig. 6.5 - *Estimated time taken for complete pyritisation of the highly reactive iron pool within a sediment (i.e. the time taken for Fe_{PY}/Fe_{HR} to increase from 0 to 1) based on total iron content in the sediment (1-10%). High and low sulfide fluxes correspond to 400 pMol cm^{-3} d^{-1} and 200 pMol cm^{-3} d^{-1} respectively. A higher Fe_{HR}/Fe_T ratio for the same Fe_T value means that more of the iron is highly reactive, and thus susceptible to pyritisation.*

Samples which plot in the diagenetic portion of the modelled iron-speciation space could still potentially be generated by euxinia; this model simply suggests that such samples can be explained by solely diagenetic processes. This model cannot parse the proportion caused

by diagenetic effects versus water column effects, nor the timing of the process: it instead offers an indication of the robustness of the interpretation of water column euxinia in the geological record.

The diagenetic model is first tested in a modern-day analogous environment (Bornholm Basin). It is then used to offer a re-evaluation of the Sperling et al. (2015) composite dataset.

6.2.3 Model results from the Bornholm Basin

A recently published study offered an exciting dataset looking at diagenetic reactions in the Bornholm Basin (Liu et al., 2020). The authors of this study showed that the interpretation of the environment using iron speciation data did not fit the known redox conditions of the environment. This site was particularly applicable as an analogue given the strongly sulfidic sediments overlaying previously deposited sediment.

As stated above, there is an increase in the Fe_{PY}/Fe_{HR} ratio with age of deposition (Figure 6.4). Sediments recently deposited in the Bornholm Basin have an Fe_{PY}/Fe_{HR} which rapidly increases (within 1500 years) to 0.8–0.9. This represents burial of iron minerals (deposited at the sediment-water interface) into the sulfate reduction zone where they are exposed to dissolved sulfide and so the iron speciation signature is altered. In sediments that are older than 8000 years old, this effect is not observed. This represents the transition from lacustrine clays deposited at the last glacial maximum into the current organic-rich environment (Liu et al., 2020). Notably, one sample from the lacustrine clay lies between the higher Fe_{PY}/Fe_{HR} and the pre-8000-year Fe_{PY}/Fe_{HR} values; this may reflect downward diffusion of the dissolved sulfide produced in the overlying organic-rich sediment.

The iron speciation data from three cores in the study are tested using the diagenetic model (Figure 6.6). I use the highest Fe_T from each sediment core to establish the minimum effect of diagenesis over time. If the minimum Fe_T measured is used, all samples lie beneath the modelled zone that can be explained by diagenetic overprinting. A constant sedimentation rate is assumed and a sulfide input of 300 pMol cm^{-3} day^{-1} is used, based on the roughly 150% higher dissolved sulfide concentrations present in the Bornholm Basin compared to the Black Sea. Despite these conservative inputs, the Fe_{PY}/Fe_{HR} ratio of only nine samples are not explained by diagenesis alone. By lowering the Fe_T value even modestly, all samples can be explained readily.

This lends credence to the model as a test for diagenetic effects. Had the Bornholm Basin samples had a high Fe_{HR}/Fe_T ratio and high Fe_T contents, diagenetic effects would not have been a suitable explanation for the iron speciation measurements.

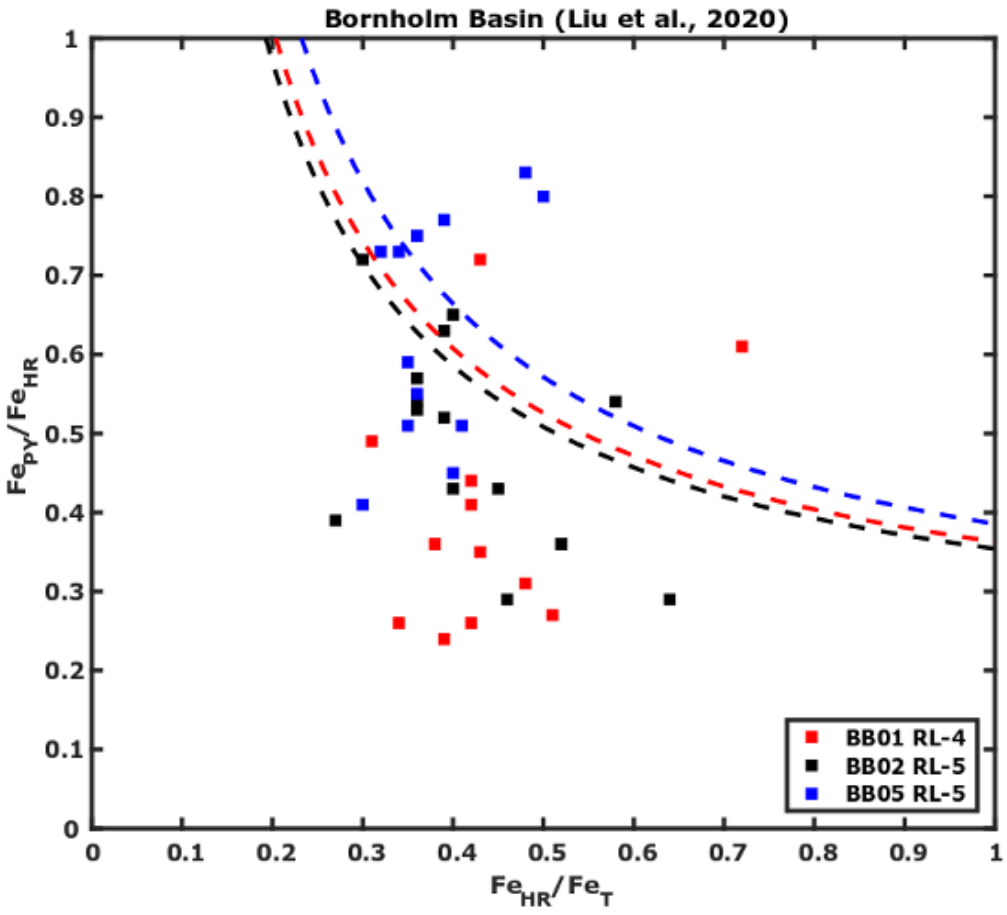

Fig. 6.6 - *Recently published data from the Bornholm Basin plotted on to the iron-speciation framework against the modelled region where diagenesis could explain the iron speciation of samples (total iron and sedimentation rates from Liu et al. (2020)). The area beneath the dashed line reflects the region where samples could be solely explained by diagenetic effects. I used a starting Fe_{PY}/Fe_{HR} ratio of 0.2 as this appears to be the approximate value of sediment at the sediment-water interface (Figure 6.4). The maximum Fe_T for each sediment core is used to representing the maximum resistance to the diagenetic effect. Red dashed line (Run for 1231 years, 0.2343 mMol/g Fe_T) represents simulated BB01 RL-4 core. Black dashed line (Run for 1132 years, 0.2365 mMol/g Fe_T) represents simulated BB02 RL-5 core. Blue dashed line (Run for 1378 years, 0.2390 mMol/g Fe_T) represents simulated BB05 RL-5 core. I used 300 pMol cm^{-3} day^{-1} as the sulfide flux based on scaling the sulfide concentrations to the Black Sea estimates (Egger et al., 2016).*

6.2.4 Re-evaluation of euxinic samples in the Sperling et al. (2015) dataset

Using my diagenetic model, I estimated how many samples of the Sperling et al. (2015) dataset which were defined as euxinic in that study could be explained by sulfidisation during diagenesis. Differences in the amount of sulfide (either 100 or 200 pMol cm^{-3} day^{-1}), differences in the starting value of Fe_{PY}/Fe_{HR} (whether the samples begin at Fe_{PY}/Fe_{HR} = 0 or 0.1), and variations in the total iron used for samples are tested to provide estimates of what proportion of samples can be explained by only diagenetic reactions (Table 6.1).

Using variations in the model inputs, the maximum proportion of samples which can be explained by solely diagenetic processes is 98%. This occurs when all samples initially contain a Fe_{PY}/Fe_{HR} of 0.1 at deposition, the total iron content is at the lowest boundary for each fraction (ie. 0.1wt%, 2.5wt% and 5 wt%) and dissolved sulfide is supplied at the high rate of 200 pMol cm^{-3} day^{-1}. All of the samples in the <2.5 wt% iron fraction can be completely explained by diagenesis in six of the eight model runs implying how susceptible sediments with low total iron are to over-printing.

A more reasonable range is that between 75 and 80% of samples previously identified as euxinic can be explained solely by post-depositional diagenesis. As many of the model inputs have similar effects on the results (i.e. a halving of sulfide production rate has the same effect as doubling the total iron), this range of estimates is more likely to correspond to the majority of samples if the sample set has a normal Gaussian distribution. The effect of time was not tested, though this can be intuitively understood as a longer time will result in more samples being diagenetically overprinted.

I acknowledge that certain samples may well have conditions that lie outside the model inputs described here. The fact that roughly three quarters of iron-speciation samples can be reasonably explained by diagenesis however, is striking.

6.2.5 Temporal variation in diagenetic overprinting

To ascertain whether samples in certain time periods may be more or less susceptible to this diagenetic effect, I split the revised estimates by age bins used in Sperling et al. (2015) (Figure 6.7). The conditions in model run 4 are used to split samples into a refined true euxinic vs diagenetically altered samples (Table 6.1). Roughly 7% of the 2300–1100 Ma samples (depicted by oldest age bin in Figure 6.7) from the Sperling et al. (2015) dataset show true euxinia. This is a large decrease from the original estimated proportion of euxinic samples ($\sim$25%) but is more in line with independent estimates from marine carbonates (Gilleaudeau et al., 2019). The limited number of samples from 1000–365 Ma makes any further interpretations tricky. All modern samples can be explained by solely diagenesis,

Model parameters	**Model Run**							
	1	**2**	**3**	**4**	**5**	**6**	**7**	**8**
Time (yrs)	30000	30000	30000	30000	30000	30000	30000	30000
Initial Fe_{PY}/Fe_{HR}	0	0	0	0	0.1	0.1	0.1	0.1
Sulfide added (pMol cm^3 day^{-1})	200	200	100	100	200	200	100	100
Total Iron	*High*	*Low*	*High*	*Low*	*High*	*Low*	*High*	*Low*
Fe_T (Wt%)	**Percentage of samples explained by diagenetic overprinting (%)**							
< 2.5	100	100	73	100	100	100	84	100
2.5–5	87	100	9	87	94	100	26	94
> 5	14	79	0	15	24	92	0	24
Total	**75**	**95**	**28**	**75**	**80**	**98**	**40**	**80**

Table 6.1 - *Estimations of the proportion of samples originally identified as 'euxinic' in Sperling et al. (2015) which may be explained by diagenetic effects alone. The initial Fe_{PY}/Fe_{HR} is varied between 0 and 0.1 which should reflect the variation in samples on deposition at the sediment-water interface in a ferruginous/oxic water column (these samples initially have no pyrite so have been exposed to no dissolved sulfide in their history). I tested the effect of sulfide addition at 100 and 200 pMol cm^{-3} day^{-1} based on estimates in (Egger et al., 2016). I tested the effect of total iron by running the models at the lower and higher estimates of Fe_T in each range: Low corresponds to 0.1, 2.5 and 5 wt% iron from the <2.5%, 2.5–5% and >5% fractions respectively. High corresponds to 2.5, 5 and 10 wt% iron from the <2.5%, 2.5–5% and >5% fractions respectively. I ran eight model simulations with each combination of these parameters. For a graphical representation of how samples were interpreted, see Figure 6.7.*

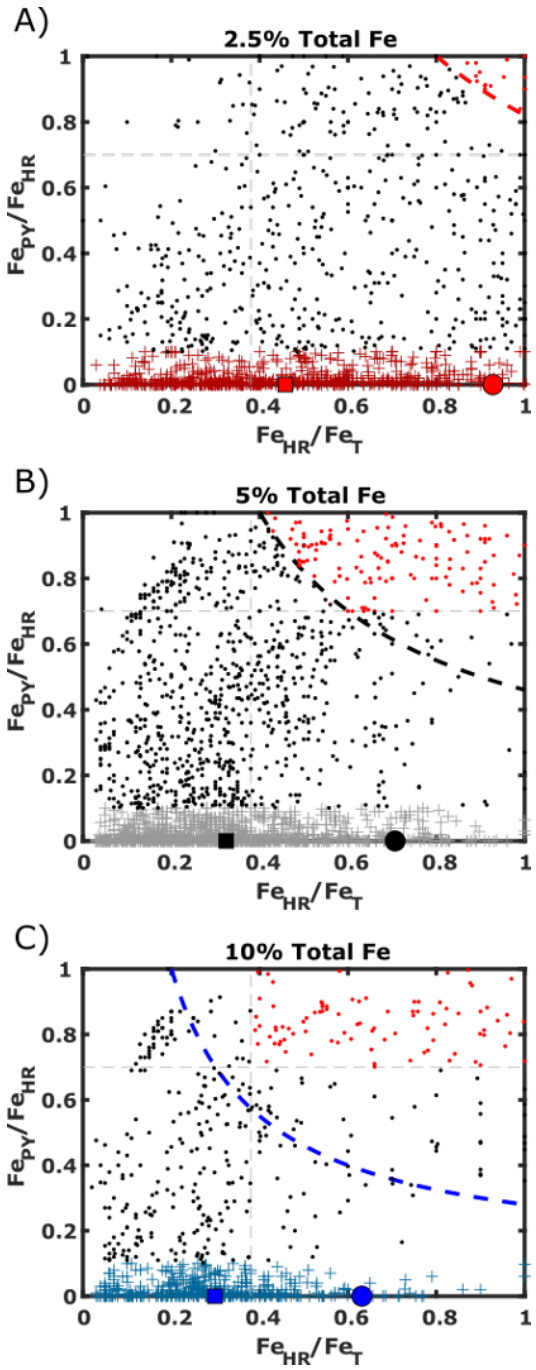

Fig. 6.7 - *Graphical representation of the selection criteria shown in model run 7 of Table 6.1. Dashed line represents the diagenetic model (Figure 6.3) run for (A) 2.5% Fe_T, (B) 5% Fe_T and, (C) 10% Fe_T. Iron speciation data is from Sperling et al. (2015) for (A) >2.5% Fe_T samples, (B) 2.5% - 5% Fe_T samples and (C), >5% Fe_T samples. Samples (circles) highlighted red lay in the classical criteria for interpretation of an environment as euxinic under iron speciation criteria and also cannot be explained by diagenetic processes alone.*

decreasing the extent of previously reported euxinic samples from 25% to 0%. This is quite notable considering that the Raiswell and Canfield (1998) dataset was used as the modern component of the dataset; this study specifically targeted anaerobic sites and so is heavily biased towards anoxic settings. The low iron content in modern sediments combined with high sulfate concentrations—and thus high concentrations of sulfide—means that diagenetic overprinting would be very common in modern sediments, though the oxic nature of the modern ocean prevents this from imparting a major bias in the record.

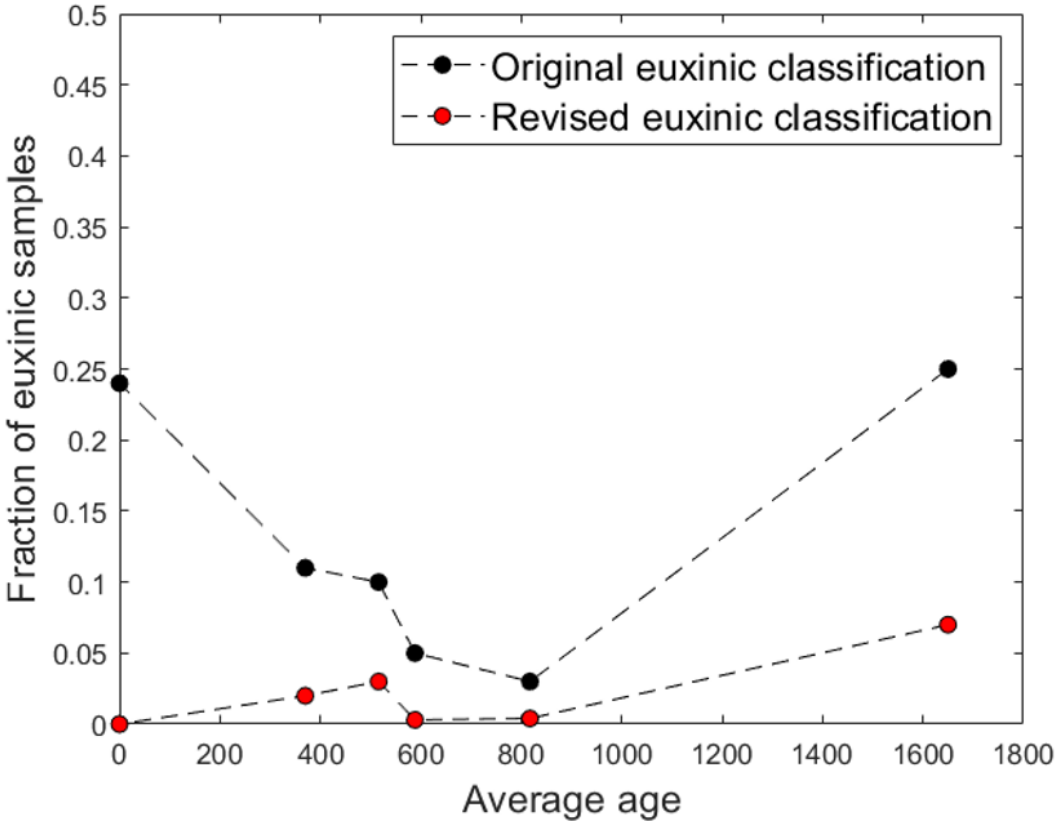

Fig. 6.8 - *Proportion of age-binned iron speciation samples from Sperling et al. (2015) according to the original euxinic classification of Poulton and Canfield (2011) (Black circles) and to the revised euxinic classification using model run 4 of Table 6.1 (Red circles). The mid-point of each age bin is used.*

6.3 Effect of diagenesis on trace metal enrichments and the δ^{98}Mo system

Diagenetic sulfidisation of iron minerals influences trace metal enrichments and the molybdenum isotopic composition of sediments (δ^{98}Mo)—two widely used geochemical proxies which are hosted in or influenced by iron mineralogy. The effect of this reaction on sediment (δ^{98}Mo) is comprehensively described in **Chapter 4**.

6.3.1 Trace metal enrichments

Trace metal enrichments (e.g. Mo, Re and U) rely on the assumption that once the trace metal is sequestered into the sediment, there is no further remobilisation within the sediment. Since the efficiency in sequestration of the trace element depends on the water column redox conditions, it is assumed that sediment concentration changes reflect water column redox changes (Algeo and Li, 2020). However, as highly-reactive iron minerals are potential sinks for many trace metals (through adsorption or co-precipitation), the breakdown of these iron minerals during sedimentary exposure to dissolved sulfide will release the mineral-bound trace metals into the surrounding porefluid, subjecting these metals to redistribution through the sediment. This has been observed in modern marginal marine environments where there are changing redox conditions (Scholz et al., 2013). The metal redistribution shifts the interpreted redox boundary; or causes a lower or higher enrichment than would be expected for a certain redox condition. This would have implications for proxies which use enrichments of trace metals to infer global seafloor euxinia (Reinhard et al., 2013; Scott and Lyons, 2012).

6.3.2 Sedimentary δ^{98}Mo

A full discussion of diagenetic effects on the sedimentary δ^{98}Mo proxy is described in **Chapter 4**. Briefly, shales deposited in euxinic conditions are assumed to record contemporaneous seawater δ^{98}Mo (Arnold, 2004). This seawater δ^{98}Mo, in turn, is interpreted to reflect the balance of a high δ^{98}Mo sink in euxinic environments (due to quantitative scavenging) and a lower δ^{98}Mo sink from absorption onto Fe-Mn oxides in oxic and suboxic conditions (Kendall et al., 2017; Siebert et al., 2003). If sediment was deposited in ferruginous conditions with Mo adsorbed to iron oxides with a low δ^{98}Mo (Goldberg et al., 2009), the breakdown of these iron oxide minerals during later exposure to dissolved sulfide would release and re-distribute this ^{95}Mo-enriched molybdenum, lowering the bulk δ^{98}Mo of the

sediment (**Chapter 4**). In such a case, the lower measured δ^{98}Mo, interpreted as contemporaneous seawater δ^{98}Mo, would lead to an overestimate of euxinic seafloor coverage. Testing sedimentary rocks using the iron speciation scheme outlined above may help to determine which δ^{98}Mo may be reflecting true seawater δ^{98}Mo and which might have been influenced by post-depositional diagenesis.

6.3.3 Other potential geochemical proxies

Geochemical proxies that consistently point to lower estimates of euxinia in the geological past are largely derived from systems where exposure of sedimentary iron minerals to dissolved sulfide is not possible, for example in the record of δ^{238}U in carbonate rocks (Gilleaudeau et al., 2019). These geochemical proxies, not reliant on highly reactive iron, largely point to between 1 and 8% seafloor euxinia in the Proterozoic.

6.4 Paleoclimate implications

The preservational bias towards euxinic conditions would have been particularly strong in the Proterozoic relative to other time points in Earth history (Figure 6.1). In the Archean, marine sulfate concentrations were minimal, therefore there was less opportunity to generate dissolved sulfide (Fakhraee et al., 2019) and the oceans were almost certainly ferruginous (Rouxel et al., 2005).

In the mid-Proterozoic, sulfate concentrations in the oceans had likely increased, introducing the potential for microbial or thermochemical sulfate reduction and the production of dissolved sulfide. Furthermore, there were lower and more variable dissolved oceanic Fe concentrations than in the Archaean due to increased oxygen in the surface environment (Derry, 2015). Thus, the sediment would be poised to enable the production of dissolved sulfide and the sulfidisation of deposited highly reactive iron.

The results of this study suggest that euxinic sediments are over-recorded in the geological record during the Proterozoic, as even short transient pulses of euxinia or sedimentary sulfide generation would introduce sulfide up to several meters into the sediment via diffusion, altering previously deposited sediments. Such an effect has been observed in the modern Black Sea (Egger et al., 2016; Neretin et al., 2004). This process would be ubiquitous in the predominantly ferruginous conditions of the mid-Proterozoic; without deep ocean oxygen, there is no feasible back-reaction to 'unreact' any iron sulfide minerals. Therefore, the mid-Proterozoic would naturally preserve more iron-sulfide-containing sediments, regardless of the extent of true water-column euxinia. Multiple brief and infrequent episodes of dissolved

sulfide production may produce an integrated signal indistinguishable from an elongated period of water-column euxinia. My results suggest that absolute extent of euxinia was up to fourfold less in the mid-Proterozoic than previously thought. This indicates some other factor than the presence of dissolved sulfide may have influenced eukaryotic evolution in the mid-Proterozoic.

In the Phanerozoic, an increase in oxygen overall, and in particular in the deep ocean means this preservational bias is lost. In the modern ocean, oxic waters interact with sediments to provide a mechanism to oxidise sedimentary sulfide; it is estimated that 95% of the dissolved sulfide produced in modern marine sediments is reoxidised to sulfate (Jørgensen, 1982). More importantly, highly reactive iron minerals in the modern ocean, and likely through most of the Phanerozoic are limited to marginal-marine and shallow-marine environments, and rarely found in the vast majority of ocean sediments. Thus, the decrease in euxinic conditions observed in the Phanerozoic may represent the cessation of this euxinic preservational bias on a wider scale.

6.5 Conclusion

The estimated extent of euxinia in the mid-Proterozoic oceans varies widely among different geochemical redox proxies (Arnold, 2004; Gilleaudeau et al., 2019; Reinhard et al., 2013; Sperling et al., 2015). The work here suggests that at least some part of this disagreement may be the result of early diagenetic overprinting of iron mineralogy during early sediment diagenesis. This would particularly affect certain proxies, such as iron speciation and metal isotope systems influenced by Fe-cycling in the subsurface, whereas proxies not dependent on iron mineralogy (e.g. carbonate hosted isotope systems) would not be affected by this.

A model based on the Sperling et al. (2015) dataset shows that a large proportion of samples previously classified as euxinic can be explained by solely diagenetic processes. This model also highlights the importance of the total iron present in a sediment, which suggests that more accurate paleoredox reconstructions may come from high-iron containing sediments (which should be more abundant in the mid-Proterozoic).

The work conducted in this chapter is a natural extension from the conclusions drawn from the previous chapters. If we wish to deconvolve diagenetic effects from the geological record, modelling work such as this will be necessary to constrain the extent of individual diagenetic reactions. This work is still in its early stages; laboratory experiments will be necessary to support the parameters used in this model and more modern analogous environments would provide further knowledge of early diagenetic reactions.

Chapter 7

Conclusion

7.1 Salt marsh geochemistry

While this thesis' primary objective was to understand the fate of trace metals during early diagenesis in a well constrained redox environment, the work undertaken has developed our understanding of the fascinating geochemical phenomenon observed in East Anglian salt marsh pond sediments.

To observe both anoxic iron-rich and sulfide-rich conditions at the surface in such close proximity is the result of a truly unique set of circumstances. Other modern analogues of anoxic iron-rich and anoxic sulfide-rich conditions exist, such as Lake Sulawesi (Indonesia) (analogous to ferruginous conditions) and the Black Sea (analogous to euxinic conditions). At such sites however, only one anoxic condition is present at the sediment surface and so comparisons between the two redox systems will require many assumptions. In East Anglian salt marshes, the controls on the pond sediment geochemistry has been found to be the result of a subtle, convolved set of conditions. The proximity of a pond in relation to creek drainage networks appears to provide a first order control on the geochemistry of pond sediments, though the age of the pond, the amount of carbon added in relation to the balance of electron acceptors and, groundwater flows may all potentially influence this relationship.

The role creek dynamics plays in shaping the geochemistry of the pond sediments is of particular interest considering the impact of anthropogenic drainage and/or climate change. More efficient creek networks will prevent ponds from forming in future, as saline water will be more efficiently exported during the ebb tide. Under these circumstances, sulfide-rich ponds would surely also become rarer, as these tend to be more distally located from creek networks. The next step would be to create a larger spatial dataset to ascertain the specific role that geomorphology of salt marshes plays on driving geochemistry, as opposed to factors such as background sedimentology or ground water flow. If geomorphology does control

pond chemistry, as is suspected, a predictive framework (e.g. using neural networks) can be developed from satellite data to extend classifications for larger salt marsh systems. Salt marshes have long been considered a hotspot of carbon sequestration, yet few attempts have been made to construct budgets which consider the spatial heterogeneity of the surface. Different pond sediment chemistries will have different total organic carbon breakdown rates to both each other and to the vegetated platform. A prediction of pond sediment chemistry will therefore offer far more accurate carbon budgets of these environments in the future.

7.2 Pond sediments as an analogue for Proterozoic ocean sediments

The fundamental premise behind using the salt marsh environment to understand the behaviour of commonly used trace-metal paleoredox systems was that these environments mimic that of ancient ocean sediments. Iron-rich pond sediment and sulfide-rich pond sediment are hypothesised to correspond to the sediments deposited under ferruginous and euxinic water columns during the mid-Proterozoic. Is this comparison justified?

The largest difference is that the water column in the mid-Proterozoic was predominantly anoxic, whereas the water column overlying the sediments in the salt marsh ponds are largely oxic. At times, organic matter can eutrophy the above pond water column, but anecdotally I have only observed this in the early morning in spring and summer months. An anoxic water column is a much more efficient sorter of redox-active elements than anoxic sediment beneath an oxic water column. Simply put, this is because there is no mechanism of transport needed to move the trace elements into the redox conditions which sequesters them. The closeness of the sedimentary molybdenum concentrations between the iron-rich and sulfide-rich pond sediment is, at least in part, a result of this. I also note that organic matter loading in wetland environments is likely larger than would have been the case on continental margins in ancient oceans. Additionally, a higher terrestrial flux of material in the salt marshes brings with it a multitude of different organic compounds which would not have been present in ancient oceans.

The regular periodic flushing of the salt marsh ponds prevents isotopic distillation, and thus quantitative capture of an isotopic signature, which is perhaps a better approximation of mid-Proterozoic ocean basins than modern restricted basins, such as the Black Sea. The combination of euxinic and ferruginous water columns in the mid-Proterozoic would likely mean water was in constant movement between these two redox conditions and that quantitative capture of elements from seawater except in very enclosed regions seems unlikely.

Scaling the processes which are occurring in a pond to the complexities of an ocean basin, however, is overly simplistic.

There are certain similarities between ancient ocean sediments and the studied salt marsh sediments which still makes the conclusions from this thesis applicable. Firstly, the high sedimentary iron concentrations in these salt marshes are perhaps the most likely to reflect ancient ocean sediments. Modern open ocean sediments contain lower total iron due to the efficient capture of iron minerals at the ocean-continental transition. Early diagenetic reactions have been shown to be a function of total Fe, therefore this environment reflects a more suitable mineralogical baseline. Second, the close poising between sulfate-reduction and iron-reduction is perhaps the best reflection of what redox conditions were like in the mid-Proterozoic. The evidence for "switching" of sediment from iron-rich to sulfide-rich would have almost certainly occurred in a similar manner in an ocean where these types of sediment co-existed. Finally, the overlying saline water is a better approximation of the conditions of ancient ocean sediments than modern lake environments, where differences in ionic composition and pH would result in a different set of diagenetic reactions and mineralogy in the sediment. The early diagenetic chemical reactions described for these salt marsh sediments are therefore possibly among the best representations of the diagenetic reactions of marine shales that are preserved in the geological record.

7.3 Early diagenetic processes on trace metal behaviour

In this thesis, I have looked at two metal isotope systems commonly used for reconstructing paleoredox conditions: chromium, and molybdenum. These elements work in conjunction with each other and were the ideal preliminary isotope systems for my objectives. Both elements are influenced by redox conditions in different ways. For chromium, the Cr(VI) species itself becomes insoluble upon reduction to Cr(III) in response to the redox potential of the environment. Other elements such as rhenium and uranium behave similarly, albeit with different redox thresholds (Algeo and Li, 2020). Molybdenum also depends on redox conditions, but it depends on the redox cycling of other elements (predominantly sulfide) rather than the Mo species itself changing with changes in Eh. This discrepancy is what causes Mo to be a potential tracer of euxinia, whilst Cr is potentially a tracer of anoxia. A robust understanding of these two elements therefore provides the fundamental groundwork behind the mechanisms which most other metal redox proxies should adhere to.

The results here suggest that metal isotope signatures do not remain constant during the initial period of burial in sediments. During the transformation of iron and sulfide mineralogy, trace metals "tag along for the ride" and become redistributed too. The very condition that

makes them so suitable for paleoredox studies could become the downfall of these metals, as they isotopically fractionate during redox changes in the early stages of diagenesis.

A pertinent question is whether these changes would become averaged out upon compaction and lithification. There is certainly an argument that the small differences observed in δ^{53}Cr would not affect the bulk sediment value. On the other hand, δ^{98}Mo of sediment varies largely during early diagenesis and would thus overwrite the initial signature of the sediment upon deposition. Two reasons can explain why Mo is so much more susceptible to diagenetic overprinting than Cr under these conditions: First, far more Mo is stripped from seawater under sulfide-containing conditions, and with a significantly higher δ^{98}Mo signature. This means there is a large difference in the end member conditions which may become diagenetically mixed. In comparison, Cr uptake quantities and δ^{53}Cr are not largely different, hence there are no large concentration gradients nor differences in δ^{53}Cr between the two types of pond sediment. The second reason relates to where the trace metal is bound within the sediment. Molybdate ions are bound by adsorption to surface of iron minerals whilst Cr ions have the additional sink of being coprecipitated with iron minerals via substitution into the lattice, and thus are more resistant to desorption or reductive dissolution of the iron minerals. Simple mass balance suggests that reactions which affect an iron mineral surface, of which there are plenty in redox active environments, are proportionally going to affect more Mo ions than Cr ions. Hence, redistribution happens faster and more comprehensively. This can be simply observed by Cr and Fe correlating in these sediments, whilst Mo and Fe do not.

7.4 The future of paleoredox proxies

I suggest that the future analysis of the geological record will have to include more paleoredox proxies applied to the same samples. All isotope systems used as paleoredox proxies so far have proven fallible in some environments, or under certain conditions. There are simply too many diagenetic reactions for this not to be the case.

Therefore, there needs to be a shift towards targeting what is wrong with an isotope system as a paleoredox proxy first and foremost. Once these characteristics are known, then another paleoredox system can be used to compensate for the drawbacks. δ^{98}Mo is a good indicator of truly euxinic conditions in the past but a well constrained iron speciation signature is needed to confirm this. “Oxic environments” characterised by near zero δ^{53}Cr values can be separated into anoxic and oxic sediments underneath an oxic water column using corresponding δ^{98}Mo signatures (Figure 5.9). Iron speciation work can prove a valuable indicator of euxinic and ferruginous conditions but depends heavily on the baseline total

iron of the sediment. In all of these cases, there are still plenty of caveats which need to be investigated to understand the veracity of paleoredox datasets.

7.5 Concluding remarks

My work has also elucidated some of the geochemical processes in the salt marsh pond sediment which are otherwise not observed in major element cycles. The novel use of trace metals as tracers of biogeochemical reactions in early sediment diagenesis is a potential direction of further exploration.

This thesis also outlines how important it is to understand a paleoredox tracer works before applying it to reconstruct past conditions. The process of an element dissolved in the ocean being sequestered into sediment and subsequently into the geological record is a long and complex process. It cannot just be assumed that the signal measured in a rock reflects the oceanic conditions of that time. The work here outlines how water column flushing, bioturbation, iron mineralogy and porewater chemistry all work in tandem to create—and potentially alter—the isotopic signature and element concentration at the sediment surface for Mo, Cr and Fe. These elements will not be unique in this capacity, and work of a similar nature is required for all paleoredox tracers if we truly wish to reconstruct past sediment conditions. No modern analogue exists which can perfectly encapsulate conditions of the widespread anoxic oceans. This means, as a community, we must go back to the mechanisms behind how elements behave in a sedimentary environment to be able to apply this understanding to the geological record.

References

Ahm, A. C., Bjerrum, C. J., and Hammarlund, E. U. (2017). Disentangling the record of diagenesis, local redox conditions, and global seawater chemistry during the latest ordovician glaciation. *Earth and Planetary Science Letters*, 459:145–156.

Albarède, F. and Beard, B. (2004). Analytical methods for non-traditional isotopes. *Reviews in Mineralogy and Geochemistry*, 55:113–152.

Alcott, L. J., Mills, B. J. W., and Poulton, S. W. (2019). Stepwise earth oxygenation is an inherent property of global biogeochemical cycling. *Science*, 366:1333–1337.

Algeo, T. J. and Li, C. (2020). Redox classification and calibration of redox thresholds in sedimentary systems. *Geochimica et Cosmochimica Acta*, 287:8–26.

Algeo, T. J. and Lyons, T. W. (2006). Mo-total organic carbon covariation in modern anoxic marine environments: Implications for analysis of paleoredox and paleohydrographic conditions. *Paleoceanography*, 21:PA1016.

Allen, J. (2000). Morphodynamics of holocene salt marshes: a review sketch from the atlantic and southern north sea coasts of europe. *Quartenary Science Reviews*, 19:1155–1231.

Anbar, A. D., Duan, Y., Lyons, T. W., Arnold, G. L., Kendall, B., Creaser, R. A., Kaufman, A. J., Gordon, G. W., Scott, C., Garvin, J., and Buick, R. (2007). A whiff of oxygen before the great oxidation event? *Science*, 317:1903–1906.

Anderson, T. F. and Raiswell, R. (2004). Sources and mechanisms for the enrichment of highly reactive iron in euxinic black sea sediments. *American Journal of Science*, 304:203–233.

Antler, G., Mills, J. V., Hutchings, A. M., Redeker, K. R., and Turchyn, A. V. (2019). The Sedimentary Carbon-Sulfur-Iron Interplay – A Lesson From East Anglian Salt Marsh Sediments. *Frontiers in Earth Science*, 7.

Arnold, G. L. (2004). Molybdenum isotope evidence for widespread anoxia in mid-proterozoic oceans. *Science*, 304:87–90.

Babechuk, M. G., Kleinhanns, I. C., and Schoenberg, R. (2017). Chromium geochemistry of the ca. 1.85 ga flin flon paleosol. *Geobiology*, 15:30–50.

Bain, D. J. and Bullen, T. D. (2005). Chromium isotope fractionation during oxidation of cr(iii) by manganese oxides. *Geochimica et Cosmochimica Acta Supplement*, 69:A212.

Ball, J. W. and Bassett, R. L. (2000). Ion exchange separation of chromium from natural water matrix for stable isotope mass spectrometric analysis. *Chemical Geology*, 168:123–134.

Barbier, E. B., Hacker, S. D., Kennedy, C., Koch, E. W., Stier, A. C., and Silliman, B. R. (2011). The value of estuarine and coastal ecosystem services. *Ecological Monographs*, 81:169–193.

Barling, J. and Anbar, A. D. (2004). Molybdenum isotope fractionation during adsorption by manganese oxides. *Earth and Planetary Science Letters*, 217:315–329.

Barnes, I. L., Garner, E. L., Gramlich, J. W., Moore, L. J., Murphy, T. J., Machlan, L. A., Shields, W. R., Tatsumoto, M., and Knight, R. J. (1973). Determination of lead, uranium, thorium, and thallium in silicate glass standard materials by isotope dilution mass spectrometry. *Analytical Chemistry*, 257:880–885.

Basu, A. and Johnson, T. M. (2012). Determination of hexavalent chromium reduction using cr stable isotopes: Isotopic fractionation factors for permeable reactive barrier materials. *Environmental Science & Technology*, 46:5353–5360.

Basu, A., Johnson, T. M., and Sanford, R. A. (2014). Cr isotope fractionation factors for cr(vi) reduction by a metabolically diverse group of bacteria. *Geochimica et Cosmochimica Acta*, 142:349–361.

Bauer, K. W., Cole, D. B., Asael, D., Francois, R., Calvert, S. E., Poulton, S. W., Planavsky, N. J., and Crowe, S. A. (2019). Chromium isotopes in marine hydrothermal sediments. *Chemical Geology*, 529:119286.

Bauer, K. W., Gueguen, B., Cole, D. B., Francois, R., Kallmeyer, J., Planavsky, N. J., and Crowe, S. A. (2018). Chromium isotope fractionation in ferruginous sediments. *Geochimica et Cosmochimica Acta*, 223:198–215.

Bekker, A., Slack, J. F., Planavsky, N. J., Krapez, B., Hofmann, A., Konhauser, K. O., and Rouxel, O. J. (2010). Iron formation: The sedimentary product of a complex interplay among mantle, tectonic, oceanic, and biospheric processes. *Economic Geology*, 105:467–508.

Berna, E. C., Johnson, T. M., Makdisi, R. S., and Basu, A. (2010). Cr stable isotopes as indicators of cr(vi) reduction in groundwater: A detailed time-series study of a point-source plume. *Environmental Science & Technology*, 44:1043–1048.

Berner, R. (1981). A new geochemical classification of sedimentary environments. *Journal of Sedimentary Research*, 51:359–365.

Bethke, C. M., Sanford, R. A., Kirk, M. F., Jin, Q., and Flynn, T. M. (2011). The thermodynamic ladder in geomicrobiology. *American Journal of Science*, 311:183–210.

Biorad (2000). Ag1, ag mp-1 and ag 2 strong anion exchange resin. Technical report, Biorad.

Birck, J. and Allègre, C. J. (1988). Manganese—chromium isotope systematics and the development of the early solar system. *Nature*, 331:579–584.

Blonder, B., Boyko, V., Turchyn, A. V., Antler, G., Sinichkin, U., Knossow, N., Klein, R., and Kamyshny, A. (2017). Impact of aeolian dry deposition of reactive iron minerals on sulfur cycling in sediments of the gulf of aqaba. *Frontiers in Microbiology*, 8:1131.

Bonnand, P., James, R. H., Parkinson, I. J., Connelly, D. P., and Fairchild, I. J. (2013). The chromium isotopic composition of seawater and marine carbonates. *Earth and Planetary Science Letters*, 382:10–20.

Bonnand, P., Parkinson, I. J., James, R. H., Karjalainen, A.-M., and Fehr, M. A. (2011). Accurate and precise determination of stable cr isotope compositions in carbonates by double spike mc-icp-ms. *Journal of Analytical Atomic Spectrometry*, 26:528–535.

Bristow, C. R., Lake, R. D., Wood, C. J., Bigg, J. P., Medd, A. W., Hughes, M. J., Gregory, D. M., Evans, R. B., Harrison, R. K., Lawrence, A. R., Clarke, M. R., and Simmons, M. B. (1985). *Geology of the country around Chelmsford Memoir for 1:50,000 geological Sheet 241*. Memoirs of the Geological Survey of Great Britain, England and Wales (Sheet - New Series). HMSO, London.

Bruggmann, S., Scholz, F., Klaebe, R. M., Canfield, D. E., and Frei, R. (2019). Chromium isotope cycling in the water column and sediments of the peruvian continental margin. *Geochimica et Cosmochimica Acta*, 257:224–242.

Brüske, A., Weyer, S., Zhao, M.-Y., Planavsky, N. J., Wegwerth, A., Neubert, N., Dellwig, O., Lau, K. V., and Lyons, T. W. (2020). Correlated molybdenum and uranium isotope signatures in modern anoxic sediments: Implications for their use as paleo-redox proxy. *Geochimica et Cosmochimica Acta*, 270:449–474.

Burd, F. (1992). *Erosion and vegetation change on the saltmarshes of Essex and north Kent between 1973 and 1988. Research and Survey in Nature Conservation*. 42. Nature Conservancy Council, Peterborough.

Canfield, D. E. (1998). A new model for proterozoic ocean chemistry. *Science*, 396:450–453.

Canfield, D. E. and Farquhar, J. (2009). Animal evolution, bioturbation, and the sulfate concentration of the oceans. *Proceedings of the National Academy of Sciences*, 106:8123–8127.

Canfield, D. E., Raiswell, R., and Bottrell, S. H. (1992). The reactivity of sedimentary iron minerals toward sulfide. *American Journal of Science*, 292:659–683.

Chappaz, A., Lyons, T. W., Gregory, D. D., Reinhard, C. T., Gill, B. C., Li, C., and Large, R. R. (2014). Does pyrite act as an important host for molybdenum in modern and ancient euxinic sediments? *Geochimica et Cosmochimica Acta*, 126:112–122.

Chroston, P. N., Jones, R., and Makin, B. (1999). Geometry of quaternary sediments along the north norfolk coast, uk: a shallow seismic study. *Geological Magazine*, 136:465–474.

Clark, S. K. and Johnson, T. M. (2008). Effective isotopic fractionation factors for solute removal by reactive sediments: A laboratory microcosm and slurry study. *Environmental Science & Technology*, 42:7850–7855.

Cline, J. D. (1969). Spectrophotometric determination of hydrogen sulfide in natural waters. *Limnology and Oceanography*, 14:454–458.

Cornell, R. M. and Schwertmann, H. C. U. (2003). *The Iron Oxides: Structure, Properties, Reactions, Occurences and Uses, Second Edition*. Wiley-VCH Verlag GmbH & Co. KGaA.

Crowe, S. A., Døssing, L. N., Beukes, N. J., Bau, M., Kruger, S. J., Frei, R., and Canfield, D. E. (2013). Atmospheric oxygenation three billion years ago. *Nature*, 501:535–538.

Dahl, T. W., Anbar, A. D., Gordon, G. W., Rosing, M. T., Frei, R., and Canfield, D. E. (2010). The behavior of molybdenum and its isotopes across the chemocline and in the sediments of sulfidic lake cadagno, switzerland. *Geochimica et Cosmochimica Acta*, 74:144–163.

Dahl, T. W., Chappaz, A., Hoek, J., McKenzie, C. J., Svane, S., and Canfield, D. E. (2017). Evidence of molybdenum association with particulate organic matter under sulfidic conditions. *Geobiology*, 15:311–323.

D'arcy, J., Babechuk, M. G., Døssing, L. N., Gaucher, C., and Frei, R. (2016). Processes controlling the chromium isotopic composition of river water: Constraints from basaltic river catchments. *Geochimica et Cosmochimica Acta*, 186:296–315.

Dass, C. (2007). *Fundamentals of contemporary mass spectrometry*. Wiley-Interscience series on mass spectrometry. Wiley-Interscience, Hobroken, N.J.

Davidson, C. M., Duncan, A. L., Littlejohn, D., Ure, A. M., and Garden, L. M. (1998). A critical evaluation of the three-stage bcr sequential extraction procedure to assess the potential mobility and toxicity of heavy metals in industrially-contaminated land. *Analytica Chimica Acta*, 363:45–55.

Deegan, L. A., Johnson, D. S., Scott, W. R., Peterson, B. J., Fleeger, J. W., Fagherazzi, S., and Wollheium, W. M. (2012). Coastal eutrophication as a driver of salt marsh loss. *Nature*, 490:388–392.

Derry, L. A. (2015). Causes and consequences of mid-proterozoic anoxia. *Geophysical Research Letters*, 42:8538–8546.

Dickson, A., Cohen, A. S., and Coe, A. L. (2014). Continental margin molybdenum isotope signatures from the early eocene. *Earth and Planetary Science Letters*, 404:389–395.

Dickson, A. J. (2017). A molybdenum-isotope perspective on phanerozoic deoxygenation events. *Nature Geoscience*, 10:10.

Dickson, A. J., Jenkyns, H. C., Porcelli, D., van der Boorn, S., and Idiz, E. (2016). Basin-scale controls on the molybdenum-isotope composition of seawater during oceanic anoxic event 2 (late cretaceous). *Geochimica et Cosmochimica Acta*, 178:291–306.

Døssing, L. N., Dideriksen, K., Stipp, S. L. S., and Frei, R. (2011). Reduction of hexavalent chromium by ferrous iron: A process of chromium isotope fractionation and its relevance to natural environments. *Chemical Geology*, 285:157–166.

Egger, M., Kraal, P., Jilbert, T., Sulu-Gambari, F., Sapart, C. J., Röckmann, T., and Slomp, C. P. (2016). Anaerobic oxidation of methane alters sediment records of sulfur, iron andphosphorus in the black sea. *Biogeosciences*, 13:5333–5355.

Ellis, A. S., Johnson, T. M., and Bullen, T. D. (2002). Chromium isotopes and the fate of hexavalent chromium in the environment. *Science*, 295:2060–2062.

Ellis, A. S., Johnson, T. M., and Bullen, T. D. (2004). Using chromium stable isotope ratios to quantify cr(vi) reduction: Lack of sorption effects. *Environmental Science & Technology*, 38:3604–3607.

Emerson, S. R. and Huested, S. S. (1991). Ocean anoxia and the concentrations of molybdenum and vanadium in seawater. *Marine Chemistry*, 34:177–196.

Emmerson, R. H. C., O'Reilly-Wiese, S. B., Macleod, C. L., and Lester, J. N. (1997). A multivariate assessment of metal distribution in inter-tidal sediments of the blackwater estuary, uk. *Marine Pollution Bulletin*, 34:960–968.

Erickson, B. E. and Helz, G. R. (2000). Molybdenum(vi) speciation in sulfidic waters: Stability and lability of thiomolybdates. *Geochimica et Cosmochimica Acta*, 64:1149–1158.

Fakhraee, M., Hancisse, O., Canfield, D. E., Crowe, S. A., and Katsev, S. (2019). Proterozoic seawater sulfate scarcity and the evolution of ocean–atmosphere chemistry. *Nature Geoscience*, 12:375–380.

Fantle, M. S. and Bullen, T. D. (2009). Essentials of iron, chromium, and calcium isotope analysis of natural materials by thermal ionization mass spectrometry. *Chemical Geology*, 258:50–64.

Farkaš, J., Frỳda, J., Paulukat, C., Hathorne, E. C., Matouškovà, S., Rohovec, J., Frỳdovà, B., Francovà, M., and Frei, R. (2018). Chromium isotope fractionation between modern seawater and biogenic carbonates from the great barrier reef, australia: Implications for the paleo-seawater δ^{53}cr reconstruction. *Earth and Planetary Science Letters*, 498:140–151.

Farquhar, J., Bao, H., and Thiemens, M. (2000). Atmospheric influence of earth's earliest sulfur cycle. *Science*, 289:756–758.

Fike, D. A., Grotzinger, J. P., Pratt, L. M., and Summons, R. E. (2006). Oxidation of the ediacaran ocean. *Nature*, 444:744–747.

Fike, D. A., Houghton, J. L., Moore, S. E., Gilhooly, W. P., Dawson, K. S., Druschel, G. K., Amend, J. P., and Orphan, V. J. (2017). Spatially resolved capture of hydrogen sulfide from the water column and sedimentary pore waters for abundance and stable isotopic analysis. *Marine Chemistry*, 197:26–37.

Filgueiras, A. V., Lavilla, I., and Bendicho, C. (2002). Chemical sequential extraction for metal partitioning in environmental solid samples. *Journal of Environmental Monitoring*, 4:823–857.

Frei, R., Gaucher, C., Poulton, S. W., and Canfield, D. E. (2009). Fluctuations in precambrian atmospheric oxygenation recorded by chromium isotopes. *Nature*, 461:250–253.

Frei, R., Poiré, D., and Frei, K. M. (2014). Weathering on land and transport of chromium to the ocean in a subtropical region (misiones, nw argentina): A chromium stable isotope perspective. *Chemical Geology*, 381:110–124.

Frei, R. and Rosing, M. T. (2005). Search for traces of the late heavy bombardment on earth—results from high precision chromium isotopes. *Earth and Planetary Science Letters*, 236:28–40.

French, J. R. and Spencer, T. (1993). Dynamics of sedimentation in a tide-dominated backbarrier salt marsh, norfolk, uk. *Marine Geology*, 110:315–331.

Froelich, P. N., Klinkhammer, G. P., Bender, M. L., Luedtke, N. A., Heath, G. R., Cullen, D., Dauphin, P., Hammond, D., Hartman, B., and Maynard, V. (1979). Early oxidation of organic matter in pelagic sediments of the eastern equatorial atlantic: suhoxic diagenesis. *Geochimica et Cosmochimica Acta*, 43:1075–1090.

Füger, A., Bruggmann, S., Frei, R., Leis, A., Dietzel, M., and Mavromatis, V. (2019). The role of ph on cr(vi) partitioning and isotopic fractionation during its incorporation in calcite. *Geochimica et Cosmochimica Acta*, 265:520–532.

Gilleaudeau, G. J., Romaniello, S. J., Luo, G., Kaufman, A. J., Zhang, F., Klaebe, R. M., Kah, L. C., Azmy, K., Bartley, J. K., Zheng, W., Knoll, A. H., and Anbar, A. D. (2019). Uranium isotope evidence for limited euxinia in mid-proterozoic oceans. *Earth and Planetary Science Letters*, 521:150–157.

Goldberg, T., Archer, C., Vance, D., and Poulton, S. W. (2009). Mo isotope fractionation during adsorption to fe (oxyhydr)oxides. *Geochimica et Cosmochimica Acta*, 73:6502–6516.

Goldberg, T., Archer, C., Vance, D., Thamdrup, B., McAnena, A., and Poulton, S. W. (2012). Controls on mo isotope fractionations in a mn-rich anoxic marine sediment, gullmar fjord, sweden. *Chemical Geology*, 296–297:73–82.

Goldberg, T., Gordon, G. W., Izon, G., Archer, C., Pearce, C. R., McManus, J., Anbar, A. D., and Rehkämper, M. (2013). Resolution of inter-laboratory discrepancies in mo isotope data: an intercalibration. *Journal of Analytical Atomic Spectrometry*, 28:724.

Goring-Harford, H. J., Klar, J. K., Donald, H. K., Pearce, C. R., Connelly, D. P., and James, R. H. (2020). Behaviour of chromium and chromium isotopes during estuarine mixing in the beaulieu estuary, uk. *Earth and Planetary Science Letters*, 536:116166.

Goring-Harford, H. J., Klar, J. K., Pearce, C. R., Connelly, D. P., Achterberg, E. P., and James, R. H. (2018). Behaviour of chromium isotopes in the eastern sub-tropical atlantic oxygen minimum zone. *Geochimica et Cosmochimica Acta*, 236:41–59.

Goto, K. T., Sekine, Y., Shimoda, G., Hein, J. R., Aoki, S., Ishikawa, A., Suzuki, K., Gordon, G. W., and Anbar, A. D. (2020). A framework for understanding mo isotope records of archean and paleoproterozoic fe- and mn-rich sedimentary rocks: Insights from modern marine hydrothermal fe-mn oxides. *Geochimica et Cosmochimica Acta*, 280:221–236.

Gueguen, B., Reinhard, C. T., Algeo, T. J., Peterson, L. C., Nielsen, S. G., Wang, X., Rowe, H., and Planavsky, N. J. (2016). The chromium isotope composition of reducing and oxic marine sediments. *Geochimica et Cosmochimica Acta*, 184:1–19.

Guilbaud, R., Poulton, S. W., Butterfield, N. J., Zhu, M., and Shields-Zhou, G. A. (2015). A global transition to ferruginous conditions in the early neoproterozoic oceans. *Nature Geoscience*, 8:466–470.

Gumsley, A. P., Chamberlain, K. R., Bleeker, W., Söderlund, U., de Kock, M. O., Larsson, E. R., and Bekker, A. (2017). Timing and tempo of the great oxidation event. *Proceedings of the National Academy of Sciences*, 114:1811–1816.

Haber, F. and Goldschmidt, F. (1906). Der anodische angriff des eisens durch vagabundierende strome im erdreich und die passivitat des eisens. *Zeitschrift fur Elektrochemie*, 12:49–76.

Hamblin, R. J. O., Moorlock, B. S. P., Booth, S. J., Jeffery, D. H., and Morigi, A. N. (1997). The red crag and norwich crag formations in eastern suffolk. *Proceedings of the Geologists' Association*, 108:11–23.

Hansel, C. M., Lentini, C. J., Tang, Y., Johnston, D. T., Wankel, S. D., and Jardine, P. M. (2015). Dominance of sulfur-fueled iron oxide reduction in low-sulfate freshwater sediments. *The ISME Journal*, 9:2400–2412.

Hausladen, D. M. and Fendorf, S. (2017). Hexavalent chromium generation within naturally structured soils and sediments. *Environmental Science & Technology*, 51:2058–2067.

Hawco, N. J., Lam, P. J., Lee, J.-M., Ohnemus, D. C., Noble, A. E., Wyatt, N. J., Lohan, M. C., and Saito, M. A. (2018). Cobalt scavenging in the mesopelagic ocean and its influence on global mass balance: Synthesizing water column and sedimentary fluxes. *Marine Chemistry*, 201:151–166.

Helz, G. R., Bura-Nakić, E., Mikac, N., and Ciglenečki, I. (2011). New model for molybdenum behavior in euxinic waters. *Chemical Geology*, 284:323–332.

Helz, G. R. and Vorlicek, T. P. (2019). Precipitation of molybdenum from euxinic waters and the role of organic matter. *Chemical Geology*, 509:178–193.

Holland, H. D. (1984). *The chemical evolution of the atmosphere and oceans.* Princeton University Press; Princeton, NJ.

Holland, H. D. (2006). The oxygenation of the atmosphere and oceans. *Philosophical Transactions of the Royal Society B: Biological Sciences*, 361:903–915.

Holmden, C., Jacobson, A. D., Sageman, B. B., and Hurtgen, M. T. (2016). Response of the cr isotope proxy to cretaceous ocean anoxic event 2 in a pelagic carbonate succession from the western interior seaway. *Geochimica et Cosmochimica Acta*, 186:277–295.

Holmkvist, L., Ferdelman, T. G., and Jørgensen, B. B. (2011). A cryptic sulfur cycle driven by iron in the methane zone of marine sediment (aarhus bay, denmark). *Geochimica et Cosmochimica Acta*, 75:3581–3599.

Hughes, R. G., Fletcher, P. W., and Hardy, M. J. (2009). Successional development of saltmarsh in two managed realignment areas in se england, and prospects for saltmarsh restoration. *Marine Ecology Progress Series*, 384:13–22.

Hutchings, A. M., Antler, G., Wilkening, J. V., Basu, A., Bradbury, H. J., Clegg, J. A., Gorka, M., Lin, C. Y., Mills, J. V., Pellerin, A., Redeker, K. R., Sun, X., and Turchyn, A. V. (2019). Creek dynamics determine pond subsurface geochemical heterogeneity in east anglian (uk) salt marshes. *Frontiers in Earth Science*, 7.

Hutchings, A. M., Basu, A., Dickson, A. J., and Turchyn, A. V. (2020). Molybdenum geochemistry in salt marsh pond sediments. *Geochimica et Cosmochimica Acta*, 284:75–91.

Hydes, D. (1977). Dissolved aluminium concentration in sea water. *Nature*, 268:136–137.

Izbicki, J. A., Ball, J. W., Bullen, T. D., and Sutley, S. J. (2008). Chromium, chromium isotopes and selected trace elements, western mojave desert, usa. *Applied Geochemistry*, 23:1325–1352.

Izbicki, J. A., Bullen, T. D., Martin, P., and Schroth, B. (2012). Delta chromium-53/52 isotopic composition of native and contaminated groundwater, mojave desert, usa. *Applied Geochemistry*, 27:841–853.

Janssen, D. J., Rickli, J., Quay, P. D., White, A. E., Nasemann, P., and Jaccard, S. L. (2020). Biological control of chromium redox and stable isotope composition in the surface ocean. *Global Biogeochemical Cycles*, 34.

Javaux, E. J., Knoll, A. H., and Walter, M. R. (2004). Tem evidence for eukaryotic diversity in mid-proterozoic oceans. *Geobiology*, 2:121–132.

Joe-Wong, C. and Maher, K. (2020). A model for kinetic isotope fractionation during redox reactions. *Geochimica et Cosmochimica Acta*, 269:661–677.

Johnston, D. T., Farquhar, J., and Canfield, D. E. (2007). Sulfur isotope insights into microbial sulfate reduction: When microbes meet models. *Geochimica et Cosmochimica Acta*, 71:3929–3947.

Jørgensen, B. B. (1982). Mineralization of organic matter in the sea bed—the role of sulphate reduction. *Nature*, 296:643–645.

Kendall, B., Dahl, T. W., and Anbar, A. D. (2017). The stable isotope geochemistry of molybdenum. *Reviews in Mineralogy and Geochemistry*, 82:683–732.

Kennish, M. J. (2001). Coastal salt marsh systems in the u.s.: A review of anthropogenic impacts. *Journal of Coastal Research*, 17:731–748.

King, E. K., Perakis, S. S., and Pett-Ridge, J. C. (2018). Molybdenum isotope fractionation during adsorption to organic matter. *Geochimica et Cosmochimica Acta*, 222:584–598.

Kirwan, M. L. and Megonigal, J. P. (2013). Tidal wetland stability in the face of human impacts and sea-level rise. *Nature*, 504:53–60.

Kitchen, J. W., Johnson, T. M., Bullen, T. D., Zhu, J., and Raddatz, A. (2012). Chromium isotope fractionation factors for reduction of cr(vi) by aqueous fe(ii) and organic molecules. *Geochimica et Cosmochimica Acta*, 89:190–201.

Klinkhammer, G. P. and Bender, M. L. (1980). The distribution of manganese in the pacific ocean. *Earth and Planetary Science Letters*, 46:361–384.

Knoll, A. H., Javaux, E. J., Hewitt, D., and Cohen, P. (2006). Eukaryotic organisms in proterozoic oceans. *Philosophical Transactions of the Royal Society B: Biological Sciences*, 361:1023–1038.

Konhauser, K. O., Lalonde, S. V., Planavsky, N. J., Pecoits, E., Lyons, T. W., Mojzsis, S. J., Rouxel, O. J., Barley, M. E., Rosiere, C., Fralick, P. W., Kump, L. R., and Bekker, A. (2011). Aerobic bacterial pyrite oxidation and acid rock drainage during the great oxidation event. *Nature*, 478:369–373.

Koretsky, C. M., Moore, C. M., Kristine, L. L., Meile, C., Dichristina, T. J., and van Cappellen, P. (2003). Seasonal oscillation of microbial iron and sulfate reduction in saltmarsh sediments (sapelo island, ga, usa). *Biogeochemistry*, 64:179–203.

Ku, T.-L., Knauss, K. G., and Mathieu, G. G. (1977). Uranium in open ocean: concentration and isotopic composition. *Deep Sea Research*, 24:1000–1017.

Kump, L. R. and Barley, M. E. (2007). Increased subaerial volcanism and the rise of atmospheric oxygen 2.5 billion years ago. *Nature*, 448:1033–1036.

Laakso, T. A. and Schrag, D. P. (2017). A theory of atmospheric oxygen. *Geobiology*, 15:366–384.

Lawrence, D. S. L., Allen, J. R. L., and Havelock, G. M. (2004). Salt marsh morphodynamics: an investigation of tidal flows and marsh channel equilibrium. *Journal of Coastal Research*, 201:301–316.

Lenton, T. M., Boyle, R. A., Poulton, S. W., Shields-Zhou, G. A., and Butterfield, N. (2014). Co-evolution of eukaryotes and ocean oxygenation in the neoproterozoic era. *Nature Geoscience*, 7:257–265.

Lin, C. Y., Turchyn, A. V., Krylov, A., and Antler, G. (2020). The microbially driven formation of siderite in salt marsh sediments. *Geobiology*, 18:207–224.

Liu, J., Pellerin, A., Antler, G., Kasten, S., Findlay, A. J., Dohrmann, I., Roy, H., Turchyn, A. V., and Jørgensen, B. B. (2020). Early diagenesis of iron and sulfur in bornholm basin sediments: the role of near-surface pyrite formation. *Geochimica et Cosmochimica Acta*, 284:43–60.

Lovley, D. R. and Chapelle, F. H. (1995). Deep subsurface microbial processes. *Reviews of Geophysics*, 33:365–381.

Lukman, S., Bukhari, A., Al-Malack, M. H., Mu'azu, N. D., and Essa, M. H. (2014). Geochemical modeling of trivalent chromium migration in saline-sodic soil during lasagna process: Impact on soil physicochemical properties. *The Scientific World Journal*, 2014:1–20.

Lyons, T. W., Anbar, A. D., Severmann, S., Scott, C., and Gill, B. C. (2009). Tracking euxinia in the ancient ocean: A multiproxy perspective and proterozoic case study. *Annual Review of Earth and Planetary Sciences*, 37:507–534.

Lyons, T. W., Reinhard, C. T., and Planavsky, N. J. (2014). The rise of oxygen in earth's early ocean and atmosphere. *Nature*, 506:307–315.

Lyons, T. W. and Severmann, S. (2006). A critical look at iron paleoredox proxies: New insights from modern euxinic marine basins. *Geochimica et Cosmochimica Acta*, 70:5698–5722.

Masiello, C. A., Chen, Y., Gao, X., S., L., Cheng, H., Bennett, M. R., Rudgers, J. A., Wagner, D. S., Zygourakis, K., and Silberg, J. J. (2013). Biochar and microbial signaling: Production conditions determine effects on microbial communication. *Environmental Science & Technology*, 47.

McCave, I. N. (1987). Fine sediment sources and sinks around the east anglian coast (uk). *Journal of the Geological Society*, 144:149–152.

McClain, C. N. and Maher, K. (2016). Chromium fluxes and speciation in ultramafic catchments and global rivers. *Chemical Geology*, 426:135–157.

McLeod, E., Chmura, G. L., Bouillon, S., Salm, R., Björk, M., Duarte, C. M., Lovelock, C. E., Schlesinger, W. H., and Silliman, B. R. (2011). A blueprint for blue carbon: toward an improved understanding of the role of vegetated coastal habitats in sequestering co_2. *Frontiers in Ecology and the Environment*, 9:552–560.

McManus, J., Berelson, W. M., Severmann, S., Poulson, R. L., Hammond, D. E., Klinkhammer, G. P., and Holm, C. (2006). Molybdenum and uranium geochemistry in continental margin sediments: Paleoproxy potential. *Geochimica et Cosmochimica Acta*, 70:4643–4662.

McManus, J., Nägler, T. F., Siebert, C., Wheat, C. G., and Hammond, D. E. (2002). Oceanic molybdenum isotope fractionation: Diagenesis and hydrothermal ridge-flank alteration. *Geochemistry, Geophysics, Geosystems*, 3:1–9.

Mel'nikov, N. N. (2005). Errors of the double spiking technique in the isotopic analysis of common lead. *Geochemistry International*, 43:1228–1234.

Mertz, W. (1992). Chromium: History and nutritional importance. *Biological Trace Element Research*, 32:3–8.

Meysman, F. J. R. (2018). Cable bacteria take a new breath using long-distance electricity. *Trends in Microbiology*, 26:411–422.

Middag, R., de Baar, H. J. W., Bruland, K. W., and van Heuven, S. M. A. C. (2020). The distribution of nickel in the west-atlantic ocean, its relationship with phosphate and a comparison to cadmium and zinc. *Frontiers in Marine Science*, 7:105.

Miller, C. A., Peucker-Ehrenbrink, B., Walker, B. D., and Marcantonio, F. (2011). Reassessing the surface cycling of molybdenum and rhenium. *Geochimica et Cosmochimica Acta*, 75:7146–7179.

Mills, J. (2014). Microbially-mediated cryptic sulfur cycling in salt marsh sediments: Evidence and implications. Master's thesis, University of Cambridge, Department of Earth Sciences, Cambridge.

Mills, J. V., Antler, G., and A.V., T. (2016). Geochemical evidence for cryptic sulfur cycling in salt marsh sediments. *Earth and Planetary Science Letters*, 453:23–32.

Moos, S. B. and Boyle, E. A. (2019). Determination of accurate and precise chromium isotope ratios in seawater samples by mc-icp-ms illustrated by analysis of safe station in the north pacific ocean. *Chemical Geology*, 511:489–493.

Moos, S. B., Boyle, E. A., Altabet, M. A., and Bourbonnais, A. (2020). Investigating the cycling of chromium in the oxygen deficient waters of the eastern tropical north pacific ocean and the santa barbara basin using stable isotopes. *Marine Chemistry*, 265:103756.

Mortimer, R. J. G., Galsworthy, A. M. J., Bottrell, S. H., Wilmot, L. E., and Newton, R. J. (2011). Experimental evidence for rapid biotic and abiotic reduction of fe (iii) at low temperatures in salt marsh sediments: a possible mechanism for formation of modern sedimentary siderite concretions: Iron reduction in salt marsh sediments. *Sedimentology*, 58:1514–1529.

März, C., Poulton, S. W., Beckmann, B., Küster, K., Wagner, T., and Kasten, S. (2008). Redox sensitivity of p cycling during marine black shale formation: Dynamics of sulfidic and anoxic, non-sulfidic bottom waters. *Geochimica et Cosmochimica Acta*, 72:3703–3717.

Nakagawa, Y., Takano, S., Firdaus, M. L., Norisuye, K., Hirata, T., Vance, D., and Sohrin, Y. (2012). The molybdenum isotopic composition of the modern ocean. *Geochemical Journal*, 46:131–141.

Nealson, K. H. (1997). Sediment bacteria: Who's there, what are they doing, and what's new? *Annual Review of Earth and Planetary Sciences*, 25:403–434.

Neretin, L. N., Böttcher, M. E., Jørgensen, B. B., Volkov, I. I., Lüschen, H., and Hilgenfeldt, K. (2004). Pyritization processes and greigite formation in the advancing sulfidization front in the upper pleistocene sediments of the black sea. *Geochimica et Cosmochimica Acta*, 68:2081–2093.

Neubert, N., Nägler, T. F., and Böttcher, M. E. (2008). Sulfidity controls molybdenum isotope fractionation into euxinic sediments: Evidence from the modern black sea. *Geology*, 36:775–778.

Nisbet, E. G. and Sleep, N. H. (2001). The habitat and nature of early life. *Nature*, 409:1083–1091.

Nägler, T. F., Anbar, A. D., Archer, C., Goldberg, T., Gordon, G. W., Greber, N. D., Siebert, C., Sohrin, Y., and Vance, D. (2014). Proposal for an international molybdenum isotope measurement standard and data representation. *Geostandards and Geoanalytical Research*, 38:149–151.

Nägler, T. F., Neubert, N., Böttcher, M. E., Dellwig, O., and Schnetger, B. (2011). Molybdenum isotope fractionation in pelagic euxinia: Evidence from the modern black and baltic seas. *Chemical Geology*, 289:1–11.

Och, L. M. and Shields-Zhou, G. A. (2012). The neoproterozoic oxygenation event: Environmental perturbations and biogeochemical cycling. *Earth-Science Reviews*, 110:26–57.

Orians, K. J., Boyle, E. A., and Bruland, K. W. (1990). Dissolved titanium in the open ocean. *Nature*, 348:322–325.

Oze, C., Bird, D. K., and Fendorf, S. (2007). Genesis of hexavalent chromium from natural sources in soil and groundwater. *Proceedings of the National Academy of Sciences*, 104:6544–6549.

Oze, C., Fendorf, S., Bird, D. K., and Coleman, R. G. (2004). Chromium geochemistry in serpentinized ultramafic rocks and serpentine soils from the franciscan complex of california. *American Journal of Science*, 304:67–101.

Oze, C., Sleep, N. H., Coleman, R. G., and Fendorf, S. (2016). Anoxic oxidation of chromium. *Geology*, 44:543–546.

Palmer, C. and Pulis, R. (1994). Ground water issue: Natural attenuation of hexavalent chromium in groundwater and soils. *EPA Ground Water Issue EPA/540/5-94/505*, page 1–12.

Paulukat, C., Døssing, L. N., Mondal, S. K., Voegelin, A. R., and Frei, R. (2015). Oxidative release of chromium from archean ultramafic rocks, its transport and environmental impact – a cr isotope perspective on the sukinda valley ore district (orissa, india). *Applied Geochemistry*, 59:125–138.

Paulukat, C., Gilleaudeau, G. J., Chernyavskiy, P., and Frei, R. (2016). The cr-isotope signature of surface seawater — a global perspective. *Chemical Geology*, 444:101–109.

Pearce, C. R., Cohen, A. S., and Parkinson, I. J. (2009). Quantitative separation of molybdenum and rhenium from geological materials for isotopic determination by mc-icp-ms. *Geostandards and Geoanalytical Research*, 33:219–229.

Pereira, N. S., Voegelin, A. R., Paulukat, C., Sial, A. N., Ferreira, V. P., and Frei, R. (2016). Chromium-isotope signatures in scleractinian corals from the rocas atoll, tropical south atlantic. *Geobiology*, 14:54–67.

Pethick, J. S. (1974). The distribution of salt pans on tidal salt marshes. *Journal of Biogeography*, 1:57.

Pethick, J. S. (1980). Salt-marsh initiation during the holocene transgression: The example of the north norfolk marshes, england. *Journal of Biogeography*, 7.

Pett-Ridge, J. and Firestone, M. K. (2005). Redox fluctuation structures microbial communities in a wet tropical soil. *Applied and Environmental Microbiology*, 71:6998–7007.

Pettine, M., Campanella, L., and Millero, F. J. (2002). Reduction of hexavalent chromium by h_2o_2 in acidic solutions. *Environmental Science & Technology*, 36:901–907.

Phelan, N., Shaw, A., and Baylis, A. (2011). The extent of saltmarsh in england and wales: 2006–2009. Technical report, Environment Agency.

Planavsky, N. J., McGoldrick, P., Scott, C. T., Li, C., Reinhard, C. T., Kelly, A. E., Chu, X., Bekker, A., Love, G. D., and Lyons, T. W. (2011). Widespread iron-rich conditions in the mid-proterozoic ocean. *Nature*, 477:448–451.

Planavsky, N. J., Reinhard, C. T., Wang, X., Thomson, D., McGoldrick, P., Rainbird, R. H., Johnson, T., Fischer, W. W., and Lyons, T. W. (2014). Low mid-proterozoic atmospheric oxygen levels and the delayed rise of animals. *Science*, 346:635–638.

Poulson, R. L., Siebert, C., McManus, J., and Berelson, W. M. (2006). Authigenic molybdenum isotope signatures in marine sediments. *Geology*, 34:617–620.

Poulson-Brucker, R. L., McManus, J., Severmann, S., and Berelson, W. M. (2009). Molybdenum behavior during early diagenesis: Insights from mo isotopes. *Geochemistry, Geophysics, Geosystems*, 10:Q06010.

Poulton, S. W. and Canfield, D. E. (2011). Ferruginous conditions: A dominant feature of the ocean through earth's history. *Elements*, 7:107–112.

Poulton, S. W., Fralick, P. W., and Canfield, D. E. (2010). Spatial variability in oceanic redox structure 1.8 billion years ago. *Nature Geoscience*, 3:486–490.

Poulton, S. W. and Raiswell, R. (2002). The low-temperature geochemical cycle of iron: From continental fluxes to marine sediment deposition. *American Journal of Science*, 302:774–805.

Puzon, G. J., Roberts, A. G., Kramer, D. M., and Xun, L. (2005). Formation of soluble organo-chromium(iii) complexes after chromate reduction in the presence of cellular organics. *Environmental Science & Technology*, 39:2811–2817.

Pye, K., Dickson, J. A. D., Schiavon, N., Coleman, M. L., and Cox, M. (1990). Formation of siderite-mg-calcite-iron sulphide concretions in intertidal marsh and sandflat sediments, north norfolk, england. *Sedimentology*, 37:325–343.

Rai, D., Eary, L. E., and Zachara, J. M. (1989). Environmental chemistry of chromium. *Science of The Total Environment*, 86:15–23.

Rai, D., Sass, B. M., and Moore, D. A. (1987). Chromium(iii) hydrolysis constants and solubility of chromium(iii) hydroxide. *Inorganic Chemistry*, 26:345–349.

Raiswell, R. and Canfield, D. E. (1996). Rates of reaction between silicate iron and dissolved sulfide in peru margin sediments. *Geochimica et Cosmochimica Acta*, 60:2777–2787.

Raiswell, R. and Canfield, D. E. (1998). Sources of iron for pyrite formation in marine sediments. *American Journal of Science*, 298:219–245.

Rauret, G., López-Sánchez, J. F., Sahuquillo, A., Rubio, R., Davidson, C., Ure, A., and Quevauviller, P. (1999). Improvement of the bcr three step sequential extraction procedure prior to the certification of new sediment and soil reference materials. *Journal of Environmental Monitoring*, 1:57–61.

Redfield, A. C. (1972). Development of a new england salt marsh. *Ecological Monographs*, 42:201–237.

Reinhard, C. T., Planavsky, N. J., Robbins, L. J., Partin, C. A., Gill, B. C., Lalonde, S. V., Bekker, A., Konhauser, K. O., and Lyons, T. W. (2013). Proterozoic ocean redox and biogeochemical stasis. *Proceedings of the National Academy of Sciences*, 110:5357–5362.

Rodler, A., Sánchez-Pastor, N., Fernández-Díaz, L., and Frei, R. (2015). Fractionation behavior of chromium isotopes during coprecipitation with calcium carbonate: Implications for their use as paleoclimatic proxy. *Geochimica et Cosmochimica Acta*, 164:221–235.

Rouxel, O. J., Bekker, A., and Edwards, K. J. (2005). Iron isotope constraints on the archean and paleoproterozoic ocean redox state. *Science*, 307:1088–1091.

Rudge, J. F., Reynolds, B. C., and Bourdon, B. (2009). The double spike toolbox. *Chemical Geology*, 265:420–431.

Saad, E. M., Wang, X., Planavsky, N. J., Reinhard, C. T., and Tang, Y. (2017). Redox-independent chromium isotope fractionation induced by ligand-promoted dissolution. *Nature Communications*, 8:1590.

Sagan, C. and Chyba, C. (1997). The early faint sun paradox: Organic shielding of ultraviolet-labile greenhouse gases. *Science*, 276:1217–1221.

Sahoo, S. K., Planavsky, N. J., Jiang, G., Kendall, B., Owens, J. D., Wang, X., Shi, X., Anbar, A. D., and Lyons, T. W. (2016). Oceanic oxygenation events in the anoxic ediacaran ocean. *Geobiology*, 14:457–468.

Saito, M. A., Sigman, D. M., and Morel, F. M. M. (2003). The bioinorganic chemistry of the ancient ocean: the co-evolution of cyanobacterial metal requirements and biogeochemical cycles at the archean–proterozoic boundary? *Inorganica Chimica Acta*, 356:308–318.

Santos, I. R., Burnett, W. C., Dittmar, T., Suryaputra, I. G. N. A., and Chanton, J. (2009). Tidal pumping drives nutrient and dissolved organic matter dynamics in a gulf of mexico subterranean estuary. *Geochimica et Cosmochimica Acta*, 73:1325–1339.

Schauble, E., Rossman, G. R., and Taylor, H. P. (2004). Theoretical estimates of equilibrium chromium-isotope fractionations. *Chemical Geology*, 205:99–114.

Scheiderich, K., Amini, M., Holmden, C., and Francois, R. (2015). Global variability of chromium isotopes in seawater demonstrated by pacific, atlantic, and arctic ocean samples. *Earth and Planetary Science Letters*, 423:87–97.

Schimel, J. (2016). Microbial ecology: Linking omics to biogeochemistry. *Nature Microbiology*, 1.

Schoenberg, R., Merdian, A., Holmden, C., Kleinhanns, I. L., Haßler, K., Wille, M., and Reitter, E. (2016). The stable cr isotopic compositions of chondrites and silicate planetary reservoirs. *Geochimica et Cosmochimica Acta*, 183:14–30.

Schoenberg, R., Zink, S., Staubwasser, M., and von Blanckenburg, F. (2008). The stable cr isotope inventory of solid earth reservoirs determined by double spike mc-icp-ms. *Chemical Geology*, 249:294–306.

Scholz, F., Baum, M., Siebert, C., Eroglu, S., Dale, A. W., Naumann, M., and Sommer, S. (2018). Sedimentary molybdenum cycling in the aftermath of seawater inflow to the intermittently euxinic gotland deep, central baltic sea. *Chemical Geology*, 491:27–38.

Scholz, F., McManus, J., and Sommer, S. (2013). The manganese and iron shuttle in a modern euxinic basin and implications for molybdenum cycling at euxinic ocean margins. *Chemical Geology*, 355:56–68.

Scholz, F., Siebert, C., Dale, A. W., and Martin, F. (2017). Intense molybdenum accumulation in sediments underneath a nitrogenous water column and implications for the reconstruction of paleo-redox conditions based on molybdenum isotopes. *Geochimica et Cosmochimica Acta*, 213:400–417.

Schulz, H. D., Dahmke, A., Schinzel, U., Wallmann, K., and Zabel, M. (1994). Early diagenetic processes, fluxes, and reaction rates in sediments of the south atlantic. *Geochimica et Cosmochimica Acta*, 58:2041–2060.

Scott, C. and Lyons, T. W. (2012). Contrasting molybdenum cycling and isotopic properties in euxinic versus non-euxinic sediments and sedimentary rocks: Refining the paleoproxies. *Chemical Geology*, 324–325:19–27.

Seeberg-Elverfeldt, J., Schlüter, M., Feseker, T., and Kölling, M. (2005). Rhizon sampling of porewaters near the sediment-water interface of aquatic systems: Rhizon porewater sampling. *Limnology and Oceanography: Methods*, 3:361–371.

Semeniuk, D. M., Maldonado, M. T., and Jaccard, S. L. (2016). Chromium uptake and adsorption in marine phytoplankton – implications for the marine chromium cycle. *Geochimica et Cosmochimica Acta*, 184:41–54.

Shaw, T. J., Gleskes, J. M., and Jahnke, R. A. (1990). Early diagenesis in differing depositional environments: The response of transition metals in pore water. *Geochimica et Cosmochimica Acta*, 54:1233–1246.

Shields, W. R., Murphy, T. J., Catanzaro, E. J., and Garner, E. L. (1966). Absolute isotopic abundance ratios and the atomic weight of a reference sample of chromium. *Journal of Research of the National Bureau of Standards Section A: Physics and Chemistry*, 70A:193–197.

Siebert, C., Nägler, T. F., von Blanckenburg, F., and Kramers, J. D. (2003). Molybdenum isotope records as a potential new proxy for paleoceanography. *Earth and Planetary Science Letters*, 211:159–171.

Skierszkan, E. K., Robertson, J. M., Lindsay, M. B. J., Stockwell, J. S., Dockrey, J. W., Das, S., Weis, D., Beckie, R. D., and Mayer, K. U. (2019). Tracing molybdenum attenuation in mining environments using molybdenum stable isotopes. *Environmental Science & Technology*, 53:5678–5686.

Skierszkan, E. K., Stockwell, J. S., Dockrey, J. W., Weis, D., Beckie, R. D., and Mayer, K. U. (2017). Molybdenum (mo) stable isotopic variations as indicators of mo attenuation in mine waste-rock drainage. *Applied Geochemistry*, 87:71–83.

Soetaert, K., Hofmann, A. F., Middelburg, J. J., Meysman, F. J. R., and Greenwood, J. (2007). The effect of biogeochemical processes on ph. *Marine Chemistry*, 105:30–51.

Sperling, E. A., Wolock, C. J., Morgan, A. S., Gill, B. C., Kunzmann, M., Halverson, G. P., Macdonald, F. A., Knoll, A. H., and Johnston, D. T. (2015). Statistical analysis of iron geochemical data suggests limited late proterozoic oxygenation. *Nature*, 523:451–454.

Spivak, A. C., Gosselin, K., Howard, E., Mariotti, G., Forbrich, I., Stanley, R., and P., S. S. (2017). Shallow ponds are heterogeneous habitats within a temperate salt marsh ecosystem. *Journal of Geophysical Research: Biogeosciences*, 122:1371–1384.

Stookey, L. L. (1970). Ferrozine—a new spectrophotometric reagent for iron. *Analytical Chemistry*, 42:779–781.

Sun, Z., Wang, X., and Planavsky, N. J. (2019). Cr isotope systematics in the connecticut river estuary. *Chemical Geology*, 506:29–39.

Szecsody, J. E., Fruchter, J. S., Phillips, J. L., Rockhold, M. L., Vermeul, V. R., Williams, M. D., Devary, B. J., and Liu, Y. (2005). Effect of geochemical and physica lheterogeneity on the hanford 100 d area in situ redox manipulation barrier longevity. *Pacific Northwest National Laboratory*, PNNL-15499 Rev. 1:276.

Tagliabue, A., Mtshali, T., Aumont, O., Bowie, A. R., Klunder, M. B., Roychoudhury, A. N., and Swart, S. (2012). A global compilation of dissolved iron measurements: focus on distributions and processes in the southern ocean. *Biogeosciences*, 9:2333–2349.

Tang, Y., Elzinga, E. J., Jae Lee, Y., and Reeder, R. J. (2007). Coprecipitation of chromate with calcite: Batch experiments and x-ray absorption spectroscopy. *Geochimica et Cosmochimica Acta*, 71:1480–1493.

Thirlwall, M. F. (2000). Inter-laboratory and other errors in pb isotope analyses investigated using a ^{207}pb–^{204}pb double spike. *Chemical Geology*, 163:299–322.

Traynor, M. (2016). Trace element redox response to organic diagenesis. Master's thesis, University of Cambridge, Department of Earth Sciences, Cambridge.

Trinquier, A., Birck, J.-L., and Allègre, C. J. (2008). High-precision analysis of chromium isotopes in terrestrial and meteorite samples by thermal ionization mass spectrometry. *Journal of Analytical Atomic Spectrometry*, 23:1565–1574.

Valiela, I., Teal, J. M., Volkmann, S., Shafer, D., and Carpenter, E. J. (1978). Nutrient and particulate fluxes in a salt marsh ecosystem: Tidal exchanges and inputs by precipitation and groundwater 1: Salt marsh nutrient exchange. *Limnology and Oceanography*, 23:798–812.

van de Velde, S. J., Hidalgo-Martinez, S., Callebaut, I., Antler, G., James, R. K., Leermakers, M., and Meysman, F. (2020). Burrowing fauna mediate alternative stable states in the redox cycling of salt marsh sediments. *Geochimica et Cosmochimica Acta*, 276:31–49.

van Huissteden, J. and van de Plassche, O. (1998). Sulphate reduction as a geomorphological agent in tidal marshes ('great marshes' at barnstable, cape cod, usa). *Earth Surface Processes and Landforms*, 23:233–236.

Volkenborn, N., Polerecky, L., Hedtkamp, S. I. C., van Beusekom, J. E. E., and de Beer, D. (2007). Bioturbation and bioirrigation extend the open exchange regions in permeable sediments. *Limnology and Oceanography*, 52:1898–1909.

Vorlicek, T. P., Helz, G. R., Chappaz, A., Vue, P., Vezina, A., and Hunter, W. (2018). Molybdenum burial mechanism in sulfidic sediments: Iron-sulfide pathway. *ACS Earth and Space Chemistry*, 2:565–576.

Vuillemin, A., Friese, A., Alawi, M., Henny, C., Nomosatyro, S., Wagner, D., Crowe, S. A., and Kallmeyer, J. (2016). Geomicrobiological features of ferruginous sediments from lake towuti, indonesia. *Frontiers in Microbiology*, 7:1007.

Wasylenki, L. E., Weeks, C. L., Bargar, J. R., Spiro, T. G., Hein, J. R., and Anbar, A. D. (2011). The molecular mechanism of mo isotope fractionation during adsorption to birnessite. *Geochimica et Cosmochimica Acta*, 75:5019–5031.

Wei, W., Klaebe, R., Ling, H., Huang, F., and Frei, R. (2020). Biogeochemical cycle of chromium isotopes at the modern earth's surface and its applications as a paleo-environment proxy. *Chemical Geology*, 541:119570.

Wilkening, J. (2017). Euxinic and Ferruginous Conditions in Salt Marsh Sediments - Dynamics of Subsurface Redox Cycles and Volatile Formation. Master's thesis, University of Cambridge, Department of Earth Sciences, Cambridge.

Wilkening, J. V., Turchyn, A. V., Redeker, K. R., Mills, J. V., Antler, G., Carrión, O., and Todd, J. D. (2019). The production and fate of volatile organosulfur compounds in sulfidic and ferruginous sediment. *Journal of Geophysical Research: Biogeosciences*, 124:3390–3402.

Wilson, C. A., Hughes, Z. J., Fitzgerald, D. M., Hopkinson, C. S., Valentine, V., and Kolker, A. S. (2014). Saltmarsh pool and tidal creek morphodynamics: Dynamic equilibrium of northern latitude saltmarshes? *Geomorphology*, 213:99–115.

Worsfold, P. J., Lohan, M. C., Ussher, S. J., and Bowie, A. R. (2014). Determination of dissolved iron in seawater: A historical review. *Marine Chemistry*, 166:25–35.

Xu, N., Christodoulatos, C., and Braida, W. (2006). Adsorption of molybdate and tetrathiomolybdate onto pyrite and goethite: Effect of ph and competitive anions. *Chemosphere*, 62:1726–1735.

Zhang, Q., Amor, K., Galer, S. J. G., Thompson, I., and Porcelli, D. (2018). Variations of stable isotope fractionation during bacterial chromium reduction processes and their implications. *Chemical Geology*, 481:155–164.

Zhang, Q., Amor, K., Galer, S. J. G., Thompson, I., and Porcelli, D. (2019). Using stable isotope fractionation factors to identify cr(vi) reduction pathways: Metal-mineral-microbe interactions. *Water Research*, 151:98–109.

Zhu, J.-M., Wu, G., Wang, X., Han, G., and Zhang, L. (2018). An improved method of cr purification for high precision measurement of cr isotopes by double spike mc-icp-ms. *Journal of Analytical Atomic Spectrometry*, 33:809–821.

Zink, S., Schoenberg, R., and Staubwasser, M. (2010). Isotopic fractionation and reaction kinetics between cr(iii) and cr(vi) in aqueous media. *Geochimica et Cosmochimica Acta*, 74:5729–5745.

Appendix A

Double Spike Calibration

Deconvolving the measured isotope ratios to produce the actual ratios requires precise measurement of the ^{50}Cr, ^{52}Cr, ^{53}Cr and ^{54}Cr isotope signals in both the double spike (DS) solution and the standard (SRM979) used to measure δ^{53}Cr (Rudge et al., 2009). It is not necessary to know the absolute values of the Cr beams for the double spike inversion since this merely alters the intercept point (i.e. where 0‰ is based), however the relative proportions must be well constrained (Mel'nikov, 2005).

The issue with determining the precise concentration of each isotope in the two solutions is that during the measurement, there will be a mass dependent instrument fractionation (usually corrected for by the double spike method). This is a particular issue with TIMS measurement as the filament loading will heterogeneous, so the isotopic fractionation will be different for each sample (Figure 3.12).

I measured the four Cr isotope beams in three aliquots of the DS solution and 4 unspiked SRM979 standards. The instrumental mass fractionation factor (p) was calculated by comparing the measured ^{53}Cr/^{52}Cr ratio in the unspiked SRM979 solutions to the absolute value reported in Shields et al. (1966) (Equation A.1). This mass fractionation factor was used to calculate the true ^{50}Cr/^{52}Cr and ^{54}Cr/^{52}Cr ratios in SRM979 to ascertain whether only mass dependent fractionation was occurring during the run (Equation A.2). The calculated average values from four SRM979 aliquots (Table A.1) are within the reported error of Shields et al. (1966) so we can assume that these corrections are working during each measurement.

$$p = \frac{\ln\left(\frac{\left(\frac{^{53}Cr}{^{52}Cr}\right)_{Shields1966}}{\left(\frac{^{53}Cr}{^{52}Cr}\right)_{Measured}}\right)}{\ln\left(\frac{^{53}Cr_{AtomicMass}}{^{52}Cr_{AtomicMass}}\right)} \tag{A.1}$$

Measurement Ratio (±2SD)	**DS Solution**	**SRM979**
^{50}Cr / ^{52}Cr	423.54701 ± *7.07335*	0.51926896 ± *0.0000282*
^{53}Cr / ^{52}Cr	13.362008 ± *0.226674*	0.11339†
^{54}Cr / ^{52}Cr	287.62152 ± *4.98277*	0.02822008 ± *0.0000256*
Spike abundance %		
^{50}Cr	58.40	4.35
^{52}Cr	0.14	83.80
^{53}Cr	1.84	0.95
^{54}Cr	39.60	0.24

Table A.1 - *The isotopic composition of the SRM979 standard and double spike solution. The $^{53}Cr/^{52}Cr$ ratio of SRM979 is used to normalise the other ratios of SRM979 assuming mass dependency. The determined ratios are within error of Shields et al. (1966). Spike abundance refers to the relative percentage of each isotope of Cr.*

$$\left(\frac{^{53}Cr}{^{52}Cr}\right)_{True} = \left(\frac{^{53}Cr}{^{52}Cr}\right)_{Meas} \left(\frac{^{53}Cr_{AtomicMass}}{^{52}Cr_{AtomicMass}}\right)^{p} \tag{A.2}$$

The issue with applying an average isotope fractionation factor to correct the double spike solution is that the fractionation factor varies both between different aliquots of SRM979 solution and during the measurement of the SRM979 standard. As such, I used the fractionation factor calculated at each point along the 200 run measurement and applied the same factor to each of the ratios in the double spike solution (i.e. position 1 fractionation factor from the SRM979 measurement was applied to position 1 of the double spike-solution). Assuming that the fractionation factor is the same for each sample run on the TIMS, this should produce accurate isotope ratios.

As the error on the double spike-solution is going to largely dictated by the smallest (^{52}Cr) beam, I used the double spike-solution run which was run at the highest voltage, and thus gave the lowest internal error. I applied the fractionation factors from each of the four measured unspiked SRM979 solutions to produce 800 measurements (4 x 200 raw measurements of double spike-solution) of the three isotope ratios. This gave me a good first estimate of the relative isotopic abundance of the solutions.

The best way to test the precision of the ratios in the double spike-solution is to alter the proportions of double spike-solution to SRM979 solution in a mixture. Whilst there is an optimum double spike-SRM979 ratio, a correctly calibrated double spike solution should produce the same δ^{53}Cr value after double spike inversion with a variety of double spike:SRM979 ratios. The double spike inversion of six measurements of double spike-

SRM979 mixtures with varying double spike:SRM979 ratio produced near identical δ^{53}Cr values (Figure A.1 - *Black squares*). In contrast, if a small perturbation (1%) was applied to the ^{54}Cr/^{50}Cr ratio, the δ^{53}Cr ratio shifted largely based on the proportion of double spike to SRM979 solution (Figure A.1 - *White triangles*). I therefore trust the calibration of the double spike-solution to produce the correct δ^{53}Cr values during inversion. A small correction is necessary to alter the absolute value to the first SRM979 measured. This was done mass dependently, so that the relative ratios were not altered relative to one another. As stated earlier, this would not alter the calibration of the double spike, it would simply change the baseline.

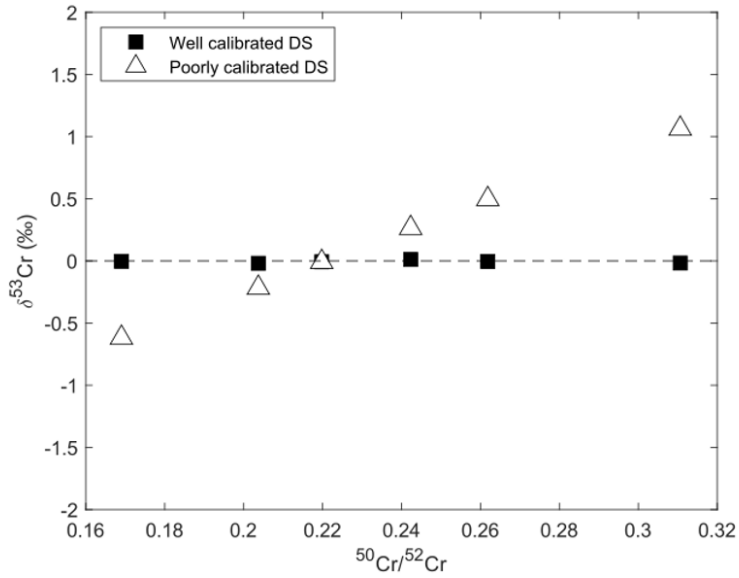

Fig. A.1 - *δ^{53}Cr produced from SRM979 with well calibrated values and poorly calibrated values of the double spike solution. Accurate measurements of the relative Cr isotope ratios mean the δ^{53}Cr does not vary with varying fractions of double spike to standard after double spike deconvolution. Poorly calibrated double spike artificially creates an incorrect δ^{53}Cr value away from the optimal ratio during double spike deconvolution.*

Appendix B

Double Spike Inversion

Double spike inversion is achieved using the Newton-Raphson method (Albarède and Beard, 2004). During double spike deconvolution, there are three unknowns: ϕ_{52}^{sp}, β_{sample} and, β_{mix}. The ϕ_{52}^{sp} refers to the mixing proportions of the double spike sample mix. β_{sample} and β_{mix} are the mass dependent fractionation factor which has occurred to the sample (unspiked) and sample-spike mix respectively. Hence, the aim of the Newton-Raphson method is to solve for these such that we reach the root of the function (F) (Equation B.1) (Albarède and Beard, 2004).

$$F_{53}(\phi_{52}^{sp},\beta_{sample},\beta_{mix}) = \phi_{52}^{sp}\left(\frac{^{53}Cr}{^{52}Cr_{spike}}\right) + (1-\phi_{52}^{sp})\left(\frac{^{53}Cr}{^{52}Cr_{SRM979}}\right)\left(\frac{52.9406527}{51.9405131}\right)^{\beta_{mix}} - \left(\frac{^{53}Cr}{^{52}Cr_{mix}}\right)\left(\frac{52.9406527}{51.9405131}\right)^{\beta_{sample}} = 0 \tag{B.1}$$

Which requires the solving of three partial derivatives of the function as follows:

$$\frac{\delta F_{53}}{\delta \phi_{52}^{sp}} = \left(\frac{^{53}Cr}{^{52}Cr_{spike}}\right) - \left(\frac{^{53}Cr}{^{52}Cr_{SRM979}}\right)\left(\frac{52.9406527}{51.9405131}\right)^{\beta_{sample}} \tag{B.2}$$

$$\frac{\delta F_{53}}{\delta \beta_{sample}} = ln\left(\frac{52.9406527}{51.9405131}\right)(1-\phi_{52}^{sp})\left(\frac{^{53}Cr}{^{52}Cr_{SRM979}}\right)\left(\frac{52.9406527}{51.9405131}\right)^{\beta_{sample}} \tag{B.3}$$

$$\frac{\delta F_{53}}{\delta \beta_{mix}} = -ln\left(\frac{52.9406527}{51.9405131}\right)\left(\frac{^{53}Cr}{^{52}Cr_{mix}}\right)\left(\frac{52.9406527}{51.9405131}\right)^{\beta_{mix}} \tag{B.4}$$

The corresponding equation is applied for the $^{50}Cr/^{52}Cr$ ratio and the $^{54}Cr/^{50}Cr$ ratio. By making initial guesses of the unknowns, a (3,3) matrix is produced from Equations B.2, B.3 and B.4. The determinant or Jacobian, (J_o), can be solved for by taking the cross product of the matrix (Equation B.5):

$$J_o = \begin{vmatrix} \frac{\delta F_{50}}{\delta \phi_{52}^{sp}} & \frac{\delta F_{53}}{\delta \phi_{52}^{sp}} & \frac{\delta F_{53}}{\delta \phi_{52}^{sp}} \\ \frac{\delta F_{50}}{\delta \beta_{sample}} & \frac{\delta F_{53}}{\delta \beta_{sample}} & \frac{\delta F_{54}}{\delta \beta_{sample}} \\ \frac{\delta F_{50}}{\delta \beta_{mix}} & \frac{\delta F_{53}}{\delta \beta_{mix}} & \frac{\delta F_{54}}{\delta \beta_{mix}} \end{vmatrix} = \frac{\delta F_{50}}{\delta \phi_{52}^{sp}} \begin{vmatrix} \frac{\delta F_{53}}{\delta \beta_{sample}} & \frac{\delta F_{54}}{\delta \beta_{sample}} \\ \frac{\delta F_{53}}{\delta \beta_{mix}} & \frac{\delta F_{54}}{\delta \beta_{mix}} \end{vmatrix} - \frac{\delta F_{53}}{\delta \phi_{52}^{sp}} \begin{vmatrix} \frac{\delta F_{50}}{\delta \beta_{sample}} & \frac{\delta F_{54}}{\delta \beta_{sample}} \\ \frac{\delta F_{50}}{\delta \beta_{mix}} & \frac{\delta F_{54}}{\delta \beta_{mix}} \end{vmatrix} + \frac{\delta F_{54}}{\delta \phi_{52}^{sp}} \begin{vmatrix} \frac{\delta F_{50}}{\delta \beta_{sample}} & \frac{\delta F_{53}}{\delta \beta_{sample}} \\ \frac{\delta F_{50}}{\delta \beta_{mix}} & \frac{\delta F_{53}}{\delta \beta_{mix}} \end{vmatrix} \tag{B.5}$$

To find the inverse of the Jacobian, this is calculated using (Equation B.6):

$$J_o^{-1} = \frac{1}{J_o} \begin{vmatrix} \frac{\delta F_{50}}{\delta \phi_{52}^{sp}} & \frac{\delta F_{50}}{\delta \beta_{sample}} & \frac{\delta F_{50}}{\delta \beta_{mix}} \\ \frac{\delta F_{53}}{\delta \phi_{52}^{sp}} & \frac{\delta F_{53}}{\delta \beta_{sample}} & \frac{\delta F_{53}}{\delta \beta_{mix}} \\ \frac{\delta F_{54}}{\delta \phi_{52}^{sp}} & \frac{\delta F_{54}}{\delta \beta_{sample}} & \frac{\delta F_{54}}{\delta \beta_{mix}} \end{vmatrix} \tag{B.6}$$

At this point, it is a simple case of multiplying the inverse of the Jacobian by the solutions to Equation B.2, B.3 and B.4 with the initial guesses of ϕ_{52}^{sp}, β_{sample} and, β_{mix} for each isotope. The next iteration of the guesses, or x_1, is thus progressed, and the same procedure is applied to calculate x_2 and so on (B.7):

$$x_1 = x_o - J_o^{-1} y_o \tag{B.7}$$

This iteration continues until convergence is reached, or where $x_i = x_{(i+1)}$. At this point, the values for ϕ_{52}^{sp}, β_{sample} and, β_{mix} are solved and the deconvolved isotope ratios can be calculated.

Appendix C

Isotope Dilution Calculation

Isotope dilution utilises the known isotopic composition of the double-spike solution to calculate the concentration of a sample. There are two artificially enriched isotopes in the double-spike solution, hence two single-isotope spike dilution concentrations can be calculated (the concentration difference calculated between the ^{50}Cr and ^{54}Cr isotope dilution method is <0.5%). For the case of the ^{54}Cr isotope dilution method, the concentration of Cr can be calculated using Equation C.1.

$$[Cr]_{Sample} = V_{Spike} \times [Cr]_{Spike} \times \left(\frac{A_{Natural}}{S_{Spike}} \right) \times \frac{\left(\frac{\left({}^{54}F_{Spike} - \frac{54}{52}Cr_{SampleCorr} \times {}^{52}F_{Spike} \right)}{\left(\frac{54}{52}Cr_{SampleCorr} \times {}^{52}F_{Nature} - {}^{54}F_{Nature} \right)} \right)}{V_{Sample}} \quad \text{(C.1)}$$

Where V_{Spike} and $[Cr]_{Sample}$ are the volume and concentration of the spike solution respectively, A refers to the weighted atomic mass of nature/double-spike mixture, $\frac{54}{52}Cr_{SampleCorr}$ refers to the double-spike corrected isotope ratio of the sample, ${}^{i}F_{Spike}$ refers to fraction of the (i) isotope of Cr within the double spike and ${}^{i}F_{Nature}$ refers to the fraction of the (i) isotope of Cr in nature. The exact volume of double-spike solution and sample needs to be known precisely to use this technique; therefore, all spike additions were weighed gravimetrically.

Appendix D

Sequential extractions of chromium from sediments

Early during my project, I attempted to measure the Cr content in different sedimentary pools to understand the mineral phases which host Cr. A plethora of sequential extraction protocols exist, ranging from 3-step extractions to 7-step extractions of sedimentary phases (Filgueiras et al., 2002; Rauret et al., 1999). I used the community accepted BCR method of extracting three pools of Cr: the soluble/exchangeable fraction (targeted by a 0.11 M acetic acid leach), the reducible fraction (targeted by a hydroxylamine hydrochloride leach), the oxidisable fraction (targeted by hydrogen peroxide followed by an ammonium acetate leach) and, a residual fraction (targeted by concentrated aqua regia leach) (Rauret et al., 1999). The results are shown in Figure D.1 for sediment extracted from 10 cm and 25 cm in an iron-rich pond sediment core. Sub-aliquots of the sediment were digested with concentrated aqua regia and agreed with the summed total of the other pools within 25% (the discrepancy likely due to a mixture of contamination blanks, sample losses and sample heterogeneity.

The exchangeable fraction is predictably small, which agrees with the low concentrations of Cr in porewater. The reducible fraction (Cr hosted in iron oxides) is roughly 20% across the pond sediments which is perhaps surprising given the association of Cr with iron (oxyhydr)oxides. The oxidisable fraction (organic matter and iron sulfide hosted Cr) makes up the majority of the Cr and is marginally higher in the deeper part of the core. The residual fraction of Cr roughly agrees with the Cr/Ti correction (Equation 5.5).

The lack of specificity of the sequential extraction methods means that these defined fractions should be treated with some caution (Davidson et al., 1998).

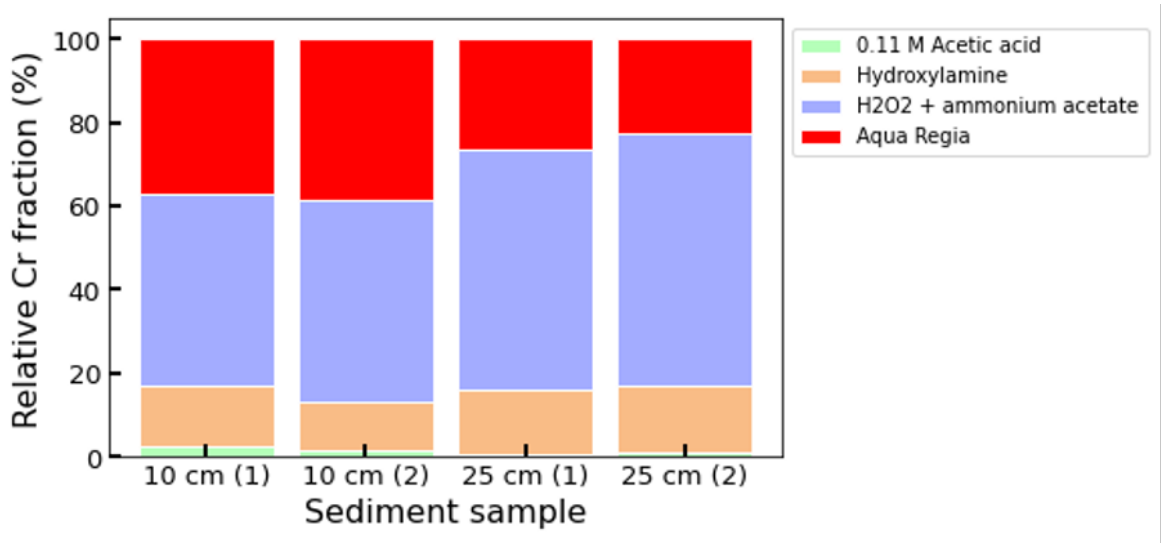

Fig. D.1 - *Sequential extraction of chromium from salt marsh iron-rich pond sediment using the BCR method (Rauret et al., 1999). Two replicates of sediment samples from 10 cm and 25 cm from an iron-rich pond sediment were analysed. Fractions were normalised to total summed concentrations of the different pools.*

Appendix E

Data tables

E.1 Data table index

Tables E1–E18 – Data tables for Chapter 2

Tables E19–E28 – Data tables for Chapter 4

Tables E29–E31 – Data tables for Chapter 5

Depth (cm)	Fe^{2+} (mM)	$\delta^{34}S_{SO_4}$ (‰)	HS^- (mM)	SO_4^{2-} (mM)	Cl (mM)	pH	Alkalinity (mEq/L)
0.7	0.01	27.7	1.6	14.4	330.8	6.14	7.2
2.7	0.00	40.3	3.5	14.9	449.0	6.56	24.0
4.7	0.00	50.5	3.7	11.6	444.1	6.94	30.2
6.7	0.00	57.7	3.9	10.2	455.2	6.88	36.5
8.7	0.00	59.3	3.9	9.5	446.7	6.87	36.3
10.7	0.00	59.1	3.8	9.5	444.0	6.82	33.3
12.7	0.00	59.3	3.5	9.3	434.0	6.97	32.0
14.7	0.00	59.2	3.6	9.1	421.9	6.89	31.3
16.7		58.8	3.0			7.09	31.2
18.7	0.00	58.9	2.6	8.2	363.4	6.95	30.2
20.7	0.00	59.2	2.8	9.0	395.3	7.08	31.4
22.7	0.00	57.5	2.6	8.4	347.7	7.15	33.9
24.7	0.00	56.8	2.3	9.6	396.2	7.18	31.1
26.7	0.00	56.2	2.4	9.5	383.8	7.16	32.2
28.7	0.00	56.3	2.1	9.4	377.1	7.12	29.9
30.7	0.00	55.4	2.3	10.3	407.3	7.08	29.9
32.7	0.00	53.6	1.8	10.7	407.4	7.21	30.2
34.7	0.00	52.3	1.5	11.5	423.0	7.15	29.5
36.7	0.00	52.5	1.0	9.9	373.9	7.17	28.6
38.7	0.00	51.8	0.7	10.6	386.1	7.37	30.4
40.7	0.00	50.6	0.6	11.4	403.2	7.34	30.1
42.7	0.00	50.4	0.0	10.7	372.1	7.27	28.7
44.7	0.00	50.0	0.0	10.4	357.2	7.53	30.3
46.7		48.1	0.0	9.8	336.9		
48.7			0.1	12.4	403.3		

Table E.1 *Geochemical characteristics of porewater in the sulfide-rich pond sediment shown in Figure 2.5*

Depth (cm)	Fe^{2+} (mM)	$\delta^{34}S_{SO_4}$ (‰)	HS^- (mM)	SO_4^{2-} (mM)	Cl (mM)	pH	Alkalinity (mEq/L)
0.5	0.09	24.1	0.0	10.7	223.5		
2.5	0.35	26.6	0.1	10.2	211.9	6.90	8.7
4.5	0.28	25.3	0.1	11.5	236.4	6.60	5.4
6.5	0.21	24.6	0.1	12.1	243.8	6.75	5.1
8.5	0.26	23.9	0.1	12.9	256.7	6.62	5.8
10.5	0.37	23.3	0.1	14.8	287.5	6.71	4.6
12.5	0.34	22.8	0.1	16.4	315.9	6.15	3.9
14.5	0.53	22.1	0.1	17.6	338.3	6.50	4.9
16.5	0.83	20.9	0.1	23.1	411.3	6.59	5.2
18.5	1.02	20.4	0.0	25.0	446.6	6.62	5.5
20.5	1.24	19.9	0.1	25.1	456.5	6.59	5.1
22.5	1.28	20.0	0.1	25.7	476.5	6.45	5.3
24.5	1.37	20.0	0.1	26.5	495.3		
26.5	1.33	19.9	0.1	25.3	481.9	6.33	5.2
28.5	1.38	20.1	0.0	25.7	493.3	6.44	5.3
30.5	1.90		0.1	25.6	506.7		
32.5	1.58	20.4	0.0	24.8	481.5	6.52	6.4
34.5	1.63	20.7	0.0	23.8	467.5	6.42	7.1
36.5	1.54	21.0	0.0	23.9	468.0	6.27	4.5
38.5			0.0				
40.5			0.0				

Table E.2 *Geochemical characteristics of porewater in the iron-rich pond sediment shown in Figure 2.5*

Nov-13 Iron-rich pond Warham			**Nov-13 Iron-rich pond Stiffkey**			**Jan-14 Iron-rich pond Warham**		
Depth (cm)	**Fe^{2+} (mM)**	**$\delta^{34}S_{SO_4}$ (‰)**	**Depth (cm)**	**Fe^{2+} (mM)**	**$\delta^{34}S_{SO_4}$ (‰)**	**Depth (cm)**	**Fe^{2+} (mM)**	**$\delta^{34}S_{SO_4}$ (‰)**
5		20.6	0		20.7	0	0.04	20.4
7	0.34	20.9	1.9	0.15	20.6	1.5	0.71	20.4
9	0.12	20.6	3.9	0.28	21.7	3.5	0.65	20.4
11	0.25	20.9	5.9	0.16	21.2	5.5	0.26	20.1
13	0.27	20.6	7.9	0.17	21.3	7.5	0.21	20.2
15	0.39	21.3	9.9	0.15	21.3	9.5	0.07	20.1
17	0.13	21.4	11.9	0.07	21.4	13.5	0.30	20.6
19	0.19	21.2	13.9	0.00	21.3	15.5	0.42	20.7
21	0.35	21.1	15.9	0.09	21.3	17.5	0.27	20.8
23	0.13	20.8	17.9	0.12	21.6	19.5	0.64	21.0
27	0.98	20.6	19.9	0.20		21.5	0.99	21.1
31	1.18	20.5	21.9	0.13	21.4	23.5	1.60	21.0
33	1.53	20.6	23.9	0.14	22.4	25.5	1.65	20.9
			25.9	0.44	22.4			
			27.9	1.86	22.8			
			29.9	1.38	22.8			

Table E.3 *Fe^{2+} concentrations and $\delta^{34}S_{SO_4}$ of porewater in multiple iron-rich pond sediment cores shown in Figure 2.6a/e (Table 1/2)*

May-14 Iron-rich pond Warham			**Oct-15 Iron-rich pond Stiffkey**			**Oct-17 Iron-rich pond Blakeney**	
Depth (cm)	**Fe^{2+} (mM)**	**$\delta^{34}S_{SO_4}$ (‰)**	**Depth (cm)**	**Fe^{2+} (mM)**	**$\delta^{34}S_{SO_4}$ (‰)**	**Depth (cm)**	**Fe^{2+} (mM)**
0.75	0.47	21.6	1	0.58	20.9	3.25	0.1114
2.75	0.40	23.3	3	0.43	23.1	5.25	0.0369
4.75	0.38	22.9	5	0.47	23.2	7.25	0.0502
6.75	0.34	22.3	7	0.34	22.9	9.25	0.0693
8.75	0.27	22.4	9	0.44	22.3	11.25	0.0356
10.75	0.36		11	0.45	22.5	13.25	0.0262
12.75	0.52	21.7	13	0.48	22.6	15.25	0.0845
14.75	0.69	21.6	15	0.65	23.6	17.25	0.1892
16.75	0.94	21.6	17	0.68	24.6	19.25	0.311
18.75	1.14	21.5	19	0.79	25.6	21.25	0.7147
20.75	1.18	21.4	21	0.65	25.9	23.25	0.9978
22.75	1.37	21.4	23	0.74	27.1		
24.75	1.46	21.5	25	0.71	27.4		
26.75	1.61	21.2	27	0.63	28.2		
28.75	1.81	21.2	29	0.60	28.8		
30.75	1.77	21.3					
32.75	1.93	21.3					
34.75	2.20	21.6					

Table E.4 *Fe^{2+} concentrations and $\delta^{34}S_{SO_4}$ of porewater in multiple iron-rich pond sediment cores shown in Figure 2.6a/e (Table 2/2)*

Nov-13 Iron-rich pond Stiffkey			**Nov-13 Iron-rich pond Stiffkey**			**Mar-14 Iron-rich pond Warham**		
Depth (cm)	**Fe^{2+} (mM)**	**$\delta^{34}S_{SO_4}$ (‰)**	**Depth (cm)**	**Fe^{2+} (mM)**	**$\delta^{34}S_{SO_4}$ (‰)**	**Depth (cm)**	**Fe^{2+} (mM)**	**$\delta^{34}S_{SO_4}$ (‰)**
0	0.059	20.3	0	0.260	20.6	0	0.00	20.1
2.4	0.193	21.0	1.2	1.250	21.7	0.9	0.37	20.9
4.4	0.157	20.8	3.2	1.119	21.5	2.9	0.40	21.0
6.4	0.049	20.6	5.2	0.759	21.5	4.9	0.15	20.8
8.4	0.104	20.6	7.2	0.589	21.3	6.9	0.12	20.7
10.4	0.079	20.7	9.2	0.443	21.2	8.9	0.16	20.7
12.4	0.031	20.7	11.2	0.468	21.2	10.9	0.18	20.8
14.4	0.040		13.2	0.303	21.2	12.9	0.08	20.8
16.4	0.050		15.2	0.433	21.2	14.9	0.01	20.8
18.4	0.016	20.6	17.2	0.602	21.1	16.9	0.02	20.6
20.4	0.000	20.5	19.2	0.454	21.1	18.9	0.00	20.7
22.4	0.093	19.8	21.2	0.393	21.3			
			23.2	0.312	21.2			
			25.2	0.024	21.1			
			27.2	0.023	21.0			
			29.2	0.016	20.9			
			31.2	0.011	21.1			
			33.2	0.044	21.0			
			35.2	0.010	21.2			

Table E.5 *Fe^{2+} concentrations and $\delta^{34}S_{SO_4}$ of porewater in multiple iron-rich pond sediment cores shown in Figure 2.6b/f (Table 1/2)*

Dec-17 Iron-rich pond Blakeney		**Dec-17 Iron-rich pond Blakeney**	
Depth (cm)	**Fe(II) (mM)**	**Depth (cm)**	**Fe(II) (mM)**
1	0.71	0.5	0.83
3	0.43	2.5	0.45
5	0.51	4.5	0.54
7	0.44	6.5	0.46
9	0.59	8.5	0.63
11	0.52	10.5	0.55
13	0.39	12.5	0.40
15	0.31	14.5	0.31
17	0.29	16.5	0.29
19	0.29	18.5	0.29
21	0.23	20.5	0.11
23	0.15	22.5	0.16
25	0.13	24.5	0.13
27	0.14	26.5	0.14
29	0.16	28.5	0.17
31	0.16	30.5	0.13

Table E.6 *Fe^{2+} concentrations of porewater in multiple iron-rich pond sediment cores shown in Figure 2.6b/f (Table 2/2)*

Nov-13 Sulfide-rich pond Blakeney		Nov-13 Sulfide-rich pond Blakeney		Nov-13 Sulfide-rich pond Blakeney	
Depth (cm)	$\delta^{34}S_{SO_4}$ (‰)	**Depth (cm)**	$\delta^{34}S_{SO_4}$ (‰)	**Depth (cm)**	$\delta^{34}S_{SO_4}$ (‰)
0.5	25.8	0	20.6	0	20.7
1.5	34.4	0.5	22.8	2	34.3
2.5	37.9	2.5	40.1	4	48.5
3.5	43.7	4.5	54.3	6	61.4
4.5	49.9	6.5	65.2	8	69.7
5.5	53.1	8.5	63.4	10	74.2
6.5	55.4	10.5	57.0	12	72.0
7.5	57.0	12.5	52.7	14	72.5
8.5	57.3	14.5	47.8	16	71.1
9.5	57.4	16.5	44.5	18	67.1
10.5	56.6	18.5	40.5	20	
		20.5	37.0	22	65.9
		22.5	33.4	24	64.9
		24.5	30.6	26	63.3
		26.5	28.1	28	62.8
		28.5	27.1		
		30.5	28.2		
		32.5	28.8		
		34.5	30.2		

Table E.7 *$\delta^{34}S_{SO_4}$ of porewater in multiple sulfide-rich pond sediment cores shown in Figure 2.6g (Table 1/2)*

Oct-15 Sulfide-rich pond Blakeney			**Dec-17 Sulfide-rich pond Blakeney**	
Depth (cm)	**Fe(II) (mM)**	$\delta^{34}S_{SO_4}$ (‰)	**Depth (cm)**	**Fe(II) (mM)**
1	0.00	30.8	0.5	0.00
2	0.00	33.1	2.5	0.00
3	0.00	46.3	4.5	0.00
4	0.00	49.7	6.5	0.00
5	0.00		8.5	0.00
6	0.00		10.5	0.00
7	0.00		12.5	0.00
8	0.00		14.5	0.00
9	0.00		16.5	0.00
10	0.00		18.5	0.00
11	0.00		20.5	0.00
12	0.00		22.5	0.00
14	0.00		24.5	0.00
16	0.00	70.9	26.5	0.00
18	0.00	68.4	28.5	0.00
20	0.00	61.9	30.5	0.00
24	0.00	63.0		
25	0.00			
27	0.00	61.2		
30	0.00	60.4		
32	0.00	58.3		

Table E.8 *Fe^{2+} concentrations and $\delta^{34}S_{SO_4}$ of porewater in multiple sulfide-rich pond sediment cores shown in Figure 2.6c/g (Table 2/2)*

Oct-15			**Nov-13**		
Warham			**Warham**		
Vegetated platform			**Vegetated platform**		
Depth (cm)	**Fe(II) (mM)**	$\delta^{34}S_{SO_4}$ (‰)	**Depth (cm)**	**Fe(II) (mM)**	$\delta^{34}S_{SO_4}$ (‰)
2.5	0.05	22.1	1	0.01	
3.5	0.00	22.8	3	0.01	20.8
4.5	0.00	23.2	5	0.01	21.2
5.5	0.01	23.7	6	0.01	21.2
6.5	0.00	24.3	8	0.01	21.2
7.5	0.00	24.8	10	0.02	21.5
8.5	0.01	25.1	12	1.18	21.8
9.5	0.59	25.9	14	1.19	22.2
10.5	1.07	26.7	16	1.26	22.4
11.5	1.82	26.6	18	1.15	22.9
12.5	2.61	28.3			
14.5	3.08	28.9			
16.5	3.42	29.4			
18.5	2.95	29.8			
20.5	2.78	30.4			
23.5	2.34	30.9			
26.5	2.00	31.6			
29.5	1.87	32.9			
32.5	1.95	34.4			
35.5	1.26	35.6			

Table E.9 *Fe^{2+} concentrations and $\delta^{34}S_{SO_4}$ of porewater in multiple sulfide-rich pond sediment cores shown in Figure 2.6d/h*

Month **Depth (cm)**	**March-17** $\delta^{34}S_{SO_4}$ (‰)	**April-17** $\delta^{34}S_{SO_4}$ (‰)	**May-17** $\delta^{34}S_{SO_4}$ (‰)	**July-17** $\delta^{34}S_{SO_4}$ (‰)	**Nov.-17** $\delta^{34}S_{SO_4}$ (‰)	**May-18** $\delta^{34}S_{SO_4}$ (‰)	**HS (mM)**
0	27.6	29.2	56.6	40.6	44.3	37.6	1.2
2	33.5	35.7	36.8	47.6	55.1	45.6	1.9
4	38.8	41.5	42.0	48.7	60.7	48.9	2.9
6	42.3	45.3	45.1	51.5	63.0	51.0	2.0
8	47.5	48.0	48.6	56.5	62.8	52.8	2.2
10	52.2	49.0	50.9	58.3	62.4		1.8
12	53.6	53.2	53.4	58.3	64.7	55.4	2.1
14	56.6	56.1	56.1	57.9	61.5	58.0	2.8
16	56.4	57.4	57.1	58.3	63.9		
18	55.7	57.4	57.2	58.2	63.4	59.4	2.6
20	56.1	56.6	56.8	58.2	62.3	59.2	2.0
22	55.1	56.5	56.6	58.0		59.8	1.9
24	51.6	53.5	55.0	56.4	60.4	59.2	2.1
26	50.2	53.3	54.4	55.0	56.8	56.4	1.9
28	51.6	53.4	53.9	55.5	57.9	57.8	1.5
30	49.9	51.6	52.7	54.0	54.5	57.2	0.9
32	48.3	50.7	51.2	53.0	54.5	55.4	0.5
34	49.3	50.8	50.5	51.3	54.3	55.8	0.3

Table E.10 $\delta^{34}S_{SO_4}$ *of porewater over a 14-month period collected by in situ samplers in sulfide-rich pond sediment at Warham shown in Figure 2.11a*

Month **Depth (cm)**	**March-17** $\delta^{34}S_{SO_4}$ (‰)	**April-17** $\delta^{34}S_{SO_4}$ (‰)	**May-17** $\delta^{34}S_{SO_4}$ (‰)	**July-17** $\delta^{34}S_{SO_4}$ (‰)	**Nov.-17** $\delta^{34}S_{SO_4}$ (‰)	**May-18** $\delta^{34}S_{SO_4}$ (‰)	**HS (mM)**
0	20.2	20.2	20.7	20.8	20.6	21.4	0.0
4		27.2	31.0	44.1	26.3	22.5	0.0
6			31.5	49.3	31.7	23.6	0.1
8	27.5	28.9	35.3	56.0	41.1	27.2	0.3
10	27.1	28.7	34.6	52.8	45.7	29.5	0.3
12	27.3	28.6	33.9	47.9	48.5	32.4	0.6
14	27.1	28.6	32.5	43.5	49.1	35.0	0.8
16	26.3	27.3	29.9	36.7	45.4	34.1	1.1
18	26.0	27.4	29.8	35.5	45.0	35.4	1.2
20	26.4	27.3	29.5	34.8	43.5	36.7	0.8
22	25.9	26.7	28.8	33.3	41.5	36.8	1.1
24	25.7	26.6	28.3	31.9	39.7	36.5	1.2
26	25.8	25.9	27.4	29.7	37.9	37.4	1.3
28	25.6	25.5	27.0	29.4	36.7	37.4	0.9
30	25.4	25.6	25.6	28.3	34.8	36.9	1.1
32		25.4	26.1	27.8	32.9	36.6	0.9
34	25.4	25.0	25.5	26.4	31.9	36.0	0.8

Table E.11 *$\delta^{34}S_{SO_4}$ of porewater over a 14-month period collected by in situ samplers in suspected intermediate pond sediment at Warham shown in Figure 2.11b*

V-Core 1 **Depth (cm)**	**Cl (M)**	**SO_4 (M)**	**SO_4/Cl**	$\delta^{34}S_{SO_4}$ (‰)	**Fe(II) (mM)**
7	0.63	0.032	0.051	21.9	0.02
9	0.65	0.034	0.052	21.9	0.01
11	0.66	0.034	0.052	21.8	0.04
15	0.60	0.030	0.050	22.1	0.86
19	0.53	0.026	0.049	22.2	1.27
23	0.51	0.025	0.050	22.7	0.79
27	0.49	0.024	0.049	23.0	0.62
29	0.49	0.024	0.049	23.2	0.72
31	0.49	0.024	0.050	23.0	0.81
33	0.51	0.025	0.050	22.9	0.91
35	0.49	0.024	0.050		1.12
37	0.50	0.025	0.050	22.9	1.51

Table E.12 *Geochemical data for V-Core 1 from the core transect at Abbotts Hall salt marsh (Figure 2.17)*

V-Core 2 **Depth (cm)**	**Cl (M)**	**SO_4 (M)**	**SO_4/Cl**	$\delta^{34}S_{SO_4}$ (‰)	**Fe(II) (mM)**
2.5	1.05	0.063	0.060	20.1	0.01
6.5	0.99	0.050	0.051	20.9	0.00
10.5	0.89	0.047	0.052	21.6	0.00
14.5	0.82	0.044	0.054	22.2	0.01
18.5	0.80	0.045	0.057	22.7	0.02
22.5	0.80	0.048	0.059	23.3	0.09
24.5	0.81	0.048	0.060	23.5	0.06
26.5	0.82	0.049	0.060	24.0	0.06
30.5	0.84	0.050	0.060	24.6	0.15
34.5	0.86	0.050	0.059	25.0	0.39
38.5	0.89	0.050	0.056	25.7	0.64
42.5	0.88	0.048	0.055	26.0	1.42

Table E.13 *Geochemical data for V-Core 2 from the core transect at Abbotts Hall salt marsh (Figure 2.17)*

V-Core 3 Depth (cm)	Cl (M)	SO_4 (M)	SO_4/Cl	$\delta^{34}S_{SO_4}$ (‰)	Fe(II) (mM)
7	0.74	0.035	0.047	22.4	0.04
9	0.73	0.036	0.049	23.0	0.01
11	0.73	0.037	0.050	23.3	0.00
13	0.72	0.037	0.051	23.5	0.01
15	0.69	0.036	0.051	23.6	0.02
17	0.66	0.034	0.051	24.0	0.08
19	0.66	0.034	0.052	23.9	0.16
21	0.66	0.035	0.052	24.2	0.43
23	0.67	0.035	0.052	24.4	0.50
27	0.68	0.036	0.052	24.9	1.01
31	0.70	0.036	0.052	25.4	1.22
33	0.71	0.036	0.051	25.6	1.02

Table E.14 *Geochemical data for V-Core 3 from the core transect at Abbotts Hall salt marsh (Figure 2.17)*

I-Core Depth (cm)	Cl (M)	SO_4 (M)	SO_4/Cl	$\delta^{34}S_{SO_4}$ (‰)	Fe(II) (mM)
1.5	0.58	0.031	0.054	18.6	0.23
3.5	0.58	0.033	0.056	17.7	0.41
5.5	0.60	0.033	0.055	18.0	0.15
9.5	0.60	0.032	0.054	18.6	0.18
11.5	0.58	0.031	0.053	18.9	0.28
13.5	0.59	0.030	0.052	19.7	0.48
15.5	0.57	0.029	0.051	20.0	0.49
17.5	0.57	0.029	0.051	21.1	1.44
21.5	0.56	0.028	0.051	22.4	1.65
25.5	0.57	0.030	0.053	22.4	2.12
29.5	0.57	0.030	0.053	22.7	3.11
33.5	0.57	0.030	0.053	22.1	4.02

Table E.15 *Geochemical data for I-Core from the core transect at Abbotts Hall salt marsh (Figure 2.17)*

S-Core Depth (cm)	Cl (M)	SO_4 (M)	SO_4/Cl	$\delta^{34}S_{SO_4}$ (‰)	Fe(II) (mM)
2	0.62	0.029	0.047	27.5	0.00
4	0.66	0.028	0.042	33.4	0.00
8	0.63	0.023	0.036	36.3	0.00
10	0.61	0.022	0.036	36.7	0.00
12	0.59	0.021	0.037	38.6	0.00
14	0.58	0.019	0.034	41.2	0.00
16	0.58	0.019	0.033	45.5	0.00
20	0.60	0.018	0.030	49.2	0.00
24	0.61	0.019	0.030	48.7	0.00
28	0.63	0.020	0.031	47.6	0.00
32	0.62	0.020	0.032	46.6	0.00
34	0.63	0.020	0.032	45.6	0.00
36	0.63	0.021	0.033	45.2	0.01
38	0.64	0.022	0.034	44.4	0.13
40	0.63	0.022	0.034	43.0	0.08

Table E.16 *Geochemical data for S-Core from the core transect at Abbotts Hall salt marsh (Figure 2.17)*

Creek Core Depth (cm)	Cl (M)	SO_4 (M)	SO_4/Cl	$\delta^{34}S_{SO_4}$ (‰)	Fe(II) (mM)
0	0.58	0.029	0.050	23.7	1.64
2	0.56	0.027	0.048	24.7	3.38
4	0.54	0.025	0.047	25.5	3.69
6	0.51	0.024	0.047	25.8	5.40
8	0.52	0.025	0.048	25.9	4.95
10	0.52	0.025	0.049	25.8	4.70
12	0.51	0.025	0.048	25.8	4.96
14	0.51	0.025	0.049	25.7	4.42
18	0.52	0.025	0.049	25.8	4.14
20	0.51	0.025	0.049	25.8	3.95

Table E.17 *Geochemical data for Creek Core from the core transect at Abbotts Hall salt marsh (Figure 2.18)*

Sample No.	Organic Carbon content (%)	Distance from boundary layer (Fig. 2-9) (m)
1	10.6	72
2	9.1	73
2 (Repeat)	8.6	73
2 (Repeat)	9.2	73
3	8.0	54
4	7.3	
5	9.2	60
6	11.2	201
7	8.2	188
7 (Repeat)	9.4	
7 (Repeat)	9.6	
7 (Acid cleaned)	9.7	
8	15.0	80
9	12.0	193
10	8.7	170
10 (Acid cleaned)	11.1	170
11	11.0	187
11 (Acid cleaned)	11.9	187
12	6.3	237
13	8.9	205
14	7.6	245
15	5.6	248
15 (Acid cleaned)	6.0	248
16	7.7	289
17	6.9	272
18	7.0	309
19	7.6	337
20	9.0	350
21	7.2	415
22	9.3	253
23	10.3	210
24	12.7	184
25	10.7	183
26	6.6	244
27	7.8	251
27 (Acid cleaned)	9.5	251
28	8.5	275
29	8.6	265
30	8.1	317

Table E.18 *Organic carbon content (%) in the surface sediment in ponds as shown in Figure 2.16*

Depth (cm)	**δ^{98}Mo (‰)**	**Mo (ppb)**	**Mn (ppb)**	**Fe^{2+} (mM)**	**HS^- (mM)**	**Cl (mM)**	**SO_4 (mM)**	**SO_4/Cl**
0 (Pond)	2.36 ± *0.03*	7.33 ± 0.08				0.533 ± *0.014*	0.027 ± *0.002*	0.0507
0.5	2.55 ± *0.08*	11.35 ± *0.17*	1053	1.26	0.000	0.595 ± *0.016*	0.032 ± *0.002*	0.0546
2.5	1.84 ± *0.09*	12.87 ± *0.21*	1148	1.04	0.000	0.605 ± *0.016*	0.033 ± *0.002*	0.0554
4.5	1.88 ± *0.11*	11.37 ± *0.16*	1243	1.00	0.000	0.610 ± *0.016*	0.034 ± *0.002*	0.0550
6.5	2.25 ± *0.11*	19.35 ± *0.29*	1476	1.05	0.000	0.616 ± *0.016*	0.034 ± *0.002*	0.0551
8.5	2.50 ± *0.11*	32.65 ± *0.45*	1600	1.06	0.000	0.626 ± *0.017*	0.034 ± *0.002*	0.0550
10.5	2.19 ± *0.05*	12.92 ± *0.16*	1767	1.22	0.000	0.641 ± *0.017*	0.035 ± *0.002*	0.0552
12.5	1.62 ± *0.07*	19.12 ± *0.33*	2110	1.19	0.001	0.650 ± *0.017*	0.036 ± *0.002*	0.0554
14.5	2.35 ± *0.06*	18.94 ± *0.34*	2965	1.61	0.000	0.676 ± *0.018*	0.038 ± *0.002*	0.0563
16.5	2.53 ± *0.03*	9.84 ± *0.11*	3561	1.72	0.000	0.697 ± *0.018*	0.039 ± *0.002*	0.0559
18.5	1.96 ± *0.04*	27.70 ± *0.41*	3901	1.81	0.000	0.711 ± *0.019*	0.040 ± *0.002*	0.0557
20.5	2.03 ± *0.03*	18.40 ± *0.23*	4945	1.75	0.000	0.722 ± *0.019*	0.040 ± *0.002*	0.0557
22.5	2.96 ± *0.05*	8.55 ± *0.09*	5517	1.47	0.000	0.717 ± *0.019*	0.040 ± *0.002*	0.0556
24.5	2.72 ± *0.05*	4.69 ± *0.05*	6272	1.13	0.000	0.763 ± *0.020*	0.043 ± *0.002*	0.0558
26.5	2.59 ± *0.05*	3.77 ± *0.04*	7100	1.11	0.000	0.723 ± *0.019*	0.040 ± *0.002*	0.0559
28.5	2.13 ± *0.02*	4.09 ± *0.04*	7421	0.99	0.000	0.771 ± *0.020*	0.043 ± *0.002*	0.0562
30.5	2.11 ± *0.02*	9.05 ± *0.09*	4950	0.54	0.000	0.692 ± *0.018*	0.039 ± *0.002*	0.0561
8.5 (Repeat)	2.77 ± *0.08*	33.74 ± *1.23*						

Table E.19 *Molybdenum isotope values and porewater chemistry in iron-rich pond sediments shown in Figure 4.2 and 4.5*

Iron-rich sediments					
Depth (cm)	δ^{98}**Mo (‰)**	**Mo (μg/g)**	**Mn (μg/g)**	**Fe (mg/g)**	**Al (mg/g)**
0.5	1.54 ± *0.02*	2.20 ± *0.02*	40.6	19.5	6.0
2.5	1.65 ± *0.04*	2.17 ± *0.02*	29.0	10.1	6.5
4.5	1.54 ± *0.04*	2.51 ± *0.02*	32.2	11.5	8.3
6.5	1.59 ± *0.03*	5.43 ± *0.04*	34.2	12.4	8.4
8.5	1.60 ± *0.03*	5.84 ± *0.05*	59.6	18.1	12.8
10.5	1.18 ± *0.03*	8.55 ± *0.07*	40.7	11.8	9.5
12.5	1.39 ± *0.04*	3.32 ± *0.03*	37.7	9.7	9.7
14.5	0.93 ± *0.02*	1.99 ± *0.02*	34.0	6.2	8.3
16.5	1.06 ± *0.02*	2.09 ± *0.02*	39.1	9.0	8.9
18.5	1.01 ± *0.02*	2.03 ± *0.02*	39.7	7.4	10.0
20.5	0.83 ± *0.02*	5.04 ± *0.04*	51.4	10.8	13.3
22.5	0.53 ± *0.02*	1.61 ± *0.01*	38.7	7.5	9.9
24.5	0.28 ± *0.05*	1.12 ± *0.01*	45.4	7.9	11.4
26.5	0.69 ± *0.05*	1.15 ± *0.01*	55.9	9.4	14.4
28.5	0.61 ± *0.05*	0.77 ± *0.01*	69.8	15.7	15.5
30.5	1.11 ± *0.02*	1.79 ± *0.01*	68.9	17.6	18.9
6.5 (repeat)	1.75 ± *0.02*	4.20 ± *0.04*	33.1	13.4	7.3
22.5 (repeat)	0.56 ± *0.02*	1.27 ± *0.01*	36.6	7.8	8.9
30.5 (repeat)	0.80 ± *0.02*	2.69 ± *0.02*	79.7	24.1	21.5
Phosphate-leached samples					
0.5	1.33 ± *0.03*	1.10 ± *0.01*	35.5	17.1	4.6
20.5	0.51 ± *0.03*	0.82 ± *0.01*	32.1	6.1	5.7
28.5	0.46 ± *0.02*	0.63 ± *0.00*	42.0	10.6	8.6

Table E.20 *Sedimentary Mo isotope composition and sedimentary concentrations of Mo, Mn, Fe and Al in iron-rich ponds shown in Figure 4.2 and 4.5*

Depth (cm)	δ^{98}Mo (‰)	Mo (ppb)	Mn (ppb)	Fe^{2+} (mM)	HS^- (mM)	Cl (mM)	SO_4 (mM)	SO_4/Cl
0 (pond)	2.20 ± *0.02*	10.72 ± *0.09*	17	0.000	0.00	0.532 ± *0.014*	0.027 ± *0.002*	0.050
1	2.28 ± *0.06*	49.17 ± *1.71*	159	0.002	0.633	0.972 ± *0.015*	0.049 ± *0.002*	0.050
3	2.61 ± *0.04*	5.04 ± *0.08*	107	0.001	3.396	0.854 ± *0.013*	0.037 ± *0.001*	0.044
5	1.95 ± *0.04*	2.41 ± *0.04*	14	0.001	4.592	0.800 ± *0.012*	0.032 ± *0.001*	0.040
7	1.72 ± *0.02*	1.57 ± *0.01*	3	0.001	4.938	0.636 ± *0.010*	0.021 ± *0.001*	0.033
9	1.64 ± *0.02*	1.74 ± *0.01*	0	0.001	4.662	0.608 ± *0.009*	0.020 ± *0.001*	0.032
11	2.03 ± *0.05*	2.17 ± *0.04*	5	0.001	4.131	0.609 ± *0.009*	0.021 ± *0.001*	0.034
13	1.98 ± *0.03*	2.01 ± *0.03*	4	0.001	3.829	0.586 ± *0.009*	0.019 ± *0.001*	0.033
15	1.94 ± *0.04*	1.58 ± *0.02*	19	0.001	4.800	0.537 ± *0.008*	0.016 ± *0.001*	0.029
17	1.65 ± *0.04*	1.87 ± *0.03*	78	0.002	4.166	0.543 ± *0.008*	0.015 ± *0.001*	0.028
19	1.54 ± *0.04*	1.96 ± *0.03*	134	0.002	4.211	0.550 ± *0.008*	0.016 ± *0.001*	0.029
21	1.57 ± *0.04*	2.19 ± *0.04*	222	0.002	3.946	0.564 ± *0.009*	0.016 ± *0.001*	0.028
23	1.33 ± *0.04*	3.74 ± *0.08*	309	0.002	3.730	0.555 ± *0.009*	0.015 ± *0.001*	0.026
25	1.61 ± *0.03*	1.55 ± *0.03*	443	0.002	3.301	0.574 ± *0.009*	0.015 ± *0.001*	0.026
27	0.74 ± *0.04*	1.16 ± *0.02*	562	0.002	2.388	0.567 ± *0.009*	0.015 ± *0.001*	0.026
29	1.20 ± *0.04*	1.38 ± *0.02*	684	0.001	2.520	0.562 ± *0.009*	0.015 ± *0.001*	0.026
31	0.71 ± *0.05*	1.07 ± *0.02*	764	0.002	3.037	0.543 ± *0.008*	0.014 ± *0.001*	0.026
33	-0.73 ± *0.04*	0.74 ± *0.01*	959	0.002	2.821	0.548 ± *0.008*	0.014 ± *0.001*	0.026
35	-1.87 ± *0.05*	0.28 ± *0.00*	1114	0.002	1.355	0.551 ± *0.008*	0.014 ± *0.001*	0.026
37	-1.66 ± *0.06*	0.25 ± *0.00*	1248	0.004	1.151	0.559 ± *0.009*	0.015 ± *0.001*	0.028

Table E.21 *Molybdenum isotope values and porewater chemistry in sulfide-rich pond sediments shown in Figure 4.2 and 4.5*

Depth (cm)	Ba (M)	Ca (M)	K (M)	Li (M)	Mg (M)	Na (M)	S (M)	Sr (M)	pH
1	7.21E-05	2.26E-02	1.63E-02	4.25E-02	1.02E-01	8.08E-01	5.29E-02	1.81E-04	6.78
3	6.63E-05	2.11E-02	1.54E-02	3.90E-02	9.47E-02	7.64E-01	4.50E-02	1.68E-04	6.93
5	6.84E-05	1.83E-02	1.35E-02	3.18E-02	7.87E-02	6.56E-01	3.17E-02	1.45E-04	6.97
7	7.21E-05	1.59E-02	1.15E-02	2.55E-02	6.64E-02	5.53E-01	2.32E-02	1.26E-04	7.04
9	7.14E-05	1.46E-02	1.01E-02	2.20E-02	6.00E-02	4.85E-01	1.96E-02	1.14E-04	7.11
11	6.04E-05	1.42E-02	9.87E-03	2.18E-02	5.97E-02	4.73E-01	1.91E-02	1.12E-04	7.17
13	9.25E-05	1.36E-02	9.21E-03	2.03E-02	5.68E-02	4.42E-01	1.71E-02	1.06E-04	7.08
15	4.81E-05	1.32E-02	9.03E-03	1.94E-02	5.61E-02	4.35E-01	1.64E-02	1.05E-04	7.03
17	3.79E-05	1.27E-02	8.75E-03	1.84E-02	5.45E-02	4.20E-01	1.55E-02	1.00E-04	7.03
19	4.30E-05	1.29E-02	8.85E-03	1.83E-02	5.54E-02	4.25E-01	1.55E-02	1.03E-04	7.02
21	3.71E-05	1.27E-02	8.57E-03	1.77E-02	5.44E-02	4.17E-01	1.50E-02	1.00E-04	7.18
23	2.84E-05	1.28E-02	8.62E-03	1.76E-02	5.50E-02	4.20E-01	1.50E-02	1.02E-04	7.25
25	3.71E-05	1.30E-02	8.75E-03	1.73E-02	5.63E-02	4.29E-01	1.50E-02	1.03E-04	7.30
27	1.60E-05	1.26E-02	8.18E-03	1.60E-02	5.33E-02	4.05E-01	1.43E-02	9.82E-05	7.39
29	1.24E-05	1.25E-02	8.26E-03	1.58E-02	5.33E-02	4.06E-01	1.45E-02	9.70E-05	7.40
31	9.47E-06	1.20E-02	8.11E-03	1.54E-02	5.16E-02	3.95E-01	1.38E-02	9.47E-05	7.39
33	1.09E-05	1.29E-02	8.75E-03	1.67E-02	5.51E-02	4.23E-01	1.47E-02	1.00E-04	7.37
35	4.37E-06	1.30E-02	8.82E-03	1.70E-02	5.53E-02	4.23E-01	1.52E-02	1.00E-04	7.45
37	2.91E-06	1.27E-02	8.39E-03	1.61E-02	5.28E-02	4.03E-01	1.46E-02	9.70E-05	7.59

Table E.22 *Major cation and pH measurements in sulfide-rich pond sediment porewater.*

Sulfide-rich sediments					
Depth (cm)	δ^{98}**Mo (‰)**	**Mo (μg/g)**	**Mn (μg/g)**	**Fe (μg/g)**	**Ti (μg/g)**
3	1.76 ± *0.05*	1.84 ± *0.02*	29.2	5447	48.2
7	1.86 ± *0.04*	2.64 ± *0.02*	41.6	6429	54.7
11	1.89 ± *0.05*	3.44 ± *0.03*	36.4	5477	45.0
15	1.73 ± *0.05*	4.54 ± *0.04*	69.5	8613	57.6
19	1.70 ± *0.04*	4.27 ± *0.04*	88.2	10075	65.7
23	1.52 ± *0.04*	3.31 ± *0.03*	98.7	8550	68.9
27	1.37 ± *0.04*	3.15 ± *0.03*	59.5	7398	72.1
31	0.98 ± *0.04*	2.38 ± *0.02*	51.9	7663	89.5
35	1.92 ± *0.06*	2.78 ± *0.02*	80.3	13152	110.2
19 (Repeat)	1.74 ± *0.06*	3.81 ± *0.03*	74.4	9075	58.8

Table E.23 *Sedimentary Mo isotope composition and sedimentary concentrations of Mo, Mn, Fe and Ti in sulfide-rich ponds shown in Figure 4.2 and 4.5*

Depth (cm)	δ^{98}Mo (‰)	Mo (ppb)	Mn (ppb)	Fe^{2+} (mM)	HS^- (mM)	Cl (mM)	SO_4 (mM)	SO_4/Cl
0 (Pond)	2.36 ± *0.03*	8.37 ± *0.07*	16.4	0.0		0.533 ± *0.014*	0.027 ± *0.002*	0.051
2	3.01 ± *0.03*	3.88 ± *0.07*	296	0.008	5.17	1.018 ± *0.016*	0.041 ± *0.001*	0.040
4	-0.19 ± *0.03*	1.00 ± *0.01*	113	0.003	8.97	0.880 ± *0.014*	0.030 ± *0.000*	0.034
6	0.07 ± *0.03*	0.96 ± *0.01*	20	0.003	8.60	0.747 ± *0.011*	0.023 ± *0.000*	0.031
8	0.46 ± *0.08*	1.83 ± *0.03*	8	0.001	7.15	0.650 ± *0.010*	0.020 ± *0.000*	0.031
10	-0.50 ± *0.07*	1.22 ± *0.02*	1	0.002	5.92	0.594 ± *0.009*	0.018 ± *0.000*	0.030
12	0.16 ± *0.07*	1.43 ± *0.02*	-11	0.002	5.90	0.580 ± *0.009*	0.018 ± *0.000*	0.031
14	-0.01 ± *0.03*	1.09 ± *0.02*	-3	0.001	5.26	0.555 ± *0.009*	0.017 ± *0.000*	0.031
16	1.42 ± *0.03*	2.91 ± *0.05*	-3	0.001	5.88	0.559 ± *0.009*	0.018 ± *0.000*	0.032
18	0.59 ± *0.10*	9.24 ± *0.17*	6	0.001	4.34	0.541 ± *0.008*	0.017 ± *0.000*	0.032
20	0.63 ± *0.10*	62.83 ± *1.21*	27	0.001	2.99	0.544 ± *0.008*	0.017 ± *0.000*	0.032
22	0.77 ± *0.10*	100.97 ± *1.98*	31	0.002	2.78	0.568 ± *0.009*	0.018 ± *0.000*	0.032
24	1.62 ± *0.06*	35.42 ± *0.72*	33	0.001	2.56	0.551 ± *0.008*	0.018 ± *0.000*	0.032
26	1.77 ± *0.04*	6.42 ± *0.11*	54	0.001	2.52	0.560 ± *0.009*	0.018 ± *0.000*	0.032
28	1.63 ± *0.02*	8.89 ± *0.13*	64	0.001	2.74	0.555 ± *0.009*	0.018 ± *0.000*	0.032
30	1.27 ± *0.04*	10.83 ± *0.21*	73	0.001	2.23	0.557 ± *0.009*	0.018 ± *0.000*	0.032
32	1.32 ± *0.04*	7.10 ± *0.14*	104	0.002	1.94	0.555 ± *0.009*	0.018 ± *0.000*	0.032
34	1.39 ± *0.04*	6.58 ± *0.14*	109		1.17	0.569 ± *0.009*	0.018 ± *0.000*	0.032

Table E.24 *Molybdenum isotope values and porewater chemistry in intermediate pond sediments shown in Figure 4.2 and 4.5*

Depth (cm)	Ba (M)	Ca (M)	K (M)	Li (M)	Mg (M)	Na (M)	S (M)	Sr (M)	pH
0 (Pond)									
2	1.7E-04	2.0E-02	1.5E-02	3.7E-02	9.6E-02	7.6E-01	4.4E-02	1.7E-04	6.83
4	9.1E-05	1.7E-02	1.3E-02	3.0E-02	7.8E-02	6.4E-01	2.9E-02	1.4E-04	6.85
6	9.3E-05	1.4E-02	1.1E-02	2.4E-02	6.4E-02	5.3E-01	2.1E-02	1.2E-04	6.87
8	7.9E-05	1.3E-02	9.7E-03	2.1E-02	5.7E-02	4.7E-01	1.8E-02	1.1E-04	6.95
10	5.9E-05	9.1E-03	6.6E-03	1.4E-02	4.1E-02	3.2E-01	1.3E-02	7.5E-05	7.05
12	5.8E-05	9.6E-03	7.0E-03	1.5E-02	4.3E-02	3.4E-01	1.4E-02	7.9E-05	7.03
14	6.3E-05	1.1E-02	8.0E-03	1.8E-02	4.9E-02	3.8E-01	1.6E-02	8.9E-05	6.90
16	6.1E-05	1.1E-02	8.6E-03	1.9E-02	5.2E-02	4.1E-01	1.7E-02	9.5E-05	6.87
18	5.0E-05	1.0E-02	7.5E-03	1.6E-02	4.6E-02	3.6E-01	1.6E-02	8.3E-05	6.95
20	6.1E-05	1.2E-02	9.4E-03	2.0E-02	5.6E-02	4.3E-01	1.9E-02	9.9E-05	7.09
22	6.6E-05	1.1E-02	8.8E-03	1.9E-02	5.3E-02	4.1E-01	1.8E-02	9.5E-05	7.23
24	6.5E-05	1.2E-02	9.0E-03	1.9E-02	5.3E-02	4.2E-01	1.8E-02	9.6E-05	7.10
26	6.7E-05	1.2E-02	9.1E-03	1.9E-02	5.5E-02	4.3E-01	1.9E-02	9.8E-05	7.16
28	5.7E-05	1.2E-02	9.0E-03	1.9E-02	5.3E-02	4.2E-01	1.8E-02	9.5E-05	7.21
30	5.9E-05	1.2E-02	8.9E-03	1.8E-02	5.3E-02	4.1E-01	1.8E-02	9.5E-05	7.29
32	6.0E-05	1.2E-02	9.3E-03	1.9E-02	5.4E-02	4.3E-01	1.8E-02	9.7E-05	7.41
34	7.5E-05	1.1E-02	8.7E-03	1.7E-02	5.0E-02	4.0E-01	1.7E-02	9.1E-05	7.41

Table E.25 *Major cation and pH measurements in intermediate pond sediment porewater.*

Sulfide-rich sediments					
Depth (cm)	**δ^{98}Mo (‰)**	**Mo (μg/g)**	**Mn (μg/g)**	**Fe (μg/g)**	**Ti (μg/g)**
2	1.80 ± *0.05*	2.67 ± *0.02*	34.4	5513	52.2
6	1.66 ± *0.05*	3.46 ± *0.03*	33.2	5551	47.2
10	1.87 ± *0.04*	4.05 ± *0.03*	38.9	6285	52.3
14	1.87 ± *0.05*	4.51 ± *0.04*	41.4	7249	53.8
18	1.50 ± *0.04*	4.76 ± *0.04*	48.1	7907	59.3
22	1.41 ± *0.04*	2.97 ± *0.02*	37.1	7351	67.0
26	1.53 ± *0.06*	3.62 ± *0.03*	28.2	11336	66.0
30	1.67 ± *0.05*	3.78 ± *0.03*	49.3	13481	93.5
34	1.76 ± *0.04*	4.21 ± *0.04*	46.9	10895	88.4

Table E.26 *Sedimentary Mo isotope composition and sedimentary concentrations of Mo, Mn, Fe and Ti in intermediate ponds shown in Figure 4.2 and 4.5*

Depth (cm)	Ionic Strength (M)	Activity coefficient	[H_2S]	yMoS	AMS3	Predicted Mo (nM)	Measured Mo (nM)
1	1.27	0.50	0.0003	0.023	0.037	4.1	512.4
3	1.14	0.44	0.0016	0.027	0.008	31.6	52.5
5	1.01	0.39	0.0020	0.034	0.007	38.6	25.1
7	0.82	0.34	0.0020	0.042	0.007	41.9	16.4
9	0.75	0.33	0.0017	0.047	0.008	45.3	18.1
11	0.75	0.32	0.0013	0.047	0.010	48.0	22.6
13	0.71	0.32	0.0014	0.049	0.009	31.5	21.0
15	0.67	0.31	0.0019	0.050	0.007	33.0	16.5
17	0.66	0.31	0.0017	0.052	0.008	27.9	19.5
19	0.67	0.31	0.0017	0.051	0.008	28.2	20.4
21	0.67	0.31	0.0013	0.052	0.010	42.5	22.9
23	0.67	0.31	0.0011	0.051	0.012	50.1	38.9
25	0.68	0.31	0.0009	0.050	0.015	52.6	16.2
27	0.66	0.31	0.0005	0.053	0.024	48.1	12.1
29	0.66	0.31	0.0006	0.053	0.023	51.4	14.4
31	0.64	0.30	0.0007	0.054	0.019	59.0	11.2
33	0.66	0.31	0.0007	0.051	0.020	55.0	7.7
35	0.66	0.31	0.0003	0.051	0.045	33.6	2.9
37	0.65	0.31	0.0002	0.053	0.068	41.9	2.7

Table E.27 *odel inputs used for the model described by Helz et al. (2011) (see paper for definitions of terms) to predict Mo concentrations in sulfide-rich pond sediment porewaters. Data is plotted in Figure 4.8*

Depth (cm)	Ionic Strength (M)	Activity coefficient	[H_2S]	yMoS	AMS3	Predicted Mo (nM)	Measured Mo (nM)
2	1.23	0.48	0.0027	0.025	0.005	36.9	40.4
4	1.03	0.40	0.0045	0.034	0.003	50.9	10.4
6	0.86	0.35	0.0042	0.043	0.003	40.8	10.0
8	0.75	0.33	0.0032	0.049	0.004	39.5	19.1
10	0.60	0.30	0.0023	0.066	0.006	33.5	12.8
12	0.61	0.30	0.0024	0.063	0.006	32.9	14.9
14	0.63	0.30	0.0025	0.057	0.005	21.1	11.3
16	0.66	0.31	0.0029	0.054	0.005	22.6	30.3
18	0.61	0.30	0.0019	0.060	0.007	19.7	96.3
20	0.67	0.31	0.0011	0.051	0.012	25.1	654.8
22	0.67	0.31	0.0008	0.053	0.016	34.5	1052.3
24	0.66	0.31	0.0009	0.053	0.014	21.5	369.1
26	0.68	0.31	0.0008	0.052	0.016	26.0	67.0
28	0.67	0.31	0.0008	0.053	0.015	32.3	92.7
30	0.66	0.31	0.0006	0.053	0.022	33.1	112.9
32	0.67	0.31	0.0004	0.052	0.030	42.1	74.0
34	0.66	0.31	0.0003	0.055	0.049	24.4	68.6

Table E.28 *odel inputs used for the model described by Helz et al. (2011) (see paper for definitions of terms) to predict Mo concentrations in intermediate pond sediment porewaters. Data is plotted in Figure 4.8*

Iron-rich pond sediment				Sulfide-rich pond sediment			
Depth (cm)	**pH**	**Fe^{2+} (mM)**	**HS^- (mM)**	**Depth (cm)**	**pH**	**Fe^{2+} (mM)**	**HS^- (mM)**
0.5	6.89	0.510	0.000	0.5	6.66	0.001	1.055
2.5	6.81	0.465	0.002	2.5	6.71	0.000	2.345
4.5	6.89	0.339	0.000	4.5	6.76	0.001	4.066
6.5	6.78	0.306	0.000	6.5	6.89	0.001	4.640
8.5	6.67	0.286	0.000	8.5	7.00	0.001	4.898
10.5	6.60	0.277	0.001	10.5	7.06	0.002	3.280
12.5	6.60	0.383	0.001	12.5	7.03	0.001	3.901
14.5	6.51	0.365	0.001	14.5	7.03	0.001	4.233
16.5	6.51	0.336	0.001	16.5	7.12	0.000	4.184
18.5	6.42	0.195	0.002	18.5	7.04	0.000	4.170
20.5	6.42	0.262	0.001	20.5	7.09	0.001	3.919
22.5	6.46	0.300	0.001	22.5	7.10	0.000	3.098
24.5	6.41	0.286	0.000	24.5	7.11	0.000	3.508
26.5		0.557	0.001	26.5	7.14	0.001	3.083
28.5	6.47	0.680	0.000	28.5	7.16	0.000	2.108
30.5	6.26	0.746	0.000	30.5	7.23	0.000	1.688
32.5	6.48	0.858	0.000	32.5	7.25	0.000	1.988
				34.5	7.30	0.000	1.262
				36.5	7.37	0.001	0.474

Table E.29 *Porewater pH, ferrous iron concentrations and sulfide concentrations in the pond sediments collected for Cr isotope analysis. Data shown in Figure 5.4*

Depth (cm)	Mo (μg/g)	U (μg/g)	V (μg/g)	Co (μg/g)	Ni (μg/g)	Al (μg/g)	Fe (μg/g)	Mn (μg/g)	Ti (μg/g)
0	3.38	2.04	135.59	16.76	1.11	38177	70826	348.66	708.52
2	3.72	2.47	148.38	16.98	1.18	42937	72848	268.81	781.36
4	4.13	2.97	134.16	16.89	1.15	36748	63024	245.67	686.03
6	5.05	3.29	131.87	17.13	1.18	35777	59482	242.49	686.75
8	6.14	3.45	139.64	16.43	1.14	43004	55985	228.91	806.41
10	8.35	3.64	139.12	15.37	1.08	45622	57910	203.87	874.75
12	7.50	2.78	108.17	14.51	0.93	27956	49582	180.62	567.64
14	9.12	3.56	117.48	14.91	0.99	30526	50173	178.67	508.80
16	10.85	4.39	119.67	17.80	1.17	29918	45721	178.37	554.39
18	6.84	4.54	145.27	19.08	1.26	41719	46274	233.26	720.00
20	5.44	3.03	145.68	17.96	2.60	44697	39360	198.51	817.98
22	10.28	4.74	159.57	23.43	1.34	46617	54285	246.12	822.52
24	8.79	4.15	143.75	22.25	1.26	38498	49225	273.46	494.47
26	7.43	3.40	142.65	19.04	1.14	48832	50168	249.16	771.99
28	2.88	3.73	133.02	18.27	1.12	45983	43098	261.13	654.07
30	1.25	1.75	153.75	17.47	1.07	47275	56878	283.36	660.36
32	1.87	2.01	148.57	16.57	1.03	45738	49487	258.21	612.92
34	2.91	2.30	150.63	15.94	0.99	38049	51960	241.14	535.52
2 (repeat)	3.36	2.03	122.02	14.49	0.96	30135	75936	243.77	681.80
14 (repeat)	8.05	3.49	119.61	13.86	0.92	30741	51204	175.26	639.30
28 (repeat)	4.17	3.96	147.74	17.72	1.13	49450	47859	252.43	816.05

Table E.30 *Metal concentrations in sediments from the iron-rich pond sediment core for Cr isotope determination. Data shown in Figure 5.6*

Depth (cm)	Mo (μg/g)	U (μg/g)	V (μg/g)	Co (μg/g)	Ni (μg/g)	Al (μg/g)	Fe (μg/g)	Mn (μg/g)	Ti (μg/g)
0	11.15	2.64	125.78	19.75	1.16	43593	51758	484.45	848.18
2	10.47	2.87	98.17	16.49	0.98	39082	44247	313.71	780.22
4	12.82	3.41	101.36	18.80	1.17	34656	49074	393.12	744.34
6	13.81	3.35	107.77	17.82	1.04	37394	48143	422.42	760.79
8	16.55	3.70	86.00	16.57	0.89	23185	48496	453.48	485.53
10	16.58	4.22	120.55	20.49	1.18	34489	59476	483.48	692.26
12	12.35	3.91	146.76	22.50	1.83	52679	63029	666.22	1021.88
14	9.81	3.30	131.93	20.48	1.18	41737	57931	502.19	781.10
16	10.67	3.92	149.37	24.58	1.40	44019	69896	553.24	873.45
18	8.71	2.98	128.16	19.96	1.19	33689	57513	546.61	625.50
20	7.93	3.00	142.33	21.52	1.33	38606	65716	536.29	571.05
22	7.63	2.72	141.84	19.02	1.22	43174	60205	425.51	767.57
24	6.73	2.66	139.06	19.11	1.17	48019	59620	426.74	824.60
26	8.29	3.01	139.57	18.60	1.14	41421	57577	389.73	670.31
28	6.08	2.71	110.40	17.28	1.12	31678	49202	299.94	463.78
30	8.31	4.01	142.78	17.07	1.08	37322	56875	322.71	574.19
32	9.46	3.11	131.94	19.13	1.20	46282	66901	383.32	706.91
34	6.98	3.02	119.54	17.04	1.12	38564	56271	325.44	555.69
36	4.87	2.67	102.78	17.86	1.15	31618	53552	328.00	452.11
4 (repeat)	11.99	3.07	94.02	15.95	1.00	31496	43808	334.61	556.75
30 (repeat)	9.08	4.69	162.04	16.86	1.07	29651	56447	323.44	550.12

Table E.31 *Metal concentrations in sediments from the sulfide-rich pond sediment core for Cr isotope determination. Data shown in Figure 5.6*